Efficient Single Photon Collection for Single Atom Quantum Nodes

Robert Sebastian Garthoff

München 2021

Efficient Single Photon Collection for Single Atom Quantum Nodes

Robert Sebastian Garthoff

Dissertation
an der Fakultät für Physik
der Ludwig–Maximilians–Universität
München

vorgelegt von
Robert Sebastian Garthoff
aus München

München, den 27.09.2021

Erstgutachter: Prof. Dr. Harald Weinfurter
Zweitgutachter: Prof. Dr. Jörg Schreiber
Tag der mündlichen Prüfung: 18.11.2021

Zusammenfassung

Zu Beginn des 20. Jahrhunderts führte die Entwicklung der Quantenmechanik revolutionäre neue Konzepte ein, die bisher in der klassischen Physik kein Pendant fanden. Eine faszinierende Neuerung ist das Phänomen der Verschränkung. Es beschreibt einen nicht-separablen Zustand zwischen zwei oder mehr Quantensystemen, welcher eine spezielle Verbindungsart aufweist, die nicht-lokale Korrelationen zwischen den Teilchen unabhängig von ihrer Entfernung ermöglicht. Diese kontraintuitiven Konsequenzen stehen einigen etablierten klassischen Vorstellungen einer lokal-realistischen Weltanschauung entgegen, woraus sich grundlegende Diskussionen über die Interpretation der Quantenmechanik ergaben. Mit der Etablierung der Quantenmechanik, führten ihre einzigartigen Merkmale zu einem völlig neuen Forschungsfeld der Quanteninformationswissenschaft, welche eine Vielzahl möglicher Quantentechnologien mit Verschränkung als Schlüsselressource hervorbrachte. Darüber hinaus ist die Verschränkung getrennter stationärer Quantenspeicher das zentrale Element zur Realisierung eines Quantennetzwerks.

Diese Arbeit berichtet über signifikante Verbesserungen einer Quantennetzwerkverbindung, die auf der Verschränkung zwischen zwei Rubidium-87 Atomen basiert, welche in getrennten Laboren in einem Abstand von 398 m gefangen werden. Die Verschränkung der Atome wird unter Verwendung des 'entanglement swapping' Protokolls erzeugt. Zunächst wird der Spin jedes der Atome mit der Polarisation eines Photons verschränkt, welches bei einem spontanen Zerfall des Atoms emittiert wurde. Anschließend werden die emittierten Photonen in Einzelmoden-Fasern eingekoppelt, die zu einem Bellzustandsanalysator führen. Durch die Projektion der Photonen auf einem Bell-Zustand werden dann die Atome miteinander verschränkt. In diesem Schema ist die Atom-Atom-Verschränkungsrate durch die Effizienz begrenzt, mit der Licht aus Quantenspeichern aufgesammelt und in Einzelmoden-Fasern eingekoppelt wird. Die Qualität der verwendeten Optik ist also von großer Bedeutung.

Um eine signifikante Verbesserung zu erreichen, wurden neue Objektiv-Aufbauten mit hoch-NA Linsensystemen entworfen und implementiert. Es wurde dazu ein detailliertes Modell entwickelt, das den Aufsammel- und Kopplungsprozess einzelner emittierter Photonen beschreibt, wodurch die Auswahl geeigneter Optiken für die neuen Objektiv-Aufbauten ermöglicht wurde. Ferner wurden die Objektive vollständig charakterisiert und Justage-Kriterien für einen beugungsbegrenzten Betrieb spezifiziert. Zudem wurden verschiedene Justage-Methoden und -Werkzeuge für die Implementierung entwickelt, um eine optimale Leistung zu gewährleisten. Die lokalen Kopplungseffizienzen konnten dadurch um den Faktor ~ 2,5 und ~ 3,5 für das System in Labor 1 bzw. Labor 2 gesteigert werden, was zur Verbesserung der Atom-Atom-Verschränkungseffizienz um einen Faktor von ~ 6,5 im Vergleich zu früheren Messungen führt. Die damit verbundene gesteigerte Atom-Atom-Verschränkungsrate ermöglicht es die Messdauer deutlich zu verkürzen, wodurch die Präzision der Experimente gesteigert werden kann.

Die Verbesserung der Aufsammeloptik ermöglichte zudem die Realisierung einer ersten Quantenkommunikationsanwendung, nämlich der Verteilung von Atom-Photon-Verschränkung über eine Länge von 20 km optischer Glasfaser mit einer Quantenzustandstreue von $78.5 \pm 0.9\,\%$. Um die Transmissionsverluste des Einzelphotons in der Glasfaser bei seiner Emissionwellenlänge von 780 nm zu überwinden, wurde die Wellenlänge des Photons mit Hilfe von Quantenfrequenzkonversion in den Telekom-Wellenlängenbereich zu 1522 nm umgewandelt. Dies stellt einen wichtigen Schritt für den

nächsten Meilenstein des Experiments dar, welcher die Vergrößerung der Distanz der Quantennetzwerkverbindung umfasst.
Des Weiteren wird in dieser Arbeit ein Test der Bell'schen Ungleichung vorgestellt, der mit der Quantennetzwerkverbindung durchgeführt wurde, bevor diese mit den besseren Aufsammlungsoptiken aufgerüstet war. Daher kann diese Messung als Referenz für die Systemleistung in Bezug auf Verschränkungsrate und Quantenzustandstreue dienen. Durch die Sicherstellung raumartig getrennter Messungen und der Verwendung eines 'Ereignis-bereiten' ('event-ready') Verschränkungsschemas wurden das Lokalitäts- und Detektionsschlupfloch gleichzeitig geschlossen. Eine Messung von 10000 verschränkten Atom-Atom-Paaren ergab einen CHSH S-Parameter von $S = 2.221 \pm 0.033$, was mit einer statistischen Signifikanz (P-Wert) von $1.739 \cdot 10^{-10}$ zu einer starken Ablehnung des lokalen Realismus führt.

Abstract

In the early 20th century, the development of quantum mechanics introduced revolutionary new concepts that have no counterpart in classical physics. One fascinating new feature is the phenomenon of entanglement. It describes a non-separable state between two or more quantum systems with a particular type of connection, which allows for non-local correlations between the particles independent of their separation. These counter-intuitive consequences oppose some well-established classical ideas of a local-realistic world view, which led to fundamental discussions about the interpretation of quantum mechanics. However, once quantum mechanics was established, its unique features gave rise to an entirely new research field of quantum information science that brought up a wide variety of possible quantum technologies with entanglement as an essential resource. Moreover, entanglement between distant stationary quantum memories is the central element for realizing a quantum network. This work reports on significant improvements of a quantum network link, which is based on the entanglement between two Rubidium-87 atoms trapped in separated laboratories 398 m apart. The entanglement of the atoms is generated by utilizing the entanglement swapping protocol. First, the spin of each atom is entangled with the polarization of a photon emitted in a spontaneous decay of the atom. Afterwards, the emitted photons are coupled into single-mode fibers that guide them to a Bell state measurement setup, where a joint measurement of the photons projects the atoms onto an entangled state. In this scheme, the atom-atom entanglement rate is limited by the efficiency of collecting light from the quantum memories and coupling it into single-mode fibers. Hence, the quality of the employed optics is of great importance.

In order to achieve a significantly improved performance, new objective setups with high-NA lens systems were designed and implemented. For this purpose, a detailed model was developed that describes the collection and coupling process of single emitted photons, which allowed selecting suitable optics for the new objective setups. Further, the objectives were fully characterized, and alignment criteria for a diffraction-limited operation were specified. In addition, several alignment methods and tools were developed that guarantee an implementation yielding an optimal performance. As a result, the local coupling efficiencies could be increased by a factor of ~ 2.5 and ~ 3.5 for the system in Lab 1 and Lab 2, respectively. This improved the atom-atom entanglement efficiency by a factor of ~ 6.5 compared to previous measurements. The associated increase in the atom-atom entanglement rate makes it possible to shorten the measurement time significantly and thus allows for enhanced precision of the experiments.

The improved collection optics enabled the realization of a first quantum communication application, namely the distribution of atom-photon entanglement over 20 km of optical fiber with a fidelity of $78.5 \pm 0.9\,\%$. For the implementation, it was essential to overcome the photon transmission losses in optical fibers for the emission wavelength of the single photon at 780 nm by employing quantum frequency conversion to the telecom wavelength at 1522 nm. This represents a crucial step towards the next milestone of the experiment, i.e. increasing the range of the quantum network link.

Furthermore, this thesis presents a test of Bell's inequality performed on the quantum network link before it was upgraded with better collection optics. Hence, this measurement can serve as a reference for the system performance in terms of entanglement rate and fidelity. The locality and the detection loophole were closed simultaneously by ensuring space-like separated measurements and using an

event-ready entanglement scheme. A measurement with 10000 entangled atom-atom pairs yielded a CHSH S-parameter of $S = 2.221 \pm 0.033$, allowing for a strong rejection of local realism with a statistical significance (P-value) of $1.739 \cdot 10^{-10}$.

Contents

1. Introduction

At the turn of the 20th century, technological progress enabled observations like the black-body radiation, the stability of atoms, and discrete atomic energy spectra, which could not be explained within the framework of classical physics. Hence, a more extensive theory was required to resolve these mysteries. In 1900, Max Planck formulated the law of black-body radiation by assuming a quantization of light-matter interaction in discrete energy packets of $h\nu$ [1], with the light frequency ν and a newly introduced fundamental constant h. This marked the starting point for the development of quantum mechanics, which in the following decades was developed further by Niels Bohr [2], Werner Heisenberg [3, 4], Erwin Schrödinger [5], and many others, enabling a consistent description of the problems mentioned above.

Quantum mechanics not only provided a more accurate description of nature but also introduced new concepts, which led to surprising and counter-intuitive consequences. For example, Heisenberg's uncertainty principle prohibits the simultaneous measurement of two non-commuting observables (e.g. position and momentum) with absolute precision. Moreover, before measuring a quantum system, quantum mechanics generally describes it as a coherent superposition of different states, which at the moment of measurement is projected onto an eigenstate of the measured observable. An especially fascinating new property is the concept of entanglement. Entangled particles are in a common quantum state, which cannot be described independently of one another. The particles show a particular type of connection, which immediately correlates the measurement result of one particle to the result of the other, independent of the distance between the particles. As their consequences oppose certain well-established classical ideas of a local-realistic world view, these controversial new concepts led to discussions about the interpretation of quantum mechanics, as can be seen in the historical debate between Niels Bohr and Albert Einstein [6]. Following this discussion, Albert Einstein, Boris Podolsky, and Nathan Rosen questioned the completeness of quantum mechanics in their famous EPR-paradox paper in 1935 [7], where they postulated the existence of so-called local hidden variables (LHV), which would extend quantum mechanics to a complete theory while maintaining the concept of local realism.

The controversy about the existence of LHV and the completeness of quantum mechanics continued for the coming years [8–10], however, merely on a theoretical level. In 1964 the situation changed when John Bell showed the possibility of testing the validity of LHV concepts experimentally [11]. He formulated his findings in the form of an inequality, which for all theories governed by local realism gives a strict bound on the result of correlation measurements performed on an entangled pair of particles. In contrast, the quantum mechanical prediction exceeds this bound for certain measurement settings. However, necessitating perfect correlations, Bell's inequality in its original formulation is experimentally impracticable. Clauser, Horne, Shimony, and Holt reformulated the inequality a few years later, making it more applicable for experiments [12]. In subsequent decades, many experiments violating the CHSH inequality were performed, e.g. [13–16], and by this contradicting a local-realistic description. However, all of these measurements were dependent on further assumptions that open up so-called loopholes [17] to the LHV theories allowing them at least in principle to explain the experimental outcomes. Only recently, experiments free from the most important loopholes could be conducted [18–21], which provide strong evidence against local realism.

Apart from this fundamental controversy, it was realized that the unique properties of quantum mechanics carry great potential for possible quantum technologies. This gave rise to the completely new research field of quantum information science, which over the years, brought up a wide variety of different quantum information protocols with entanglement as an essential resource. Some examples are, dense coding [22], quantum metrology [23], quantum computing [24, 25], quantum teleportation [26], entanglement swapping [27], and quantum key distribution [28]. Besides, there is a new type of so-called device-independent protocols, e.g. for quantum key distribution [29] and random number generation [30], which rely on the violation of Bell's inequality to obtain trusted results, albeit the measurement devices are faulty and possibly not trustworthy.

To utilize the full capacity of quantum information science, several of these protocols must be brought together within a future, large-scale quantum network [31], as it enables applications like distributed quantum computing and secure communication over long distances. The general structure of such a network consists of numerous stationary quantum bits (qubits), serving as quantum memories, which are connected via photonic quantum channels allowing for the exchange of quantum information. A central resource for quantum networks is the ability to share and distribute entanglement between separated quantum memories. Evidently, for this an efficient light-matter interface is mandatory. Here, the properties of the applied photon collection optics determine the rate at which quantum information can be exchanged and hence are of great importance. Possible candidates for quantum memories are, e.g., trapped neutral atoms [32, 33], trapped ions [34, 35], atomic ensembles [36–38], color centers in diamond [39, 40], quantum dots [41, 42] or rare-earth ions in solids [43, 44]. However, the range of the quantum connection is limited by photon loss in optical fibers. Even with recently developed tools of quantum frequency conversion [45, 46], which allow converting photons to the low loss telecom bands of optical fibers, the achievable range is still limited to distances of $< 100\,\mathrm{km}$. The development of a quantum repeater will therefore be essential for the scalability of a quantum network, as it allows to overcome this exponential photon loss [47]. Additionally, quantum repeater schemes utilize error correction protocols like entanglement distillation or state purification to counteract imperfections and state decoherence of the entanglement distribution.

This work presents the clear improvement of a quantum network link by designing and implementing high-NA photon collection optics. The enhanced performance of this link, which is based on the entanglement between two neutral Rubidium-87 atoms, enables the realization of a first quantum communication application, i.e. long-distance distribution of atom-photon entanglement over several kilometers using the tool of quantum frequency conversion.

This work's basic quantum network link uses single atoms as quantum memories trapped [48] in two separate laboratories 398 m apart. Entanglement between the atoms is generated in two steps. First, the spin of each atom is entangled with the polarization of a single photon emitted in the spontaneous decay of the atom [32, 49], which combines the storage and transmission capability of quantum information. Second, the entanglement of the atom-photon pairs is transferred to the atoms using the entanglement swapping protocol [27]. Therefore, both photons are coupled into single-mode fibers that guide the photons to a Bell state measurement setup, where a two-photon coincidence detection heralds a successful generation of atom-atom entanglement [50, 51]. Combined with a high fidelity and fast atomic state measurement [52], the quantum network link enables space-like separated measurements on the distant atoms [53], which is an essential requirement for a conclusive Bell test.

There are three main parts of the thesis. The first covers a Bell experiment performed using atom-atom entanglement distributed via the quantum network link described above. Here, the event-ready measurement scheme together with the ability of space-like separated measurements and the usage of quantum random number generators [54] for an independent setting choice allow violating Bell's inequality with both the locality and the detection loophole closed. Further, this enables refuting

local realism up to the so-called free will loophole, which would require the space-like separated generation of random numbers. The second part describes an upgrade of the system with improved high-NA collection optics relative to the ones used for the Bell test. Thematically, this contains a detailed model describing the collection and coupling process of the single photon into a single-mode fiber. With that, it is possible to find suitable optics to design the objective setups and estimate the expected performance. In addition, a complete characterization of the lens system is provided, which analyzes its optical quality in terms of wave aberrations and specifies alignment criteria for optimal performance. Also, details of the objectives' design, construction, and implementations are discussed, and their measured performance is compared to the previous system. Finally, a quantum communication application is presented in the third part, which is enabled by the improved collection optics, i.e. the distribution of atom-photon entanglement over up to 20 km of optical fiber. Quantum frequency conversion of the single photon wavelength to the telecom regime is realized in one of the laboratories to overcome the photon transmission losses. This manifests the first step towards a significantly increased distance between the entangled atoms, which requires another conversion system for the second laboratory and a Bell state measurement at telecom wavelength.
The thesis is structured as follows: Chapter 2 describes the experimental setup and methods employed to trap single atoms, generate atom-photon and atom-atom entanglement, and measure the atomic states. In Chapter 3, the experimental realization and the results of the Bell test are shown, which allow for a significant violation of Bell's inequality and providing strong evidence against local realism. Moreover, a detailed statistical analysis of all bits generated by the quantum random number generator during the Bell test is performed, which allows identifying potential artifacts or malfunctioning of the generators. The following three chapters focus on the improved collection optics. While Chapter 4 covers the model of the photon collection and coupling process, Chapter 5 contains a complete characterization of a high-NA objective in terms of wave aberrations, which would limit the achievable coupling efficiency. Chapter 6 concludes this discourse by providing details about the new objective setups, their design and implementation, and an analysis of the increased performance. Finally, enabled by the upgraded system, Chapter 7 reports on realizing long-distance atom-photon entanglement distribution over up to 20 km of optical fiber by employing quantum frequency conversion of the spontaneously emitted single photon to the telecom wavelength regime.

2. Long-Distance Entanglement of Two Rubidium-87 Atoms

The generation of long-distance entanglement of quantum memories is one of the major requirements for future scalable quantum networks. In this thesis, the entanglement swapping protocol is utilized to generate heralded entanglement between two atomic qubits located in two laboratories separated by a distance of $398\,\mathrm{m}$ (Fig.2.1). This process involves several experimental steps and a high level of control over the quantum systems.
In this chapter, the experimental methods and theoretical concepts relevant for understanding the experiment are discussed. It starts by introducing the physical properties of ^{87}Rb-atoms, which will be used as quantum memories. After that, the experimental setup and the techniques needed for trapping single atoms and controlling and measuring their atomic spin states are explained. Finally, the chapter concludes with a description of the entanglement process of the two remote atoms.

2.1. Quantum Memory on ^{87}Rb

A single neutral Rubidium-87 atom constitutes a suitable candidate for a quantum memory, as it offers a stable ground state, in which a qubit can be encoded and relatively long coherence times can be achieved. Furthermore, the atom provides a light-matter interface, which allows distributing entanglement over long distances. Here, the spontaneous decay of an excited atom is used to generate entanglement between its Zeeman spin state and the polarization state of the emitted photon (Subsec. 2.3.2), which can be distributed over long distances via optical fibers. By these means, it is possible to interconnect two remote quantum memories in an event-ready scheme (Sec. 2.6). In such schemes, the atomic state readout will only be initiated after a so-called 'heralding' signal indicates a successful atom-atom entanglement generation. Coherence times of the quantum memories longer than the signal transmission time are therefore desirable, which can be provided by the stable and well-controlled ground state. Finally, the rubidium atom provides the possibility to implement a high fidelity atomic state readout (Sec. 2.4.2), which is useful in any case but especially for a test of Bell's inequality, it is also required to be very fast to ensure space-like separation.

Rubidium-87 is an alkaline atom with only one valence electron. As such, it has a relatively simple and well understood hydrogen-like level structure, which offers all necessary optical transitions for cooling, trapping and coherent control of the quantum system (e.g. state preparation and analysis). All relevant energy levels are shown in Fig. 2.2. The ground state is denoted as $5^2S_{1/2}$ and the first excited state as 5^2P, which splits up due to fine-structure splitting into two levels $5^2P_{1/2}$ and $5^2P_{3/2}$. Transitions from the ground state to these two excited states are named D1- and D2-line, respectively. The nuclear spin $I = 3/2$ leads to further splittings into hyperfine levels, which are for the $5^2S_{1/2}$ ground state the two levels $F = 1, 2$ and for the excited states $5^2P_{1/2}$ and $5^2P_{3/2}$ the levels $F' = 1, 2$ and $F' = 0, 1, 2, 3$, respectively. Each hyperfine level is divided into Zeeman states with the quantum number m_F, which in the following will be written for the ground state F as $|F, m_F\rangle$ and for the excited state F' as $|F', m_{F'}\rangle$. These states are degenerate in the absence of external electromagnetic fields.

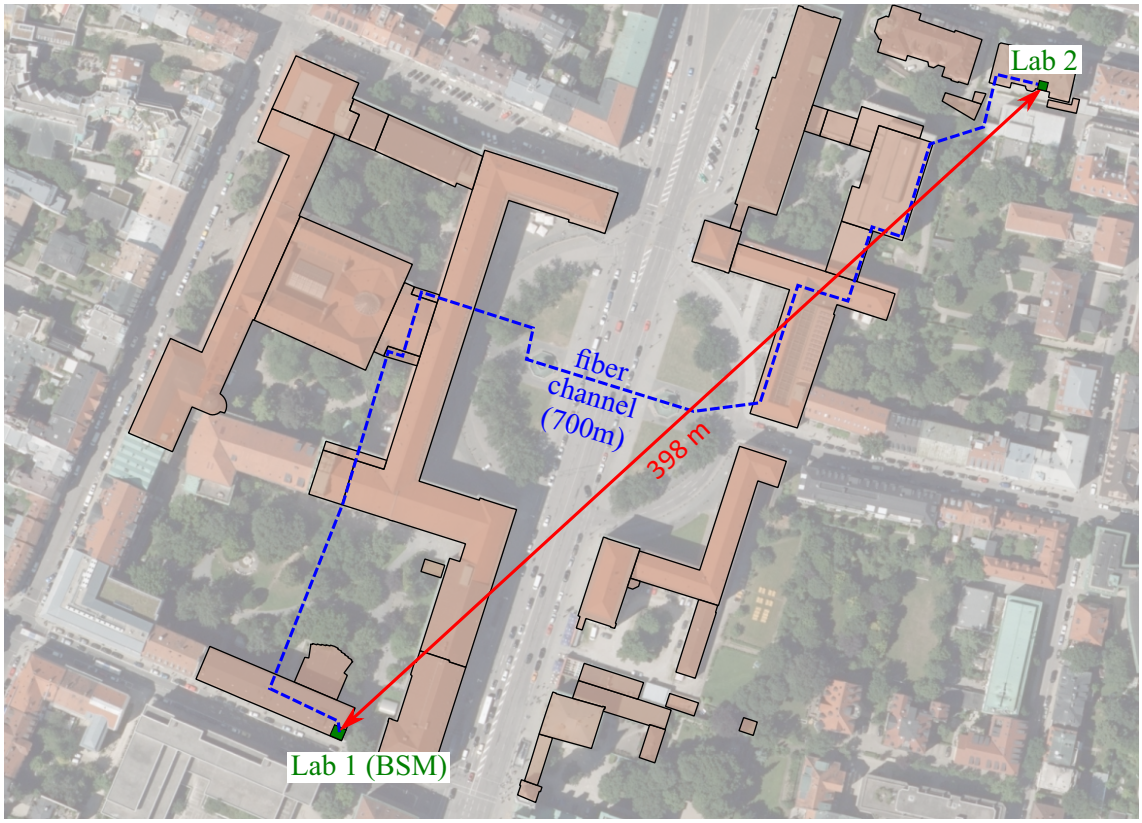

Figure 2.1.: The laboratories (Lab 1 and Lab 2) are located in different buildings at the main campus of the Ludwig-Maximilians-Universität in Munich. They have a separation of $398\,\mathrm{m}$ and are connected with a $700\,\mathrm{m}$ long fiber channel [21, 53, 55]. This channel contains several optical fibers to establish communication and synchronization between the trap setups and guide the fluorescence emitted by the atoms. The map data is provided by the 'Bayerisches Landesamt für Digitalisierung, Breitband und Vermessung'.

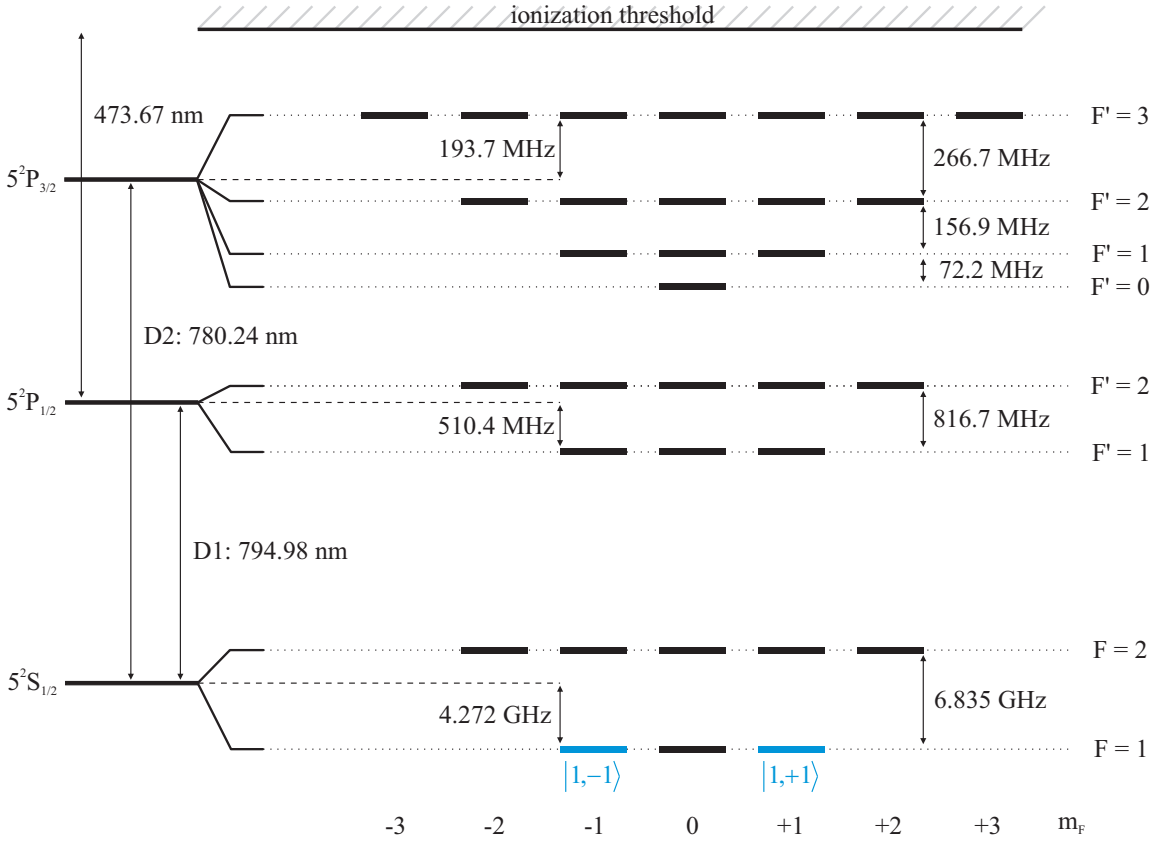

Figure 2.2.: Energy level structure of ^{87}Rb [56]. The ground state $5^2S_{1/2}$ splits into the hyperfine-levels $F = 1$ and $F = 2$. The first excited state 5^2P splits due to fine structure and hyperfine structure splitting into the levels $5^2P_{1/2}$, $F' = 1, 2$ and $5^2P_{3/2}$, $F' = 0, 1, 2, 3$. Each of the hyperfine levels is subdivided into Zeeman sublevels with the quantum number m_F. The wavelength of the transition from $5^2S_{1/2}$ to $5^2P_{1/2}$ (D1) is $794.98\,\mathrm{nm}$ and of the transition from $5^2S_{1/2}$ to $5^2P_{3/2}$ (D2) is $780.24\,\mathrm{nm}$. The ionization threshold for the $5^2P_{1/2}$ level is $473.67\,\mathrm{nm}$. The atomic qubit is encoded in the Zeeman sublevels $m_F = \pm 1$ of the ground state $5^2S_{\frac{1}{2}}$, $F = 1$. Here $m_F = -1$ is labeled with $|1, -1\rangle = |\downarrow\rangle_z$ and $m_F = +1$ with $|1, +1\rangle = |\uparrow\rangle_z$ (blue).

The atomic qubit is encoded in the Zeeman states $|\downarrow\rangle_z = |F=1, m_F=-1\rangle$ and $|\uparrow\rangle_z = |F=1, m_F=+1\rangle$ of the $5^2S_{1/2}$ ground state. The two qubit states together with the state $|F'=0, m_{F'}=0\rangle$ of the $5^2P_{3/2}$ excited state form a so-called Λ-System used to generate an entangled atom-photon state. Here, the entanglement arises from the spontaneous decay of the state $|F'=0, m_{F'}=0\rangle$ to the ground state through the emission of a single photon, the polarization of which is entangled with the Zeeman substates of the $F=1$ ground state (Subsec. 2.3.2). Thus, a fast and efficient atomic state readout scheme can be implemented by exploiting dipole selection rules and using polarized light to address individual Zeeman substates (Sec. 2.4.2). Furthermore, the closed transition $5^2S_{1/2}, F=2 \rightarrow 5^2P_{3/2}, F'=3$ offers a convenient way for efficient laser cooling.

2.2. Trapping Single Atoms

In order to perform experiments on single ^{87}Rb atoms a trapping method is required, which keeps an atom at a stable and fixed position. Additionally, shielding the atom from external influences is necessary to achieve precise control over the quantum system and obtain long coherence times. However, trapping single atoms is only possible in an ultra-high vacuum (UHV) environment, which significantly reduces the probability of collisions with other atoms or molecules.
The actual trapping is done in two steps: First, a cloud of cold atoms is formed from the background gas using a magneto-optical trap (MOT) [57]. This reduces the velocity of the atoms enough for the second stage where a single atom can be loaded from the MOT into an optical dipole trap (ODT) [58].

2.2.1. Laser and Vacuum System

One technical advantage of using ^{87}Rb as the quantum system of choice is the great variety of standard optical components and laser systems, which are commercially available for the desired atomic transition wavelengths. For the most important optical transitions, the D1 line at $795\,\mathrm{nm}$ and the D2 line at $780\,\mathrm{nm}$, grating-stabilized diode lasers are used. The laser diodes are frequency stabilized with an external resonator formed by an actively controlled diffraction grating using the signal of Doppler-free saturation spectroscopy. Acousto-optic modulators (AOMs) are further used to fine-tune the light frequency for addressing different hyperfine levels of the atom and to generate the required pulse sequences.

The lifetime of the atoms in an ODT is mainly limited by collisions with the background gas. Thus the atoms are trapped inside a UHV setup composed of a glass cell, steel parts with pumps, and metal vapor dispensers as the source of the Rb atoms. After evacuating the vacuum system it allows for pressures below $10^{-9}\,\mathrm{mbar}$, which can be maintained with an ion getter pump. The glass cell provides good optical access for all needed laser beams while having enough space inside for two particle detectors used for the fast and efficient atomic state readout. For more details about the vacuum system see [52].

2.2.2. Magneto-Optical Trap

For trapping atoms in an optical dipole trap, their kinetic energy should be lower than $\sim 1\,\mathrm{mK}$. Moreover, for efficient loading, it is necessary to have a high density of cold atoms at the focus position of the dipole trap. Both can be achieved with a magneto-optical trap as it combines cooling and confining the atoms.
The MOT is formed by pairs of counter-propagating laser beams, one for each spatial direction. The beams overlap in a common intersection point, which coincides with the center of a magnetic

quadrupole field generated by a pair of coils in an anti-Helmholtz configuration. The optical wavelengths used for the beams are the cooling light (CL) red-detuned to the cycle transition $5^2S_{1/2}, F = 2 \rightarrow 5^2P_{3/2}, F' = 3$ and the repump light (RP) resonant to the transition $5^2S_{1/2}, F = 1 \rightarrow 5^2P_{3/2}, F' = 2$. The latter is needed since there is the probability that the atoms leave the cooling cycle by decaying into the $5^2S_{1/2}, F = 1$ ground state due to off-resonant excitation. Applying repump light transfers the atoms back to the $5^2S_{1/2}, F = 2$ ground state and closes the cooling cycle. Due to the Doppler effect, light from the red-detuned cooling beams will preferentially be scattered from atoms moving opposite to the beam propagation direction. This leads to a directed momentum transfer which slows down, i.e. cools the atoms in all three spatial degrees of freedom. This dissipative friction force only cools the atoms but does not trap them. Therefore, the magnetic quadrupole field is needed, which induces a spatially dependent shift of the atomic Zeeman states. When this shift is combined with a proper choice of circularly polarized light in the six beams, it leads to spatial confinement of the atoms. By these means, a cold atom cloud containing $> 10^4$ atoms confined in a space < 1 mm in diameter can be created. Due to the effect of polarization gradient cooling [59], the temperatures achieved in the experiment are in the order of $30\,\mu\mathrm{K} - 50\,\mu\mathrm{K}$, well below the so-called Doppler limit of $146\,\mu\mathrm{K}$ for ^{87}Rb [56].

2.2.3. Optical Dipole Trap

The principle of an optical dipole trap is based on the AC-stark effect. Here the interaction of the atom with light, which is far detuned from all atomic transitions, causes a shift of the energy levels depending on the light intensity. Due to this large detuning, unwanted processes like off-resonant excitation and photon scattering can be neglected. In the case of ^{87}Rb, a red-detuned light field causes a lowering of the ground-state hyperfine levels resulting in an attractive trapping potential, whereas blue-detuned light results in a repulsive potential. In this experiment, a tightly focused Gaussian laser beam is used to create an attractive trapping potential. As the potential depth depends on the local intensity of the beam, the atoms will be trapped in the focus position.
For large detunings, the complex level structure of ^{87}Rb can be well approximated by an effective three-level system consisting of the ground state $5^2S_{1/2}$ and the two excited states $5^2P_{1/2}$ and $5^2P_{3/2}$. The resulting trap potential $U_{dip}(r, z)$ for an atom in a given hyperfine level F and intensity distribution $I(r, z)$ of the light field can be written as [60]

$$U_{dip}(r,z) = \frac{\pi c^2 \Gamma}{2\omega_0^3}\left(\frac{2 + g_F m_F P}{\Delta_{2,F}} + \frac{1 - g_F m_F P}{\Delta_{1,F}}\right) \cdot I(r,z), \tag{2.1}$$

with the spontaneous decay rate of the excited states Γ and the central transition frequency of the D-line ω_0. g_F is the Landé-factor of the particular ground state $5^2S_{1/2}, F$ with the corresponding Zeeman state m_F. The detunings $\Delta_{2,F}$ and $\Delta_{1,F}$ refer to the central transition frequency of the hyperfine level F to the excited states $5^2P_{3/2}$ and $5^2P_{1/2}$, respectively. The parameter P describes the polarization of the dipole trap and can take the values $P\epsilon\,[-1, +1]$. For linear polarized light $P = 0$, while for circular $\sigma^{\pm}$ polarized light $P = \pm 1$.
Equation 2.1 reveals that the degeneracy for different Zeeman states (m_F) gets lifted for not linear polarized light, which leads to an unwanted state evolution (Sec. 2.5). In the setup, the dipole trap is linearly polarized to eliminate the splitting of different m_F states.
The spatial shape of the trapping potential is given by the intensity distribution of the TEM_{00} mode of a Gaussian beam propagating along the z-direction:

$$I(r,z) = I_0 \cdot \left(\frac{w_D}{w(z)}\right)^2 \cdot e^{-\frac{2r^2}{w(z)^2}}, \tag{2.2}$$

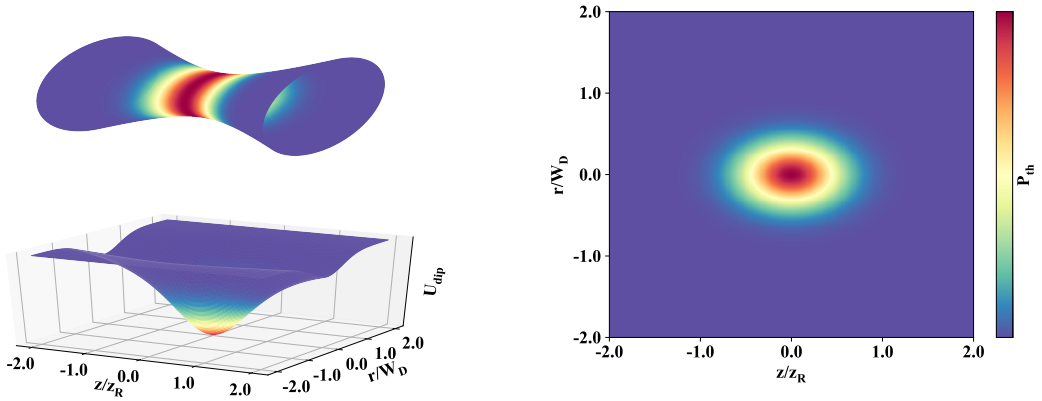

(a) Schematic surface plot of the TEM_{00} mode of a Gaussian beam and the corresponding trapping potential U_{dip}.

(b) Contour plot of the thermal density distribution of an atom inside the optical dipole trap.

Figure 2.3.: Schematic plot of a TEM_{00} Gaussian beam with the corresponding trapping potential U_{dip}. The overlayed color plot resembles the thermal density distribution of an atom inside the potential of the ODT. Here red colors indicate high probability densities, while blue colors show low probability densities.

with $w(z) = w_D \cdot \sqrt{1 + \left(\frac{z}{z_R}\right)^2}$ the waist of the Gaussian beam at position z, w_D the waist at the focus ($z = 0$), $z_R = \frac{\pi w_D^2}{\lambda}$ the Rayleigh length, and λ the wavelength of the laser. The maximal intensity at the center of the focus is I_0.
Since the thermal energy of the atom is much smaller than the trap depth ($k_B T \ll U_0$), the trap potential is approximated as harmonic [48], which results in the following trapping frequencies:

$$\omega_r = \sqrt{\frac{4U_0}{m_{Rb} w_D^2}}, \tag{2.3}$$

$$\omega_z = \sqrt{\frac{2U_0}{m_{Rb} z_R^2}}. \tag{2.4}$$

Here ω_r and ω_z denote the transverse and the longitudinal trap frequency, respectively, $U_0 = U_{dip}(0,0)$ is the potential trap depth at the focus position, and m_{Rb} is the mass of ^{87}Rb.
In this low-energy approximation, one can write the thermal density distribution $P_{th}(r, z, T)$ of an atom inside a harmonic trapping potential as [60]:

$$P_{th}(r, z, T) = \frac{1}{(2\pi)^{\frac{3}{2}} \sigma_z \sigma_r^2} \cdot e^{-\frac{r^2}{2\sigma_r^2}} \cdot e^{-\frac{z^2}{2\sigma_z^2}}, \tag{2.5}$$

with $\sigma_i = \sqrt{\frac{k_B T}{m_{Rb} \omega_i^2}}$ the Gaussian spatial standard distribution (for $i = r$ along the transverse direction and $i = z$ along the longitudinal direction). A graphical representation of the transverse and longitudinal shape of the trapping potential together with the corresponding thermal probability distribution of the atom are shown in Fig. 2.3.

By focusing the dipole trap into the cold cloud of ^{87}Rb atoms created by the MOT, atoms can be loaded in the ODT 2.2.4. With a proper choice of trap parameters such as depth and size together with the cooling light, the collision blockade effect [61] guarantees that only a single atom is trapped. The experimental realization of the dipole trap in Lab 1[1] uses a wavelength of $\lambda_D = 849.5\,\mathrm{nm}$ with a beam waist of $w_D = 2.05\,\mu\mathrm{m}$ and operates with an optical power of $P_0 = 60\,\mathrm{mW}$ resulting in a trap depth of $U_0 = k_B \cdot 2.78\,\mathrm{mK}$. The corresponding trap frequencies are $\omega_r = 2\pi \cdot 80.7\,\mathrm{kHz}$ and $\omega_z = 2\pi \cdot 7.6\,\mathrm{kHz}$.

2.2.4. Confocal Microscope Objective - Observing Single Atoms

Collecting and analyzing the light emitted by a single atom is crucial for all main steps in the experimental sequence: the loading of the atom, the generation of atom-photon entanglement, and subsequently atom-atom entanglement, as well as the atomic state readout. For all of this, the central optical component used in the experiment is a custom made microscope objective[2]. Considering that the objective is placed outside the UHV glass cell and thus needs a long working distance of $14\,\mathrm{mm}$, it still has a high numerical aperture (NA) of 0.5. Fluorescence light can be efficiently collected with this NA, which is discussed in detail in Chapter 4. Besides collecting light from the atom, it is also used to focus down the ODT trapping beam and a pulsed laser beam to ionize the atom for the atomic state readout (Subsec. 2.4.2). Since these applications operate at three different wavelengths ($\lambda_{flou} = 780\,\mathrm{nm}$, $\lambda_{ODT} = 849\,\mathrm{nm}/857\,\mathrm{nm}$ and $\lambda_{ion} = 450\,\mathrm{nm}$ / $473\,\mathrm{nm}$), the microscope objective is specially designed for this purpose. The design is corrected for the $3.5\,\mathrm{mm}$ thick wall of the glass cell, which allows nicely focusing laser beams from the outside and collecting light emitted from the inside in a confocal arrangement. Two dichroic mirrors are used to superimpose the different wavelengths so that the three foci coincide at one point inside the glass cell. An overview of the microscope objective setup is shown in Fig. 2.4. Details about the used components and the techniques to align the objective will be elaborated in Chapter 6.

The quantization axis for the atom is experimentally defined by the microscope objective setup and coincides with the direction of fluorescence collection (the optical axis of the objective). In the experiment, this axis is defined as the z-axis of the coordinate system. For more details about the definition, see Appendix B.

Sequence to Trap a Singe Atom

Loading a pre-cooled atom from the MOT into the ODT requires the scattering of additional cooling photons to lose the gained potential energy. Fluorescence light can efficiently be collected by the objective once the atom is trapped in the ODT and its position coincides with the focus of the collection optics. The collected light is coupled into a single-mode fiber and guided to single-photon counting modules (SPCMs). A sudden increase of the detected photon count rate above a certain threshold indicates successful loading of an atom into the ODT. Directly afterwards the electrical current of the MOT coils is shut off and the cold cloud of atoms immediately starts to expand, thus leaving the single atom undisturbed for further experiments. At the moment the atom is lost from the trap the count rate drops under another threshold and the MOT coils are turned on again, switching the experiment to the loading procedure to load the next atom. The process of reloading an atom is completely automatized by continuously monitoring the photon count rate with a computer.

[1] The trap parameters for Lab 2 are slightly different and for completeness are given here: $\lambda_D = 857\,\mathrm{nm}$, $w_D = 2.42\,\mu\mathrm{m}$, $P_0 = 52\,\mathrm{mW}$, $U_0 = k_B \cdot 2.15\,\mathrm{mK}$, $\omega_r = 2\pi \cdot 59.7\,\mathrm{kHz}$, $\omega_z = 2\pi \cdot 4.8\,\mathrm{kHz}$.

[2] Custom designed by PhotonGear

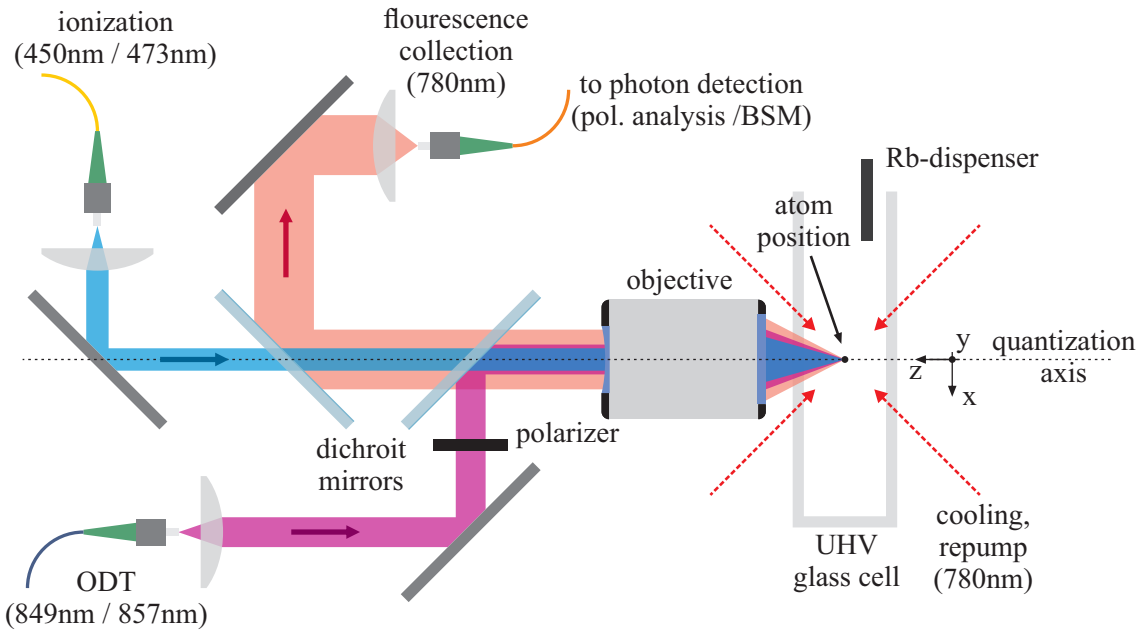

Figure 2.4.: Overview of the confocal microscope objective setup. The objective creates the trapping potential for a single atom by focusing the laser beam of the ODT (magenta) into the cold cloud of ^{87}Rb atoms formed by the MOT at the intersection point of the cooling beams (dashed red arrows). The single atom is trapped in the focus position of the ODT beam (black dot). In a confocal arrangement, the objective collects fluorescence light emitted by the atom (red) and couples it into a single-mode fiber leading to a single photon detection and polarization analysis setup. Two dichroic mirrors superimpose the different wavelengths such that the three foci coincide inside the UHV glass cell. The quantization axis (z) for the atom is defined by the optical axis of the microscope objective.

2.3. Atom-Photon Entanglement

As a first step towards atom-atom entanglement over a long distance, the generation of atom-photon entanglement in two independent laboratories is needed. The spontaneous emission process of a well-defined excited state in principle leads to an entanglement of the emitted photon state with the final state of the atom. In this experiment, the atom is initially prepared in the $|F = 1, m_F = 0\rangle$ state by optical pumping, from where it is excited to the state $|F' = 0, m_F = 0\rangle$. The subsequent spontaneous decay into the $5^2S_{1/2}, F = 1$ manifold of the ground state generates an entangled atom-photon state.

2.3.1. Initial State Preparation

After successfully cooling and trapping a single atom, it will be found in one of the two ground-state levels $5^2S_{1/2}, F = 1, 2$ and, after the cooling cycle, with a high probability in $F = 2$. Preparing the atom in the $|F = 1, m_F = 0\rangle$ state is done by optical pumping with two simultaneously applied lasers that excite all other states of the ground levels. The first laser is resonant to the transition $5^2S_{1/2}, F = 2 \rightarrow 5^2P_{3/2}, F' = 1$ ('$\mathrm{pump}_{2\rightarrow1}$') and excites the atom to $5^2P_{3/2}, F' = 1$, from where it can decay either back to $F = 2$ or $F = 1$ (Fig. 2.5a). Irradiating the atom continuously with this laser will eventually empty the $F = 2$ level, and the atom population will end up in $F = 1$. Alternately pumping from different directions and by that with different polarizations will address all Zeeman substates of the $F = 2$ level, leaving no dark state for this transition. This is crucial as the population in a potential dark state will stay in $F = 2$ and thus decrease the achievable pump efficiency. A second laser, π-polarized and resonant to the transition $5^2S_{1/2}, F = 1 \rightarrow 5^2P_{3/2}, F' = 1$ ('$\mathrm{pump}_{1\rightarrow1}$'), is needed to empty the two states $|F = 1, m_F = \pm1\rangle$ (Fig. 2.5b). The transition $|F = 1, m_F = 0\rangle \rightarrow |F' = 1, m_F = 0\rangle$ is forbidden due to dipole selection rules, leaving $|F = 1, m_F = 0\rangle$ as the only dark state. The atom will ultimately decay into the dark state by continuously scattering photons from those two lasers, which completes the optical pumping. With this scheme, a state preparation efficiency of $\eta_{pump} = 0.8$ is achieved in less than $4\,\mu$s. For more details, see [53].

2.3.2. Generation of Atom-Photon Entanglement

The optical pumping process prepares the atom in the state $|F = 1, m_F = 0\rangle$ from where it is excited with a short π-polarized laser pulse to the excited state $|F' = 0, m_F = 0\rangle$. This state spontaneously decays with a lifetime of $26.24\,\mathrm{ns}$ to the $5^2S_{1/2}, F = 1$ manifold via three possible decay channels by emitting a single photon (Fig. 2.5c and 2.5d). The photon polarization is directly related to the final Zeeman substate of the atom due to the conservation of angular momentum. In more detail: A decay into $|F = 1, m_F = -1\rangle$ leads to an emission of a σ^+-polarized photon, a decay into $|F = 1, m_F = 0\rangle$ leads to an emission of a π-polarized photon, and a decay into $|F = 1, m_F = +1\rangle$ leads to an emission of a σ^--polarized photon. All polarizations and atomic spin states are defined according to the quantization axis of the system, i.e. the optical axis of the collection optics. The Clebsch-Gordan coefficients [56] for all three decay channels are equal and hence have the same probability of $1/3$ to occur. Thus, the system is in a coherent superposition of the three decay paths yielding the following entangled atom-photon state:

$$|\Psi\rangle_{AP} = \frac{1}{\sqrt{3}} \left(|1, -1\rangle \left|\sigma^+\right\rangle + |1, 0\rangle \left|\pi\right\rangle + |1, +1\rangle \left|\sigma^-\right\rangle \right). \tag{2.6}$$

Depending on the polarization of the emitted single photon, its spatial mode differs for a $\sigma^\pm$- or π-decay and is given by dipole emission characteristics [49, 62]. Calculations show that the probability

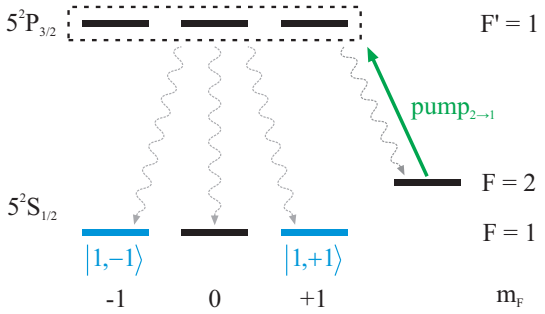

(a) The $\mathrm{pump}_{2\to1}$ laser transfers the population from the $F = 2$ level to the $F = 1$ ground state. Applying it from different directions and with different polarizations enables addressing all Zeeman substates of the $F = 2$ manifold without leaving any dark state. The subdivision into Zeeman states for the $F = 2$ level is therefore omitted, and the $F' = 1$ level as a whole is symbolized with a dashed box around it.

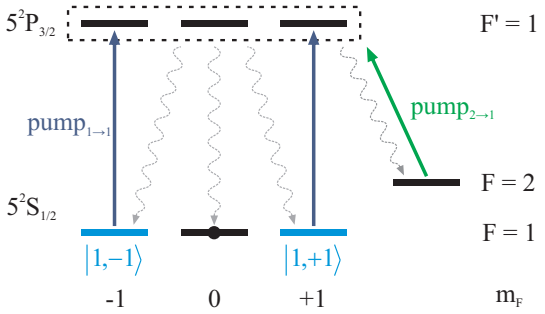

(b) The $\mathrm{pump}_{1\to1}$ laser transfers the population from the $m_F = \pm1$ states to the $m_F = 0$ state of the $F = 0$ ground state. The black dot symbolizes the state population after the optical pumping.

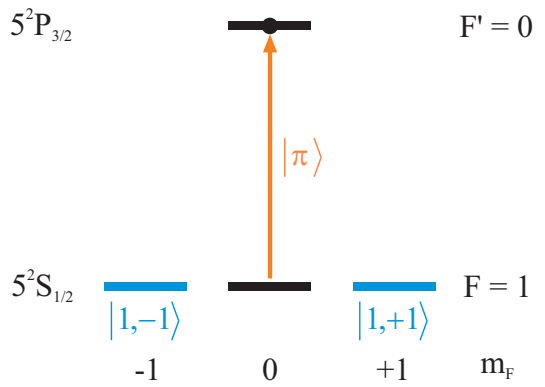

(c) The Excitation pulse excites the atom from the prepared $F = 1, m_F = 0$ state to the $F' = 0, m_{F'} = 0$ state. The black dot symbolizes the state population after the excitation.

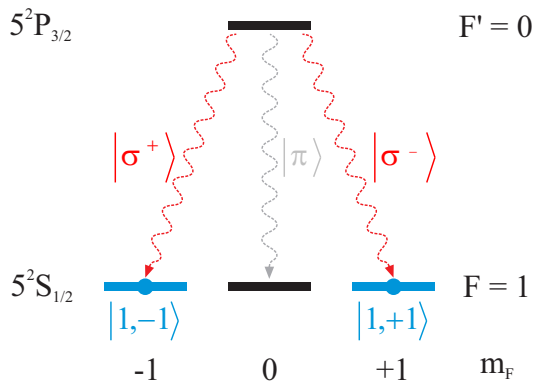

(d) The excited state $F' = 0, m_{F'} = 0$ decays with equal probability to the three Zeeman substates of the F=1 manifold. Only $\sigma^{\pm}$-polarized photons (red) emitted from decays into $m_F = \pm1$ Zeeman substates can be coupled into a single-mode fiber and hence be detected. The coupling efficiency for the π-polarized photon (grey) originating from the decay into the $m_F = 0$ Zeeman substate is highly suppressed and hence will not be observed. The resulting entangled atom-photon state is $|\Psi\rangle_{AP} = \frac{1}{\sqrt{2}}\left(|1,-1\rangle\,|\sigma^+\rangle + |1,+1\rangle\,|\sigma^-\rangle\right)$. The blue dots symbolize the final state population in the qubit subspace.

Figure 2.5.: Optical pumping and excitation process: Initial state preparation via optical pumping into $5^2S_{1/2}, F = 1, m_F = 0$ state (a), (b) and generation of the atom-photon entangled state (c), (d).

to couple a π-polarized photon into a single-mode fiber vanishes for an atom located at the quantization axis. Therefore, even if all of the three decay channels occur with the same probability, only photons originating from a $\sigma^{\pm}$-decay are observed in the experiment and the resulting atom-photon state can be written as

$$|\Psi\rangle_{AP} = \frac{1}{\sqrt{2}} \left(|1,-1\rangle \left|\sigma^{+}\right\rangle + |1,+1\rangle \left|\sigma^{-}\right\rangle \right) \tag{2.7}$$

$$\equiv \frac{1}{\sqrt{2}} \left(|\downarrow\rangle_z \left|\sigma^{+}\right\rangle + |\uparrow\rangle_z \left|\sigma^{-}\right\rangle \right). \tag{2.8}$$

Here $|\downarrow\rangle_z$ and $|\uparrow\rangle_z$ define the qubit notation of the atomic spin states $|1,-1\rangle$ and $|1,+1\rangle$, respectively. A representation of the entangled state for all three orthogonal atomic basis states of the Pauli operators $\hat{\sigma}_x$, $\hat{\sigma}_y$ and $\hat{\sigma}_z$ can be found in Appendix B. More details about the calculations of the collection efficiencies for different polarizations, taking the emission characteristics into account, are presented in Chapter 4.

2.4. Photonic and Atomic State Readout

For reading out information encoded on the physical qubits, high fidelity projection measurements are necessary. For the photon, this implies an analysis of its polarization, while for the atom, a state-selective readout of individual Zeeman substates of the $5^2S_{1/2}, F = 1$ ground level is needed. Such readout schemes enable a characterization of the entangled atom-photon state as well as the entangled atom-atom state. Furthermore, the entanglement can also be verified by performing correlation measurements in several bases. Therefore, the flexibility to freely choose the measurement direction in both readout schemes is required.

2.4.1. Photonic Polarization Analysis

The single photon emitted during the atom-photon entanglement process is coupled into a single-mode fiber by the collection optics. The fiber guides the photon to a polarization analysis setup[3] consisting of a $\lambda/2$-waveplate, a $\lambda/4$-waveplate and a polarizing beam splitter (PBS) with an avalanche photodiode (APD) in each output port (Fig. 2.6). Considering only the PBS and the single-photon detectors, this acts as a projection measurement in the H/V-basis. Applying additional phase shifts with the two wave plates in front of the PBS allows for projections along arbitrary measurement directions.
Unwanted rotations of the photon's polarization due to birefringence in the single-mode fiber or other optical components in between the emission point of the photon (i.e. the atom position inside the vacuum glass cell) and the measurement setup lead to potential errors in the desired measurement direction. Therefore, a fiber polarization controller is used to counteract these rotations and cancel all unwanted additional phase shifts. Furthermore, to ensure that the polarization is preserved for all incoming polarizations, it is enough to compensate the system for two well-defined conjugate polarizations, e.g. V and $+45°$.
The photonic polarization analysis also plays an important role in experiments involving two atom-trap setups, as it is employed in the entanglement generation of the atom-atom state (Subsec. 2.6).

[3] This configuration is used in Lab 2. In Lab 1, the bell-state measurement (BSM) setup is used for the photonic projection measurement. For more details, see Sec. 2.6.2.

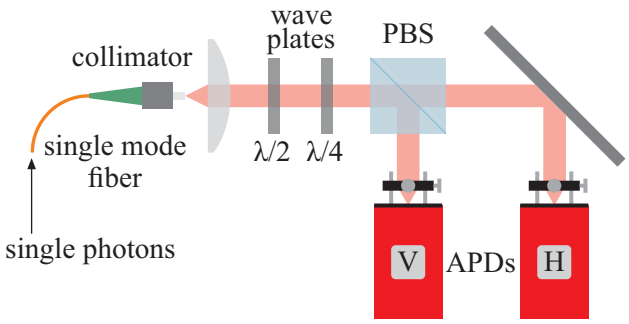

Figure 2.6.: Single photon polarization analysis setup: Projection measurements on single photons in the H/V-basis are implemented with a PBS, which splits the polarization into an H- and a V-path. The photons are then detected with single-photon detectors (APDs). Other measurement directions can be chosen by appropriately setting the waveplates ($\lambda/2$ and $\lambda/4$) in front of the PBS.

2.4.2. Atomic State Readout

The atomic readout scheme is composed of two steps: It starts with a state-selective ionization of the atom by first exciting a specific superposition of Zeeman states from the $5^2S_{1/2}$ ground state to the $5^2P_{1/2}$ excited state from where the atom is subsequently ionized. Since trapping atoms with the ODT is based on lowering the ground state energy of the valance electron, the ionized atom can no longer be trapped and is immediately lost from the trap. The second step of the readout scheme verifies whether or not the atom has been ionized by using cooling light and counting the number of collected fluorescence photons.
For the loophole-free Bell experiment [21, 53, 55], also presented in this thesis (Chapter 3), a very fast atomic state readout with high fidelity is indispensable to ensure space-like separation (Sec. 3.3). However, while the state-selective ionization is very fast and can be done with high fidelity, the fluorescence detection in this setup needs a long integration time of several tens of milliseconds to distinguish between 'atom in' and 'atom out' precisely. Even if there are more advanced possibilities to shorten the integration time to a few tens of microseconds, e.g. by using cavities or better collection optics [18, 63, 64], it would still require larger separations of the two atoms to enable space-like separation and thereby close the so-called 'locality loophole'. Therefore, particle detectors are used to directly observe the ionization fragments [52, 65] to circumvent these limitations.

Zeeman State-Selective Ionization

The state-selective excitation of the atom is realized by applying a laser resonant to the transition $5^2S_{1/2}, F = 1 \rightarrow 5^2P_{1/2}, F' = 1$ with a wavelength of $794.98\,\mathrm{nm}$ ('readout-laser') along the quantization axis (Fig. 2.7). Due to dipole selection rules, a specific superposition of Zeeman substates of the $5^2S_{1/2}, F = 1$ level can be selectively excited by choosing the polarization χ_{ro} of the readout-laser accordingly. Simultaneously irradiating with a second laser ('ionization laser') with a wavelength shorter than the ionization threshold of the first excited state[4] of $473.67\,\mathrm{nm}$ but longer than

[4]Different wavelengths for the ionization laser are used in the two labs, in Lab 1 $\lambda_{ion} = 450nm$ and in Lab 2 $\lambda_{ion} = 473nm$. However, despite different wavelengths, there is no fundamental difference in the performance of the ionization scheme.

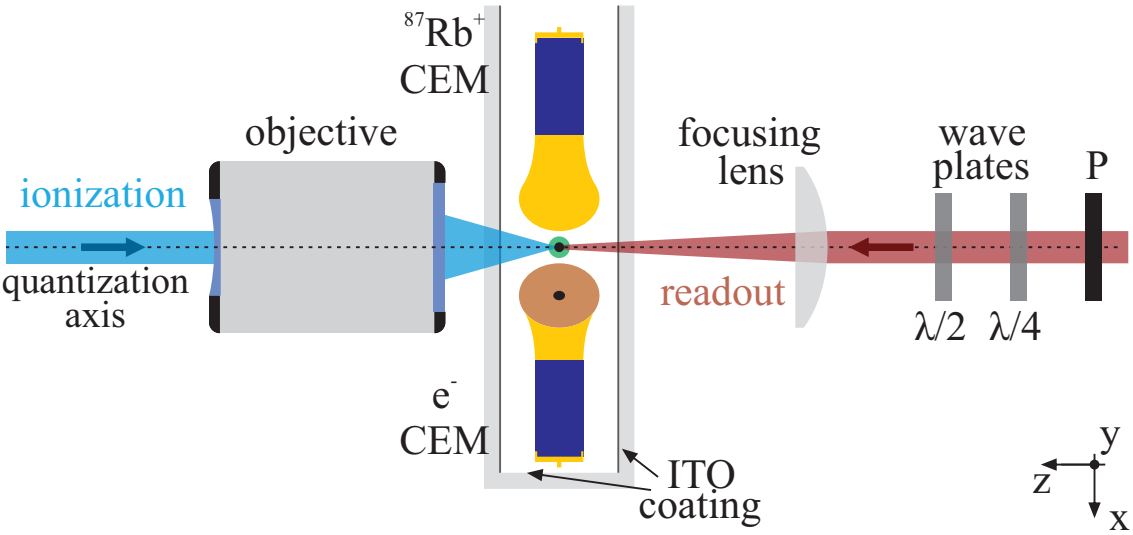

(a) Top view: The readout laser (brown) propagates along the optical axis in the positive z-direction and is focused onto the atom (black dot) with a focusing lens. Counterpropagating to it is the ionization laser (blue) focused by the microscope objective. The cycling laser is indicated as a green dot and propagates along the negative y-direction. A linear polarizer (P) and two waveplates ($\lambda/2$ and $\lambda/4$) define the readout polarization χ_{ro}, and any measurement polarization can be selected. For detecting the $^{87}Rb^{+}$-ion and the electron, two channel electron multipliers (CEMs) are placed inside the vacuum symmetrically around the trapped atom position. Two sidewalls of the glass cell are coated with a transparent, conductive and antireflective coating made out of indium tin oxide (TIO) to apply electric fields.

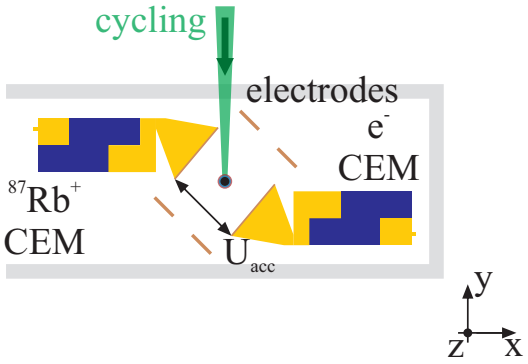

(b) Side view: A high voltage U_{acc} is applied between the front caps of the CEMs to separate and accelerate the ionization fragments towards the particle detectors. The electric field inside the vacuum chamber is fine-tuned with additional electrodes (light brown) and the conductive sidewalls of the glass cell to achieve a high detection efficiency. By this, the ionization fragments are guided to the active areas of the detectors with the highest detection efficiency. One particle detector registers the electrons (e^- CEM) and the other the ions ($^{87}Rb^{+}$ CEM).

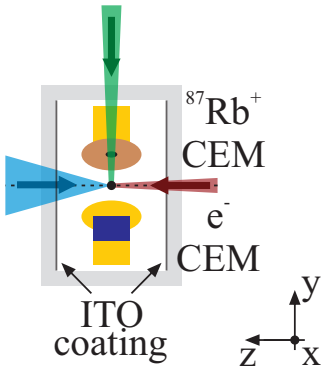

(c) Front view: The three laser beams involved in the atomic state readout are shown. The readout and ionization laser are counterpropagating along the quantization axis, while the cycling laser propagates perpendicular to it from the top. Thus, all three beams intersect at the position of the atom surrounded by the particle detectors.

Figure 2.7.: Schematic of the atomic state readout setup [55].

the ionization threshold of the ground state of $296.82\,\mathrm{nm}$ [56] leads to the ionization of only the excited atoms. Figure 2.8 depicts all for this process relevant atomic states and optical transitions. The scheme can easily be understood for the example of σ^+-polarized readout light (Fig 2.8a). Here, only the qubit state $|1,-1\rangle$ will be excited to $|F'=1,m_{F'}=0\rangle$, while the other qubit state $|1,+1\rangle$ cannot be excited since the corresponding target state $|F'=1,m_{F'}=+2\rangle$ does not exist. In general, this argument holds for any superposition of σ^+- and σ^--polarized readout light. For a given polarization χ_{ro}, the transferred superposition state $|B\rangle_{\chi_{ro}}$ is denoted as 'bright state' and the superposition which is not transferred $|D\rangle_{\chi_{ro}}$ as 'dark state':

$$\chi_{ro} = cos\,(\alpha)\cdot V - e^{-i\phi} sin\,(\alpha)\cdot H, \tag{2.9}$$

$$|B\rangle_{\chi_{ro}} = cos\,(\alpha)\,|{\downarrow}\rangle_x + e^{-i\phi} sin\,(\alpha)\,|{\uparrow}\rangle_x\,, \tag{2.10}$$

$$|D\rangle_{\chi_{ro}} = sin\,(\alpha)\,|{\downarrow}\rangle_x - e^{-i\phi} cos\,(\alpha)\,|{\uparrow}\rangle_x\,. \tag{2.11}$$

Here the atomic states are given in the σ_x basis (the atomic and photonic definitions, as well as their transformations, can be found in Appendix B). Any readout polarization can be set by adjusting the two parameters α and ϕ using a combination of a $\lambda/2$-waveplate and a $\lambda/4$-waveplate, and consequently, the measurement direction can be freely chosen (Fig. 2.7).
Note that for any readout polarization χ_{ro} not only the bright state $|B\rangle_{\chi_{ro}}$ but also the state $|F=1,m_F=0\rangle$ will get ionized. Consequently, only for the measurement outcome 'atom not ionized', the atom is projected onto a specific state, the dark state $|D\rangle_{\chi_{ro}}$, whereas the result 'atom ionized' solely indicates the projection onto any other state of the $5^2S_{1/2}$ ground state. Therefore, to interpret the result 'atom ionized' as a projection onto the bright state $|B\rangle_{\chi_{ro}}$, the atom needs to be well prepared and kept in the qubit subspace.
The achievable readout fidelity is limited by imperfections of the state-selective ionization scheme arising from the lifetime of the excited state and off-resonant excitation of the dark state. The atom is not ionized instantaneously, but it takes a finite time depending on the applicable intensity of the ionization laser. Thus the excited atom can spontaneously decay back into the ground state before it gets ionized. The timescale for this process is given by the decay rate of the $D1$-transition of $\Gamma_1 = 36.10\,\mathrm{MHz}$, which corresponds to a lifetime of $\tau_1 = 1/\Gamma_1 = 27.70\,\mathrm{ns}$ [56]. Not all of the possible decays back to the ground state will reduce the readout fidelity, as it depends on the final state the atom decays into. The Clebsch-Gordan coefficients give the splitting ratio of the different decay channels, whereby a decay to the $5^2S_{1/2}, F=2$ manifold is most probable with a relative probability of $10/12$. Here the photon energy of the ionization laser is not enough to directly ionize the atom from the $F=2$ level without any additional laser. Therefore, a laser resonant to the cycling transition $5^2S_{1/2}, F=2 \rightarrow 5^2P_{3/2}, F'=3$ ('cycling laser') is irradiated onto the atom, efficiently transferring all the population to the $F'=3$ excited state, which also gets ionized. Further, the atom decays back to the bright state with a probability of $1/12$, from where it is re-excited by the readout laser and subsequently ionized. As these two decay channels lead to a correct ionization, they do not reduce the readout fidelity. However, with a probability of $1/12$, the atom will decay into the dark state, limiting the fidelity as the atom cannot be re-excited and thus will not be ionized. The two hyperfine states $5^2P_{1/2}, F'=1$ and $5^2P_{1/2}, F'=2$ have an energy difference of $816.7\,\mathrm{MHz}$ with a natural line width of $5.746\,\mathrm{MHz}$. Off-resonant excitation of the dark state is therefore highly suppressed. Nevertheless, the high intensity of the ionization laser leads to a reduction of the lifetime for the excited states due to a possible fast ionization of the excited atom. Effectively, this leads to a broadening of the line width, which favors off-resonant excitation of the dark state and thus limits the atomic readout fidelity [52, 66]. Moreover, a high-intensity blue-detuned light field leads to a repulsive potential, which acts against the trapping potential of the ODT. Thus, increasing the ionization intensity will lead to an

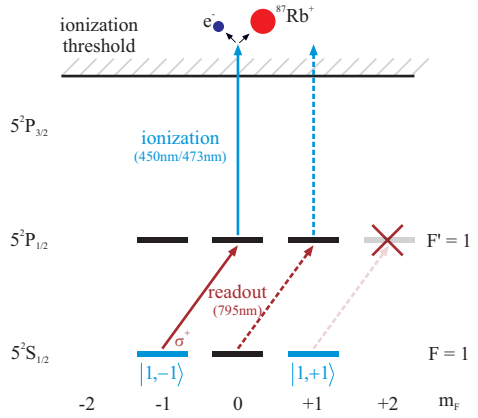

(a) Simplified atomic readout scheme: σ^+-polarized readout light (brown) can only excite the state $|1,-1\rangle$ to $|F'=1,m_{F'}=0\rangle$, while for the other qubit state $|1,+1\rangle$ the corresponding target state $|F'=1,m_{F'}=+2\rangle$ is missing. The excited atoms will subsequently be ionized with an ionization laser (blue), generating ionization fragments. It is instructive to note that the $F=1,m_F=0$ state will always get ionized independent of the used readout polarization.

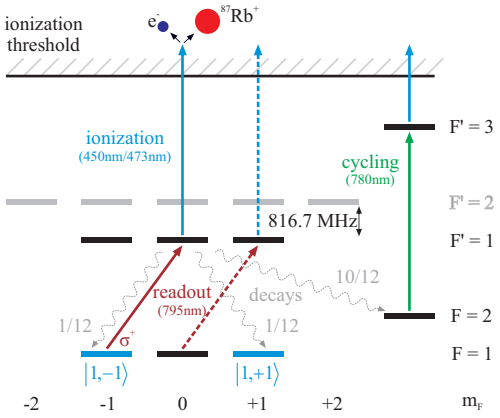

(b) Complete atomic readout scheme: Due to the limited lifetime of the excited state, possible decay channels back to the ground states open up. With the highest relative probability of $^{10}/_{12}$, the atom decays to the $F=2$ manifold from where it is exited with an additional cycling laser (green) to the $5^2P_{\frac{3}{2}}, F'=3$ level and hence be ionized. With the probability of $^1/_{12}$ it decays back to the $|1,-1\rangle$ state from where it can be re-excited and get ionized, but it also decays with equal probability to the $|1,+1\rangle$ state from where it will not be re-excited and thus not get ionized.

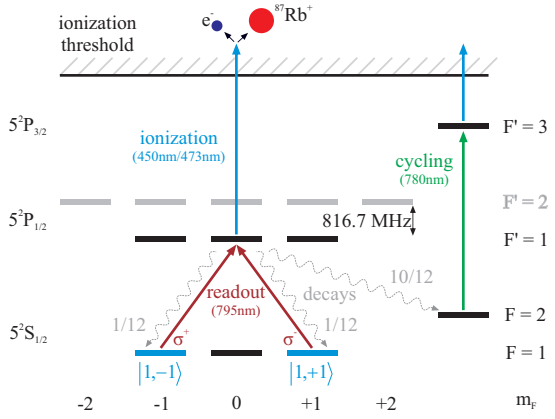

(c) General atomic readout scheme: Depending on the readout polarization χ_{ro}, a specific superposition of the qubit subspace (bright state $|B\rangle_{\chi_{ro}}$) will get excited to the $5^2P_{\frac{1}{2}}, F'=1$ level and ionized from there, while the orthogonal superposition (dark state $|D\rangle_{\chi_{ro}}$) will not get excited and thus not ionized. Therefore, to receive a measurement outcome, one needs to verify if an ionization event occurred. This can be done by simply checking for fluorescence photons or directly detecting the generated ionization fragments with two particle detectors inside the vacuum.

Figure 2.8.: Scheme of the Zeeman state selective ionization process. A specific example with σ^+-polarized readout light is depicted in (a) and (b). The general case for an arbitrary readout polarization χ_{ro} is shown in (c).

increased atom loss probability independent of the actual atomic state.
Aside from these fundamental limitations, errors in the readout polarization and its alignment can further reduce the readout fidelity. One reason is the residual birefringence of all the optical components in the readout beam path, which could not be compensated for with additional phase plates. Consequently, the atom is irradiated with a slightly different polarization as intended, which causes an error in the measurement outcome. Furthermore, if the readout beam is not perfectly aligned along the quantization axis, polarization components parallel to the quantization axis will emerge. These π-polarized components lead to unwanted ionization of the dark state.

Detection of the Ionization Fragments

An ionized atom splits up into a $^{87}Rb^{+}$-ion and an electron e^{-}. The fragments are no longer trapped in the ODT potential and a simple test, if the atom is still there by collecting fluorescence light, reveals the measurement outcome. An alternative and much faster possibility to verify the occurrence of an ionization event is by directly detecting the ionization fragments with two particle detectors placed on opposing sides of the trapping position inside the UVH glass cell (Fig. 2.7). By applying a high voltage between the two channel electron multipliers (CEMs), the $^{87}Rb^{+}$ and the e^{-} are separated and accelerated towards the CEMs. Typical acceleration voltages U_{acc} are in the range of $3.6\,\mathrm{kV}$ ... $4.6\,\mathrm{kV}$ [52]. With the help of additional electrodes and electrical-conductive coated sidewalls of the UHV glass cell[5], electric fields can be applied to efficiently guide the ionization fragments to the active areas of the CEMs, where an electron avalanche is triggered. This electrical pulse gets amplified in the CEM and converted into a logic TTL-signal using a comparator. The appearance of this signal indicates the projection onto the bright state, while its absence announces the projection onto the dark state.
With this setup, detection efficiencies of $\eta_{ion} = 0.9...0.94$ for the ion and $\eta_{e^-} = 0.75...0.9$ for the electron can be achieved. The dark count rates of these detectors are pretty low, with $< 10\,\mathrm{Hz}$ for the ion and $< 10\,\mathrm{kHz}$ for the electron [52, 65] and therefore are negligible considering the short acceptance time windows of $240\,\mathrm{ns}$ for detecting the ionization fragments. Thus, detecting only one of the fragments is sufficient to get a result and the detection efficiency to verify an ionization event is ≥ 0.98. The overall duration of this scheme from the start of the ionization process till the end of the acceptance time window for detecting ionization fragments is shorter than $725\,\mathrm{ns}$ [21, 53].

Performance of the Readout Scheme

The contrast C is used as a figure of merit to quantify the quality of the atomic readout scheme. It is defined as the difference in ionization probability $Pr_{ionized}$ of atoms prepared in the bright state $|B\rangle$ and atoms prepared in the dark state $|D\rangle$:

$$C = Pr_{ionized}\left(|B\rangle\right) - Pr_{ionized}\left(|D\rangle\right), \tag{2.12}$$

assuming the atom stays in the qubit subspace. The contrast is optimized by finding the optimal combination of the optical pulse lengths and powers of the involved laser pulses. This leads to a readout pulse length of 140 ns and an optical power of 1.24 μW, resulting in a contrast of C=0.938 [52].

[5]The transparent conductive antireflection coating is made out of Indium Tin Oxide (ITO).

2.5. Atomic State Coherence

For the experiments presented in this thesis, not only a high fidelity atomic state readout but also a long coherence time of the atomic spin state is required, especially for two atom-trap experiments in which the atom-atom entanglement is generated in an event-ready scheme (Subsec. 2.6). In these measurements, the atomic state readout is only performed after a successfully generated atom-atom state is heralded by the photonic Bell state measurement (BSM). Therefore, the atomic readout is delayed by additional waiting times consisting of the photon travel times to the BSM, the time needed for the electronics to evaluate the photonic measurement and the time to send the heralding signal back to the trap setups. In the current configuration, a $700\,\mathrm{m}$ long fiber is used to connect both labs, corresponding to a minimum readout delay of about $7\,\mu\mathrm{s}$. For future experiments, good atomic coherence becomes more and more critical, as there are plans to increase the distance of the two setups to several tens of kilometers. The first results in this direction are presented in Chapter 7. During this time span, the atomic spin state is susceptible to external decoherence effects like magnetic fields (Zeeman effect) and the light of the dipole trap (AC-Stark effect). Therefore, the atomic coherence must be preserved for these timescales to perform experiments successfully.

2.5.1. Atomic State Evolution in Magnetic Fields

In the presence of a magnetic field, the atomic spin states obtain different energy shifts due to the Zeeman effect, resulting in different time evolutions of these states. The derivation of the formulas to calculate the time evolution follows earlier descriptions presented in [53, 55, 67]. The interaction of a magnetic field

$$\vec{B} = B_0 \begin{pmatrix} b_x \\ b_y \\ b_z \end{pmatrix} \tag{2.13}$$

with the spin-1 system of the atomic ground level $5^2S_{1/2}, F = 1$ given by the basis vectors $|1,-1\rangle_z$, $|1,0\rangle_z$ and $|1,+1\rangle_z$ in the σ_z-basis can be described by the interaction Hamiltonian

$$\hat{H}_B = \frac{g_F \mu_B}{\hbar} \cdot \vec{B}\vec{\hat{F}} = \hbar\omega_L \begin{pmatrix} b_z & \frac{1}{\sqrt{2}}(b_x - ib_y) & 0 \\ \frac{1}{\sqrt{2}}(b_x + ib_y) & 0 & \frac{1}{\sqrt{2}}(b_x - ib_y) \\ 0 & \frac{1}{\sqrt{2}}(b_x + ib_y) & -b_z \end{pmatrix}. \tag{2.14}$$

Here b_x, b_y and b_z are the normalized components, and B_0 is the magnitude of the magnetic field vector $\vec{B}$ whereby $\sqrt{b_x^2 + b_y^2 + b_z^2} = 1$, g_F denotes the Landé-factor of the hyperfine state, μ_B the Bohr magneton, $\omega_L \coloneqq \frac{1}{\hbar} g_F \mu_B B_0$ the Larmor frequency and $\vec{\hat{F}} = \begin{pmatrix} \hat{F}_x \\ \hat{F}_y \\ \hat{F}_z \end{pmatrix}$ the angular momentum operator of a spin-1 system defined as [68]

$$\hat{F}_x = \frac{\hbar}{\sqrt{2}} \begin{pmatrix} 0 & 1 & 0 \\ 1 & 0 & 1 \\ 0 & 1 & 0 \end{pmatrix}, \hat{F}_y = \frac{\hbar}{\sqrt{2}} \begin{pmatrix} 0 & -i & 0 \\ i & 0 & -i \\ 0 & i & 0 \end{pmatrix}, \text{ and } \hat{F}_x = \frac{\hbar}{\sqrt{2}} \begin{pmatrix} 1 & 0 & 0 \\ 0 & 0 & 0 \\ 0 & 0 & -1 \end{pmatrix}. \tag{2.15}$$

The eigenvalues for the Hamiltonian $\hat{H}_B$ using cylindrical coordinates defined as $b_x \coloneqq \sqrt{1 - b_z^2} cos\,(\phi)$ and $b_y \coloneqq \sqrt{1 - b_z^2} sin\,(\phi)$ are given by $\lambda_\pm = \pm\hbar\omega_L$ and $\lambda_0 = 0$, and the corresponding eigenvectors

are

$$|\Phi_{\pm}\rangle = \begin{pmatrix} -\frac{1}{2}(b_z \pm 1)\, e^{-i\phi} \\ -\sqrt{\frac{1-b_z^2}{2}} \\ \frac{1}{2}(b_z \mp 1)\, e^{i\phi} \end{pmatrix}, |\Phi_0\rangle = \begin{pmatrix} -\sqrt{\frac{1-b_z^2}{2}} e^{-i\phi} \\ b_z \\ \sqrt{\frac{1-b_z^2}{2}} e^{i\phi} \end{pmatrix}. \tag{2.16}$$

Thus, the time evolution of an arbitrary state in a constant magnetic field can be calculated as

$$|\Psi(t)\rangle = c_{-1}|\Phi_-\rangle e^{i\omega_L t} + c_0|\Phi_0\rangle + c_{+1}|\Phi_+\rangle e^{-i\omega_L t} \tag{2.17}$$

with $c_{\pm}, c_0 \epsilon \mathbb{C}$ and $\sqrt{\|c_{-1}\|^2 + \|c_0\|^2 + \|c_{+1}\|^2} = 1$.

Magnetic Field Control

The state evolution of an atom in a constant magnetic field of known strength is a coherent process, which does not lead to decoherence. Therefore, the initial state of the time evolution can be measured by delaying the atomic state readout for a multiple of a full Larmor oscillation period. However, the situation is more complicated in the actual experiment since there are several sources for magnetic fields with varying strength acting on different time scales. The origin of these sources can be inside the laboratory, e.g. a strong magnet of the ion getter pump for the vacuum setup, various power supplies, and other electronics but they also can be outside the laboratory like the Munich subway line at a distance of about $60\,\mathrm{m}$ or the earth magnetic field.
The magnetic fields are actively stabilized to control the atomic state evolution and suppress magnetic field fluctuations. The magnetic field is controlled by applying electrical currents on three pairs of compensation coils located symmetrically around the trap (Fig. 2.9). A magneto-resistive sensor[6] is mounted as close as possible to the atom position while not blocking the optical access for the laser beams to stabilize the magnetic field at the atom position. For that, the measured fields are put into a PID controller giving a feedback signal to the current supply of the compensation coils. Each pair generates a magnetic field along one of the spatial directions such that the sensor measures a constant field defined by the set point of the active stabilization system.
With this system, magnetic fields in any direction can be generated with field strengths in the range of $\pm 5000\,\mathrm{mG}$. Furthermore, the feedback loop can stabilize field fluctuations up to a bandwidth of $\sim 200\,\mathrm{Hz}$ with a residual noise level at the atom position of $\sim 0.5\,\mathrm{mG}$ (RMS) [53, 67]. Thus, there are now two possibilities to minimize the decoherence caused by magnetic fields. The first is to stabilize the magnetic field to an effective zero field at the atom position, leaving the atom only in the residual noise level of the stabilization system. The other option is to apply a magnetic guiding field in one direction. The advantage of this approach is that field fluctuations along directions orthogonal to the guiding field will be strongly suppressed [67], and the atomic spin state undergoes a controlled Larmor precession.

2.5.2. Circular Polarization Components of the Optical Dipole Trap - AC Stark Shift

Besides the effect of magnetic fields, the interaction with laser light also needs to be taken into account when considering the coherence of the atomic state. In the time between the entanglement generation process and the atomic state readout, only the optical dipole trap light is applied to the atom. As already mentioned in Subsec. 2.2.3, the dominant interaction of the ODT laser with the atom is caused

[6] Honeywell HMC 1053

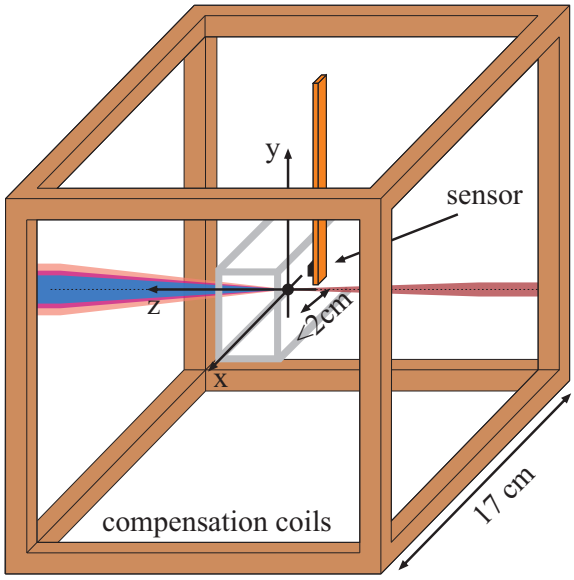

Figure 2.9.: Schematic of the magnetic field control setup. The atom (black dot) is trapped inside the vacuum glass cell (grey), which is surrounded by the compensation coils (light brown) formed from three rectangular pairs of Helmholtz coils. The magneto-resistive sensor is mounted as close as possible to the atom position at a distance of $\sim 2\,\mathrm{cm}$ while not blocking the optical access for the laser beams.

by the AC-stark effect, while other mechanisms like off-resonant excitation and photon scattering are minimized. Note, the energy shift caused by linearly polarized light is independent of the Zeeman substates (Eqn. 2.1) and will not lead to any time evolution of the qubit and hence not to any decoherence. On the other hand, this changes for circularly polarized light as it introduces different light shifts depending on the m_F state. The energy differences ΔE_{m_F} can be calculated from Equation 2.1:

$$\Delta E_{m_F}(\vec{r}) = \frac{\pi c^2 \Gamma}{2\omega_0^3}\left(\frac{1}{\Delta_{1,F}} - \frac{1}{\Delta_{2,F}}\right) \cdot g_F m_F P \cdot I(\vec{r}). \tag{2.18}$$

The parameter P describes the circularity of the polarization and is defined according to [55, 69] as

$$P = sign\,(\delta)\,\frac{2\,\|A\|\,\|B\|}{\|A\|^2 + \|B\|^2}, \tag{2.19}$$

with δ the relative phase shift between the components of an electric field and A, B the semi-axes of the polarization ellipse[7]. Defining $V := \frac{1}{\mu_B}\frac{\pi c^2 \Gamma}{2\omega_0^3}\left(\frac{1}{\Delta_{1,F}} - \frac{1}{\Delta_{2,F}}\right)$ and rewriting Equation 2.18 gives $\Delta E_{m_F}(\vec{r}) = \mu_B g_F m_F \cdot PVI(\vec{r})$, which has an equivalent form of the energy shift produced by a magnetic field oriented along the propagation direction of the dipole trap beam (z-direction) given by

[7] Following [55, 69], the polarization ellipse's major and minor half axes are given for an electric field $E_x\,(\vec{r})\,cos\,(\omega t) \cdot \hat{e_x} + E_y\,(\vec{r})\,cos\,(\omega t + \delta) \cdot \hat{e_y}$ by

$$A = \max_{0 \le \omega t \le 2\pi}\left(\sqrt{\|E_x\,(\vec{r})\|^2\,cos^2\,(\omega t) + \|E_y\,(\vec{r})\|^2\,cos^2\,(\omega t + \delta)}\right),$$
$$B = \min_{0 \le \omega t \le 2\pi}\left(\sqrt{\|E_x\,(\vec{r})\|^2\,cos^2\,(\omega t) + \|E_y\,(\vec{r})\|^2\,cos^2\,(\omega t + \delta)}\right),$$

$\Delta E_{Zeeman} = \mu_B g_F m_F \cdot B_z$. It can hence be described in terms of an effective magnetic field, which can be written for a circularity of the dipole trap polarization P_{ODT} as

$$\vec{B}_{circ}(\vec{r}) = P_{ODT} V I(\vec{r}) \cdot \hat{e_z}. \tag{2.20}$$

It is important to note that the intensity of the trapping beam $I(\vec{r})$ depends on the actual position of the atom. Since the atom oscillates in the ODT, it spreads out over the trapping volume according to the thermal density distribution (Eqn. 2.5 and Fig. 2.3). Therefore over time, it will sense varying effective magnetic fields from which only the mean effect can be canceled by applying a homogeneous actual magnetic field. Moreover, the state evolution of the Zeeman states depends on the atomic trajectory. The start position and velocity of each atom differs according to the thermal distribution in the trapping potential, and hence these paths are different from one experimental trial to the next. Thus, to get a meaningful result one needs to average over several trials and, by this, over several trajectories, which ultimately leads to a reduced fidelity of the atomic state [67].
For minimizing the circularity P_{ODT} of the ODT beam in the experiment, a linear polarizer[8] is used to define its polarization. Still, a tiny fraction of circular components will be present due to residual birefringence of the optics between the polarizer and the atom. By aligning the polarizer to the polarization eigenaxis of the system, it is possible to reduce the aforementioned effective field strength to values $P_{ODT} V I(\vec{r} = 0) < 0.5\,\mathrm{mG}$. It has, therefore, only a minor contribution to the decoherence of the atomic state.

Circular Polarization due to Strong Focusing of the ODT

When considering strongly focused laser beams with spot sizes of only a few micrometers, the paraxial approximation fails because of the large beam divergence. A mathematical framework capable of handling also larger divergence angles is introduced in [70, 71], where the electric field of a linearly polarized plane wave in the image region of a lens with focal length f is calculated by deriving exact diffraction integrals. In [67], this formalism was adapted for the use case of our experiment of the strongly focused linearly polarized optical dipole trap. Here, the shape and the polarization of the beam close to the focus position will deviate from a Gaussian beam. As a consequence of this effect, longitudinal polarization components will emerge in the vicinity of the focal position. The amplitudes of the electric field (E_x, E_y, E_z) for a beam polarized along the x-axis can be approximated in cylindrical coordinates as [67]

$$\begin{pmatrix} E_x(\vec{r}) \\ E_y(\vec{r}) \\ E_z(\vec{r}) \end{pmatrix} = E_0 F_0(0,0) \cdot \begin{pmatrix} \frac{w_D}{w(z)} + \frac{1}{(2z_R)^2}\frac{w_D^3}{w(z)^3} \cdot r^2 cos(2\phi) \\ \frac{1}{(2z_R)^2}\frac{w_D^3}{w(z)^3} \cdot r^2 sin(2\phi) \\ 2i\frac{1}{2z_R}\frac{w_D^2}{w(z)^2} \cdot r cos(\phi) \end{pmatrix} \cdot exp\left(-\frac{r^2}{w(z)^2}\right), \tag{2.21}$$

where r is the radius in the x-y plane, ϕ the angle to the x-axis and z the direction of the beam propagation. The beam parameters w_D, $w(z)$ and z_R are defined as in Subsec. 2.2.3, E_0 is a scaling

achieving the minimum and maximum for values $\omega t = t_{ext}$ and $\omega t = t_{ext} + \pi/2$ with

$$t_{ext} = \frac{1}{2} arctan\left(\frac{-\|E_y(\vec{r})\|^2 sin(2\delta)}{\|E_x(\vec{r})\|^2 + \|E_y(\vec{r})\|^2 cos(2\delta)}\right).$$

[8] CODIXX AG colorPol® IR 1100 BC4 CW02 with an extinction ratio of $\sim 1/5.000.000$ and a transmission of $> 90\%$ at $850\,\mathrm{nm}$.

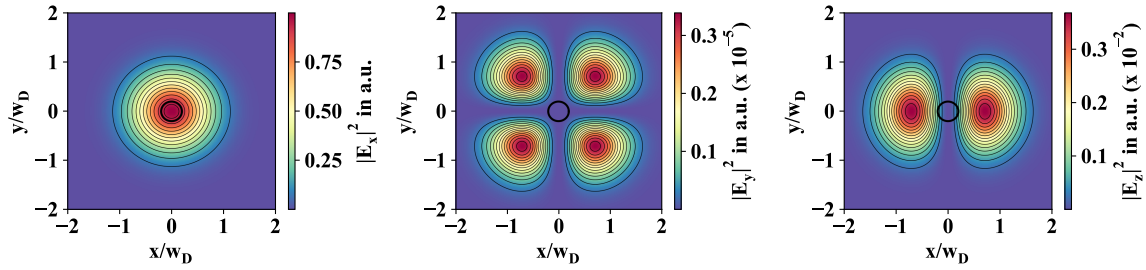

(a) Intensity of the x-component (b) Intensity of the y-component (c) Intensity of the z-component

Figure 2.10.: Intensity distribution of the electric field components of the strongly focused ODT beam in the x-y plane ($z = 0$). The black ellipses indicate the area to find an atom with a probability of 99.7% in the region $\pm 3\sigma_r$ from the center of the trap (σ_r corresponds to the transverse standard deviation of the thermal density distribution).

constant describing the electrical field strength and the value $F_0\,(0,0)$ is determined by

$$F_0\,(0,0) \coloneqq \int_0^{\alpha} d\theta\, exp\left(-\frac{f^2 tan\,(\theta)^2}{w^2}\right)\sqrt{cos(\theta)}\,(1+cos\,(\theta))\,sin\,(\theta)\,.$$

Here w is the waist of the ODT beam before the objective with a focal length f, and α is the maximum opening angle. From Eqn. 2.21, one can already see that the longitudinal field component E_z has a phase-shift $\delta \neq 0$ with respect to the transverse components E_x and E_y, resulting in an elliptical polarization. Note that the rotation of the elliptical polarization changes its direction when crossing the y-z plane, which is caused by a sign flip of E_z at $\phi = \frac{\pi}{2}, \phi = \frac{3\pi}{2}$. A more accurate approximation for the phase-relation is given in [69] with $\delta\,(z) = arctan\left(\frac{z}{Z_R}\right) + \frac{\pi}{2}$ for $x > 0$ and $\delta\,(z) = -arctan\left(\frac{z}{z_R}\right) - \frac{\pi}{2}$ for $x < 0$. Here the $\frac{\pi}{2}$-term corresponds to the factor i in the E_z component of Eqn. 2.21. Figure 2.10 depicts the intensity distribution of the three field components (E_x, E_y, E_z) in the x-y plane. It is important to mention that the color plots are of quite different scales (factor of 10^{-5} for E_y compared to E_x). These vast differences in the intensity justify the approximation to neglect the E_y component for further analysis, and the resulting elliptical polarization can therefore be treated as it is composed only of the E_x and the E_z components. As already elaborated before, these elliptical polarization components lead to an atomic state evolution. In analogy to Subsec. 2.5.2, this corresponds to a circularly polarized beam propagating along the y-direction with a circularity $P_{long}\,(\vec{r})$ causing an effective magnetic field $\vec{B}_{long}$ of form

$$\vec{B}_{long}(\vec{r}) = P_{long}\,(\vec{r})\,VI(\vec{r}) \cdot \hat{e_y} \tag{2.22}$$

with $P_{long}\,(\vec{r})$ defined according to Eqn. 2.19. Note that $P_{long}\,(\vec{r})$ is position-dependent contrary to P_{ODT}. The field distribution of $B_{long}(\vec{r})$ in the x-y plane and the x-z plane is shown in Fig. 2.11. As already discussed before, the atomic state evolution depends on the specific trajectory of each atom in the trapping potential and averaging over several of those will lead to dephasing of the atomic state. The effective magnetic field is anti-symmetric with respect to the z-axis due to the sign flip of $P_{long}(\vec{r})$ for positive and negative x values. Fortunately, after a complete transverse oscillation of the atom, the phases accumulated on both sides of the y-z plane will cancel out, restoring the initial atomic state.

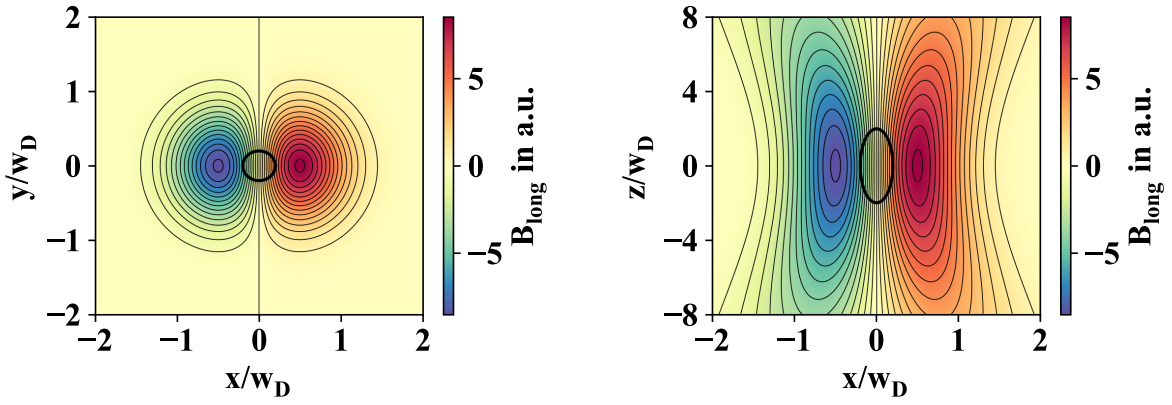

(a) $B_{long}(\vec{r})$ in the x-y plane (z=0)

(b) $B_{long}(\vec{r})$ in the x-z plane (y=0)

Figure 2.11.: Effective magnetic field distribution $B_{long}(\vec{r})$ in the x-y plane at z=0 (a) and in the x-z plane at y=0 (b). The black ellipses indicate the area to find an atom with a probability of 99.7% corresponding to a three-sigma interval from the trap center according to the thermal density distribution (Eqn. 2.5).

This 'rephasing' of the atomic state is limited mainly by two facts: First, the atom oscillates not only transversely but also along the optical axis. The effective field each atom sees is hence not perfectly anti-symmetric, which reduces the fidelity. Secondly, the trapping potential is not harmonic, and the trap frequencies for each atom slightly differ depending on its energy. Thus, each atom rephases at a slightly different time, leading on average to dephasing of the atomic spin-state, especially for later times. More information about this effect together with simulation can be found in [53].

2.5.3. Time-Resolved Evolution of the Atomic Spin State

Preparing the atom in a defined initial state is the first step to observe its temporal evolution. This can be realized by using the entangled atom-photon state (Subsec. 2.3.2) and projecting the photon onto a certain polarization. For most of the measurements presented in this thesis, the photon is analyzed in the H/V basis, preparing the atom in one of the two states $|\Psi_H\rangle = \frac{-i}{\sqrt{2}}(|1,-1\rangle - |1,+1\rangle)$ and $|\Psi_V\rangle = \frac{1}{\sqrt{2}}(|1,-1\rangle + |1,+1\rangle)$. These states together with $|\Psi_0\rangle = |1,0\rangle$ form a set of orthogonal states representing a basis for the $5^2S_{\frac{1}{2}}, F = 1$ ground state. Time-resolved measurements are performed by delaying the atomic state readout for a variable time t. When averaging over sufficiently many measurement events, the state population of the atom can be evaluated. Recall that for the state selective ionization scheme, the state $|\Psi_0\rangle$ always gets ionized and needs to be considered when interpreting the measurement outcomes.
All previously described decoherence effects are originating from magnetic fields or effective magnetic fields. By following their description in Subsec. 2.5.1, the state evolution for a given field can be calculated.

In the case of a field along the x-direction $\vec{B} = \pm B_0 \cdot \hat{e}_x$ ($b_z = 0, \phi = 0$), the state evolution is

given by

$$|\Psi_H(t)\rangle = |\Psi_H\rangle,$$
$$|\Psi_V(t)\rangle = |\Psi_V\rangle\, cos(\omega_L t) \pm i\,|\Psi_0\rangle\, sin(\omega_L t). \tag{2.23}$$

Here $|\Psi_H\rangle$ is an eigenstate to the field, and hence no time evolution is expected.

The evolution for a field along the y-direction $\vec{B} = \pm B_0 \cdot \hat{e}_y$ ($b_z = 0, \phi = \frac{\pi}{2}$) is described by

$$|\Psi_H(t)\rangle = |\Psi_H\rangle\, cos(\omega_L t) \mp |\Psi_0\rangle\, sin(\omega_L t),$$
$$|\Psi_V(t)\rangle = |\Psi_V\rangle, \tag{2.24}$$

with $|\Psi_V\rangle$ being an eigenstate to this field.

For a field along the z-direction $\vec{B} = \pm B_0 \cdot \hat{e}_z$ ($b_z = 1, b_x = b_y = 0$) the evolution is

$$|\Psi_H(t)\rangle = |\Psi_H\rangle\, cos(\omega_L t) \pm |\Psi_V\rangle\, sin(\omega_L t),$$
$$|\Psi_V(t)\rangle = |\Psi_V\rangle\, cos(\omega_L t) \mp |\Psi_H\rangle\, sin(\omega_L t). \tag{2.25}$$

Here both states will undergo a time evolution since none of them is an eigenstate to the field.

For every readout polarization χ_{ro}, a dark state $|D\rangle_{\chi_{ro}}$ and a bright state $|B\rangle_{\chi_{ro}}$ are defined according to Eqns. 2.9-2.11, which lead to different measurement outcomes ('atom not ionized' or 'atom ionized'). Thus, setting the readout polarization to V defines the dark state $|D\rangle_V = |\Psi_V\rangle$ and the bright state $|B\rangle_V = |\Psi_H\rangle$, making it possible to distinguish between them. Under the influence of a field along the x-direction an atom initially prepared in the dark state $|\Psi_V\rangle$ will rotate into the state $|\Psi_0\rangle$ and hence gets ionized. Therefore, the projection onto the dark state will show oscillations in the time-resolved measurement, while nothing changes for an atom prepared in the bright state (Eqn. 2.23). On the other side, the effect of a field along the y-direction cannot be observed with this readout polarization. An atom initially prepared in the bright state $|\Psi_H\rangle$ will rotate into the state $|\Psi_0\rangle$ and get ionized either way, and for an atom prepared in the dark state $|\Psi_V\rangle$, no temporal evolution is expected (Eqn. 2.24). However, oscillations caused by a y-field can be observed using an H-polarized readout with the associated dark state $|D\rangle_H = |\Psi_H\rangle$ and bright state $|B\rangle_H = |\Psi_V\rangle$. Now, oscillations caused by an x-field cannot be observed. The influence of a z-field, however, is visible in both cases since the temporal evolution (Eqn. 2.25) is between the dark state and the bright state for a V- as well as for an H-polarized readout.

Figure 2.12 shows time-resolved measurements of the two states $|\Psi_H\rangle$ and $|\Psi_V\rangle$ for both readout polarizations V and H. In these measurements, the magnetic fields and the circularity P_{ODT} of the dipole trap beam have been minimized. Thus, the only sources of decoherence influencing the measurement are the residual magnetic field noise and the effective fields along the y-direction caused by the strongly focused trapping beam. Measurements, performed with a V-polarized readout, are depicted in Fig. 2.12a, showing the coherence properties of the atomic qubit. After an atomic readout delay of $200\,\mu$s, atoms initially prepared in the state $|\Psi_V\rangle$ can be found in the dark state $|D\rangle_V$ with a probability of $\sim 80\%$, such as atoms initially prepared in the state $|\Psi_H\rangle$ with a probability of $\sim 12\%$. These results are consistent with an atomic state evolution with only the residual magnetic field noise present. Figure 2.12b shows the time-resolved measurements performed with an H-polarized readout. Here the influence of the longitudinal polarization components of the ODT beam on the temporal evolution of the atom state $|\Psi_H\rangle$ is clearly visible as a periodic dephasing and rephasing with the transverse trap oscillation period of $12.5\,\mu$s. Simulating this temporal evolution and matching it with the measured one allows for determining precise numbers for the trap frequencies and extracting the atom temperature [53]. The time of a rephasing can be tuned by changing the optical power of

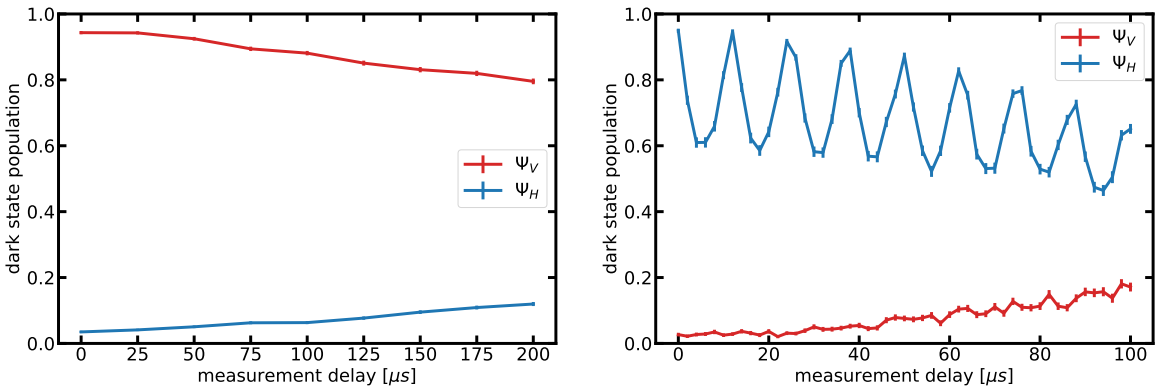

(a) V-polarized readout: The dark state for this readout polarization is given by the state $|\Psi_V\rangle$. The time evolution of the initially prepared states is visualized as the projection onto this dark state and shows decoherence caused by the residual magnetic field noise.

(b) H-polarized readout: The dark state for this readout polarization is given by the state $|\Psi_H\rangle$. The time evolution of the $|\Psi_H(t)\rangle$ state shows the expected dephasing and rephasing behavior originating from the longitudinal field components $\vec{B}_{long}(\vec{r})$ (Eqn. 2.22) of the strongly focused ODT beam with a period of 12.5 μs corresponding to one transverse trap oscillation.

Figure 2.12.: Time-resolved measurements of the initially prepared atomic states $|\Psi_H\rangle$ (blue) and $|\Psi_V\rangle$ (red) with minimized magnetic fields. The measurements are performed with a V-polarized readout (a) and an H-polarized readout (b). On the y-axis, the probability is shown to find the atom in the dark state of the corresponding readout polarization.

the trapping beam, which is vital for time-critical measurements as the loophole-free test of Bell's inequality presented in Chapter 3. Furthermore, in Chapter 4 the atom temperature and trap frequency are needed to estimate the collection-and-coupling efficiency of the microscope objectives.

2.6. Atom-Atom Entanglement

The entanglement of two single atoms trapped in independent laboratories 398 m apart from each other is generated by using the process of entanglement swapping [27, 72]. In this process, the entanglement of two entangled atom-photon pairs is swapped onto the atoms by performing a projection measurement of the photons onto an entangled two-photon Bell-state [50, 51]. An advantage of this scheme is that no direct interaction of the two particles is needed, and entanglement over large distances can be obtained.

2.6.1. Entanglement Swapping

The starting point of the entanglement swapping protocol is to provide two pairs of entangled particles, for which, in our case, the entangled atom-photon states generated in the remote laboratories are used. These two entangled atom-photon states are given by

$$|\Psi\rangle_{A_i,P_i} = \frac{1}{\sqrt{2}}\left(|\uparrow\rangle_{A_i}|\downarrow\rangle_{P_i} + |\downarrow\rangle_{A_i}|\uparrow\rangle_{P_i}\right) \tag{2.26}$$

with $(|\uparrow\rangle_{A_i}, |\downarrow\rangle_{A_i})$ and $(|\uparrow\rangle_{P_i}, |\downarrow\rangle_{P_i})$ representing pairs of orthogonal states for the atom and photon, respectively, and the index $i \in \{1, 2\}$ labels the trap. The tensor product of these two states form a

joint four-particle state $|\psi\rangle$ that can be written as

$$\begin{aligned}
|\Psi\rangle &= |\Psi\rangle_{A_1,P_1} \otimes |\Psi\rangle_{A_2,P_2} \\
&= \frac{1}{\sqrt{2}} \left(|\uparrow\rangle_{A_1} |\downarrow\rangle_{P_1} + |\downarrow\rangle_{A_1} |\uparrow\rangle_{P_1} \right) \otimes \frac{1}{\sqrt{2}} \left(|\uparrow\rangle_{A_2} |\downarrow\rangle_{P_2} + |\downarrow\rangle_{A_2} |\uparrow\rangle_{P_2} \right) \\
&= \frac{1}{2} \left(|\uparrow\rangle_{A_1} |\downarrow\rangle_{P_1} |\uparrow\rangle_{A_2} |\downarrow\rangle_{P_2} + |\downarrow\rangle_{A_1} |\uparrow\rangle_{P_1} |\uparrow\rangle_{A_2} |\downarrow\rangle_{P_2} \right) \\
&+ \frac{1}{2} \left(|\uparrow\rangle_{A_1} |\downarrow\rangle_{P_1} |\downarrow\rangle_{A_2} |\uparrow\rangle_{P_2} + |\downarrow\rangle_{A_1} |\uparrow\rangle_{P_1} |\downarrow\rangle_{A_2} |\uparrow\rangle_{P_2} \right).
\end{aligned} \tag{2.27}$$

Expanding and rearranging Eqn. 2.27 in terms of the four maximally entangled Bell-states $|\Phi^{\pm}\rangle = \frac{1}{\sqrt{2}} \left(|\uparrow\rangle |\uparrow\rangle \pm |\downarrow\rangle |\downarrow\rangle \right)$ and $|\Psi^{\pm}\rangle \frac{1}{\sqrt{2}} \left(|\uparrow\rangle |\downarrow\rangle \pm |\downarrow\rangle |\uparrow\rangle \right)$ gives [51]

$$\begin{aligned}
|\Psi\rangle = &\left|\Phi^+\right\rangle_{A_1,A_2} \otimes \left|\Phi^+\right\rangle_{P_1,P_2} \\
&+ \left|\Phi^-\right\rangle_{A_1,A_2} \otimes \left|\Phi^-\right\rangle_{P_1,P_2} \\
&+ \left|\Psi^+\right\rangle_{A_1,A_2} \otimes \left|\Psi^+\right\rangle_{P_1,P_2} \\
&+ \left|\Psi^-\right\rangle_{A_1,A_2} \otimes \left|\Psi^-\right\rangle_{P_1,P_2}.
\end{aligned} \tag{2.28}$$

As can be seen from Eqn. 2.28, projecting the photons on a Bell-state results in the entanglement of the atoms in a Bell-state of the same type. Therefore, the projection measurement 'heralds' a successful generation of an entangled atom-atom state, indicating that the system is ready for further experimental steps. In particular, this heralded entanglement generation enables us only to read out the atomic state after the entanglement was successfully established. These so-called 'event-ready' schemes are especially interesting for Bell-tests [27].

2.6.2. Photonic Bell-state Measurement

A special apparatus enabling projective measurements on maximally entangled two-photon Bell-states is required to perform joint measurements on the photons. The Bell-state measurement (BSM) apparatus consists of a fiber beam splitter (BS) with a polarization analysis setup in each output port (Fig. 2.13). The single photons emitted during the atom-photon entanglement processes are coupled into optical fibers and guided to the BSM. Here, two-photon interference at the fiber BS and subsequent polarization analysis is employed to project the photons onto an entangled state. This interference process can be understood by the Hong-Ou-Mandel effect[73], in which two indistinguishable photons that enter a BS on different inputs interfere and, as a result, leave the BS always in the same output port and never on different ones ('photon bunching'). Two-photon interference at a BS for the four Bell-states as input states was calculated, e.g. in [51]. The findings are that for the three symmetric[9] Bell-states $|\Phi^+\rangle$, $|\Phi^-\rangle$, and $|\Psi^+\rangle$, the interference leads to photon bunching and the photons leave the BS in the same output port, whereas anti-bunching occurs for the anti-symmetric Bell-state $|\Psi^-\rangle$ and the photons leave the BS in different outputs. A successful projection onto a Bell-state is indicated by the coincidence detection of the two photons for specific detector combinations. In our case, the photons are detected in the H/V-basis as it is the natural basis of a PBS without the need for additional wave plates (Sec. 2.4.1), and the corresponding photonic and atomic states are $|\uparrow\rangle_P = |H\rangle, |\downarrow\rangle_P = |V\rangle$ and $|\uparrow\rangle_A = |\uparrow\rangle_x, |\downarrow\rangle_A = |\downarrow\rangle_x$. Coincidence detection in the detector combinations $1^V \wedge 1^H$ or $2^V \wedge 2^H$ signals the projection onto the $|\Psi^+\rangle$ state, and the detector combinations

[9] Symmetric under exchange of particles.

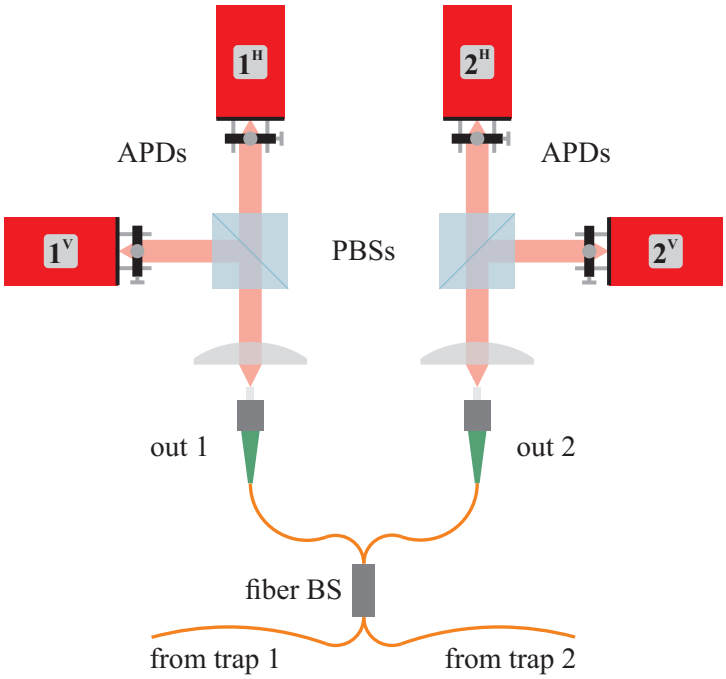

Figure 2.13.: Schematic of the Bell-State measurement apparatus. The photons from the trap setups are guided to the BSM via single-mode optical fibers and overlapped on a fiber beam splitter (BS). Two-photon interference at the BS and subsequent polarization analysis with polarizing beam splitters (PBSs) and avalanche photodiodes (APDs) project the photons onto a Bell-state. The different APDs are labeled with the number of the BS output port and the polarization of the PBS output port. Coincidence detection in the detector combinations $1^V \wedge 1^H$ or $2^V \wedge 2^H$ indicate the projection onto the $|\Psi^+\rangle$ state, and detector combinations $1^V \wedge 2^H$ or $2^V \wedge 1^H$ indicate the projection onto the $|\Psi^-\rangle$ state.

$1^V \wedge 2^H$ or $2^V \wedge 1^H$ signal the projection onto the $|\Psi^-\rangle$ state. Photons in the states $|\Phi^+\rangle$ or $|\Phi^-\rangle$ cannot be detected with the system presented here since both photons have the same polarization and will impinge on the same detector. Thus, this interferometric BSM setup allows identifying two out of four Bell-states, and a projection of the photons on $|\Psi^+\rangle_{PP} = \frac{1}{\sqrt{2}}(|H\rangle|V\rangle + |V\rangle|H\rangle)$ heralds the generation of the atomic state

$$|\Psi^+\rangle_{AA} = \frac{1}{\sqrt{2}}(|\downarrow\rangle_x|\uparrow\rangle_x + |\uparrow\rangle_x|\downarrow\rangle_x), \tag{2.29}$$

while the projection of the photons on $|\Psi^-\rangle_{PP} = \frac{1}{\sqrt{2}}(|H\rangle|V\rangle - |V\rangle|H\rangle)$ heralds the generation of the atomic state

$$|\Psi^-\rangle_{AA} = \frac{1}{\sqrt{2}}(|\downarrow\rangle_x|\uparrow\rangle_x - |\uparrow\rangle_x|\downarrow\rangle_x). \tag{2.30}$$

Two-photon Interference

In order to generate a high fidelity atom-atom state, the two-photon interference contrast needs to be maximized, requiring the interfering photons to be indistinguishable in all degrees of freedom. More specifically, the mode overlap of the photons needs to be maximized regarding their spectral mode, temporal mode and spatial mode. A detailed analysis of different influences on the interference contrast can be found in [51, 74].
In short, an excellent spectral mode overlap is achieved since both photons are emitted via the same optical decay channel of a single ^{87}Rb atom well isolated from its environment. By this, possible light shifts introduced by the Zeeman effect or the AC-stark effect are minimized, leaving the Doppler shift caused by the motion of the atoms as the largest contribution. However, the influence on the spectral mode overlap has been found to be negligible [74]. Moreover, to completely cancel the contribution of the AC-stark shift all laser lights, especially the light of the ODT beam, are turned off during the time of excitation in the atom-photon entanglement process.
An optimal temporal overlap is achieved by creating two identical temporal photonic wave packets so that their arrival times at the BS match perfectly. The shape of these wave packets depends on the excitation pulses' optical properties and the atom's spontaneous decay. Therefore, identical shapes are created by carefully setting the intensities and pulse shapes of the two excitation pulses. Furthermore, the arrival times of the wave packets are matched by synchronizing the experimental sequences in the two laboratories (Subsec. 2.6.3).
A perfect spatial overlap is achieved by using a single-mode fiber BS in which the two photons share the same spatial mode. However, even though these three criteria are well satisfied, the achievable fidelity of the entangled atom-atom state is still limited by the detector dark counts and by two-photon emissions from one atom during one excitation attempt [51, 55].

2.6.3. Operation of the Two Atom-Trap Experiment

The two independent single atom traps are separated by $398\,\mathrm{m}$ and connected to the BSM with single-mode optical fibers. Since the BSM is located in the same laboratory as one of the traps (Lab 1), these fibers differ quite a lot in length. While the trap in Lab 1 is connected with a $5\,\mathrm{m}$ fiber in an air-conditioned environment, the trap in Lab 2 is connected with a $700\,\mathrm{m}$ long fiber laid via cable ducts of the university buildings (Fig. 2.1). Hence, the long fiber is more susceptible to external influences such as, e.g. temperature, leading to drifts of its birefringence. Since the qubit of the photon is encoded in the polarization degree of freedom, a regularly automatized polarization compensation is necessary [75]. For the trapping procedure of a single atom, the number of fluorescence photons is monitored, and successful loading is recognized as a step-like increase of the detected count rate (Subsec. 2.2.4). Since the BSM is used for photon detection from both traps, the loading scheme needs to be adapted to load two atoms with the same detectors. Furthermore, the independent excitation processes in both labs need to be synchronized to achieve a high interference contrast at the BSM. Therefore additional communication and synchronization between both trap setups are required.

Control and Synchronization

Figure 2.14 depicts a schematic of the two atom-trap setup showing all relevant devices and signals needed for the experimental control. A 700 m long fiber channel[10] is used to establish communication

[10]The fiber channel (Leoni AT-VQ(ZN)H(ZN)B2Y 4SM780+4G50+12E9 2,5) consists of 20 fibers: 4 × SM780 single-mode fiber, 12 × E9/125 single-mode fiber, and 4 × G50/125 multi mode fiber.

and synchronization between the two separated labs. Electrical-optical converters (E→O, O→E) transmit electrical signals needed to control and operate the experiment via the optical fiber channel. Depending on the specific requirements of the signal to be sent, different communication modules are used, allowing for analog, digital and network communication.
Two local PCs control the individual traps, which set most of the experimental parameters like laser powers and frequencies and perform automatized calibrations (e.g. magnetic field sensor calibration (Subsec. 2.5.1)). The PC in Lab 1 serves as a master taking over the experimental control of loading two atoms and storing measurement data registered in a time-to-digital converter (TDC) located in the same lab. The PC in Lab 2 acts as a slave receiving control signals from the master PC via the dedicated optical Ethernet connection. After the master PC registers the successful loading of two atoms, it commands the slave PC to trigger the start control in Lab 2. The start control is a device sending out synchronized signals to switch each side's local control unit (CU) into the mode to run the experimental sequence (Subsec. 2.6.3). The CUs will continue to execute this sequence until an atom is lost and the PCs initiate the next loading procedure. While the PCs can perform comparatively slow tasks on the ms timescale, the CUs can also control the time-critical experimental steps. They are custom-built pattern generators with an output resolution of 20 ns, which can react on external inputs to switch between the different steps of the experimental sequence. For each part of the sequence, they control the timings of all the lasers, setting acceptance time windows and sending out marker signals to the TDC for identifying the different parts of the sequence during the data analysis.
Synchronization of the two labs is achieved by sharing and distributing a common clock signal among all time-critical devices. This includes the start control in Lab 2, the control unit of each lab, an FPGA that registers two-photon coincidence detections of the BSM during the entanglement swapping, and the TDC in Lab 1 to record the measurement data. The $100\,\mathrm{MHz}$ clock signal is generated in Lab 2 and sent via an analog communication channel to Lab 1. In both labs, the signal is distributed to all critical devices with a clock distribution board[11]. With this, the two CUs and all other components are synchronized with a time jitter of $150\,\mathrm{ps}$ (RMS) [53].

Experimental Sequence

The experimental sequence (Fig. 2.15) for the two atom-trap experiment comprises several steps: the loading of two atoms, the synchronized generation of atom-photon entanglement in both labs, the generation of atom-atom entanglement via entanglement swapping with two-photon coincidence detection at the BSM, and the atomic state readout.

Loading of the Atom Traps The procedure to individually load an atom in one of the traps is already explained in Subsec. 2.2.4. Here, a step-like increase of the detected fluorescence count rate above a certain threshold indicates the loading of a single atom. This changes in the two atom-trap experiment since the collected photons from both atoms are guided to the same detection setup (BSM). However, it is still possible to distinguish between the atoms by successively turning off and on the cooling light on both sides. Once a trap is loaded, the respective MOT current is turned off while the other side continues loading an atom. Loading of two atoms is indicated if the measured count rate exceeds a second threshold. This second threshold is higher than the individual count rates and thus cannot be reached by fluorescence light of only one atom. A decrease in the count rate indicates the loss of one or both atoms, and the PCs initiate re-loading.

[11] Analog Devices, AD9523-1 Evaluation Board

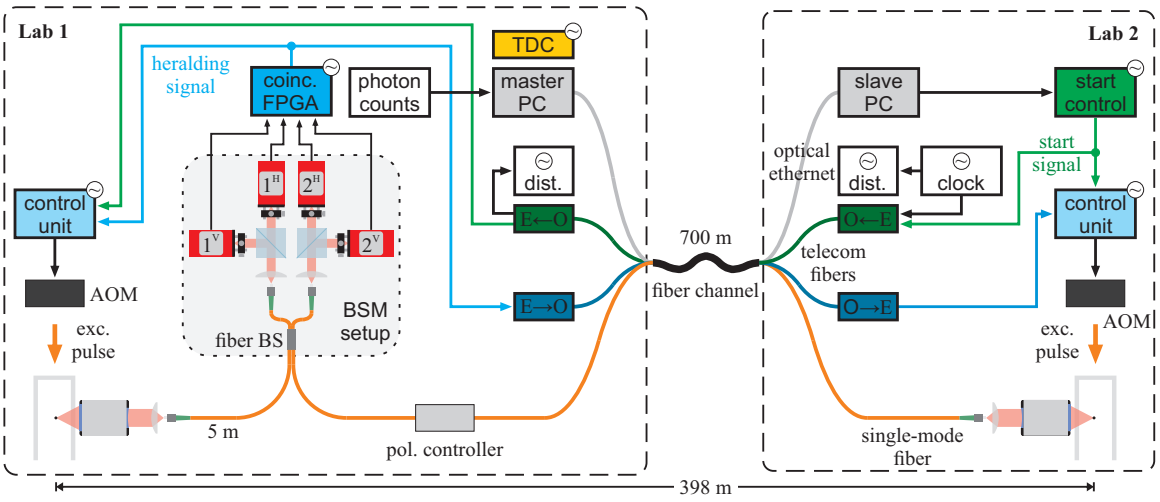

Figure 2.14.: Overview of the two atom-trap experimental setup: The two labs, each accommodating a fully independent single atom trap, are separated by a distance of 398 m and are connected via a 700 m long fiber channel based on several optical fibers. While most of these fibers are used for establishing communication and synchronization between the labs, a single-mode fiber for 780 nm (orange) is used to transmit the 780 nm fluorescence light emitted by the atom in Lab 2 to the BSM located in Lab 1. The atom trap in Lab 1 is connected to the BSM with a 5 m long single-mode fiber. All time-critical devices are synchronized with a common clock signal and marked with a clock symbol (⏦). The 100 MHz clock signal is generated in Lab 2 and transmitted via an analog communication channel to Lab 1. The procedure to load atoms in both traps is initiated and controlled by the master PC, which sends signals to command the slave PC over the dedicated optical Ethernet connection (grey). After loading of two atoms, the start control (green) is triggered, sending out a start signal (green arrow) to the control unit (CU) on each side, which initializes the synchronized excitation sequences in both labs. The emitted single photons are guided with the single-mode fibers to the BSM, where two-photon coincidence events are registered by the FPGA (blue). Whenever a two-photon coincidence is registered in a correct detector combination (Subsec. 2.6.2), the FPGA sends out a heralding signal (blue arrow), which switches the CUs (light blue) to initiate the atomic state readout. A time-to-digital converter (TDC) records all necessary events (e.g. detector clicks of the single-photon detectors and the CEMs, marker signals, etc.) to reconstruct the experimental sequence and analyze the measurement data.

Entanglement Generation Sequence After successfully loading two atoms, the CUs are triggered by the start signal to run the excitation sequence. This sequence aims to generate atom-photon entanglement in both labs in a synchronized way such that the wave packets of the emitted single photons overlap perfectly at the BSM, enabling the generation of a high-fidelity atom-atom state (Subsec. 2.6.2). The sequence starts with the initial state preparation via optical pumping (Subsec. 2.3.1), followed by the excitation pulse to generate an entangled atom-photon pair (Subsec. 2.3.2). This cycle of state preparation and excitation is repeated until an entangled atom-atom state is successfully generated. The success probability P_{S_i} ($i = 1, 2$ for trap 1, respectively trap 2) of detecting a single photon after an excitation attempt is only on the order of a few per mille[12]. Moreover, to generate an entangled atom-atom state, both photons need to be detected simultaneously, and the probability for a two-photon coincidence detection is given by $P_S = \frac{1}{2} P_{S_1} \cdot P_{S_2}$, whereby the factor $\frac{1}{2}$ accounts for the fact that the BSM can only identify two out of four Bell-states. An FPGA monitors the single-photon clicks of the BSM. Whenever a correct coincidence detection occurs during a photon acceptance time window of $208\,\mathrm{ns}$, a heralding signal is sent out to the CUs, interrupting the excitation sequence and switching to the atomic state readout (Fig. 2.14). Besides the photon transmission time from Lab 2 to the BSM of about $3.6\,\mu\mathrm{s}$, an additional delay time after each excitation try is introduced in both labs to send a possible heralding signal via an asynchronous communication channel to Lab 2. This delay time of $3.7\,\mu\mathrm{s}$ also includes the electrical signals inside the laboratories. Adding the photon and signal transmission times and the time needed for the initial state preparation before every excitation attempt results in $10.36\,\mu\mathrm{s}$ per excitation attempt.
The atom gets heated during the repeated preparation and excitation cycles due to photon scattering with the pumping and excitation beams. An increased atom temperature not only leads to a reduced lifetime of the atom in the trap but also enhances the decoherence effects due to the more extensive motion of the atom (Subsec. 2.5.2). In [53], a scheme was developed in which 40 preparation-excitation cycles are followed by a $350\,\mu\mathrm{s}$ cooling period leading to an effective repetition rate of $52.2 \cdot 10^3 \frac{1}{s}$.

Atomic State Readout The atomic state readout is initiated after receiving a heralding signal indicating a successful generation of an entangled atom-atom state. In this so-called 'event-ready' scheme, the earliest time to read out the atomic state of the atom in Lab 2 is $7.3\,\mu\mathrm{s}$ after the emission of the respective photon. A high-fidelity atomic state readout in the measurement basis affected by the dephasing mechanism caused by the strongly focused ODT beam (Subsec. 2.5.2) is only possible after a complete transverse oscillation period of the atom in the trapping potential. For typical trap parameters in these experiments, this period is $> 10\,\mu\mathrm{s}$, and an additional delay of the state readout is required. For time-critical measurements like the loophole-free test of Bell's inequality, a simultaneous readout of both atoms is possible by tuning the transverse trap periods with adjusting the individual trap intensities (Subsec. 2.2.3).

2.7. Challenges of Long-Distance Entanglement

Entanglement between separated quantum memories will be indispensable for future, scalable quantum networks [31] facilitated by quantum repeater protocols [47, 76]. These networks allow for new applications like distributed quantum computation and secure quantum communication over large distances. With the system introduced in this chapter, long-distance entanglement between two atoms separated by $398\,\mathrm{m}$ is achieved [21]. Nevertheless, for practical use of the applications mentioned

[12] Values reported in [53] are $P_{S_1} = 1.65‰$ and $P_{S_2} = 0.85‰$. With the new objectives build and implemented in the framework of this thesis, efficiencies of $P_{S_1} = 5.36$ and $P_{S_2} = 3.44‰$ are achieved.

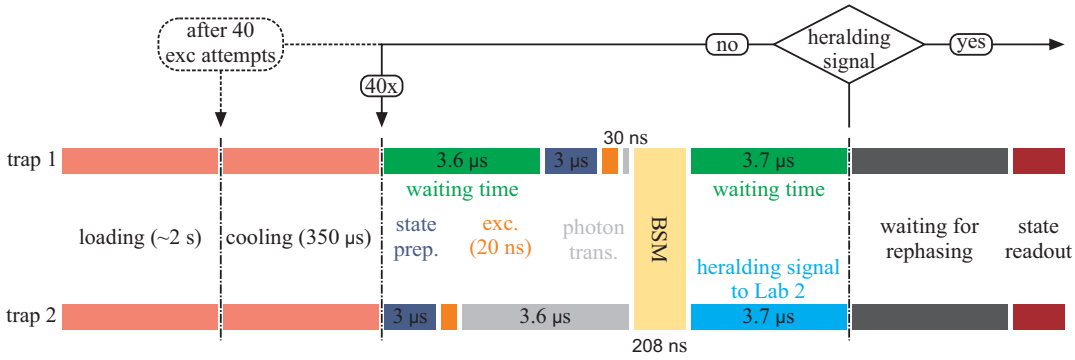

Figure 2.15.: Experimental sequence of the two atom-trap experiment: After loading an atom in each of the traps (light red), the CUs are triggered by the start signal to repeatedly run cycles of state preparation (dark blue) and excitation (orange). These cycles are synchronized such that the single photons arrive simultaneously at the BSM, taking into account additional waiting times (green) and photon transmission times (grey). An FPGA registers two-photon coincidences during a photon acceptance time window of $208\,\mathrm{ns}$, and a potential heralding signal is sent with a transmission time of $3.7\,\mu\mathrm{s}$ to the distant trap in Lab 2. When receiving a heralding signal, the atomic state readout (red) is initiated; otherwise, the preparation-excitation cycles are repeated. After 40 excitation attempts, recooling the atoms with a $350\,\mu\mathrm{s}$ cooling period (light red) is necessary.

above, the distance between the entangled atoms should be drastically extended to the range of $\sim 100\,\mathrm{km}$. Already the development of our experiment going from a separation of the atoms from $20\,\mathrm{m}$ in [50, 51] to the current distance of $398\,\mathrm{m}$ showed that substantial challenges arise when extending the distance, namely the achievable atom-atom entanglement rate and the requirement for longer coherence times of the atomic qubits. In the next step, when going to even larger distances, these challenges need to be overcome once more and shall briefly be discussed in this section.

2.7.1. Coherence

In the employed event-ready scheme, the atomic state readout can only be applied after receiving the heralding signal (Subsec. 2.6.3). Increasing the distance between the labs from 398 m to several tens of km thus requires coherence times on the order of $100-200\,\mu\mathrm{s}$. The primary sources of decoherence and currently used methods to prolong the coherence time are described in Section 2.5. Still, further optimizations are needed to reach the required coherence by reducing the influence of the two main contributions. These are the residual magnetic field noise and effective magnetic fields of the strongly focused ODT beam (Subsec. 2.5.2).
Regarding the first one, a magnetic guiding field can help reduce the effect of field fluctuations along transverse directions but not along the direction of the guiding field [67]. Therefore, preparations are already started to implement a possible scheme, based on a state transfer of the qubit states to the hyperfine states, which reduces the sensitivity to magnetic fields along this direction by several orders of magnitudes [77]. In the tightly focused trapping beam, effective magnetic fields emerge near the focus, leading to a periodic, non-perfect 'rephasing' of the atomic state. These fields depend, among others, on the atomic temperature and the beam geometry [53]. That opens the possibility to reduce this decoherence effect by cooling the atoms further and providing a more symmetric trap geometry.

The latter one was one of the design criteria for the new microscope objectives built and implemented in the scope of this thesis (Chapter 6). Moreover, using two perfectly overlapped, counter-propagating trapping beams will cancel the longitudinal field components and potentially cancel the effect altogether [69].

2.7.2. Atom-Atom Entanglement Rate

In the remote entanglement scheme used in our experiment, the generation of an entangled pair of atoms is heralded by a two-photon coincidence detection at the BSM. However, the success probability of such an event is relatively low and depends on the probabilities P_{S_i} to detect the single photon emitted by the atom after an excitation attempt ($i = 1, 2$ for Trap 1 and Trap 2, respectively). By multiplying these probabilities with the achievable repetition rate f_E of the excitation sequence (Sec. 2.6.3), the atom-atom entanglement rate R_E can be calculated:

$$R_E = \frac{1}{2} \cdot f_E \cdot P_{S_1} \cdot P_{S_2} \cdot P_{duty}. \tag{2.31}$$

Here the factor $\frac{1}{2}$ accounts for the fact that the BSM can distinguish only 2 out of the 4 Bell states, and P_{duty} represents the probability of having simultaneously an atom loaded in both traps to run the synchronized excitation sequence.
The repetition rate is determined by the time needed to prepare the atomic state before each excitation ($3\,\mu$s), the transmission times of the photons to the BSM, the time to send the heralding signal back to the trap setups, and the time to cool the atoms after a certain amount of excitation tries ($350\,\mu$s after 40 excitations). Let d_1 and d_2 be the fiber lengths from Trap 1 and Trap 2 to the BSM, respectively, then the repetition rate is given by

$$f_E = \frac{1}{\frac{350\,\mu\text{s}}{40} + 3\,\mu\text{s} + \frac{2 \cdot \max(d_1, d_2)}{\frac{2}{3}c}}, \tag{2.32}$$

with the speed of light in an optical fiber $\frac{c}{n_f} \sim \frac{2}{3}c$ (n_f: refractive index of the fiber core) and $\max(d_1, d_2)$ being equal to the larger length of d_1 or d_2. In the current configuration the BSM is located in the same laboratory as Trap 1 ($d_1 << d_2 = d$) and $\max(d1, d2) = d$.
The probabilities P_{S_i} are influenced by many factors and can be written as

$$P_{S_i} = \eta_{pump} \cdot \eta_{exc} \cdot \eta_{cc_i} \cdot \eta_{det} \cdot \eta_{loss_i} \cdot \tau_{fiber}(d_i), \tag{2.33}$$

with η_{pump} the efficiency of the state preparation, η_{exc} the efficiency of the excitation process, η_{cc_i} the efficiency of collecting and coupling an emitted photon into a single-mode optical fiber and η_{det} the efficiency of the single photon detectors. The transmission loss in the optical fiber of length d_i with an attenuation α is accounted for by the factor $\tau_{fiber}(d_i) = 10^{-\alpha \cdot d_i}$ and residual losses, e.g. unavoidable reflections at optical surfaces, are combined in the factor η_{loss_i}. Due to the short fiber length d_1 in the current configuration, the transmission loss for this fiber can be neglected. Even though some of these contributions (e.g. η_{cc_i}, η_{det} and η_{loss_i}) are not known precisely and can only be estimated, the total value of P_{S_i} can be measured accurately. Note, typically an excitation efficiency of $\eta_{exc} = 0.8$ is used to reduce two-photon emission events originating from one atom during one excitation attempt. It has been shown that these events have a limiting influence on the fidelity of the entangled atom-atom state [51].
Inserting Eqns. 2.32 and 2.33 in Eqn. 2.31 yields an event rate of:

$$R_E = \frac{1}{2} \cdot \frac{P_{duty}}{\frac{350\,\mu\text{s}}{40} + 3\,\mu\text{s} + \frac{2 \cdot d}{\frac{2}{3}c}} \cdot \eta_{cc_1} \cdot \eta_{cc_2} \cdot \eta_{pump}^2 \cdot \eta_{exc}^2 \cdot \eta_{det}^2 \cdot \eta_{loss_1} \cdot \eta_{loss_2} \cdot 10^{-\alpha \cdot d}. \tag{2.34}$$

Entanglement Rate for Longer Distances

For the experimental setup from 2016 used to perform the loophole-free Bell test [21], an event rate of $\sim 2\,{}^{events}/_{\mathrm{min}}$ at a fiber length of $700\,\mathrm{m}$ was obtained. However, according to Eqn. 2.34, this event rate will almost drop to zero for distances of several $10\,\mathrm{km}$ (Figure 2.16), e.g. one event every 100 years at a distance of 20 km. Reasons for this and possible solutions to increase the entanglement rate are stated here.

Decreased Repetition Rate The repetition rate of the experiment will drop due to longer photon and signal transmission times depending on the length of the fiber connection d. This reduction in repetition rate is unavoidable in schemes based on entanglement swapping. Therefore, besides optimizing the excitation sequence to minimize the times needed for the state preparation and the cooling [53], the only option to increase the repetition rate is by changing the experimental configuration from an asymmetric to a symmetric one with the BSM located in the middle of both trap setups. In this case, $\max(d_1, d_2) = {}^{d}/_{2}$ and the combined photon and signal transmission time reduces by a factor of 2.

Loss in Optical Fibers The limiting factor for the entanglement rate for larger distances is the wavelength-dependent attenuation loss in optical fibers. For example, for the emitted photon at a wavelength of $780\,\mathrm{nm}$, the attenuation in the fiber is $4.0\,\frac{\mathrm{dB}}{\mathrm{km}}$. To overcome these losses frequency conversion of the single photon into the low attenuation regime of telecom-wavelengths is necessary. Furthermore, the conversion process is required to preserve the quantum information encoded in the photon, e.g. the single photon polarization state, which is entangled to the spin-state of the atom. Quantum frequency conversion (QFC) [78] provides this opportunity and is implemented in our experiment converting the single photon to the telecom S-band at $1522\,\mathrm{nm}$ (fiber attenuation of $\sim 0.18\,\frac{\mathrm{dB}}{\mathrm{km}}$) with an external device conversion efficiency of 57% [79]. This allowed verifying entanglement between an atom and a telecom photon with a fidelity of $\geq (78.5 \pm 0.9)\,\%$ after transmission through $20\,\mathrm{km}$ of optical fiber (Chapter 7). Moreover, highly efficient superconducting nanowire single-photon detectors (SNSPDs) are available for telecom wavelengths with detection efficiencies $> 85\%$. Thus, combining higher detection efficiency and the lower attenuation in the optical fiber, QFC becomes beneficial, resulting in higher entanglement rates for fiber lengths longer than $678\,\mathrm{m}$ (Figure 2.16).

High NA Microscope Objective Setups From the remaining contributions in Eqn. 2.34, the collection and coupling efficiencies η_{cc_i} have the biggest potential for improving the entanglement rate. These efficiencies can be increased by the use of better collection optics. Therefore, new custom-designed high NA microscope objectives were built and implemented in both traps (Chapter 6), leading to a gain in collection-and-coupling efficiency by a factor of ~ 2.5 for the setup in Lab 1 and by a factor of ~ 3.5 in Lab 2. With these numbers, a gain in the remote entanglement rate by a factor of ~ 8.75 is expected (Fig. 2.16). These improvements can compensate for the additional conversion losses when applying the QFC, and an entanglement rate over $20\,\mathrm{km}$ fiber of $0.78\,{}^{events}/_{\mathrm{min}}$ becomes feasible. In a symmetric configuration, this number can further be increased to $1.48\,{}^{events}/_{\mathrm{min}}$.
The fidelity of the entangled atom-atom state is directly related to the generation quality of the entangled atom-photon states via the entanglement swapping. A thorough analysis of the atom-photon entanglement generation process revealed the possibility of increasing the state fidelity by finding an optimal trade-off between excitation probability, background and dark counts, and a photon acceptance time window for the BSM [51, 55]. Hence, an improved entanglement fidelity can be achieved

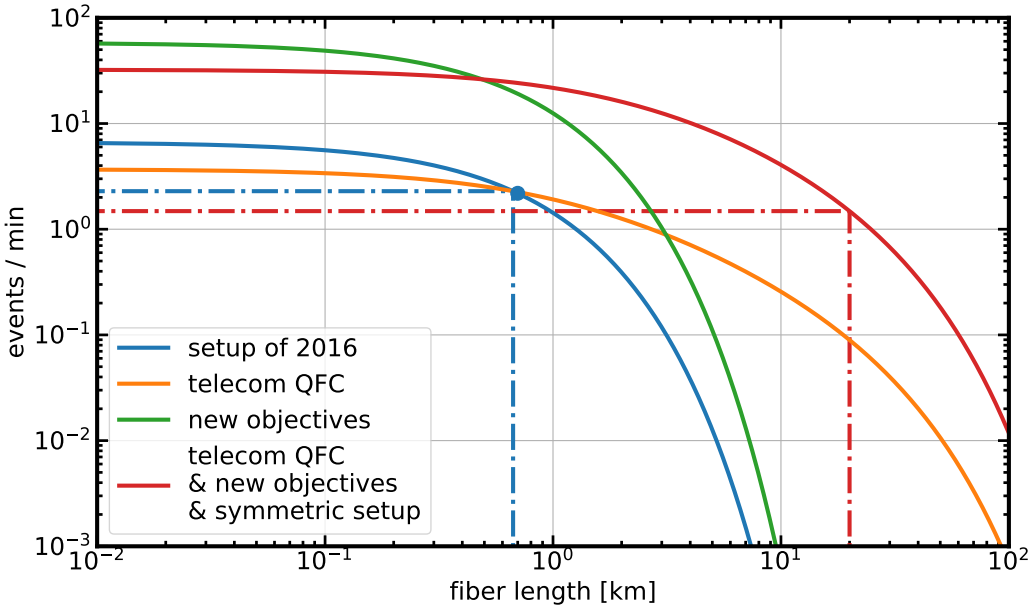

Figure 2.16.: Estimated remote entanglement rates as a function of the total fiber length connecting both traps. The event rate of $\sim 2\,^{events}/_{\mathrm{min}}$ at a fiber length of $700\,\mathrm{m}$ obtained in the Bell test [21] performed in 2016 (blue) is taken as a reference for the other graphs. The entanglement rate for the QFC (orange) compared to the reference is reduced for short distances due to the external device efficiency of the converters and becomes beneficial, resulting in higher rates for fiber lengths larger than $678\,\mathrm{m}$. The enhanced collection-and-coupling efficiencies reached by implementing the new objectives lead to an estimated increase of the entanglement rate by a factor of ~ 8.75 (green). By combining all possible improvements (QFC, new optics and a symmetric setup), reasonable event rates in the order of $\sim 1\,^{event}/_{\mathrm{min}}$ at a distance of $20\,\mathrm{km}$ can be expected (red).

at the cost of a reduced entanglement rate. Here, the enhanced collection and coupling efficiencies reached with the new collection optics allow for these optimizations without reducing the event rate to an unpractical level.

In order to optimize the collection-and-coupling efficiency, a detailed understanding of the involved processes is indispensable. Therefore, a model describing these processes is developed in Chapter 4. Following this model, a theoretical upper limit for the efficiency is calculated, and suitable optics for an optimized performance could be selected. A characterization of the involved optics can be found in Chapter 5.

The results of the loophole-free tests of Bell's inequality performed in 2016 [21] are presented in the next chapter. The data for these measurements were obtained with the old collection optics and, by this, resembles the status of the experiment before the new objectives were implemented. It can therefore be used as a reference regarding improvements in entanglement rate and achievable state fidelity.

3. Test of Bell's Inequality with Entangled Atoms

In 1964 John Bell published his famous paper "On the Einstein Podolsky and Rosen paradox" [11], where he showed that certain predictions of quantum mechanics cannot be reproduced by any classical theory that follows a local-realistic description of nature. He formulated his results in the form of an inequality, which for all theories governed by local realism gives a strict bound on the outcome of correlation measurements performed on two distant particles. Quantum mechanics, on the other hand, can exceed this bound for certain measurement settings and by that violates Bell's inequality. For the first time, this showed a way towards experiments able to answer the long and still ongoing discussion on the completeness of quantum mechanics started with the historic paper "Can Quantum-Mechanical Description of Physical Reality Be Considered Complete?" published in 1935 by Einstein, Podolsky, and Rosen (EPR) [7]. According to EPR, two fundamental principles need to be fulfilled by a physical theory to be considered complete, namely realism and locality. Realism implies that a physical quantity assigned to a system is an inherent property of this system, regardless of a potential measurement. For locality, it is required that measurements performed outside of each other's light cones cannot have any causal influence on each other. Quantum mechanics cannot fulfill these two principles at once, and hence it was considered incomplete. Therefore, the possible existence of nowadays called local hidden variables (LHV) was introduced to extend quantum mechanics to a complete theory fulfilling both principles. The LHV cannot be experimentally observed themselves but still determine the outcome of any possible measurement. The stringent bound for any local-realistic descriptions given by Bell's inequality allows now for an experimental test of all LHV theories.

Following the quantum mechanical prediction, Bell's inequality can be violated by performing measurements on an entangled pair of particles for suitable measurement settings. The inequality proposed by Bell in 1964 required perfect correlations between both particles and thus was experimentally not feasible. A reformulation not requiring perfect correlations was published in 1969 by Clauser, Horne, Shimony and Holt (CHSH) [12], making an experimental test of Bell's inequality applicable. Soon after, many experiments were performed (e.g. [13, 15, 16]) with (almost all) results in favor of the quantum mechanical prediction. However, most of the experiments conducted so far relied on additional assumptions on the observer or the observed system, opening potential loopholes to the LHV theories [14, 17]. Only recently, experiments free from the most important loopholes could be conducted [18–20].

Here, the results of two experimental Bell tests (started on 15th April 2016 and 14th June 2016) performed on pairs of entangled ^{87}Rb atoms are presented. Combining heralded entanglement of the atoms separated by a distance of $398\,\mathrm{m}$ with the fast and efficient readout of their spin states made it possible to close the two major loopholes - the locality and the detection loophole - in the same experiment [21, 53, 55].

setting	readout polarization χ_{ro}	angles α and ϕ in (2.9)
$A=0$	$\chi_{A=0} = V$	$\alpha = 0$ and $\phi = 0$
$A=1$	$\chi_{A=1} = \cos\left(\frac{\pi}{4}\right) V - \sin\left(\frac{\pi}{4}\right) H$	$\alpha = \frac{\pi}{4}$ and $\phi = 0$
$B=0$	$\chi_{B=0} = \cos\left(-\frac{\pi}{8}\right) V - \sin\left(-\frac{\pi}{8}\right) H$	$\alpha = -\frac{\pi}{8}$ and $\phi = 0$
$B=1$	$\chi_{B=1} = \cos\left(\frac{\pi}{8}\right) V - \sin\left(\frac{\pi}{8}\right) H$	$\alpha = \frac{\pi}{8}$ and $\phi = 0$

Table 3.1.: Readout polarizations χ_{ro} used for the different settings of the Bell test. Settings A correspond to the inputs of Lab 1 and B to the inputs of Lab 2.

3.1. CHSH Inequality

A test of Bell's inequality is based on correlation measurements on two spin-$1/2$ particles. As already mentioned above, the inequality proposed by Bell in its original form is unpractical for actual experiments since it requires perfectly (anti-)correlated pairs of particles. Therefore, the CHSH inequality is used in the experiment presented here, as it puts Bell's inequality in a more experimentally friendly form. In this scenario, pairs of particles are provided by a source and sent to two separated measurement devices (Alice and Bob). Each device receives a binary input (0 or 1) labeled for Alice with A and for Bob with B that determines the measurement direction. The results X and Y (for Alice and Bob, respectively) can take one of the two output values -1 or $+1$. The complete experiment is separated into distinct rounds. In every round, one pair of particles is sent to the devices. Each of those receives exactly one input and answers with exactly one output. The results from both sides are combined every round, forming either a correlated ($X = Y$) event or an anti-correlated ($X \neq Y$) event. The respective total number of events for the four input combinations (A, B) are counted and given by $N_{A,B}^{X,Y}$. From these numbers, the following correlators are calculated for the inputs $A = a$, $B = b$ with $a, b \in \{0, 1\}$:

$$E_{a,b} \coloneqq \frac{N_{a,b}^{X=Y} - N_{a,b}^{X\neq Y}}{N_{a,b}^{X=Y} + N_{a,b}^{X\neq Y}}. \tag{3.1}$$

Bell's inequality in the form of CHSH is then given by [12]

$$S \coloneqq |E_{1,1} + E_{1,0}| + |E_{0,1} - E_{0,0}| \leq 2, \tag{3.2}$$

with the bound for local-realistic theories of 2. On the other hand, the quantum mechanical prediction for certain measurement directions yields a value of $S = 2\sqrt{2}$, violating the inequality. In [80], this value has also been shown to be the greatest possible one for any quantum state and observable.

The heralded entanglement generation (Sec. 2.6) is used as the source of particles for the experimental Bell tests presented here. Depending on the heralding signal, one of the two entangled states $|\Psi^{\pm}\rangle_{AA} = \frac{1}{\sqrt{2}} \left(|\downarrow\rangle_x |\uparrow\rangle_x \pm |\uparrow\rangle_x |\downarrow\rangle_x\right)$ (Eqns. 2.29-2.30) is prepared. In order to perform correlation measurements, different analysis angles for the atomic state readout and thus the dark and bright states for the projection are set by the polarization χ_{ro} of the readout lasers (Sec. 2.4.2). The maximum violation is achieved for the measurement directions summarized in Table 3.1. The applied readout scheme has two possible measurement outcomes: the atom gets ionized, or the atom does not get ionized. In the latter case, no ionization fragments can be detected, and the measurement results X and Y take the value -1, while for the detection of at least one ionization fragment, they take the value $+1$.

3.2. Loopholes

Bell inequalities are derived with certain assumptions on the local realist theories under test, and the respective bound only holds when all of these assumptions are true. In an experimental realization, these assumptions transform into requirements, which need to be fulfilled. Each requirement not accounted for in the experiment opens the possibility for local realism to give a measurement result exceeding the bound of the inequality. Therefore, the number of so-called loopholes must be reduced to a minimum to perform a meaningful Bell test. In the following, the main loopholes are described.

3.2.1. Detection Loophole

While deriving the inequality, it is implicitly assumed that all provided pairs of particles are measured, producing an output X and Y for each experimental round. Experiments suffering from detector inefficiencies do not satisfy this requirement, and thus, the fair sampling assumption is required. This means that the measured events are considered a representative fraction of all events leading to the same outcome of the Bell test. For the CHSH inequality and an otherwise perfect system, a lower bound for the detector efficiencies of $\sim 83\%$ can be given, up to that the fair sampling assumption is not needed [81, 82]. The detection loophole was first closed in an experiment with entangled ions trapped only a few $\mu\mathrm{m}$ apart from each other [83], leaving the locality loophole open.
In the experiment presented here, every round of the Bell test is heralded by the BSM, and only then the state readout is triggered. In such an event-ready scheme, a measurement result is obtained for every readout attempt, making the fair sampling assumption unnecessary and thereby closes the detection loophole. Any insufficiency of the atomic state readout, e.g. the inefficiency of the particle detectors (Sec. 2.4.2), will only lead to wrong measurement results reducing the readout fidelity and thus lowering the achievable S value.

3.2.2. Locality Loophole

The locality loophole addresses the requirement for local and independent measurements. Here it is assumed that the input choice and measurement on one side is independent of the input choice and measurement on the other side. To account for this in the experiment, any communication between the two sides during this time must be prevented. By enforcing space-like separation of the measurements, any causal dependence between them can be excluded since they are outside of each other's past light cones. The locality loophole was first closed in an experiment with entangled photons created in a down-conversion source and measured at a distance of $400\,\mathrm{m}$ [84]. However, due to low detector efficiencies, the detection loophole was not closed.
In the Bell tests presented in this chapter, space-like separated measurements are realized by combining the large separation of the entangled atoms of $398\,\mathrm{m}$ with the fast atomic state readout, which takes less than $1.1\,\mu\mathrm{s}$, including the basis choice based on a fresh random number. By this also the locality loophole is closed.

3.2.3. Other Loopholes

Two further loopholes that are often referred to are the memory loophole [85] and the free-will (or freedom of choice) loophole [86]. The first one allows LHV theories for a potential memory of the previous rounds of the experiment. Local realism can exploit this knowledge due to finite statistics of the experiment, thus enabling a systematic violation of Bell's inequality, especially for a small number of events. Moreover, in statistical analysis methods, a common assumption is that the experimental

rounds are performed identically and independent from each other (i.i.d. assumption). This assumption is no longer be justified when allowing for a memory of the LHV, and methods not requiring the i.i.d. assumption to analyze the experimental results must be applied. By this, the memory loophole can be closed. Therefore, two suitable methods, [87] and [88, 89], are used in this experiment.
The freedom of choice loophole considers the independence of the input choices from the LHV and vice versa. Random number generators on both sides are used as a source for a random input selection to address this loophole. Still, a possible influence of the LHV on the generation of the random numbers cannot be excluded, which makes space-like separation of the creation of the LHV and the inputs necessary. Since it is impossible to define a specific time at which the creation of the LHV took place, this loophole can never fully be closed. A possible point in time the LHV might come into existence in an experiment based on entanglement swapping is the creation of the remote entanglement via the Bell state measurement. Assuming this for the presented Bell test, the LHV are clearly not influenced by the input selections, taking place $10.7\,\mu$s after the BSM. Contrary to that, the generation of the random numbers for the basis choices are inside the light cone of the BSM since the used quantum random number generators (QRNGs) are located in the same laboratories as the trap setups. Hence, the freedom of choice loophole is not closed in this experiment.
For a more detailed discussion of the previously described loopholes and for reviewing other not mentioned loopholes, see [17].

3.3. Space-like Separated Measurements

As discussed in the previous section closing the locality loophole requires space-like separation of the measurements performed on the two distant sites. Here, the input creation defines the beginning of the measurement process, which is completed after the measurement outcome is received and stored in a local storage unit. Space-like separation can now be guaranteed if the outcome on one side is obtained outside the light cone of the input creation of the other side.
In our case, the experimental scheme to perform space-like separated measurements is the following: After a successful coincidence detection at the BSM (Sec. 2.6), the heralding signal is sent to the two local control units initiating the measurement procedure. In both labs, a QRNG (Subsec. 3.3.1) is used, providing random inputs on request. Depending on the input, the corresponding readout polarization is selected, and the state-selective ionization is applied. Ionization fragments possibly created in the ionization process are detected by the CEMs, and a comparator converts their electrical output pulses into logical TTL signals [52]. Together with the random inputs, these classical signals are recorded in the local storage unit of the respective lab. This completes one round of the Bell test, and the experimental sequence repeats until the Bell test data are accumulated. An overview of the crucial devices and signals for the measurement process are depicted representatively for Lab 1 in Fig. 3.1.

3.3.1. Random Input Choice

For deriving the CHSH inequality, the local measurements are assumed to depend only on the respective local input and be independent of the other side's input. However, when choosing the inputs in a deterministic way, a possible connection to the measurement of the other side cannot be excluded. Independence must therefore be assumed unless the inputs are chosen in a well-defined and unpredictable way. In our case, this is experimentally realized by using quantum random number generators [54] on both sides. As any physical device requires certain assumptions on its functioning, a physical

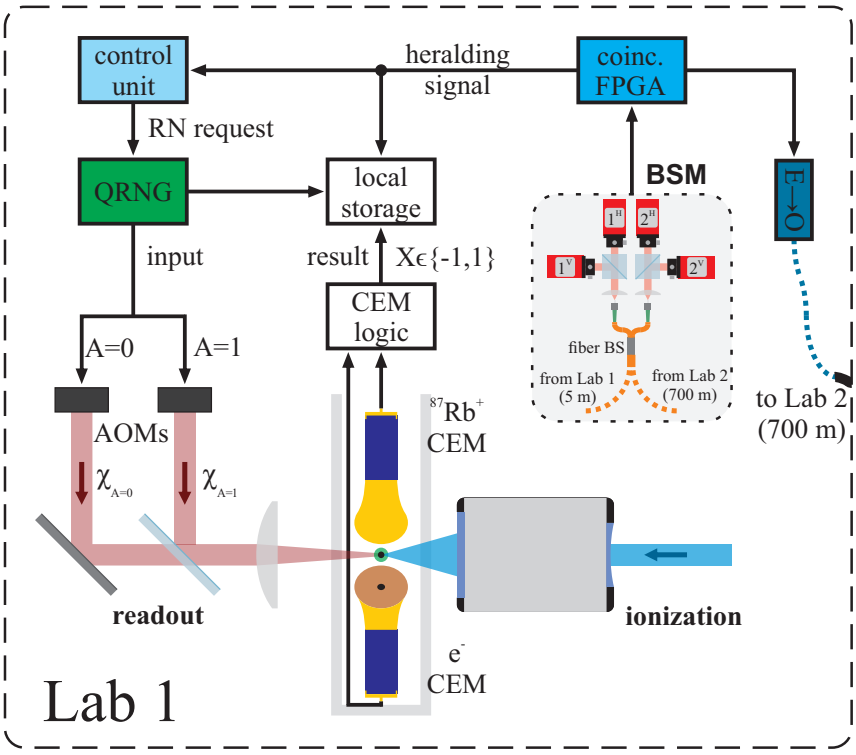

Figure 3.1.: Schematic of the measurement scheme in the Bell tests: After the FPGA registers a successful photon coincidence detection at the BSM, it sends out the heralding signal to the control units in both labs. In Lab 1 via a $0.5\,\mathrm{m}$ long coaxial cable and towards Lab 2 via an asynchronous communication over the $700\,\mathrm{m}$ long fiber channel. In each lab, the control unit requests a random bit from the QRNG, which is used as local input ($A \in \{0, 1\}$) to select the desired readout polarization χ_A according to Table 3.1 by triggering one of the two AOMs. The possible creation of ionization fragments during the state-selective ionization is detected by the CEMs and converted into logic TTL signals by a comparator. These signals are recorded together with the random inputs in a local storage to evaluate the results. The scheme for Lab 2 is designed analogously with the difference that the heralding signal is received from the optical communication and is not stored in the local storage of Lab 2. For an overview of the communication and synchronization of the two atom-trap experiment, see Fig. 2.14.

model of the QRNGs was developed within which bounds for the residual predictability for generating a particular input are given ([55] and Supplementary material of [21]). The knowledge of the predictability can be exploited by the LHVs and, therefore, has to be accounted for in the analysis of the experiment. In the following, the function of the QRNG is briefly described. A statistical analysis of the random numbers (RNs) generated during the Bell test can be found in Sec. 3.4.

Working Principle of the QRNG

The employed QRNGs rest on counting the number of photons emitted by a light-emitting diode (LED) during a certain time interval. The emitted light is first attenuated before it is detected with a photo-multiplier tube (PMT). Then, a comparator converts the generated electrical pulses into digital signals counted by an FPGA within time bins of $20\,\mathrm{ns}$. Finally, the parity of the registered photon number determines the value of the random bit output.
The source of randomness in the underlying physical model is based on photo-detection theory [90, 91]. Here the detection events from a light source of constant intensity are assumed to be fully uncorrelated on time scales of the counting interval. Thus, the generated output bit is independent of previous events as well as of the LHVs. The detected photon number follows a Poissonian distribution, which is modified by the extendable dead time of the detector, enabling the generation of output bits close to zero bias without the need for further post-processing [54]. The QRNGs can be operated at $50\,\mathrm{Mbps}$ and provide a random bit with no measurable correlations older than $80\,\mathrm{ns}$ [21, 53] (Subsec. 3.4.2).

3.3.2. Atomic State Analysis

After receiving the heralding signal, the atomic state readout starts by requesting a binary input from the QRNG, which determines the setting of the Bell test (Table 3.1). However, in the time budget for space-like separation, the time needed for selecting the measurement direction already needs to be considered. Hence, a method for fast switching to the desired measurement basis is required.

Fast Selection of the Measurement Direction

In the employed analysis scheme, the measurement direction is defined by the polarization of the readout laser. In our case, a fast selection of the correct polarization is realized using two separate optical beam paths, each for one of the polarizations, which can be independently turned on by AOMs[1]. The AOMs are operated at an acoustic frequency of $408\,\mathrm{MHz}$, and the beams are focused close to their transducers, which allows for fast switching times[52]. That enables the creation of an optical readout pulse, which reaches the atom $< 220\,\mathrm{ns}$ after the QRNG provided the RN. Furthermore, by turning on only one of the AOMs at a time, the desired polarization can be selected.

State Detection

Atoms in the bright state of the applied readout polarization will get ionized, and the created ionization fragments are accelerated towards the CEMs. Their impact on the sensitive area inside the detectors generates an electron avalanche, which is converted by a comparator into a logical signal. The duration of the readout process can be evaluated by analyzing the arrival times of the fragments, which primarily depend on the acceleration voltage U_{acc} between the CEMs. For Lab 1, this results

[1] 2x AA Opto-Electronic MT350-A0, 12-800 (Lab 1), 2x Gooch & Housego AOMO 3350-199 (Lab 2)

in a duration of $570 \pm 3\,\mathrm{ns}$ with $U_{acc} = 4250\,\mathrm{V}$ and for Lab 2 in a duration of $725 \pm 3\,\mathrm{ns}$ with $U_{acc} = 2400\,\mathrm{V}$ [2] [53]. Thus, the time for the electrical pulse to be converted into the logical TTL signal is $80\,\mathrm{ns}$ for Lab 1 and $84\,\mathrm{ns}$ for Lab 2 [53].

3.3.3. Timing of the Measurement Process

In order to determine the time budget for space-like separated measurements, it is essential to have a precise knowledge of the distances between the atom trap of one lab and the QRNG of the other. These distances were determined by linking measurements within the laboratories with precise map data provided by the 'Bayerisches Landesamt für Digitalisierung, Breitband und Vermessung'. As a result, the obtained distance between the atom trap in Lab 1 and the QRNG in Lab 2 is $398.0\,\mathrm{m}$ and the distance between the atom trap in Lab 2 and the QRNG in Lab 1 is $402.7\,\mathrm{m}$ resulting in minimal luminal signal transmission times of ${}^{(398.0\,\mathrm{m}-1\,\mathrm{m})}/_{c} = 1324.2\,\mathrm{ns}$ and ${}^{(402.7\,\mathrm{m}-1\,\mathrm{m})}/_{c} = 1339.9\,\mathrm{ns}$ [21, 53].

The total duration for the measurement process can now be calculated by adding all individual contributions, e.g. the maximum 'age' of the random number, the switching of the measurement basis, the time for the state-selective ionization and the generation of the classical output signal. For Lab 1, a duration of $947 \pm 1\,\mathrm{ns}$, and for Lab 2, a duration of $1093 \pm 1\,\mathrm{ns}$ is obtained (Fig. 3.2) [21, 53]. Besides the short duration of the local measurements, they also need to be performed simultaneously, requiring a precise synchronization of both traps (Sec. 2.6.3). As the heralding signal initiates the measurements, its transmission times to the respective labs are critical and need to be considered in the time budget. In Lab 1, the signal is transmitted via a $0.5\,\mathrm{m}$ coaxial cable in $2.5 \pm 0.2\,\mathrm{ns}$ whereas, for Lab 2, it is transmitted via an asynchronous communication module over the $700\,\mathrm{m}$ long fiber with a transmission time of $3717 \pm 7\,\mathrm{ns}$[3]. Furthermore, for a high fidelity state readout, the time of the measurement needs to be matched with the rephasing of the atomic state caused by the longitudinal field components of the ODT (Sec. 2.5.2). This can be achieved by appending additional waiting times to delay the start of the measurements in both labs. These waiting times depend on the individual trap frequencies and can be tuned by changing the intensity of the respective trapping beam (Sec. 2.2.3). With this, an almost simultaneous readout of both atoms is realized, by starting the measurement in Lab 2 $28.5\,\mathrm{ns}$ earlier than in Lab 1. Altogether, this results for Lab 1 in a time margin for space-like separation of $340\,\mathrm{ns}$ and for Lab 2 in a margin of $267\,\mathrm{ns}$ (Fig. 3.2) [21, 53].

3.4. Statistical Analysis of the Generated Inputs

All bits generated by the QRNGs during the Bell tests are continuously recorded for analysis purposes. The data for both experimental runs are organized in 115420 files of $1\,\mathrm{Gb}$ size ($115\,\mathrm{Tb}$ in total) and evaluated for bias, serial correlations and general statistical tests. Although these tests can never certify genuine randomness, they still give some information about the quality of the randomness of the bits and can reveal potential artifacts or malfunctioning of the QRNGs.

[2] The acceleration voltages are limited in their amplitudes to avoid high-voltage breakdowns of the particle detectors. However, the thresholds were found to be different for the two labs and hence the applied voltages differ as well.

[3] The error is determined by the uncertainty of the cable length and not by a jitter of the signal.

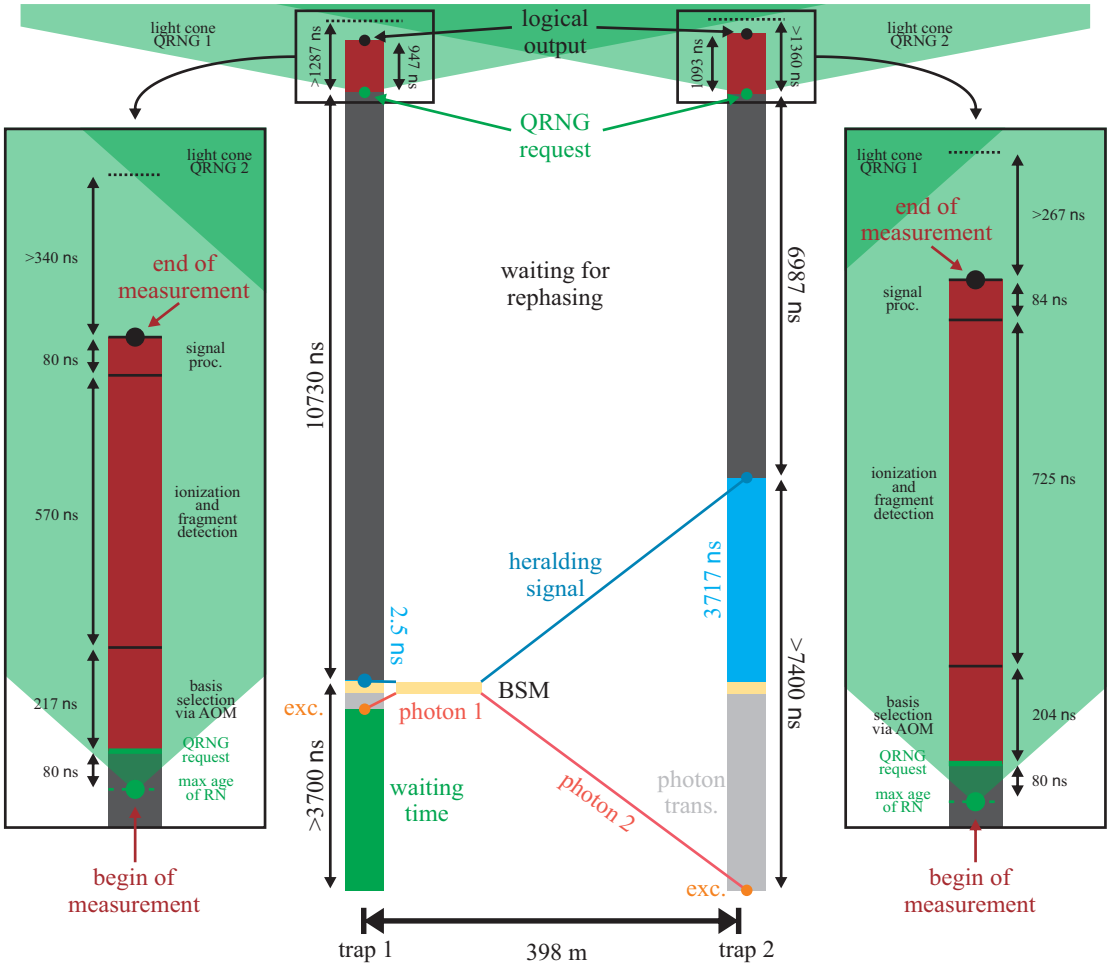

Figure 3.2.: Space-time diagram of the experimental sequence of the Bell tests [21, 53, 55]: Atom-atom entanglement is generated with a BSM on photons emitted by single atoms in Trap 1 and Trap 2 after a synchronized excitation (orange), taking the different photon transmission times (light grey) into account (Sec. 2.6.3). The heralding signal (blue) initiates the atomic state measurement and is transmitted to both setups. For a high fidelity state readout, additional waiting times (dark grey) are introduced such that the time of the measurement matches the rephasing of the atomic state (Sec. 2.5.2). The measurement process (red, see enlarged diagrams) starts by requesting a random input determining the measurement basis. Then, the atomic state is read out with the state-selective ionization scheme introduced in Section 2.4.2, and the corresponding readout polarization is set via AOMs. The end of the measurement is reached after a classical output signal is obtained. Summing up the timings for the individual steps of the measurement shows that a space-like operation is realized with time margins of $> 340\,\mathrm{ns}$ for Trap 1 and $> 267\,\mathrm{ns}$ for Trap 2.

run	#bits	mean $(\lvert B_A \rvert)$	mean $(\lvert B_B \rvert)$	max $(\lvert B_A \rvert)$	max $(\lvert B_B \rvert)$	σ
15th April 2016	$2 \times 16.0\,\mathrm{Tb}$	$1.30 \cdot 10^{-6}$	$1.67 \cdot 10^{-7}$	$4.33 \cdot 10^{-6}$	$3.22 \cdot 10^{-6}$	$8.33 \cdot 10^{-7}$
14th June 2016	$2 \times 46.6\,\mathrm{Tb}$	$4.97 \cdot 10^{-6}$	$2.67 \cdot 10^{-6}$	$8.74 \cdot 10^{-6}$	$7.15 \cdot 10^{-6}$	$8.33 \cdot 10^{-7}$

Table 3.2.: The mean and maximum value of the observed bias for both experimental runs. Values observed in Lab 1 are labeled with a subscript A (Alice) and for Lab 2 with B (Bob). σ corresponds to the standard deviation of a $360\,\mathrm{Gb}$ data point.

3.4.1. Bias

The bias B of a bit sequence of length n is given by

$$B = \frac{n_0}{n} - \frac{1}{2}, \tag{3.3}$$

with n_0 being the number of '0' and $n - n_0$ the number of '1'. It can be measured by simply counting the number of '0' or '1' in a bit sequence. In Fig. 3.3, an example of the bias observed in Lab 1 for the run from 14th June 2016 is shown as a function of time; more data can be found in Appendix C.1. Each data point contains $360\,\mathrm{Gb}$ of data and corresponds to a measurement time of $2\,\mathrm{h}$. The chosen data size is a trade-off between reducing the statistical noise to be smaller than the observed value and the observability of potential long term drifts. Analyzing the bias allows for estimating a predictability τ, which is defined such that for all output bits $q_i \in \{0, 1\}$ the probability $Pr\,(q_i = 0)$ is bounded by

$$\frac{1}{2} - \tau \leq Pr(q_i = 0) \leq \frac{1}{2} + \tau.$$

Taking the maximum value for the bias observed in both runs of $8.74 \cdot 10^{-6}$ (Tab. 3.2) and adding a 2σ margin to it yields a conservative estimate for the predictability of $\tau_1 = 1.04 \cdot 10^{-5}$ ([55] and Supplementary material of [21]). This value agrees well with the predictions of the physical model when allowing the LHVs to have information about all from the outside-accessible parameters of the QRNG, e.g. the photon count rate and the temperature inside the QRNG (both actively stabilized values). Granting the LHVs also full knowledge of all internal parameters, e.g. electrical noise, an even more conservative estimate of $\tau_2 < 6.3 \cdot 10^{-4}$ can be given ([55] and Supplementary material of [21]). This value is used in the analysis methods to evaluate the presented Bell tests (Subsec. 3.5.1).

3.4.2. Correlations

Another interesting property concerning the predictability of a bit in a bit sequence are serial correlations (or auto-correlations), which are defined as

$$SCC_l = \frac{\sum_{i=1}^{n-l} \left(q_i - \frac{1}{2}\right)\left(q_{i+l} - \frac{1}{2}\right)}{\sum_{i=1}^{n-l} \left(q_i - \frac{1}{2}\right)^2}, \tag{3.4}$$

with the bits $q_i \in \{0, 1\}$, n the length of the bit sequence and l the lag of the correlation. It is important to note that this formula is only correct in the presence of zero bias. However, for the very small bias present in our case, it is still a good approximation with an error of less than $2 \cdot 10^{-9}$. The complete data set is analyzed for serial correlations up to a lag of 56, finding correlation values with $l > 1$ consistent with zero. The average values of all correlations for the data generated during the measurement run from June 14, 2016 in Lab 1 can be found in Table 3.3. More data are presented in

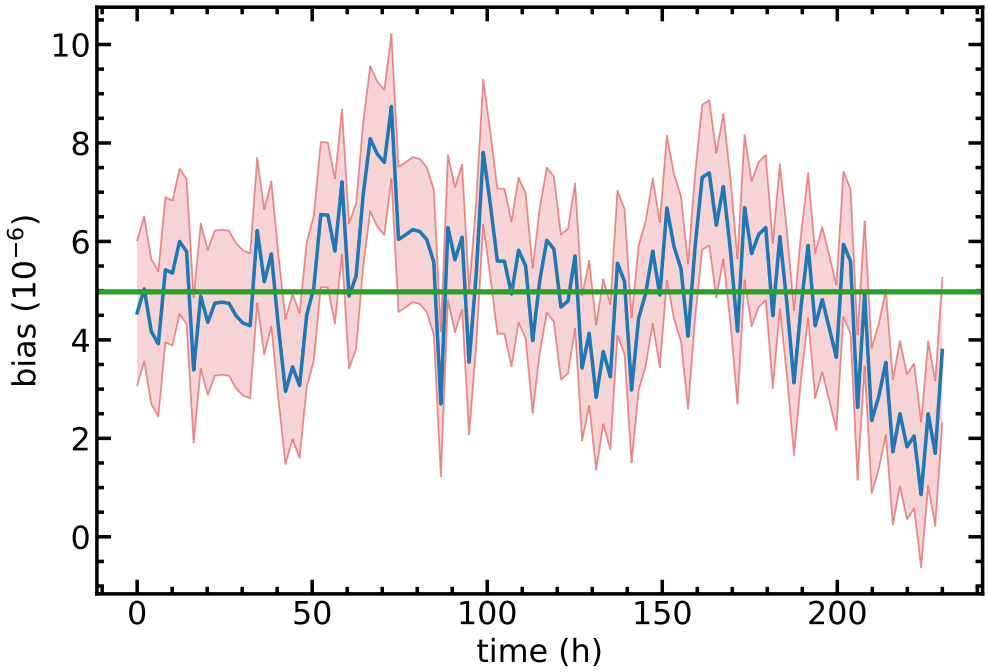

Figure 3.3.: The time evolution of the bias observed in Lab 1 for the experimental run from 14th June 2016 (blue line). Each data point contains 360 Gb of data and represents a measurement time of 2 h. The area shaded in red indicates the $\pm\sigma$ interval, and the green line shows the average bias value.

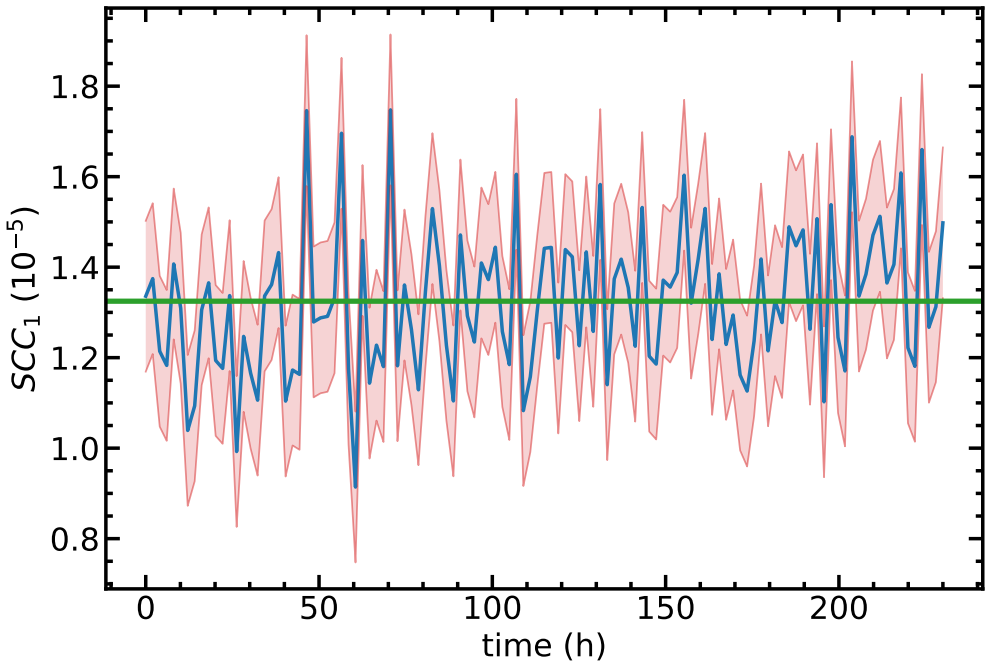

Figure 3.4.: The time evolution of SCC_1 observed in Lab 1 for the experimental run from 14th June 2016 (blue line). Each data point contains $360\,\mathrm{Gb}$ of data and represents a measurement time of $2\,\mathrm{h}$. The area shaded in red indicates the $\pm\sigma$ interval, and the green line shows the average correlation value.

Appendix C.2. The time evolution of the next neighbor correlations from this data set is shown in Fig. 3.4. Here only a slight drift over the total measurement time of $\sim 230\,\mathrm{h}$ is visible.
In order to ensure space-like separation in a Bell test, the precise start time of the measurements needs to be known. In our case, we define the start of the measurement as the earliest time the information about the input for the basis selection might already be available. The next neighbor correlation SCC_1 for both QRNGs show moderate values $> 10^{-5}$, and therefore, they need to be considered in the timings of the measurements. After a request for a random number was sent to the QRNG, it takes about $60\,\mathrm{ns}$ until the latest generated RN is available [53]. Furthermore, to account for a possible influence of the previous RN, $20\,\mathrm{ns}$ for its generation is added, thus setting the start time of the measurement $80\,\mathrm{ns}$ before the RN for the input is available (Subsec. 3.3.3).

3.4.3. Standardized Statistical Tests

Finding suitable statistical tests to analyze a random bit sequence can be, in general, a difficult task. Therefore, the standardized test suit "TestU01 Alphabit battery" [92], which contains 17 different tests, is applied to all data files of the QRNGs generated during the time of the two Bell tests. For each of the files and each of the tests, a P-value for the null hypothesis 'the bit sequence being tested is random' (i.i.d. bits with $Pr\,(q_i = 0) = Pr\,(q_i = 1) = \frac{1}{2}$) is calculated[4]. In case of true randomness, the P-values are expected to be uniformly distributed [92], which can be tested with a Pearson's χ^2-test

[4]The significance level for all the tests was chosen to be 0.001. However, the exact value is only of minor interest since the actual test for randomness is performed by checking if the P-value distribution is uniform.

l	SCC_l	l	SCC_l	l	SCC_l	l	SCC_l
1	$1.32 \cdot 10^{-5}$	17	$5.42 \cdot 10^{-8}$	33	$8.53 \cdot 10^{-8}$	49	$-2.90 \cdot 10^{-7}$
2	$1.47 \cdot 10^{-7}$	18	$6.01 \cdot 10^{-8}$	34	$2.52 \cdot 10^{-8}$	50	$1.65 \cdot 10^{-8}$
3	$-9.79 \cdot 10^{-8}$	19	$1.49 \cdot 10^{-7}$	35	$-1.22 \cdot 10^{-7}$	51	$1.57 \cdot 10^{-7}$
4	$3.41 \cdot 10^{-8}$	20	$-7.91 \cdot 10^{-8}$	36	$6.94 \cdot 10^{-8}$	52	$-3.43 \cdot 10^{-7}$
5	$5.87 \cdot 10^{-9}$	21	$-2.46 \cdot 10^{-7}$	37	$1.19 \cdot 10^{-7}$	53	$-5.15 \cdot 10^{-8}$
6	$-8.19 \cdot 10^{-8}$	22	$-1.60 \cdot 10^{-7}$	38	$-1.99 \cdot 10^{-8}$	54	$1.49 \cdot 10^{-7}$
7	$-4.74 \cdot 10^{-8}$	23	$1.94 \cdot 10^{-7}$	39	$9.53 \cdot 10^{-8}$	55	$2.20 \cdot 10^{-7}$
8	$1.38 \cdot 10^{-7}$	24	$4.48 \cdot 10^{-8}$	40	$-2.39 \cdot 10^{-7}$	56	$9.64 \cdot 10^{-9}$
9	$1.62 \cdot 10^{-7}$	25	$1.42 \cdot 10^{-7}$	41	$-3.33 \cdot 10^{-7}$		
10	$2.19 \cdot 10^{-7}$	26	$-1.22 \cdot 10^{-7}$	42	$2.74 \cdot 10^{-7}$		
11	$-2.13 \cdot 10^{-7}$	27	$-1.79 \cdot 10^{-7}$	43	$5.56 \cdot 10^{-10}$		
12	$-2.40 \cdot 10^{-7}$	28	$-3.26 \cdot 10^{-7}$	44	$1.04 \cdot 10^{-7}$		
13	$-1.52 \cdot 10^{-7}$	29	$-4.92 \cdot 10^{-8}$	45	$2.13 \cdot 10^{-8}$		
14	$-1.75 \cdot 10^{-8}$	30	$1.56 \cdot 10^{-8}$	46	$-2.45 \cdot 10^{-7}$		
15	$-3.31 \cdot 10^{-8}$	31	$-2.97 \cdot 10^{-7}$	47	$-2.83 \cdot 10^{-8}$		
16	$-1.60 \cdot 10^{-8}$	32	$8.58 \cdot 10^{-8}$	48	$-2.43 \cdot 10^{-7}$		

Table 3.3.: The average correlation values SCC_l in Lab 1 for the measurement run from 14th June 2016. The statistical error for all values is given by $\sigma = 1.55 \cdot 10^{-7}$.

of the form

$$\chi^2 = \sum_{j=1}^{k} \frac{(O_j - E_j)}{E_j}, \tag{3.5}$$

where O_j is the number of observations in the j-th bin, E_j are the expected counts of the test distribution in the j-th bin (in case of a uniform distribution $\frac{1}{k} \cdot n$), and k is the number of bins. Hence, these values should follow a χ^2-distribution with $k-1$ degrees of freedom. The test results are summarized in Table 3.4 for both measurement runs and both QRNGs. Uniform distributions can be observed for almost all the tests of the battery except the test row "smultin_MultinomialBitsOver"[5] (test on uniformity of appearance of successive output values forming bit chains of length L, evaluated in an overlapping serial approach). For these tests, P-values are more likely to be found close to 0, and the corresponding test for uniformity fails (Eqn. 3.5). Thus, to check if this points to some malfunctioning of the QRNGs, a similar test row "smultin_MultinomialBits" (same test but evaluated in a non-overlapping serial approach) is applied to the data set. Here, the expected behavior can easier be modeled by using a non-central χ^2-distribution. The model calculates the relative probabilities for the expected appearance of bit chains of length L, taking only the observed bias and next neighbor correlation as input parameters. The distribution defined by the model M, in general, differs from a uniform distribution U, which leads to a value $\chi^2(M) = \sum_{j=1}^{n} \frac{(M_j - U_j)}{U_j} \neq 0$. When analyzing bit sequences, described by this model, an offset for the corresponding χ^2-values is expected, which can be accounted for by using a non-central χ^2-distribution with a non-centrality parameter $\lambda = \chi^2(M)$. For each bin $j \in \{1, k\}$ of the measured P-value distribution, a certain interval $\left[\chi^2_{j-1}, \chi^2_j\right]$ of χ^2-values is associated. The relative frequencies for the bins of the P-value distribution can now be calculated by

[5]These tests are also based on a check of uniformity, and the same test statistic given by Eqn. 3.5 can be used to calculate the corresponding P-values.

	15th April 2016		14th June 2016	
Test	P-value Lab 1	P-value Lab 2	P-value Lab 1	P-value Lab 2
smultin_MultinomialBitsOver with L = 2	$3.83 \cdot 10^{-20}$	$1.66 \cdot 10^{-5}$	$6.06 \cdot 10^{-123}$	$4.11 \cdot 10^{-44}$
smultin_MultinomialBitsOver with L = 4	$7.65 \cdot 10^{-9}$	$1.86 \cdot 10^{-4}$	$2.95 \cdot 10^{-58}$	$6.92 \cdot 10^{-26}$
smultin_MultinomialBitsOver with L = 8	0.298	0.542	$8.14 \cdot 10^{-3}$	0.061
smultin_MultinomialBitsOver with L = 16	0.347	0.086	0.842	0.815
sstring_HammingIndep with L = 16	0.663	0.824	0.065	0.822
sstring_HammingIndep with L = 32	0.499	0.838	0.997	0.043
sstring_HammingCorr with L = 32	0.275	0.674	0.435	0.008
swalk_RandomWalk1 with L = 64 (Statistic H)	0.413	0.942	0.045	0.208
swalk_RandomWalk1 with L = 64 (Statistic M)	0.166	0.646	0.376	0.892
swalk_RandomWalk1 with L = 64 (Statistic J)	0.496	0.684	0.506	0.899
swalk_RandomWalk1 with L = 64 (Statistic R)	0.092	0.287	0.801	0.544
swalk_RandomWalk1 with L = 64 (Statistic C)	0.676	0.594	0.712	0.240
swalk_RandomWalk1 with L = 320 (Statistic H)	0.963	0.761	0.334	0.663
swalk_RandomWalk1 with L = 320 (Statistic M)	0.534	0.138	0.575	0.241
swalk_RandomWalk1 with L = 320 (Statistic J)	0.487	0.196	0.253	0.881
swalk_RandomWalk1 with L = 320 (Statistic R)	0.032	0.471	0.291	0.715
swalk_RandomWalk1 with L = 320 (Statistic C)	0.941	0.608	0.930	0.173

Table 3.4.: Results of the test suite "TestU01 Alphabit battery" for both experimental runs. All tests are applied to the complete data set consisting of 2×16072 files of $1\,\mathrm{Gb}$ for the 15th April 2016 measurement and 2×41638 files for the 14th June 2016 measurement resulting in a distribution of P-values for each test. The hypothesis for randomness can be tested by checking these distributions for uniformity with a χ^2-test. The corresponding P-values of this test are listed here.

integrating the probability density function of the non-central χ^2-distribution over this interval, which leads to the expected P-value distribution described by the model. Figure 3.5 exemplary shows the observed distribution for the data set of Lab 1 in the run from 15th April 2016 together with the expected distribution of the model. More data can be found in Appendix C.3. The model fits the data well, showing that the observed results can be described solely with the bias and next neighbor correlation of the respective data set and hence the failure of the tests does not reveal any malfunctioning of the QRNGs. On the contrary, these subtle effects become only visible because of the enormous amount of data and would have been stayed completely unnoticed otherwise. In conclusion, all applied tests support the hypothesis that the generated output bits are random and well suited for our experiment.

3.5. Measurement Results

In general, to obtain meaningful results in a scientific experiment it should be based on objective criteria only to avoid any influence of the experimenter's expectation on its outcome. If this is not taken into account when conducting an experiment, the experimenter, consciously or unconsciously, can alter the outcome of the measurement towards his expectation. An overview of this problem can be found in [93]. Therefore, to avoid expectation bias in the presented Bell tests, a list of rules on how to conduct and analyze the experiment was defined before the start of the measurement (see [55] and

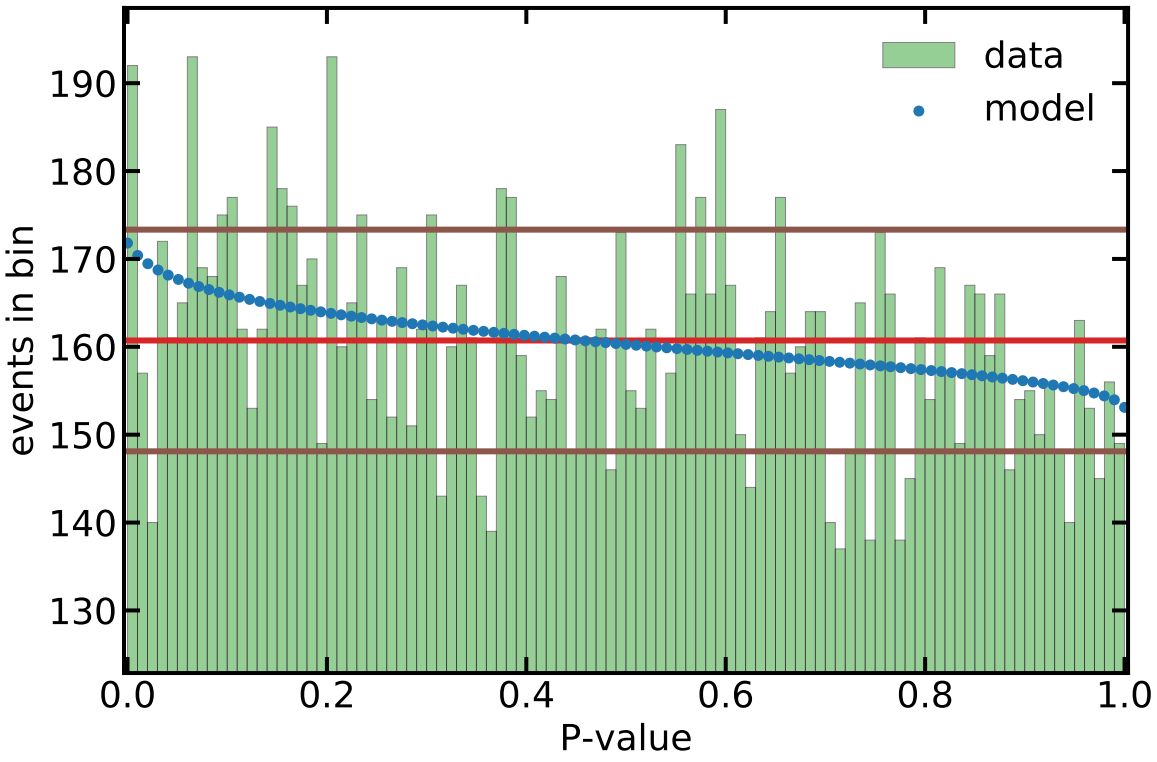

Figure 3.5.: Histogram of the P-value distribution for the test ”smultin_MultinomialBits“ (sequences of 4 bits (L=16)) applied to the data of Lab 1 in the measurement run of 15th April 2016. The blue dots represent the expected behavior of the model based on the observed bias and next neighbor correlation of this data set. The mean value and the $\pm\sigma$ interval for the histogram bins are shown as red and brown lines, respectively.

Supplementary material of [21]). It covers, e.g. the number of events to be collected, the methods to analyze the results, and a scheduled maintenance routine. Moreover, it defines specific cases when measured events are allowed to be excluded.
The target number $N^{\pm}$ of events to be collected was predefined to 5000 events for each of the two atom-atom states $|\Psi^{\pm}\rangle$ (in total 10000 events). Based on the achievable event rate[6] of $\sim \frac{2\,\text{events}}{\text{min}}$ and the expected violation from previous measurements of $S \approx 2.2$ [50], $N^{\pm}$ was chosen such that the statistics of the accumulated data allow for a significant violation of Bell's inequality in a reasonable measurement time of a few days. For both Bell tests presented in this chapter, 10000 events were accumulated, and the requirements to avoid expectation bias were fulfilled. The run started on 15th April 2016 was conducted in 4 days, including daily maintenance breaks of $\sim 3\,\text{h}$, showing a clear violation of Bell's inequality. The other run started on 14th June 2016 took a total measurement time of 10 days and was performed 'live', meaning that all data were publicly available online during the measurement.
For conclusive interpretation of a Bell experiment, the statistical method of hypothesis testing is employed to decide whether or not an experiment governed by LHVs can explain the measured data. A detailed description of the used hypothesis tests can be found in [55] and in the Supplementary material of [21], and shall only shortly be mentioned in the following.

3.5.1. Hypothesis Tests

In our case, two different methods are used to estimate a probability - the P-value - to test the null hypothesis for LHVs: A specific violation or a more extreme one can be produced by an experiment governed by LHVs.
The first method models the experimental Bell test as a supermartingale whose step size can be bounded using concentration inequalities[7], allowing to calculate a probability p_m for a local-realistic theory to result in a specific violation $S > 2$ or higher (see [55] and in the Supplementary material of [21]). In the second method, the CHSH experiment is formulated as a game [89] where Alice and Bob receive random inputs based on those they need to produce correlation events. The goal of the game is to maximize the number of win-events. A given correlation is considered a 'win' if the obtained S-value increases for a particular input combination; for the four input combinations in our case: three anticorrelations and one correlation. During one round of the game, only the local input is known to each party, making it challenging to generate correct events. The null hypothesis can now be tested by calculating the probability p_g of winning the game at least W out of N times.
Both methods do not require the i.i.d.-assumption that the experimental tries are considered independent and identically distributed and hence do not open the memory loophole (Sec. 3.2). Furthermore, the methods are also capable of handling possible residual predictability of the input choice (Sec. 3.4), which the LHV can exploit to reach a violation of Bell's inequality systematically. In the hypothesis tests, certain predictability will result in an increase of the calculated P-value.

3.5.2. Results

The data of the experimental runs started on 15th April 2016 and on 14th June 2016 were obtained while simultaneously closing the two most essential loopholes (the detection loophole and the locality loophole). The results of both runs are presented in the following and summarized in tables containing

[6] In the framework of this thesis, the event rate was significantly improved by a factor of ~ 5.6 by implementing new custom-designed collection optics in both trap setups (Chapter 6).
[7] Here the McDiarmid inequality [94] is used.

Input	$++$	$+-$	$-+$	$--$	$N_{X=Y}$	$N_{X\neq Y}$	N_{total}	$E_{a,b}$
$A=1, B=1$	172	439	483	130	302	922	1224	-0.507 ± 0.025
$A=1, B=0$	535	115	128	461	996	243	1239	0.608 ± 0.023
$A=0, B=1$	122	492	510	117	239	1002	1241	-0.615 ± 0.022
$A=0, B=0$	168	443	536	149	317	979	1296	-0.511 ± 0.024
S^-						total	5000	$\mathbf{2.240 \pm 0.047}$
p_m								$\leq 8.444 \cdot 10^{-6}$
p_g	3899 wins							$\leq 7.397 \cdot 10^{-7}$

(a) Data for $\left|\Psi^-\right\rangle$ state

Input	$++$	$+-$	$-+$	$--$	$N_{X=Y}$	$N_{X\neq Y}$	N_{total}	$E_{a,b}$
$A=1, B=1$	489	160	182	443	932	342	1274	0.463 ± 0.025
$A=1, B=0$	134	499	513	117	251	1012	1263	-0.603 ± 0.022
$A=0, B=1$	135	471	507	107	242	978	1220	-0.603 ± 0.023
$A=0, B=0$	154	483	471	135	289	954	1243	-0.535 ± 0.024
S^+						total	5000	$\mathbf{2.204 \pm 0.047}$
p_m								$\leq 2.611 \cdot 10^{-4}$
p_g	3876 wins							$\leq 2.643 \cdot 10^{-5}$

(b) Data for $\left|\Psi^+\right\rangle$ state

S	p_m	wins	p_g
2.221 ± 0.033	$2.569 \cdot 10^{-9}$	7775	$1.739 \cdot 10^{-10}$

(c) Combined S- and P-values

Table 3.5.: Experimental data from the run started on 15th April 2016.

the number of collected events for each setting, the corresponding correlators, the S-value and the calculated P-values. Further runs not shown here can be found in [55] and in the Supplementary material of [21].

Measurement Run from 15th April 2016

Due to a stable system and a constant event rate, it was possible to accumulate the 10000 events during a total measurement time of $90\,\mathrm{h}$ leading to a clear violation of the CHSH inequality. Evaluating the data (Table 3.5) using Eqns. 3.1 and 3.2 results in S-parameters for the $|\Psi^-\rangle$ and $|\Psi^+\rangle$ states of $S^- = 2.240 \pm 0.047$ and $S^+ = 2.204 \pm 0.047$, respectively. By combining the events of both states, an S-value of $S = 2.221 \pm 0.033$ is reached. Using the game-formalism for the hypothesis tests leads to P-values of $p^- \leq 7.397 \cdot 10^{-7}$ for $|\Psi^-\rangle$, $p^+ \leq 2.643 \cdot 10^{-5}$ for $|\Psi^+\rangle$ and $p \leq 1.739 \cdot 10^{-10}$ for both states combined. With this, the hypothesis that the measurement outcome can be explained with an experiment governed by LHVs can be rejected with high confidence.

Input	++	+−	−+	−−	$N_{X=Y}$	$N_{X\neq Y}$	N_{total}	$E_{a,b}$
$A=1, B=1$	104	523	484	132	236	1007	1243	-0.620 ± 0.022
$A=1, B=0$	431	159	160	454	885	319	1204	0.470 ± 0.026
$A=0, B=1$	162	466	410	207	369	876	1245	-0.407 ± 0.026
$A=0, B=0$	133	533	537	105	238	1070	1308	-0.636 ± 0.021
S^-						total	5000	$\mathbf{2.134 \pm 0.048}$
p_m								≤ 0.02
p_g	3838 wins							$\leq 2.752 \cdot 10^{-3}$

(a) Data for $\left|\Psi^-\right\rangle$ state

Input	++	+−	−+	−−	$N_{X=Y}$	$N_{X\neq Y}$	N_{total}	$E_{a,b}$
$A=1, B=1$	506	158	127	489	995	285	1280	0.555 ± 0.025
$A=1, B=0$	161	441	427	173	334	868	1202	-0.478 ± 0.022
$A=0, B=1$	144	482	450	185	329	932	1261	-0.444 ± 0.023
$A=0, B=0$	118	483	510	146	264	993	1257	-0.555 ± 0.024
S^+						total	5000	$\mathbf{2.057 \pm 0.048}$
p_m								≤ 0.52
p_g	3788 wins							≤ 0.13

(b) Data for $\left|\Psi^+\right\rangle$ state

S	p_m	wins	p_g
2.096 ± 0.034	≤ 0.0287	7626	$\leq 2.818 \cdot 10^{-3}$

(c) Combined S- and P-values

Table 3.6.: Experimental data from the run started on 14th June 2016.

Measurement Run from 14th June 2016

For the live measurement, the system suffered from more instabilities than the run from 15th April 2016, leading to a smaller violation of Bell's inequality and a lower event rate that prolonged the total measurement time to 10 days. The obtained data for this run (Table 3.6) yield S-parameters of $S^- = 2.134 \pm 0.048$ for $|\Psi^-\rangle$, $S^+ = 2.057 \pm 0.048$ for $|\Psi^+\rangle$, and $S = 2.096 \pm 0.034$ for both states combined. The corresponding hypothesis test using the game-formalism results in P-values of $p^- \leq 2.752 \cdot 10^{-3}$ for $|\Psi^-\rangle$, $p^+ \leq 0.13$ for $|\Psi^+\rangle$ and $p \leq 2.818 \cdot 10^{-3}$ for both combined.

Applications

Measurements violating Bell's inequality form the basis for several so-called 'device-independent' (DI) protocols, which can be utilized in real-world quantum applications. Device-independent in the context of quantum technology means that one can trust the measurement results even in the case of imperfect or untrusted devices. Examples for such applications are, e.g. generation of random numbers, certification of entanglement via 'self-testing' [95] and secure communication schemes like device-independent quantum key distribution (DIQKD). For example, the number of extractable random bits, certified by a violation of Bell's inequality, was calculated for our Bell data in [55] by

applying the protocol of device-independently generating RN [30]. Furthermore, self-testing was also applied to the Bell data to certify the entanglement shared by the two atoms in a DI way [55, 96].

4. Photon Collection and Coupling Efficiency

For future quantum technology applications based on the entanglement between separated quantum memories, e.g. distributed quantum computation or quantum communication, the entanglement rate limits the (secure) data transfer. In our experiment, the entanglement between the distant atoms is generated via the entanglement swapping protocol (Subsec. 2.6). Here, one of the decisive numbers defining the achievable rate is the efficiency to couple a single photon emitted by the atom during the entanglement generation process into a single-mode fiber (Eqn. 2.34). By using optics better suited for this task, an improved coupling efficiency can be achieved. Therefore, in this work, a custom-designed microscope objective setup is implemented in both laboratories (Chapter 6). For the design of these setups, it is indispensable to have a good understanding of the collection and coupling process.

In this chapter, a model describing the coupling process is presented to estimate the coupling efficiency. The overall process can be split into two nearly independent parts: the collection of the photon and the coupling into the single-mode fiber. In both cases, efficiencies are calculated for atoms located in the focus of the ODT as well as for atoms displaced from this optimal position. First, the emission process of the single photon is described in a semi-classical approach considering an oscillating atomic dipole generating the mode of the emitted photon. Depending on this emission profile, the probability to collect the photon with the objective is calculated. In the next step, the coupling efficiency is determined by calculating the mode-overlap of the emitted photon mode with the fiber mode. More realistic estimates for the collection and coupling efficiency are obtained by including the thermal distribution of the atoms (Subsec. 2.2.3) in the calculations. Analyzing the results led to developing a homemade fiber collimator optimized to increase the coupling efficiency (Subsec. 6.1.4). The model is an extension to the simplified model given in [32]. Further details about the development of the model are found in [97, 98].

4.1. Atomic Dipole Emission Characteristics

In this section, analytic expressions of the emitted photon modes are derived considering an oscillating atomic dipole in a semi-classical approach. While this description allows deriving the correct emission profiles, the spontaneous decay process cannot be explained. Within this semi-classical description, the excited state of an atom corresponds to a pure quantum state with no dipole moment associated with it; hence, the atom does not start to radiate. This problem is solved in quantum electrodynamics (QED) by the quantization of the electromagnetic field. Here the interaction of the excited atom with the different radiation field modes of the vacuum state (the state with no photons) induces a dipole moment, which leads to the spontaneous emission of a photon into one of the vacuum modes [99].

In our case, the single photon is emitted by the spontaneous decay of the $5^2P_{3/2}, F' = 0$ excited state to the $5^2S_{1/2}, F = 1$ ground state manifold. The expectation value of the associated transition dipole moment $\hat{\mathbf{p}}_{e,g}$ is given by

$$\mathbf{M}_{e,g} = \langle \hat{\mathbf{p}}_{e,g} \rangle = e \left\langle 5^2P_{3/2}, F' = 0, m_{F'} = 0 \right| \hat{\mathbf{r}} \left| 5^2S_{1/2}, F = 1, m_F = 0, \pm 1 \right\rangle , \tag{4.1}$$

with e the elementary charge and $\hat{\mathbf{r}}$ the spatial position operator. As long as at least one of the components of $\mathbf{M}_{e,g}$ is unequal to zero, the transition is allowed, and the spontaneous decay into the corresponding state can happen. For all three ground states $\left|5^2S_{1/2}, F = 1, m_F = 0, \pm 1\right\rangle$ this is the case, and hence the emission of a single photon with $\sigma^{\pm}$ or π polarization is possible. The semi-classical approach is used for the following derivations of the emission profiles, considering the atomic dipole as the source of radiation with the emitted electric field described classically. This step is justified since both classical and quantum mechanical descriptions lead to the same emission profiles [100]. The electric field of the emitted single photon generated by an oscillating dipole in the far-field approximation ($kr >> 1$) is given by [62, 100, 101]

$$\mathbf{E}^{(p)}(\mathbf{r}) = \frac{k^2}{4\pi\epsilon_0\epsilon_r}\frac{e^{ikr}}{r}\left[(\mathbf{e}_\mathrm{r} \times \mathbf{e}_\mathrm{p}) \times \mathbf{e}_\mathrm{r}\right], \tag{4.2}$$

with the radial unit vector

$$\mathbf{e}_\mathrm{r} = \begin{pmatrix} sin(\theta)\, cos(\phi) \\ sin(\theta)\, sin(\phi) \\ cos(\theta) \end{pmatrix}. \tag{4.3}$$

$\mathbf{e}_p$ is the unit vector of the dipole oscillation direction, $k = {}^{2\pi}/_{\lambda}$ represents the wavenumber, ϵ_0 and ϵ_r are the vacuum and relative permittivity, respectively, and r denotes the radial distance. In the following, $E_0 = {}^{k^2}/_{4\pi\epsilon_0\epsilon_r}$ is used. The angular momentum degree of freedom for the atomic and the photonic state is decomposed into eigenstates of the system with respect to its quantization axis (Appendix B), which in our case is defined by the optical axis of the collection optics pointing along the z-direction. For the photon, this leads to decomposition into three polarization states $\sigma^{\pm}$ and π with the electric field modes being calculated by using the respective oscillation direction of the atomic dipole: $\mathbf{e}_\mathrm{p} = \mathbf{e}_{\sigma^\pm} = {}^1/\sqrt{2}\,(\mp i\mathbf{e}_\mathrm{x} + \mathbf{e}_\mathrm{y})$ for the emission of $\sigma^{\pm}$ polarized light and $\mathbf{e}_\mathrm{p} = \mathbf{e}_\pi = \mathbf{e}_\mathrm{z}$ for π polarized light (general expressions for arbitrary oscillation directions can be found in Appendix D). Here $\mathbf{e}_\mathrm{x}, \mathbf{e}_\mathrm{y}$ and $\mathbf{e}_\mathrm{z}$ are the unit vectors of the Cartesian coordinate system (see Figure 4.1 and Appendix B). With this, the modes can be written as

$$\mathbf{E}^{(\sigma^\pm)}(\mathbf{r}) = E_0\frac{e^{ikr}}{r}\left[(\mathbf{e}_\mathrm{r} \times {}^1/\sqrt{2}\,(\mp i\mathbf{e}_\mathrm{x} + \mathbf{e}_\mathrm{y})) \times \mathbf{e}_\mathrm{r}\right], \tag{4.4}$$

$$\mathbf{E}^{(\pi)}(\mathbf{r}) = E_0\frac{e^{ikr}}{r}\left[(\mathbf{e}_\mathrm{r} \times \mathbf{e}_\mathrm{z}) \times \mathbf{e}_\mathrm{r}\right]. \tag{4.5}$$

The probability that a photon of polarization p (e.g. $p = \sigma^\pm, \pi$) is emitted into a differential solid angle $\mathrm{d}\Omega$ is obtained by normalizing the time-averaged power $\mathrm{dP^{(p)}} = \bar{\mathbf{S}}^{(p)}(\mathbf{r}) \cdot \mathrm{d}\mathbf{f}$, with $\bar{\mathbf{S}}^{(p)}(\mathbf{r}) \propto \left\|\mathbf{E}^{(p)}(\mathbf{r})\right\|^2 \mathbf{e}_r$, radiated through the surface element $\mathrm{d}\mathbf{f} = \mathrm{df}\mathbf{e}_r = \mathrm{d}\Omega\mathrm{r}^2\mathbf{e}_r$ (Figure 4.1) [62, 100, 101]:

$$\frac{\mathrm{dP^{(p)}}}{\mathrm{d}\Omega}(\mathbf{r}) = \frac{1}{N_{norm}} r^2 \left\|\mathbf{E}^{(p)}(\mathbf{r})\right\|^2, \tag{4.6}$$

with the normalization constant

$$N_{norm} = \int_{4\pi} d\Omega r^2 \left\|\mathbf{E}^{(p)}(\mathbf{r})\right\|^2 = \frac{8\pi}{3}E_0^2. \tag{4.7}$$

For the three eigenstates of the system, this yield the well-known dipole emission characteristics (see

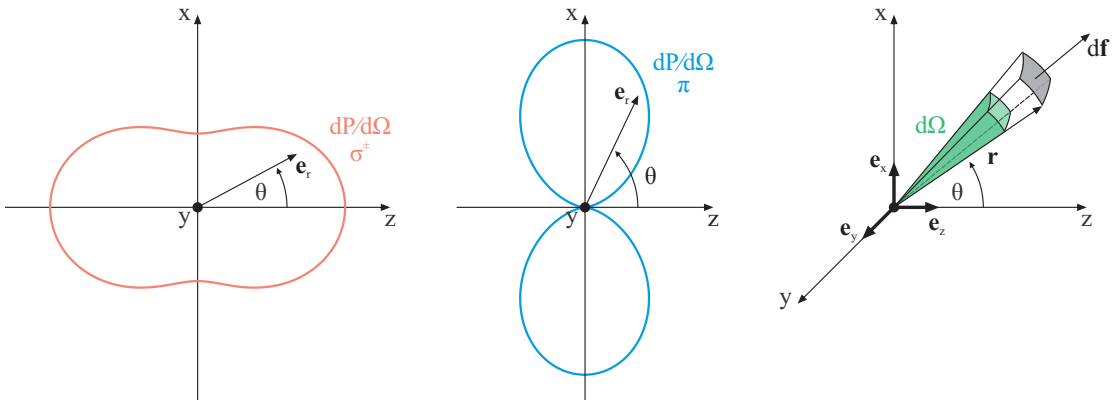

(a) $\sigma^{\pm}$-polarized light emitted from a dipole circularly oscillating around the z-axis. This polarization can be emitted in all directions with the maximal probability for $\theta = 0$ twice as large as the minimum for $\theta = \pi/2$.

(b) π-polarized light emitted from a dipole linearly oscillating along the z-axis. The emission probability for this polarization is vanishing along the direction $\theta = 0$.

(c) Differential solid angle $\mathrm{d}\Omega$ in relation to the area element $\mathrm{d}\mathbf{f}$. $\mathbf{e}_\mathrm{x}, \mathbf{e}_\mathrm{y}$ and $\mathbf{e}_\mathrm{z}$ are the unit vectors of the Cartesian coordinate system.

Figure 4.1.: Dipole emission characteristic of polarized light. The emission probability of an atom (black dot) into a differential solid angle $\mathrm{d}\Omega$ depends on the angle θ relative to the quantization axis (z-axis).

Figure 4.1):

$$\frac{\mathrm{dP}^{(\sigma^{\pm})}}{\mathrm{d}\Omega}(\mathbf{r}) = \frac{3}{8\pi}\frac{1}{2}\left(1 + cos^2(\theta)\right), \tag{4.8}$$

$$\frac{\mathrm{dP}^{(\pi)}}{\mathrm{d}\Omega}(\mathbf{r}) = \frac{3}{8\pi} sin^2(\theta). \tag{4.9}$$

In our experiment, the polarization state of the emitted photons is naturally analyzed in the H/V-basis with a PBS (Subsec. 2.4.1). Therefore, in the following calculations of this chapter, the electric field modes of the three orthogonal linear dipoles oscillating along the unit vectors of the Cartesian coordinate system $\mathbf{e}_\mathrm{x}, \mathbf{e}_\mathrm{y}$ and $\mathbf{e}_\mathrm{z}$ are considered (Fig. 4.1). The emission of a H/V-polarized photon can hence be described as a superposition of the $\sigma^{\pm}$-eigenstates with $\mathbf{e}_p = \mathbf{e}_H = {}^{i}/\sqrt{2}\,(\mathbf{e}_{\sigma^+} - \mathbf{e}_{\sigma^-}) = \mathbf{e}_x$ and $\mathbf{e}_p = \mathbf{e}_V = {}^{1}/\sqrt{2}\,(\mathbf{e}_{\sigma^+} + \mathbf{e}_{\sigma^-}) = \mathbf{e}_y$ (see Appendix B), and the corresponding fields using Eqn. 4.2 are given by

$$\mathbf{E}^{(H)}(\mathbf{r}) = E_0 \frac{e^{ikr}}{r}\left[(\mathbf{e}_\mathrm{r} \times \mathbf{e}_\mathrm{x}) \times \mathbf{e}_\mathrm{r}\right], \tag{4.10}$$

$$\mathbf{E}^{(V)}(\mathbf{r}) = E_0 \frac{e^{ikr}}{r}\left[(\mathbf{e}_\mathrm{r} \times \mathbf{e}_\mathrm{y}) \times \mathbf{e}_\mathrm{r}\right], \tag{4.11}$$

with the emission characteristics according to Eqn. 4.6

$$\frac{\mathrm{dP}^{(\mathrm{H})}}{\mathrm{d}\Omega}(\mathbf{r}) = \frac{3}{8\pi}\left(1 - sin^2(\theta)\, cos^2(\phi)\right), \tag{4.12}$$

$$\frac{\mathrm{dP}^{(\mathrm{V})}}{\mathrm{d}\Omega}(\mathbf{r}) = \frac{3}{8\pi}\left(1 - sin^2(\theta)\, sin^2(\phi)\right). \tag{4.13}$$

In this chapter, all formulas so far are written in spherical coordinates (r, θ, ϕ) to exploit rotational symmetries of the system. For an atom located exactly in the focus position of the objective, these symmetries lead to a vanishing coupling efficiency into the optical fiber of emitted π-light (Subsec. 4.3.2). The situation changes when allowing for displacements of the atom from this center position, and in general, no symmetries can be used for arbitrary atom locations. Therefore, a Cartesian coordinate system (x, y, z) (Fig. 4.3) is used. The corresponding formulas can be obtained by applying the following substitutions[1]:

$$r = \sqrt{x^2 + y^2 + z^2} \tag{4.14}$$

$$\theta = arccos\left(\frac{z}{\sqrt{x^2 + y^2 + z^2}}\right) \tag{4.15}$$

$$\phi = arctan\left(\frac{y}{x}\right). \tag{4.16}$$

The change of the coordinate system from spherical to Cartesian coordinates also implies mapping the surface element of a sphere df onto a plane. For each differential solid angle $\mathrm{d}\Omega$, the emitted spherical wavefront is therefore locally projected onto a plane leading to a stretched wavefront (Fig. 4.2). Accounting for this in the calculations requires introducing a projection factor of $cos(\theta)$ between the surface element of a sphere df and the surface element in a plane dA [102]:

$$\mathrm{d}\Omega = \frac{\mathrm{df}}{r^2} = \frac{\mathrm{dA} \cdot cos(\theta)}{r^2}. \tag{4.17}$$

This projection or apodization factor guarantees the correct transformation while fulfilling the demands of energy conservation [103]. In [98], the cosine factor was falsely omitted, leading to slightly different results for the currently used NA of 0.5. However, when considering systems with higher NAs the differences become significant.

Furthermore, for an arbitrary position of the atomic dipole, the source of the electric fields is shifted by the vector $\mathbf{r}' = (x', y', z')$ from the origin of the coordinate system. Mathematically this can be described by a transformation of the electric field coordinates (Fig. 4.3):

$$\mathbf{r} \rightarrow \mathbf{r} - \mathbf{r}' = \left(x - x', y - y', z - z'\right). \tag{4.18}$$

By applying all above-derived transformations rules (Eqns. 4.14-4.18), the following electric fields

[1] For the substitution of ϕ, the function $arctan\left(\frac{y}{x}\right)$ only leads to the correct transformation for $x > 0$. Therefore, in the calculations the two-argument function $arctan2(y, x)$ is used as it ensures the correct transformation between spherical and Cartesian coordinates over the complete parameter range.

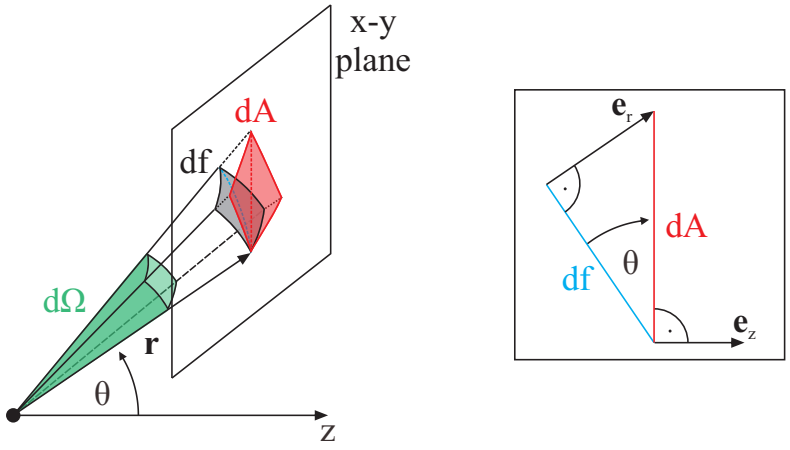

Figure 4.2.: Local projection of the surface element of a sphere df onto a plane (left). The projection plane (x-y plane) is defined by the optical axis of the microscope objective (z-axis). The relation between the two differential surface elements is visualized on the right and the projection factor $cos\,(\theta)$ can easily be derived.

for the polarization $p \in \{H, V, \pi\}$ are obtained

$$\mathbf{E}^{(H)}\left(\mathbf{r}-\mathbf{r}'\right) = E_0 \frac{e^{ik\sqrt{(x-x')^2+(y-y')^2+(z-z')^2}}\sqrt{z-z'}}{\left((x-x')^2+(y-y')^2+(z-z')^2\right)^{7/4}} \begin{pmatrix} (y-y')^2+(z-z')^2 \\ -(x-x')(y-y') \\ -(x-x')(z-z') \end{pmatrix}, \tag{4.19}$$

$$\mathbf{E}^{(V)}\left(\mathbf{r}-\mathbf{r}'\right) = E_0 \frac{e^{ik\sqrt{(x-x')^2+(y-y')^2+(z-z')^2}}\sqrt{z-z'}}{\left((x-x')^2+(y-y')^2+(z-z')^2\right)^{7/4}} \begin{pmatrix} -(x-x')(y-y') \\ (x-x')^2+(z-z')^2 \\ -(y-y')(z-z') \end{pmatrix}, \tag{4.20}$$

$$\mathbf{E}^{(\pi)}\left(\mathbf{r}-\mathbf{r}'\right) = E_0 \frac{e^{ik\sqrt{(x-x')^2+(y-y')^2+(z-z')^2}}\sqrt{z-z'}}{\left((x-x')^2+(y-y')^2+(z-z')^2\right)^{7/4}} \begin{pmatrix} -(x-x')(z-z') \\ -(y-y')(z-z') \\ (x-x')^2+(y-y')^2 \end{pmatrix}, \tag{4.21}$$

as well as the corresponding emission characteristics

$$\frac{\mathrm{dP^{(p)}}}{\mathrm{dA}}\left(\mathbf{r}-\mathbf{r}'\right) = \frac{3}{8\pi}\left\|\mathbf{E}^{(p)}\left(\mathbf{r}-\mathbf{r}'\right)\right\|^2, \tag{4.22}$$

$$\frac{\mathrm{dP^{(H)}}}{\mathrm{dA}}\left(\mathbf{r}-\mathbf{r}'\right) = \frac{3}{8\pi}\frac{(z-z')}{\left((x-x')^2+(y-y')^2+(z-z')^2\right)^{5/2}}\left((y-y')^2+(z-z')^2\right), \tag{4.23}$$

$$\frac{\mathrm{dP^{(V)}}}{\mathrm{dA}}\left(\mathbf{r}-\mathbf{r}'\right) = \frac{3}{8\pi}\frac{(z-z')}{\left((x-x')^2+(y-y')^2+(z-z')^2\right)^{5/2}}\left((x-x')^2+(z-z')^2\right), \tag{4.24}$$

$$\frac{\mathrm{dP^{(\pi)}}}{\mathrm{dA}}\left(\mathbf{r}-\mathbf{r}'\right) = \frac{3}{8\pi}\frac{(z-z')}{\left((x-x')^2+(y-y')^2+(z-z')^2\right)^{5/2}}\left((x-x')^2+(y-y')^2\right). \tag{4.25}$$

General expressions for arbitrary dipole oscillation direction can be found in Appendix D.

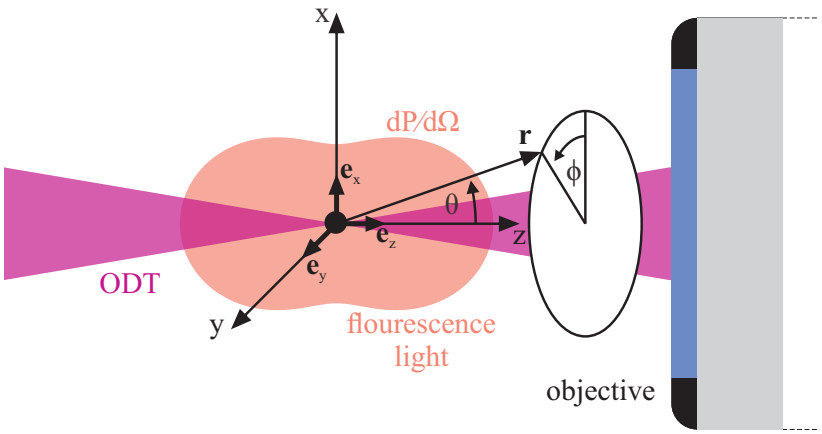

(a) Definition of the spherical coordinate system in the non-displaced case $\mathbf{r}' = 0$. The angle θ is defined relative to the z-axis and the angle ϕ relative to the x-axis.

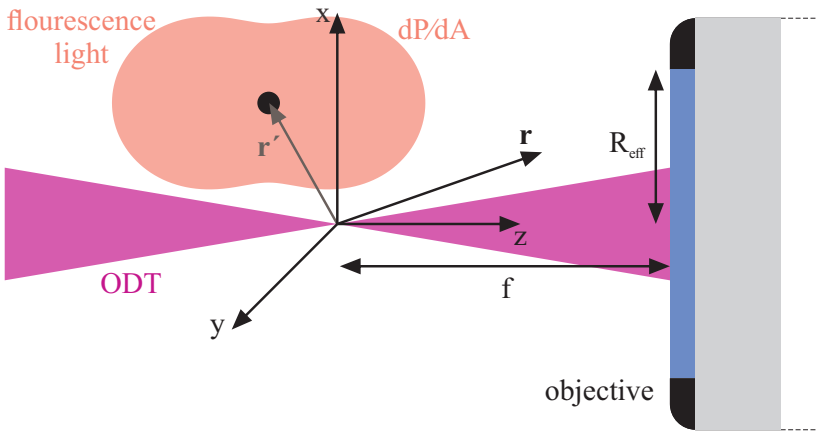

(b) Definition of the Cartesian coordinate system for displaced atom positions. Here, $\mathbf{r}'$ describes the shift of the atom from the origin, and the emitted electric fields $\mathbf{E}^{(p)}(\mathbf{r} - \mathbf{r}')$ are given by the relative coordinates $\mathbf{r} - \mathbf{r}'$.

Figure 4.3.: Definition of the coordinate systems for atoms in the center of the ODT (a) and atoms displaced from this position by a vector $\mathbf{r}´$ (b). In both cases, the origin of the coordinate system coincides with the focus position of the ODT. The entrance aperture of the objective with radius R_{eff} is centered around the z-axis at location $\mathbf{r} = (0, 0, f)$, where f is the focal length of the objective. The emission characteristic $^{\mathrm{dP}}/_{\mathrm{d}\Omega}$ in (a), respectively $^{\mathrm{dP}}/_{\mathrm{dA}}$ in (b), is exemplarily shown for a dipole circularly oscillating around the $\mathbf{e}_z$-direction.

4.2. Collection Efficiency

The ability of an optical system to collect light is given by its numerical aperture, defined as $\mathrm{NA} = n \cdot sin\left(\theta_{max}\right)$, where n is the refractive index of the medium between the emitter and the objective. It allows to bound the angular acceptance of a system with a maximal polar angle θ_{max}. Depending on this angle, an effective entrance aperture with radius R_{eff} can be defined for a point source well localized in the focus region:

$$R_{eff}\left(\theta_{max}\right) = f \cdot tan\left(\theta_{max}\right), \tag{4.26}$$

$$\theta_{max} = arcsin\left(\frac{\mathrm{NA}}{n}\right). \tag{4.27}$$

The collection efficiency is now given as the probability of a photon being emitted into the objective's entrance aperture $\mathrm{A_{ap}}$ and can be calculated by a surface integral of the dipole emission characteristic introduced in the previous section (Eqns. 4.6 and 4.22):

$$\eta_{col}^{(p)}\left(\mathbf{r}'\right) = \int_{\mathrm{A_{ap}}} \mathrm{dP^{(p)}}\left(\mathbf{r} - \mathbf{r}'\right). \tag{4.28}$$

4.2.1. Collection Efficiency of Non-displaced Atoms

This subsection considers the collection efficiency for the idealized case of an atom centered in the focus of the ODT at position $\mathbf{r}' = 0$. For this consideration, it is advantageous to perform the integration with spherical coordinates, which simplifies the calculations by exploiting the system's symmetries. Hence, Eqn. 4.28 can be rewritten as

$$\begin{aligned}
\eta_{col}^{(p)}\left(\mathbf{r}' = 0\right) &= \int_{\mathrm{A_{ap}}} \mathrm{dP^{(p)}}\left(\mathbf{r}\right) \\
&= \frac{3}{8\pi} \int_{\mathrm{A_{ap}}} \mathrm{d}\Omega r^2 \left\| \mathbf{E}^{(p)}\left(\mathbf{r}\right) \right\|^2 \\
&= \frac{3}{8\pi} \int_0^{\theta_{max}} \mathrm{d}\theta \int_0^{2\pi} \mathrm{d}\phi sin\left(\theta\right) r^2 \left\| \mathbf{E}^{(p)}\left(\mathbf{r}\right) \right\|^2.
\end{aligned} \tag{4.29}$$

Note, $r^2 \left\| \mathbf{E}^{(p)}\left(\mathbf{r}\right) \right\|^2$ is a function independent of the radial distance r. Calculations show that for any polarization purely composed of $\sigma^{\pm}$-components (e.g. H and V) equal collection efficiencies are obtained, whereas, for π-polarized photons, the specific emission characteristic (Fig. 4.1) reduces the collection probability, especially for low NA values. Figure 4.4 depicts the collection efficiency for photons emitted via a σ- or π-decay as a function of the NA. As expected, higher collection efficiencies are obtained for larger NA values due to the increase of the maximum collection angle θ_{max}. The new microscope objectives[2] with a NA of 0.5 are placed outside the vacuum glass cell (in air $n = 1$), resulting in $\theta_{max} = 30^{\circ}$. For this NA, the following collection efficiencies are expected

$$\eta_{col}^{(\sigma^{\pm})}\left(\mathbf{r}' = 0\right) = \eta_{col}^{(H)}\left(\mathbf{r}' = 0\right) = \eta_{col}^{(V)}\left(\mathbf{r}' = 0\right) = 9.405\%, \tag{4.30}$$

$$\eta_{col}^{(\pi)}\left(\mathbf{r}' = 0\right) = 1.286\%. \tag{4.31}$$

[2]The objectives used before (Mitutoyo, G Plan Apo 50) are also specified for a NA of 0.5, leading to the same expected collection efficiency. However, they are not designed for the single photon's wavelength of 780 nm, causing aberrations, which reduce the coupling efficiency and thus limit the effective usable NA to 0.267 [52].

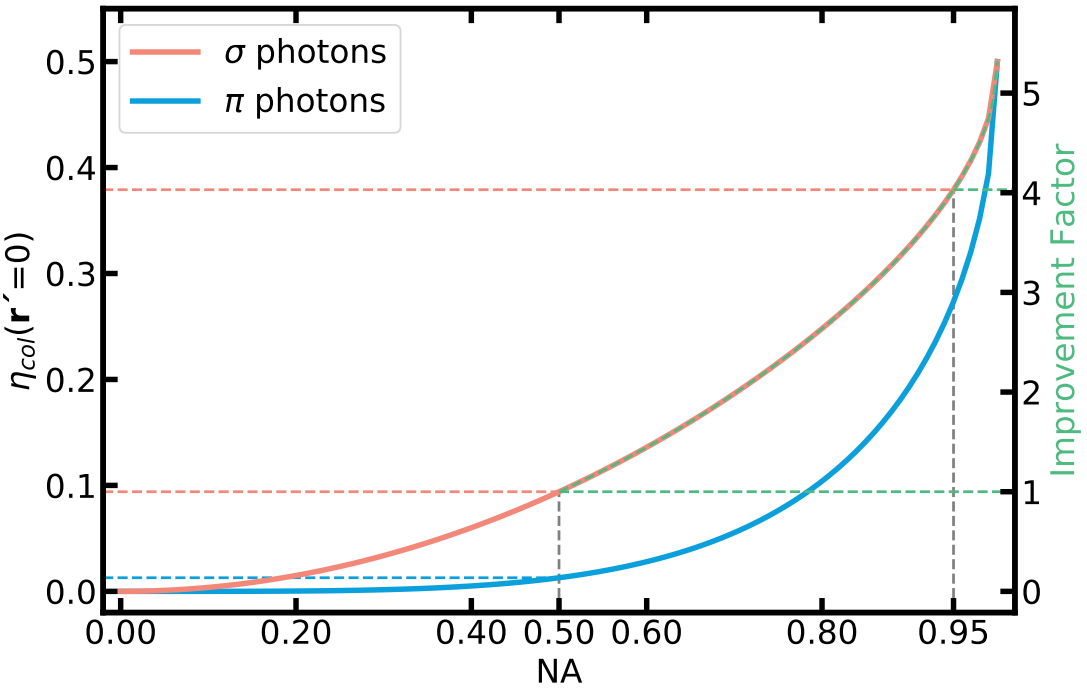

Figure 4.4.: Collection efficiency as a function of NA (left axis) for photons emitted via a σ-decay (light red) or π-decay (blue). Possible improvement factors relative to the current NA of 0.5 for σ photons (right axis).

An obvious improvement would hence be to use collection optics with a larger NA. However, this is technically challenging in our experiment since the same optics collecting the fluorescence light also focuses beams for the trapping and the atomic state readout (Subsec. 2.2.4). Moreover, the objective is located outside the vacuum due to the experimental geometry, requiring a long working distance of $> 11\,\mathrm{mm}$. Altogether, this required the custom-design of the objectives mentioned before. For the theoretical case of $\mathrm{NA} = 1$ in air ($n = 1$) with $\theta_{max} = \pi/2$, the collection efficiency of 50% resembles the situation of collecting one-half of the total 4π emission. The largest practically achievable NA with a dry lens is 0.95 [104], resulting in an efficiency of 37.91%. That leads to an estimated improvement by a factor of 4.03 compared to a NA of 0.5 and correspondingly to an increase of the remote entanglement rate by a factor of 16.24. This potential increase reflects the theoretical optimum, assuming a coupling efficiency (discussed in Sec. 4.3) equal to the currently achieved.

4.2.2. Collection Efficiency of Displaced Atoms

The atom's thermal energy allows it to move inside the trapping potential, and hence its position will vary from the ideal situation ($\mathbf{r}' = 0$) discussed previously. More precisely, the probability of finding an atom at a specific location is described by the thermal density distribution introduced in Subsection 2.2.3. In this general case, no symmetries can be exploited anymore by using a spherical coordinate system. As mentioned before, the polarization analysis of the photon in our experiment is normally performed in the H/V-basis. Therefore, it is natural to use a Cartesian coordinate system to calculate

the efficiencies for displaced atoms since its unit vectors ($\mathbf{e}_x$, $\mathbf{e}_y$, $\mathbf{e}_z$) coincide with the oscillation directions of the three atomic dipoles leading to the emission of H/V- or π-polarized photons. The collection efficiency $\eta_{col}^{(p)}(\mathbf{r}-\mathbf{r}')$ can now be calculated by rewriting Eqn. 4.28 using the Cartesian representation (Eqn. 4.22):

$$\eta_{col}^{(\mathrm{H})}(\mathbf{r}') = \frac{3}{8\pi}\int_{-R_{eff}}^{R_{eff}} \mathrm{dx} \int_{-\sqrt{R_{eff}^2-x^2}}^{\sqrt{R_{eff}^2-x^2}} \mathrm{dy} \frac{(f-z')\left((x-x')^2+(y-y')^2\right)}{\left((x-x')^2+(y-y')^2+(f-z')^2\right)^{5/2}}, \tag{4.32}$$

$$\eta_{col}^{(\mathrm{V})}(\mathbf{r}') = \frac{3}{8\pi}\int_{-R_{eff}}^{R_{eff}} \mathrm{dx} \int_{-\sqrt{R_{eff}^2-x^2}}^{\sqrt{R_{eff}^2-x^2}} \mathrm{dy} \frac{(f-z')\left((y-y')^2+(f-z')^2\right)}{\left((x-x')^2+(y-y')^2+(f-z')^2\right)^{5/2}}, \tag{4.33}$$

$$\eta_{col}^{(\pi)}(\mathbf{r}') = \frac{3}{8\pi}\int_{-R_{eff}}^{R_{eff}} \mathrm{dx} \int_{-\sqrt{R_{eff}^2-x^2}}^{\sqrt{R_{eff}^2-x^2}} \mathrm{dy} \frac{(f-z')\left((x-x')^2+(f-z')^2\right)}{\left((x-x')^2+(y-y')^2+(f-z')^2\right)^{5/2}}. \tag{4.34}$$

Here the surface integral is performed over the entrance aperture of the objective with radius R_{eff} (Eqn. 4.26) centered around $\mathbf{r} = (0, 0, f)$ (Fig. 4.3b).

Figure 4.5 depicts the collection efficiency for atoms displaced in all three spatial directions. The displacement $\mathbf{r}' = (x', y', z')$ is given in units of the transverse σ_r, respectively longitudinal σ_l standard deviation of the thermal density distribution (Subsec. 2.2.3), which depends on the specific trap parameters, e.g. its geometry and depth, as well as on the atom temperature. Here parameters resembling the current situation of the trap in Lab 1 are used exemplarily: $f = 10\,\mathrm{mm}$, $R_{eff} = 5.77\,\mathrm{mm}$, $\sigma_r = 115\,\mathrm{nm}$ and $\sigma_z = 1.23\,\mu\mathrm{m}$. The calculated collection efficiency shows only negligible variations for different atom positions distributed over the complete trap volume. For an atom well localized in the focus region of the collection optics, this behavior is expected as long as the displacements are much smaller than the focal length f and the effective aperture radius R_{eff} of the objective. Therefore, only the difference to the collection efficiency of an atom in the central position (previous subsection) is shown to visualize these small changes. Since the atom is less confined along the propagation direction of the ODT beam, changes originating from longitudinal displacements are much larger than those from transverse shifts. Furthermore, higher collection efficiencies are obtained for photons emitted closer to the objective since they are more likely to impinge the objective's entrance aperture. The influence of the different emission characteristics for the three polarizations can also be seen in the collection efficiency plots, e.g. the emission of H-polarized light is wider in the y- than in the x-direction leading to an oval shape of the efficiency distribution in the x-y plane. For V polarization, the role of the x- and y-axis are exchanged, and hence the oval shape is rotated by 90°, whereas for π-polarization, the calculated distribution is symmetric. For typical parameters in our experiment, similar results are obtained. More substantial deviations of the collection efficiency only occur when having a less confined atom or using a smaller NA.

4.3. Coupling Efficiency

In the experimental realization, the collected photons are coupled into a single-mode fiber that guides them to the polarization analysis setup (Subsec. 2.4.1). The quality of this coupling process is crucial as it influences the experiment in various ways. First, it determines the fraction of collected photons that can subsequently be used and by this also determines the achievable entanglement rate.

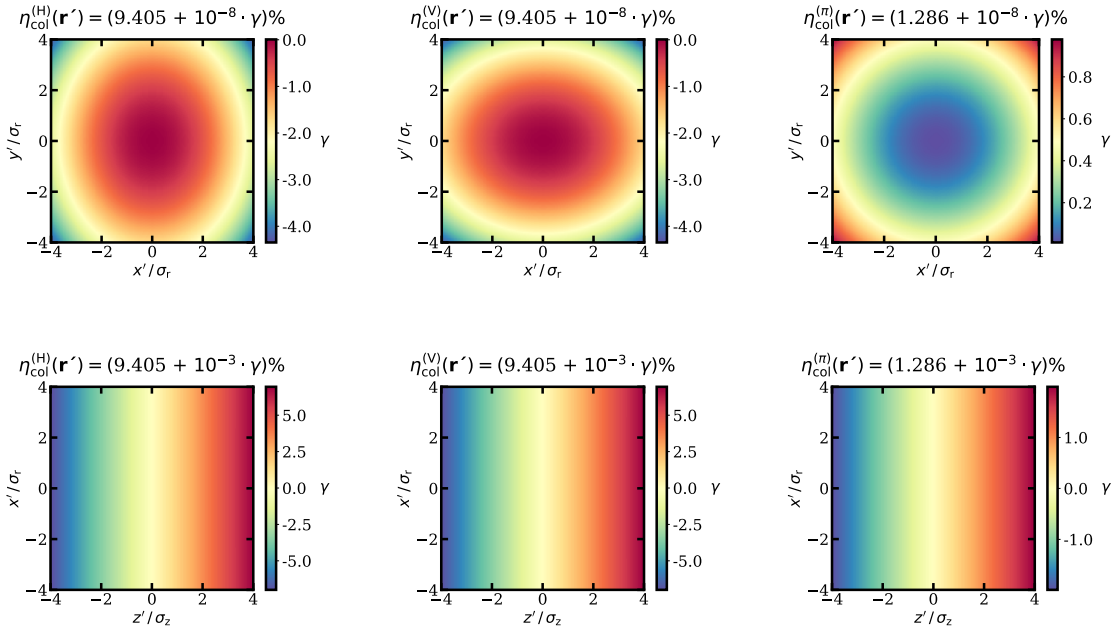

Figure 4.5.: Collection efficiency for displaced atom positions for photon polarizations H (left), V (middle) and π (right). The behavior for atoms in the x-y plane at $z = 0$ is shown in the top row and for atoms in the x-z plane at $y = 0$ in the bottom row. Generally, only negligible changes in the collection efficiency over the complete volume of the thermal density distribution defined by a $\pm 4\sigma$ interval are observable. However, longitudinal atom displacements along the z-axis have a much larger influence than transverse displacements due to less confinement of the atoms along the ODT beam propagation direction. Furthermore, photons emitted closer to the objective are more likely to impinge the entrance aperture, leading to higher collection efficiencies. The specific symmetries of the emission characteristics for the different polarizations are visible in the collection efficiency plots in the x-y plane, e.g. the oval shapes for H and V photons.

Secondly, π-polarized photons that couple into the optical fiber will reduce the fidelity of the maximally entangled qubit state (Eqn. 2.8) (Subsec. 4.4.2). From the collection efficiencies stated in the previous section, one can estimate that approximately $6.4\,\%$[3] of the collected photons (for a NA of 0.5) originate from a π-decay. For the particular case of an atom located directly on the optical axis, the coupling probability for π-photons vanishes due to symmetry reasons [49]. Nevertheless, in the general case of arbitrary atom positions, this probability is suppressed but unequal to zero and must therefore be considered. Likewise, a non-vanishing probability to couple an H-polarized photon into the V-polarization mode of the fiber or vice versa will lead to the same consequences.

4.3.1. Definition of the Coupling Efficiency

The coupling efficiency is defined as the probability of coupling a previously collected photon into the single-mode fiber. It is calculated by an overlap integral of the photon mode $\mathbf{E}^{(p)}_{photon}\left(\mathbf{r}-\mathbf{r}'\right)$ with the mode of the optical fiber $\mathbf{E}^{(q)}_{fiber}\left(\mathbf{r}, w_{coll}\right)$ as [105]

$$\eta^{(p,q)}_{cp}\left(\mathbf{r}', w_{coll}\right) = \left\| \frac{\int \mathrm{dA}\, \mathbf{E}^{(p)}_{photon}\left(\mathbf{r}-\mathbf{r}'\right) \cdot \left(\mathbf{E}^{(q)}_{fiber}\left(\mathbf{r}, w_{coll}\right)\right)^*}{N^{(p)}_{photon}\left(\mathbf{r}'\right) \cdot N^{(q)}_{fiber}\left(w_{coll}\right)} \right\|^2 , \tag{4.35}$$

where p indicates the polarization of the photon and q the polarization of the fiber mode, whereby the parameter w_{coll} defines the size of the fiber mode. The symbol $(\cdot)^*$ denotes the complex conjugate of the value. The normalization of the two modes is given by

$$N^{(p)}_{photon}\left(\mathbf{r}'\right) = \sqrt{\int \mathrm{dA}\, \left\| \mathbf{E}^{(p)}_{photon}\left(\mathbf{r}-\mathbf{r}'\right) \right\|^2}, \tag{4.36}$$

$$N^{(q)}_{fiber}\left(w_{coll}\right) = \sqrt{\int \mathrm{dA}\, \left\| \mathbf{E}^{(q)}_{fiber}\left(\mathbf{r}, w_{coll}\right) \right\|^2}. \tag{4.37}$$

The objective is approximated as a thin lens having the same optical properties regarding focal length, NA, and possible aberrations to simplify the calculations (Fig. 4.6). Note that the vacuum glass cell is already included in the objective's design and hence is not considered separately. The objective changes the emitted photon modes (Eqns. 4.19-4.21) in two ways. On the one hand, only the part of the photon mode emitted into the aperture of the objective can contribute to the coupling efficiency. Therefore, the mode is truncated such that the electric field vanishes outside of the aperture $\mathrm{A_{ap}}$. On the other hand, the mode gets collimated by the objective as it imprints a position-dependent phase factor, which corresponds to the phase shift needed to transform a spherical wavefront into a plane wave $e^{-ik\Delta} = e^{-ik\left(\sqrt{x^2+y^2+f^2}-f\right)}$ (Fig. 4.7). Moreover, the impact of possible aberrations $W\left(x,y\right)$ induced by optical components can now easily be incorporated in the calculations by an additional phase factor $e^{ikW(x,y)}$. However, as shown in the next chapter, the expected wave aberrations in the current system are pretty small with typical values of $W \simeq \lambda/10$ and therefore are neglected in the following calculations. This results in the following photon mode:

$$\mathbf{E}^{(p)}_{photon}\left(\mathbf{r}-\mathbf{r}'\right) = \mathbf{E}^{(p)}\left(\mathbf{r}-\mathbf{r}'\right) \cdot e^{-ik\left(\sqrt{x^2+y^2+f^2}-f\right)} \cdot \Theta\left(\mathrm{A_{ap}}\right), \tag{4.38}$$

[3] The emission of a σ^+-, σ^-- or π-polarized photon occurs with an equal relative probability of $1/3$ (Subsec. 2.3.2). Hence, the fraction of collected π-polarized photons can be estimated as: $\frac{\eta^{(\pi)}_{col}\left(\mathbf{r}'=0\right)}{2\cdot\eta^{\left(\sigma^\pm\right)}_{col}\left(\mathbf{r}'=0\right)+\eta^{(\pi)}_{col}\left(\mathbf{r}'=0\right)} = \frac{1.286\,\%}{2\cdot 9.405\,\%+1.286\,\%} = 6.399\,\%$.

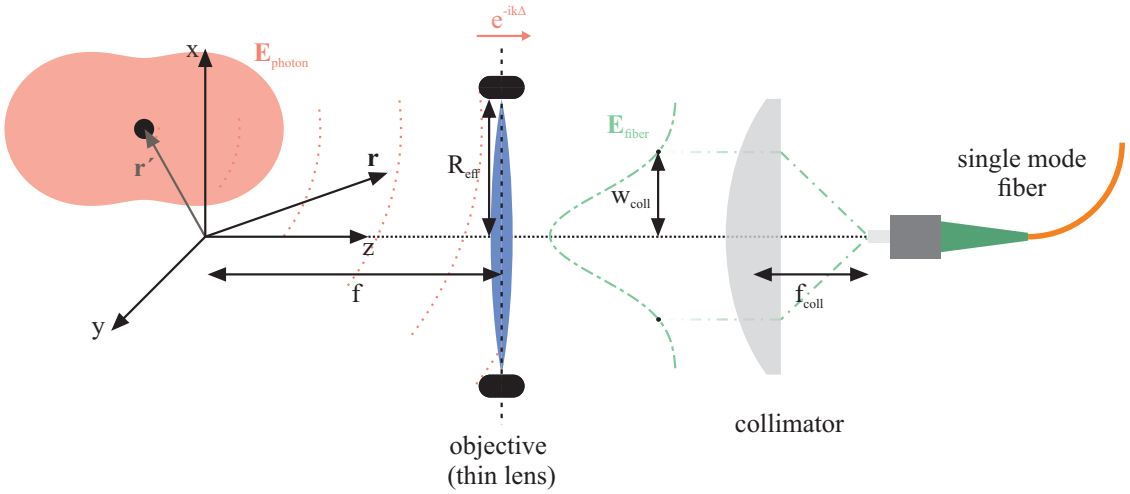

Figure 4.6.: Schematic of the coupling efficiency setup. The coupling efficiency η_{cp} is determined by the overlap integral of the photon mode $\mathbf{E}_{photon}$ (light red) and the fiber mode $\mathbf{E}_{fiber}$ (green) evaluated at the principal plane of the objective. The objective is approximated by a thin lens of the same NA and focal length f, simplifying the calculations. The photon mode is emitted by the atom (black dot) and gets collected within the entrance aperture of the objective of radius R_{eff}, where a phase shift of $e^{-ik\Delta}$ (Fig. 4.7) is imprinted on it. The fiber mode gets imaged onto the principal plane of the objective by a fiber collimator of focal length f_{coll}, resulting in a waist w_{coll} of the Gaussian TEM_{00} fiber mode.

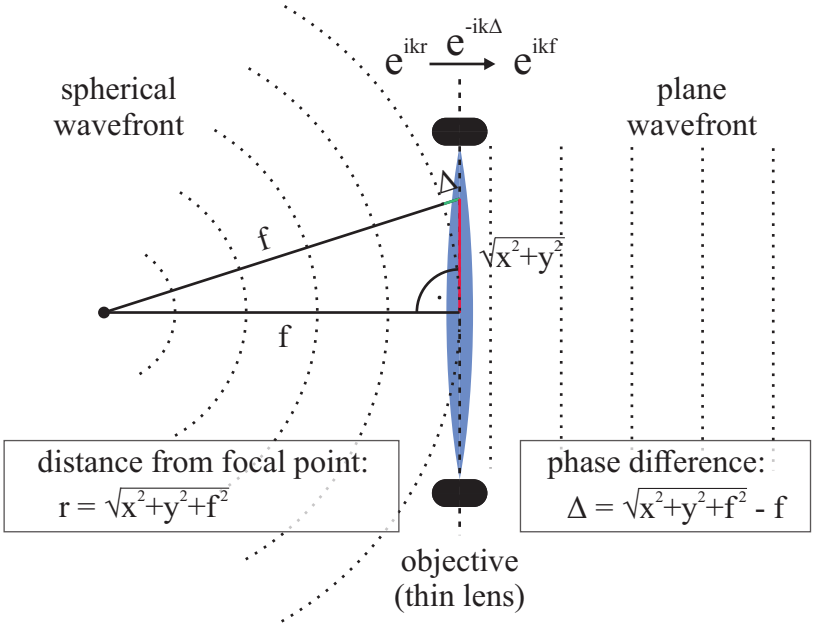

Figure 4.7.: Phase factor caused by the objective: A spherical wavefront emitted from the focal point of the objective gets transformed into a plane wavefront by imprinting a position-dependent phase shift $e^{-ik\Delta}$ on it. Here $\Delta = \left(\sqrt{x^2+y^2+f^2} - f\right)$ is the difference in propagation length of the central point $(x = 0, y = 0, f)$ to an off-axis point at (x, y, f). The objective's aperture additionally truncates the resulting wavefront.

with the Heaviside step function

$$\Theta\left(\mathrm{A_{ap}}\right) = \begin{cases} 1, & \text{for } x, y \in \mathrm{A_{ap}} \\ 0, & \text{for } x, y \notin \mathrm{A_{ap}} \end{cases} .$$

The fiber mode $\mathbf{E}^{(q)}_{fiber}$ is described by the lowest order of the linearly polarized propagation eigenmode of optical fibers LP_{01} [106], which involves a first kind Bessel function of zeroth order. For simplicity, this mode can be approximated by a TEM_{00} Gaussian mode given by

$$\mathbf{E}^{(q)}_{fiber}\left(\mathbf{r}, w_{coll}\right) = \frac{1}{\sqrt{\frac{\pi}{2}} w_{coll}} e^{-\frac{x^2+y^2}{w^2_{coll}}} \begin{pmatrix} q_x \\ q_y \\ 0 \end{pmatrix}, \tag{4.39}$$

where q_x and q_y are two parameters that define the polarization q of the fiber mode with $|q_x|^2 + |q_y|^2 = 1$. The H-polarized fiber mode ($q = H$) is obtained with $q_x = 1$ and $q_y = 0$ and the V-polarized mode ($q = V$) with $q_x = 0$ and $q_y = 1$. The fiber cannot guide polarization components along the fiber axis (e.g. π-polarization), and hence the z-component of the polarization vector is always zero (Eqn. 4.39). The waist of the collimated Gaussian mode w_{coll} is defined by the numerical aperture of the fiber NA_{fiber} and the focal length of the used fiber collimator f_{coll} as follows

$$w_{coll} = f_{coll} \frac{\mathrm{NA}_{fiber}}{\sqrt{1 - \mathrm{NA}^2_{fiber}}}. \tag{4.40}$$

In order to achieve an optimal value of the coupling efficiency the waist w_{coll} of the Gaussian mode must be adapted. Experimentally this is realized by selecting a fiber collimator with a suitable focal length.

4.3.2. Evaluation of the Coupling Efficiency

The mode overlap between the emitted single-photon mode and the fiber mode determines the coupling efficiency $\eta_{cp}^{(p,q)}$. Whereas the photon mode depends on the optical properties of the objective (e.g. NA, focal length f) and the position of the atom $\mathbf{r}'$, the fiber mode is described by the focal length of the fiber collimator f_{coll} and the fiber numerical aperture NA_{fiber}. In general, there are six possible combinations (p, q) to calculate the coupling efficiency depending on the photon polarization $p \in \{H, V, \pi\}$ and the polarization of the fiber mode $q \in \{H, V\}$. However, some of these combinations give the same results, leading to three independent categories:

(i) Equal photon and fiber mode polarization: $(p, q) = (H, H) \vee (V, V)$

(ii) Orthogonal photon and fiber mode polarization: $(p, q) = (V, H) \vee (H, V)$

(iii) Coupling of π-polarized photons: $(p, q) = (\pi, H) \vee (\pi, V)$

Intuitively, this symmetry can be seen by looking at the first two entries of the photon electric field vector (Eqns. 4.19-4.21), where the first entry contributes to the coupling into the H fiber mode and the second entry contributes to the V fiber mode. Interchanging the x (x') and y (y') coordinates reveals the implied symmetry. Therefore, it is enough to present the results for only one of the fiber modes, which in the following will be the H-polarized mode. By considering the product $\mathbf{E}_{photon}^{(p)} \cdot \left(\mathbf{E}_{fiber}^{(H)}\right)^*$, additional statements can be made. In the special case of non-displaced atoms ($\mathbf{r}' = (0, 0, 0)$), only the coupling efficiency of category (i) is unequal to zero. In this case, the product for categories (ii) and (iii) are odd function with respect to x and/or y, resulting in an integral of zero. Following the same line of argumentation, the efficiency of category (ii) is non-vanishing only if both x' and y' coordinates are non-zero, and the efficiency of category (iii) is non-vanishing only if the x' coordinate is non-zero. Moreover, the coupling efficiency $\eta_{cp}^{(p,q)}$ possesses mirror symmetries with regard to the $x'z'$- and $y'z'$-planes. The results of the calculations will be presented separately for the three categories.

(i) Equal Polarization $(\mathbf{H}, \mathbf{H})$:

One of the parameters influencing the coupling efficiency is the size of the fiber mode given by the Gaussian waist w_{coll}. The behavior of the coupling efficiency depending on the mode size is depicted in Fig. 4.8 for different atom positions $\mathbf{r}'$. The waist w_{coll} is given in relative values of the effective aperture radius R_{eff}, and the displacements are stated in units of standard deviations of the thermal density distribution σ_r and σ_z. Analog to the representations of the collection efficiency (see Sec. 4.2) parameters resembling the current situation of the trap in Lab 1 are used: $f = 10\,\mathrm{mm}$, $R_{eff} = 5.77\,\mathrm{mm}$, $\sigma_r = 115\,\mathrm{nm}$ and $\sigma_z = 1.23\,\mu\mathrm{m}$. The calculations show that an optimal w_{coll} can be found for every displacement, which maximizes the coupling efficiency. However, these optimal mode sizes shift to smaller values for larger displacements, which will be important in the next section when an overall coupling efficiency is calculated by integrating over the thermal distribution of the atom. For non-displaced atoms, the optimal waist is $w_{coll} = 0.85 R_{eff}$ with a coupling efficiency of $\eta_{cp}^{(H,H)} = 81.4\%$. All deviations from this central position will lead to a decrease in efficiency, of

which longitudinal shifts have the most significant influence. The dependency on the atom displacements is shown in Fig. 4.9 for different spatial positions.

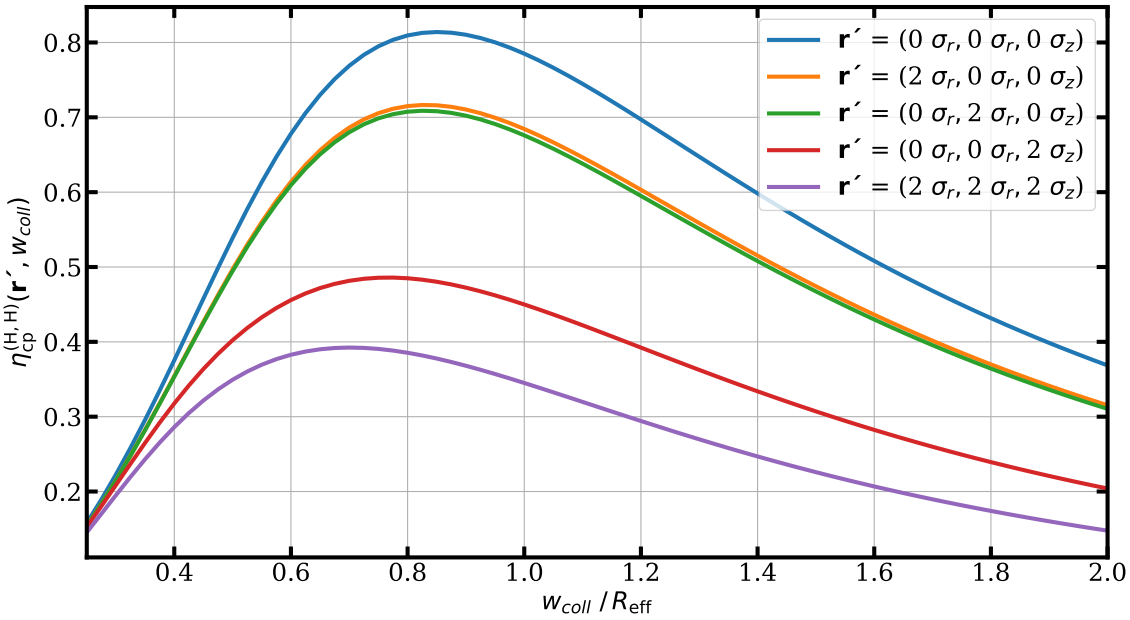

Figure 4.8.: The coupling efficiency $\eta_{cp}^{(H,H)}$ in dependence of the Gaussian waist w_{coll} for different atom positions $\mathbf{r}'$. The maximal efficiency of 81.4% is reached for a non-displaced atom with a waist $w_{coll} = 0.85R_{eff}$. For all other sets of parameters, the efficiency is reduced.

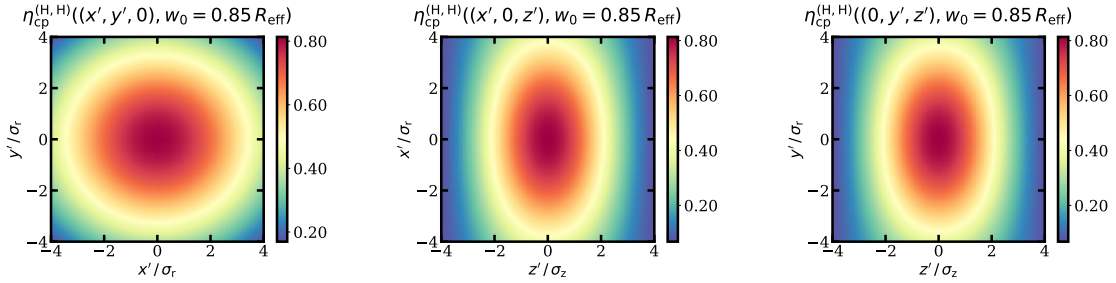

Figure 4.9.: The coupling efficiency $\eta_{cp}^{(H,H)}$ in dependence of the atom position. Longitudinal displacements along the z-axis have a larger influence than transverse displacements due to less confinement of the atoms ($\sigma_r < \sigma_z$). For all plots, a Gaussian waist of $w_{coll} = 0.85R_{eff}$ is used.

(ii) Orthogonal Polarization $(\mathbf{V}, \mathbf{H})$:

The probability to couple a V-polarized photon into the H-mode of the fiber is approximately four orders of magnitude lower compared to category (i). As discussed before, the efficiency is non-vanishing only if the displacements x' and y' are non-zero. Therefore, only plots with $x' \neq 0 \wedge y' \neq 0$ are chosen for Fig. 4.10, where the behavior of $\eta_{cp}^{(V,H)}$ is shown as a function of the Gaussian waist w_{coll}. The

coupling efficiency increases for larger diagonal shifts, whereas longitudinal shifts lead to a decrease. Besides the low coupling efficiency, it is advantageous that the waist for the maximum coupling does not correspond to the value from category (i). The dependence for different displacements is shown in Fig. 4.11.

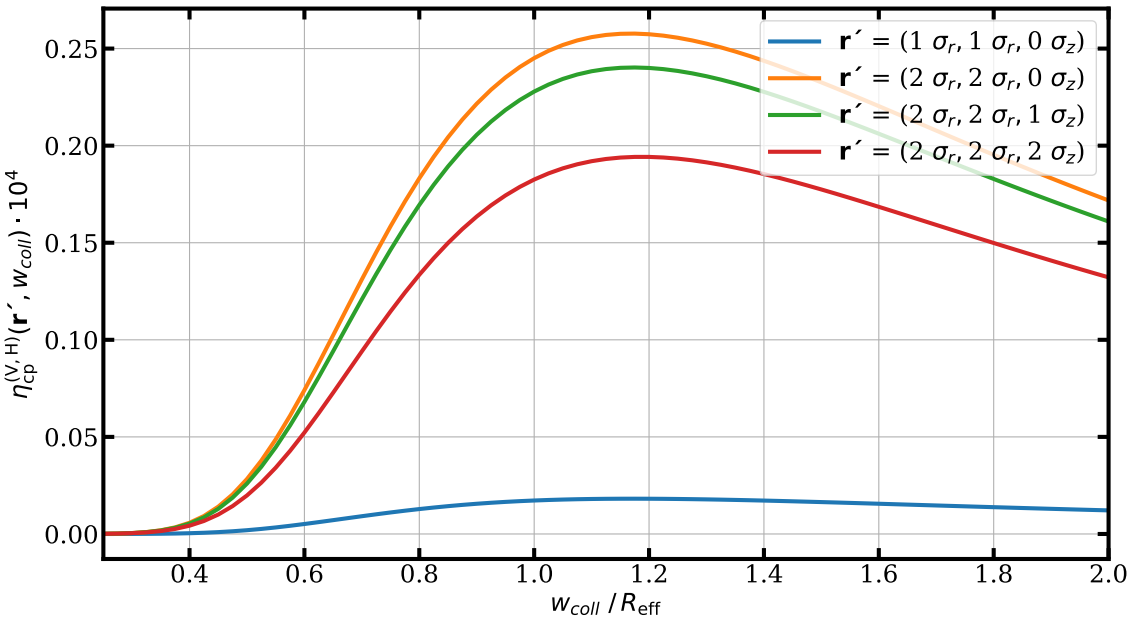

Figure 4.10.: The coupling efficiency $\eta_{cp}^{(V,H)}$ in dependence of the Gaussian waist w_{coll} for different atom positions $\mathbf{r}'$. Non-vanishing efficiencies are only possible if $x' \neq 0 \wedge y' \neq 0$.

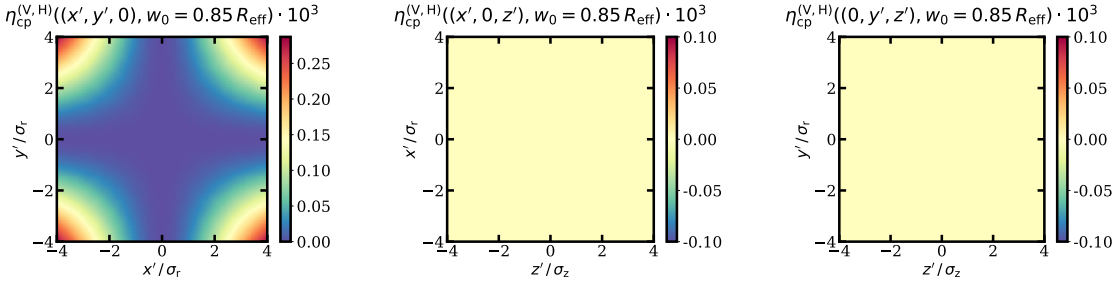

Figure 4.11.: Coupling efficiency $\eta_{cp}^{(V,H)}$ for displaced atom positions. For larger diagonal displacements, the efficiency increases. It vanishes if one of the two parameters x' or y' is zero. For a better comparison, the Gaussian waist is set to $w_{coll} = 0.85 R_{eff}$.

(iii) Coupling of π photons (π, H):

In order to couple a π-polarized photon into the H-polarized fiber mode, the atom must be displaced in the x-direction ($x' \neq 0$). The behavior of $\eta_{cp}^{(\pi,H)}$ depending on the Gaussian waist w_{coll} is shown in Fig. 4.12. For larger displacements along the x-directions, the coupling efficiency increases, whereas

it decreases for all other shifts. The values of the coupling efficiency compared to those of category (i) are typically one order of magnitude lower. The dependence on different displacements is shown in Fig. 4.13.

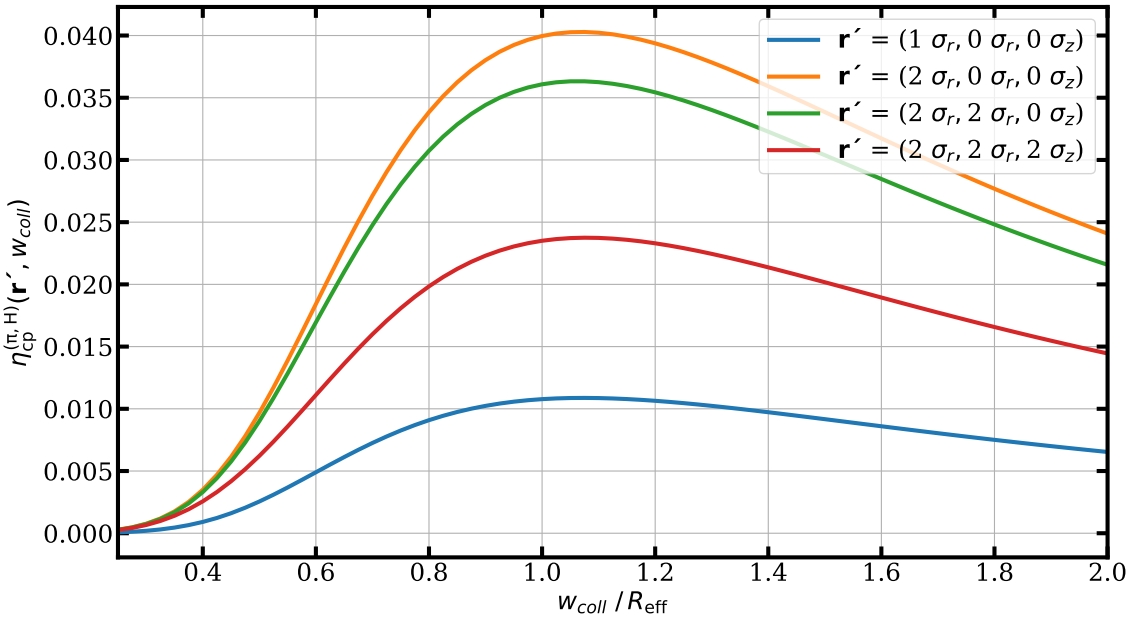

Figure 4.12.: The coupling efficiency $\eta_{cp}^{(\pi,H)}$ in dependence of the Gaussian waist w_{coll} for different atom positions $\mathbf{r}'$. Non-vanishing efficiencies are only possible if $x' \neq 0$.

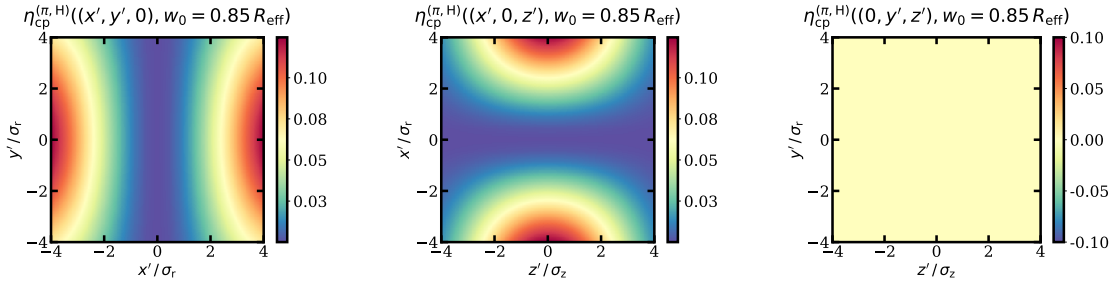

Figure 4.13.: The coupling efficiency $\eta_{cp}^{(\pi,H)}$ for displaced atom positions. A π-polarized photon cannot be coupled in case of $x' = 0$. For a better comparison, the Gaussian waist is set to $w_{coll} = 0.85 R_{eff}$.

4.4. Combined Collection-and-Coupling Efficiency

In the previous sections of this chapter, the processes of collecting and coupling the photon into a single-mode fiber are presented separately. Here, these results are combined in order to estimate an overall efficiency. This combined collection-and-coupling efficiency $\eta_{cc}^{(p,q)}(\mathbf{r}', w_{coll}) =$

$\eta_{col}^{(p)}(\mathbf{r}') \cdot \eta_{cp}^{(p,q)}(\mathbf{r}', w_{coll})$ describes the probability of a photon emitted at position $\mathbf{r}'$ with polarization p coupled in the optical fiber with polarization q. Moreover, during an excitation attempt, the atom is at an arbitrary position described by the thermal density distribution $P_{th}(\mathbf{r}', T)$ (Eqn. 2.5), yielding different efficiencies for each excitation. Consequently, an averaged value is observed in the experiment calculated by integrating the local efficiencies over the trap volume

$$\eta_{cc}^{(p,q)}(w_{coll}) = \frac{1}{3} \cdot \int \mathrm{dV}\ P_{th}(\mathbf{r}', T) \cdot \eta_{col}^{(p)}\left(\mathbf{r}'\right) \cdot \eta_{cp}^{(p,q)}\left(\mathbf{r}', w_{coll}\right). \tag{4.41}$$

Here P_{th} is used as a weight factor, and the factor of $1/3$ accounts for the relative decay probabilities leading to one of the three photon polarizations $p \in \{H, V, \pi\}$. The individual efficiencies for H- and V-polarized photons will be merged to one as both polarizations contribute equally to the generation of the entangled atom-photon state (Eqn. B.1). Note that P_{th} depends on the actual trap geometry as well as on the atom temperature T and by this differs for the respective setups. Calculations of the combined collection-and-coupling efficiency averaged for the thermal distributions of the current setups of Lab 1 and Lab 2, and the setup of 2016 (with the old objective), are shown in Figure 4.14 for the three categories of Subsec. 4.3.2. The corresponding trap parameters are summarized in Table 4.1 together with the atom temperatures T. The latter one is determined by measuring the periodic rephasing of the atomic state caused by the longitudinal field components of the ODT (Sec. 2.5.2) and fitting a model [53] on it, which describes the observed time evolution.
In general, coupling a photon via a category (i) process (equal photon and fiber mode polarization) has by far the highest probability, leading to the desired entangled atom-photon state (Eqn. B.1). On the other hand, the coupling via the processes of category (ii) (orthogonal photon and fiber mode polarization) as well as for category (iii) (coupling of π-polarized photons) lead to an unwanted reduction in the entanglement fidelity (see Subsec. 4.4.2). Fortunately, the efficiencies for those two categories are suppressed by several orders of magnitude (factor of $\sim 10^{-3} - 10^{-5}$) and can therefore be neglected. The differences in the calculated data for the respective traps can be explained entirely by their difference in thermal density distributions P_{th}. Hence, similar results are obtained for the setup of Lab 1 and the setup of 2016 due to similar atom distributions (Table 4.1). Contrary to that, a reduced collection-and-coupling efficiency of category (i) is expected for the setup of Lab 2 as the atom is less tightly bound by the ODT, resulting in a higher probability of finding the atom further away from the center of the collection optics. These larger atom displacements also imply higher efficiencies to couple photons via the unwanted processes of the categories (ii) and (iii). Despite this unfavorable trend, a less tightly focused ODT beam possesses smaller longitudinal field components, which reduce the decoherence caused by the non-perfect rephasing of the atomic state (Subsec. 2.5.2). The efficiency values for the different setups are summarized in Table 4.2.

4.4.1. Fiber Collimator for Optimal Coupling Efficiency

In order to maximize the coupling efficiency, it is vital to choose a fiber collimator, which generates a fiber mode of optimal size. The determining parameters for this are the collimator's focal length and the fiber's effective NA (Eqn. 4.40).
For the 2016 setup a Gaussian beam waist of $w_{coll} = 0.54 R_{eff}$ (Table 4.2) was found to be the best trade-off between the maximal usable collection NA (eff. NA: 0.264) and an operation that minimizes the influence of wavefront aberration introduced by the objective [52]. The full NA of 0.5 could not be used with this objective since it is designed for the visible wavelength range and therefore does not allow for a diffraction-limited operation in the NIR. Without considering the effect of aberrations, this collimator choice results in an expected coupling efficiency, which is reduced by a factor of ~ 0.78

	U_0	λ_D	w_D	T	σ_r	σ_z
current setup Lab 1	$k_B \cdot 2.78\,\mathrm{mK}$	$849.5\,\mathrm{nm}$	$2.05\,\mu\mathrm{m}$	$35\,\mu\mathrm{K}$	$115\,\mathrm{nm}$	$1.23\,\mu\mathrm{m}$
current setup Lab 2	$k_B \cdot 2.15\,\mathrm{mK}$	$857.0\,\mathrm{nm}$	$2.42\,\mu\mathrm{m}$	$31\,\mu\mathrm{K}$	$145\,\mathrm{nm}$	$1.82\,\mu\mathrm{m}$
setup of 2016 [53]	$k_B \cdot 3.21\,\mathrm{mK}$	$852.0\,\mathrm{nm}$	$1.92\,\mu\mathrm{m}$	$45\,\mu\mathrm{K}$	$114\,\mathrm{nm}$	$1.14\,\mu\mathrm{m}$

Table 4.1.: Trap parameters and atom temperature for different experimental setups. In both currently used setups, the new objectives are implemented, while in 2016, the old objective was still in use. Here U_0 is the trap depth, λ_D is the wavelength and w_D is the waist of the ODT, and T is the measured atom temperature. The resulting standard deviations of the thermal density distributions are denoted with σ_r and σ_z.

	(i)	(ii)	(iii)
optimal ($w_{coll}/R_{eff} = 0.82$)	$4.15\,\%$	$1.26 \cdot 10^{-5}\,\%$	$4.40 \cdot 10^{-3}\,\%$
implemented ($w_{coll}/R_{eff} = 0.72$)	$4.05\,\%$	$0.93 \cdot 10^{-5}\,\%$	$3.62 \cdot 10^{-3}\,\%$

(a) Current setup of Lab 1.

	(i)	(ii)	(iii)
optimal ($w_{coll}/R_{eff} = 0.81$)	$3.54\,\%$	$2.60 \cdot 10^{-5}\,\%$	$5.71 \cdot 10^{-3}\,\%$
implemented ($w_{coll}/R_{eff} = 0.84$)	$3.53\,\%$	$2.90 \cdot 10^{-5}\,\%$	$6.11 \cdot 10^{-3}\,\%$

(b) Current setup of Lab 2.

	(i)	(ii)	(iii)
optimal ($w_{coll}/R_{eff} = 0.83$)	$4.23\,\%$	$1.25 \cdot 10^{-5}\,\%$	$4.43 \cdot 10^{-3}\,\%$
implemented ($w_{coll}/R_{eff} = 0.54$)	$3.27\,\%$	$0.27 \cdot 10^{-5}\,\%$	$1.59 \cdot 10^{-3}\,\%$

(c) Setup of 2016 (Lab 1).

Table 4.2.: Efficiencies calculated for the different setups. The results are presented for the optimal fiber mode sizes (highest efficiency of category (i)) and for the actual used fiber mode size yielding the expected efficiency.

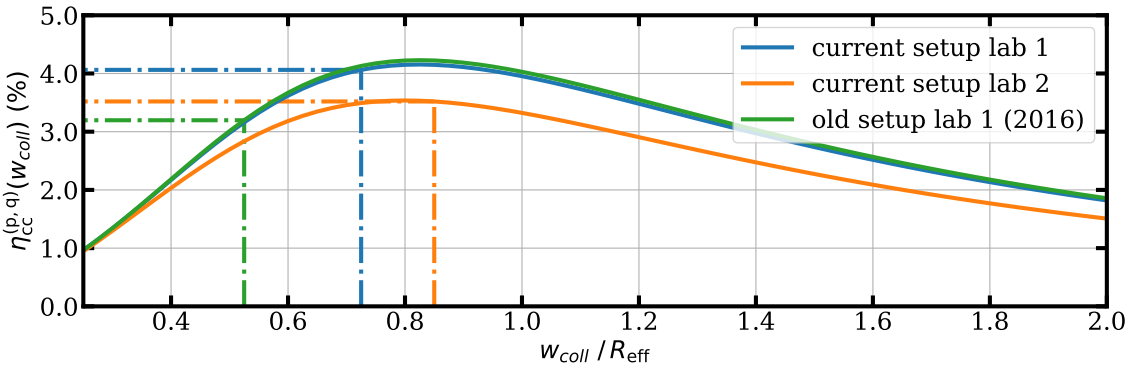

(a) Efficiency of category (i), $(p, q) = (H, H) \vee (V, V)$.

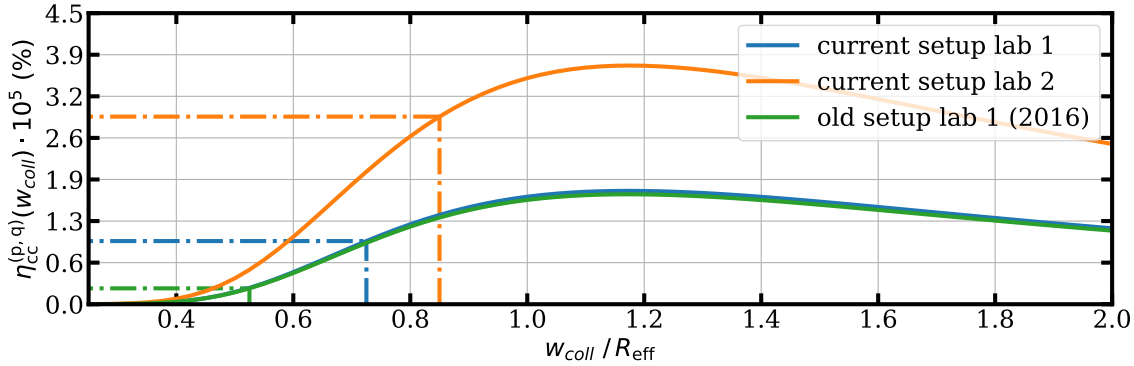

(b) Efficiency of category (ii), $(p, q) = (V, H) \vee (H, V)$.

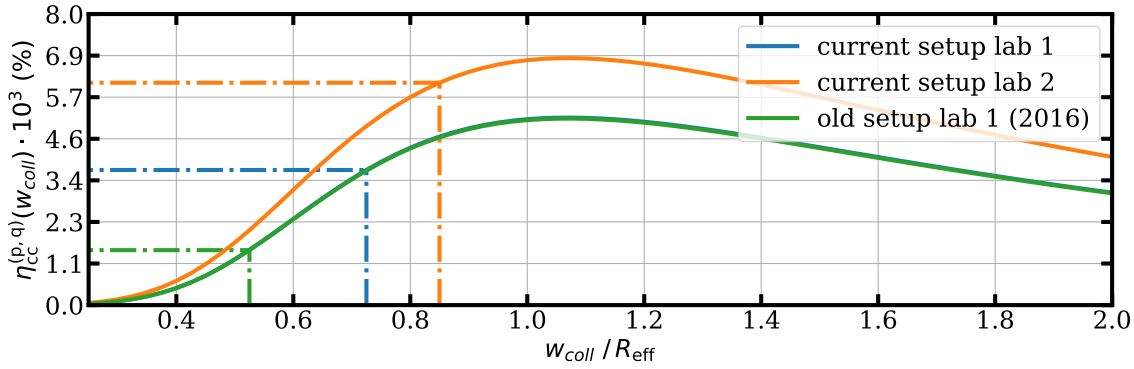

(c) Efficiency of category (iii), $(p, q) = (\pi, H) \vee (\pi, V)$.

Figure 4.14.: Collection-and-coupling efficiencies for all three categories introduced in Subsec. 4.3.2. The efficiency to couple photons into the single-mode fiber with the same polarization as emitted (category (i)) is by far the largest. In contrast, the efficiency in all other cases (category (ii) and (iii)) is several orders of magnitude smaller and can therefore be neglected. The dashed lines mark the actually used fiber mode sizes of the respective setups, which is in the current configuration of Lab 1 $w_{coll} = 0.72R_{eff}$, respectively Lab 2 $w_{coll} = 0.84R_{eff}$, and for the setup of 2016 $w_{coll} = 0.54R_{eff}$. The corresponding efficiency values are summarized in Table 4.2. The underlying thermal density distributions solely determine the different behavior of the efficiency plots. (Table 4.1).

compared to the optimum.
Due to the custom design of the new objectives, perfectly suited for the application of our experiment, a diffraction-limited operation free of aberrations is expected over the full NA of 0.5. This is validated by an optical characterization of the objective presented in the next chapter. The use of fiber collimators with focal lengths close to the optimal value is hence possible. However, finding a commercially available suitable collimator with the correct focal length, which itself does not introduce aberrations, was not possible. For the microscope objective setup, first built [97] and implemented in Lab 1, the fiber collimator with the largest available focal length[4] generates a Gaussian waist of $w_{coll} = 0.72R_{eff}$, which is closer to but not at the optimal value (Table 4.2).
This leaves room for a further potential improvement by factor of ~ 1.025 (ratio of efficiencies of category (i) of Table 4.2a). In order to achieve the highest event rate, especially for atom-atom entanglement experiments, a fiber collimator leading to an optimal coupling efficiency was designed for the second microscope objective setup implemented in Lab 2 (Subsec. 6.1.4). At the time the collimator was designed, the model describing the collection and coupling process presented in this chapter was not fully developed. The best estimate of the optimum fiber mode size back then was $w_{coll} = 0.854R_{eff}$ [97]. Knowing that averaging over the thermal distribution of the atom would lead to a slightly reduced value, the desired fiber mode size was set to $w_{design} = 0.84R_{eff}$. The expected coupling efficiency for this mode size is practically equal to the optimal case (Table 4.2). The residual mismatch in mode size is caused by the fact that the actual thermal density distribution can only be known after implementing the objective. Since the atom in Lab 2 is less tightly bound, it turned out that a slightly smaller mode size would have been preferable.

4.4.2. Fidelity Estimation

For estimating the influence of the unwanted photon couplings from category (ii) and (iii) on the atom-photon entanglement fidelity, the following state is considered:

$$|\Psi_{cc}\rangle = \frac{1}{\sqrt{P_{(i)} + P_{(ii)} + P_{(iii)}}} \left(\sqrt{P_{(i)}} \, |\Psi\rangle_{(i)} + \sqrt{P_{(ii)}} \, |\Psi\rangle_{(ii)} + \sqrt{P_{(iii)}} \, |\Psi\rangle_{(iii)} \right). \tag{4.42}$$

Here $P_{(i)}$, $P_{(ii)}$ and $P_{(iii)}$ are the probabilities that a photon is coupled via category (i), (ii) or (iii) with the corresponding final states $|\Psi\rangle_{(i)}$, $|\Psi\rangle_{(ii)}$ and $|\Psi\rangle_{(iii)}$ given by

$$|\Psi\rangle_{(i)} = \frac{1}{\sqrt{2}} \left(|H\rangle \, |\downarrow\rangle_x + |V\rangle \, |\uparrow\rangle_x \right), \tag{4.43}$$

$$|\Psi\rangle_{(ii)} = \frac{1}{\sqrt{2}} \left(|V\rangle \, |\downarrow\rangle_x + |H\rangle \, |\uparrow\rangle_x \right), \tag{4.44}$$

$$|\Psi\rangle_{(iii)} = \frac{1}{\sqrt{2}} \left(|H\rangle \, |1,0\rangle + |V\rangle \, |1,0\rangle \right). \tag{4.45}$$

The fidelity $\mathcal{F}_{cc}$ of the obtained state (Eqn. 4.42) with respect to the maximally entangled atom-photon state $|\Psi_{AP}\rangle = 1/\sqrt{2} \left(|H\rangle \, |\downarrow\rangle_x + |V\rangle \, |\uparrow\rangle_x \right)$ (Eqn. B.1) can now be calculated as

$$\mathcal{F}_{cc} = |\langle \Psi_{AP}| \, \Psi_{cc}\rangle|^2 = \frac{P_{(i)}}{P_{(i)} + P_{(ii)} + P_{(iii)}}. \tag{4.46}$$

Inserting the expected efficiencies from Table 4.2 yields the fidelities listed in Table 4.3.

[4] Thorlabs C40FC-B, $f = 40\,\mathrm{mm}$

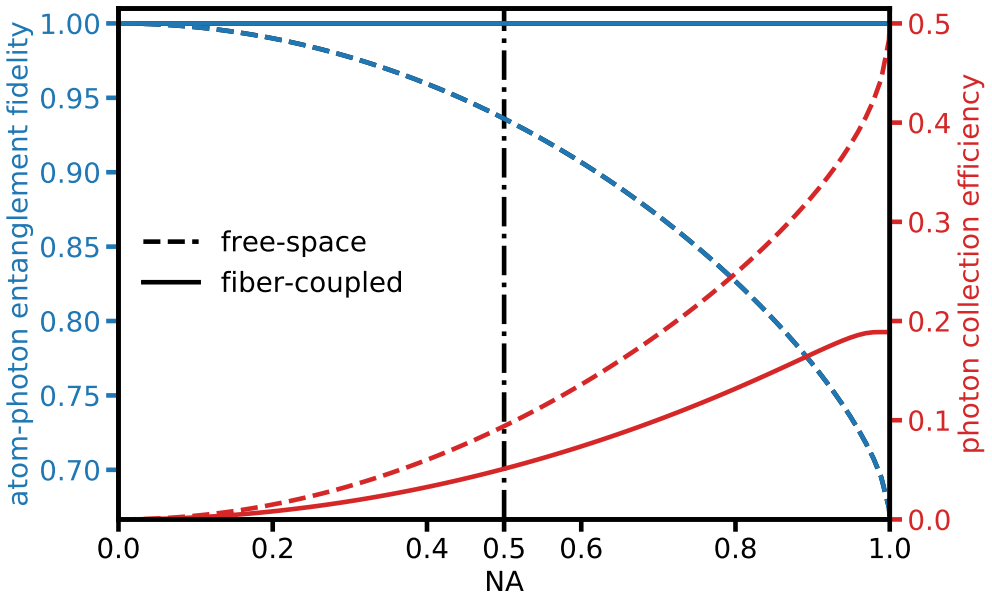

Figure 4.15.: Estimated theoretical atom-photon state fidelity (blue) and collection efficiency of emitted photons (red) in dependence of the numerical aperture. In the free-space case (dashed lines), considering only the collection of the photons but not the fiber coupling, the fidelity decreases with increasing NA due to an enhanced probability to collect π-photons. In contrast, the fidelity stays unity in the fiber-coupled case (solid lines) at the cost of reduced in-fiber collection efficiency. For these calculations, the thermal distribution of the atom is not taken into account due to computational limitations. It is therefore assumed that the atom is at rest in the center of the trap. A similar result can be found in [107].

	current setup Lab 1	current setup Lab 2	setup of 2016
fidelity $\mathcal{F}_{cc}$	0.9991	0.9983	0.9995

Table 4.3.: Estimated atom-photon entanglement fidelities for the different setups. Only for non-displaced atoms the fidelity can reach a value of one. In the general case, the unwanted photon couplings from categories (ii) and (iii) lead to a reduction in fidelity.

In Figure 4.15 a comparison to the free-space case is shown, i.e. without fiber coupling. In this case, a NA of 0.5 reduces the atom-photon entanglement fidelity by 6%, compared to 0.09% with fiber coupling. Here, the fiber acts as a mode filter that suppresses unwanted couplings and thus enables a high fidelity entangled atom-photon state. Note that the data for Fig. 4.15 are only calculated for non-displaced atoms since finding the optimal waist for best coupling together with averaging over the thermal density distribution would cost an immense amount of computational power and time. Nevertheless, the resulting data for the interesting case of the currently available NA are presented in Table 4.3.

4.4.3. Entanglement Rate Estimation

To estimate the performance of the new microscope objectives in the actual experiment, one needs to compare measured data with the theoretical expectations. The entanglement rate is estimated from the local success probability to detect a photon emitted by the atom after an excitation attempt. While this probability can be measured with high accuracy by simply counting the number of detected photons against the number of excitation tries, some of the parameters influencing this probability (Eqn. 2.33) are not known precisely. For instance, residual losses originating from, e.g. unavoidable reflections at more than 30 anti-reflection (AR) coated optical surfaces (transmission 90 %), reflection at the air-glass boundary layer of the fiber (trans. 96 %), direct fiber-to-fiber connections (trans. 95 %), and transmission through optical components (e.g. PBSs and interference filter in front of the APDs (trans. 90%)) lead to an estimated loss factor η_{loss}. These numbers are calculated based on typical specifications given by the manufactures and hence should only be seen as a reasonable estimate. Besides that, the parameter with the biggest uncertainty is the absolute detector efficiency of the APDs, which spans over the range of $\eta_{det} \simeq 0.45 \ldots 0.65$ depending on the individual APD and its alignment. Measurements with the current setups of Lab 1 and Lab 2 show a slightly higher detector efficiency of the APDs implemented in Lab 2 relative to Lab 1: $\eta_{det_2} \simeq 1.15\eta_{det_1}$. For further considerations, the efficiency in Lab 1 (Lab 2) is assumed to be $\eta_{det_1} \simeq 0.5$ ($\eta_{det_2} \simeq 0.575$), while for the setup of 2016, the mean observed value of 0.55 is used[5]. The remaining dependencies of Eqn. 2.33, the state preparation efficiency η_{pump} and the excitation efficiency η_{exc} are either measured or set to have a value of 0.8. Multiplying these factors on the calculated theoretical values for the combined collection-and-coupling efficiency η_{cc} (Table 4.2) results in the expected local success probabilities P_s (Table 4.4).

P_S	current setup Lab 1	current setup Lab 2	setup of 2016
expected	$0.92\,\%$	$0.96\,\%$	$0.82\,\%$
measured	$0.67\,\%$	$0.86\,\%$	$0.20\,\% \ldots 0.38\,\%$
rel. factor	0.73	0.90	$0.24 \ldots 0.47$

Table 4.4.: Success probabilities of detecting a single photon after an excitation attempt. For the theoretical values the combined collection-and-coupling efficiencies with the actually used waist ratios are taken from Table 4.2. Different multiplication factors must be considered (Lab 1: 0.23, Lab 2: 0.27, 2016: 0.25) due to variations in the experimental realization, e.g. different single-photon detectors. A range of measured values is presented for the setup of 2016 since different detector combinations were in use. The performance of the respective objectives is indicated by the relative factors between the expected and measured probabilities. Note, the old objective used in the setup of 2016 introduces wave aberrations limiting the coupling efficiency. However, the calculations do not account for this effect, which explains the comparatively small relative factor.

The values observed with the new objectives are slightly lower than the theoretical expected ones. Relative to each other a, higher probability is measured in Lab 2. Reasons for this are the use of an AR-coated fiber (relative gain of 1.04) and the use of index matching gel to suppress reflections at the fiber-to-fiber connections in Lab 2, and an additional fiber splice in Lab 1 between fibers of different

[5]Over the years, the APDs were frequently exchanged due to malfunctioning, every time yielding different efficiencies. An accurate quantitative comparison is therefore not possible.

types[6]. The probabilities measured with the setup of 2016 are clearly smaller since the old objective is not designed to operate in the NIR wavelength range and by this possesses a lower transmission and introduces wavefront aberrations, which reduce the coupling efficiency. The effect of aberrations is not included in the current calculations and thus is also not considered in the theoretical values, which explains the larger discrepancy between the theoretical and measured values for the setup of 2016. Moreover, all calculated theoretical values resemble upper limits for the respective configurations since perfectly aligned optics are assumed. Estimations considering possible misalignment are made in Section 6.3.

[6] 780HP and SM630

5. Optical Characterization of high-NA Optics

The performance of an optical system is determined by many factors, such as its optical design that need to match the requirements of a specific application, the quality of the involved lenses that depends on the manufacturing tolerances, and the correct usage of the optical system. For any physical realization of an optical system, deviations from the theoretical optimal situation introduce wavefront aberrations, which will lead to reduced optical performance. Moreover, even in the ideal case of a well fabricated and assembled system, wavefront aberrations inherent to the optical design itself are present. As elaborated in the previous chapter, the achievable entanglement rate in the experiment depends on the coupling efficiency of an emitted single photon into an optical fiber. Maximizing this coupling requires an optimized overlap of the fiber mode with the photon mode. Aberrations, possibly introduced by the microscope objective optics, would deform the transmitted wavefront of the photon mode and thus reduce the coupling efficiency.
In order to estimate the influence of wavefront aberrations and verify the specifications given by the manufacturer, an optical characterization of the objective and the homemade fiber collimator is presented in this chapter. It starts with a short introduction to the theory of wave aberrations with all relevant parameters needed for a theoretical description of the problem. After that, the experimental setup which allows for a characterization of high NA optics is described. The chapter ends by evaluating the measured wave aberrations. The data presented in this chapter were collected during the Master thesis of Matthias Seubert [98]. However, the analysis presented there lacks the correct treatment of so-called apodization effects (Subsec. 5.2.2), which for example led to an overestimation of the extracted objective's NA of about 4%.

5.1. Wave Aberration Theory

According to [108], wave aberrations are defined as deviations of the wavefront of an optical system relative to the wavefront of an ideal reference system. In this context, wavefronts are given by surfaces of constant phase or constant optical path lengths l_{OPL} measured from the object point (OP). It can be calculated by integrating the local refractive index $n\left(\mathbf{r}'\right)$ along rays emerging from the object point:

$$l_{OPL}\left(\mathbf{r}\right) = \int_{OP}^{\mathbf{r}} n\left(\mathbf{r}'\right) \mathrm{d}\mathbf{r}'. \tag{5.1}$$

In the case of ideal image formation, all rays converge to a single point and are consequently perpendicular to a sphere centered in the image point (IP). This sphere forms the reference wavefront of an ideal system since the optical path lengths of all rays should be constant for perfect imaging [108]. If the object point coincides with the focal point of the optical system, the sphere's radius goes to infinity, and the reference wavefront in the exit pupil is given by a plane wave truncated by the aperture of the optics. The wave aberrations $W\left(x_p, y_p\right)$ in the exit pupil can now be calculated by the difference of the optical path lengths l_{OPD} (OPD: optical path difference) as

$$W\left(x_p, y_p\right) = l_{OPD}\left(x_p, y_p\right) = l_{OPL}\left(x_p, y_p\right) - l_{OPL}\left(0, 0\right), \tag{5.2}$$

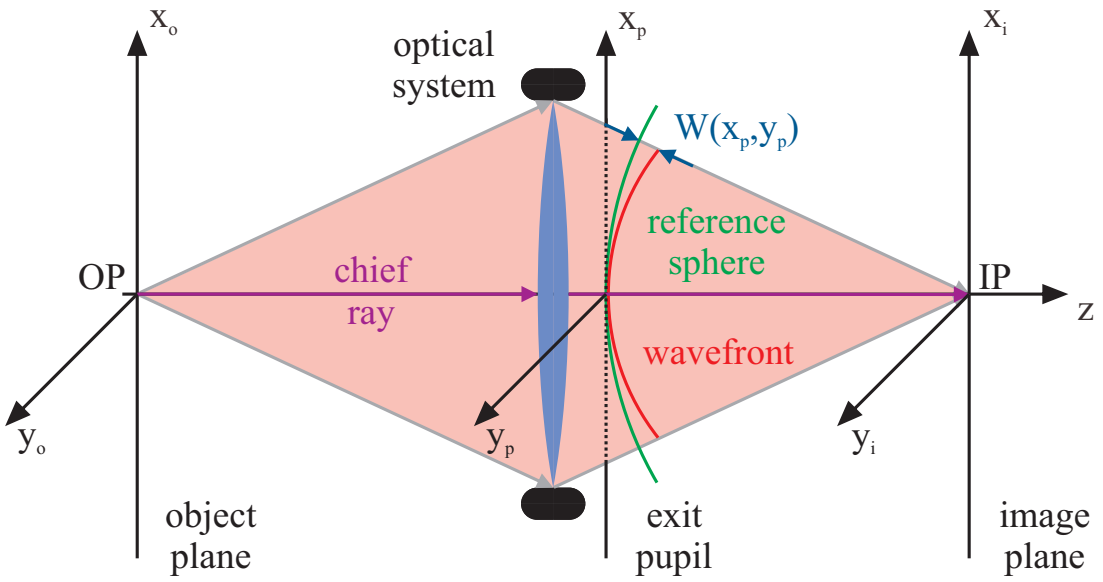

Figure 5.1.: Definition of wave aberrations [108]. Light emitted from a point in the object plane (OP) is imaged by the optical system into the image point (IP). Wavefronts are surfaces of constant optical path length (constant phase) measured along rays originating from the OP. In isotropic media, all rays are perpendicular to the wavefront. Wave aberrations are defined as deviations of the actual wavefront (red) to a reference wavefront (green) measured at the exit pupil. For an ideal system, the reference wavefront is described by a sphere.

where x_p and y_p are the coordinates in the exit pupil, and $l_{OPL}\,(0,0)$ is the optical path length of the reference sphere given by the chief ray [108] (Fig. 5.1). An optical path difference equal to the wavelength of the light λ corresponds to a phase shift of 2π. By scaling $W\,(x_p, y_p)$ in units of λ, the aberrated electric field with amplitude $\mathbf{E_0}$ can be written in the exit pupil as

$$\mathbf{E}\,(x_p, y_p) = \mathbf{E_0}\,(x_p, y_p)\, e^{i\frac{2\pi}{\lambda}W(x_p,y_p)}. \tag{5.3}$$

According to the definition of wave aberrations, they are only defined up to a global phase (or global displacement), which depends on the radius of the reference sphere and therefore their absolute values are subject to some arbitrariness. However, since a global phase does not influence the image formation, this radius can be set freely. Therefore, a reasonable choice, which makes later calculations easier (Eqn. 5.7), is to set the global offset in a way that the mean value of the wave aberrations W_{mean} vanishes (Fig. 5.3):

$$W_{mean} = \langle W \rangle = \frac{1}{A_{ep}} \int \mathrm{dx_p} \int \mathrm{dy_p} W\,(x_p, y_p) = 0, \tag{5.4}$$

with $A_{ep} = \int \mathrm{dx_p} \int \mathrm{dy_p}$ being the area of the exit pupil.

In Figure 5.2, two simple examples are given to illustrate how certain wavefront aberrations influence the image. The first example shows a spherical wavefront of the same radius R_{ref} as the reference, which is tilted with respect to the reference sphere by a small angle θ. This tilt results in a transverse shift of the image point by Δx_i caused by the wave aberration $W_{tilt} = x_p \cdot \frac{\Delta x_i}{R_{eff}} \approx x_p \cdot \theta$ [108].

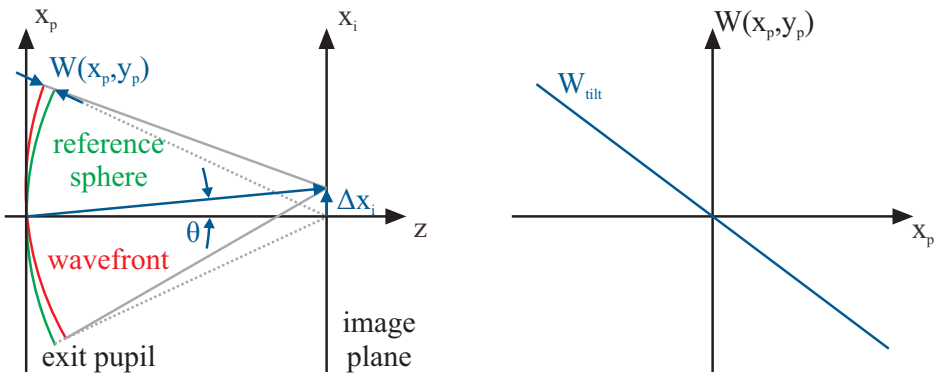

(a) Wavefront tilted with respect to the reference sphere.

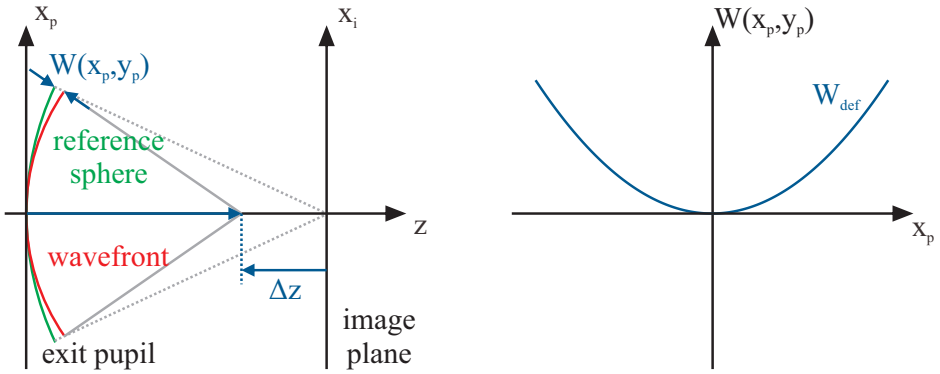

(b) Defocus of the wavefront relative to the reference sphere.

Figure 5.2.: Illustration of wavefront aberrations and their influence on the image [108].

The second example shows a spherical wavefront which is stronger convergent than the reference, resulting in a focal shift Δz caused by the wave aberration denoted as defocus $W_{def} = -\frac{x_p^2+y_p^2}{2R_{ref}^2} \cdot \Delta z$ [108].

5.1.1. Wavefront Aberration Criteria

For the characterization of an optical system, certain measures need to be introduced in order to perform a quantitative analysis. The simplest possibility would be to calculate the peak-to-valley (PV) value of the wave aberrations W_{pv} defined in the exit pupil as

$$W_{pv} = \max_{x_p,y_p \in A_{ep}} \left(W\left(x_p, y_p\right)\right) - \min_{x_p,y_p \in A_{ep}} \left(W\left(x_p, y_p\right)\right). \tag{5.5}$$

A graphical illustration of this definition can be found in Figure 5.3. One of the first image-quality criteria was given by Lord Rayleigh, which considers an optical system as diffraction-limited if the peak-to-valley value of the wave aberrations does not exceed $\lambda/4$. The idea behind this assumption is the following: In the absence of aberrations, all secondary waves are in phase, and their superposition in the image plane leads to the formation of the focal image point. According to Rayleigh, the intensity

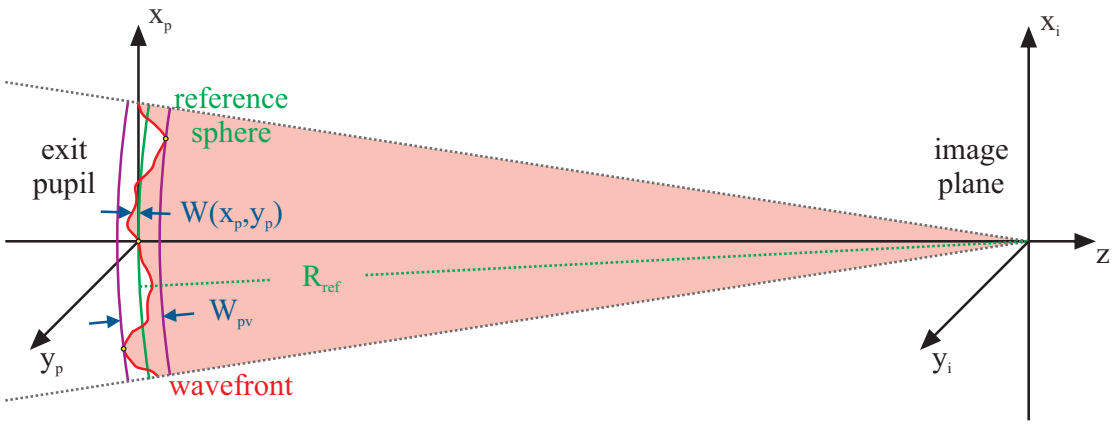

Figure 5.3.: Definition of the peak-to-valley value of the wave aberration in the exit pupil of an optical system [110]. The radius of the reference sphere is chosen such that the mean value vanishes.

of this central image point is only marginally affected by destructive interference as long as the phase deviations over the exit pupil are not too large [109]:

$$\text{Rayleigh criterion}: \ |W_{pv}| \leq \frac{\lambda}{4}. \tag{5.6}$$

However, the peak-to-valley value is a rather conservative estimate since it does not contain any information about the wavefront's functionality (e.g. smoothness) over the pupil and can therefore be misleading. This inadequacy has been exploited in [109] by constructing a wave aberration function that fulfills the Rayleigh criterion but would still yield a poor system performance. Therefore, in general, a more meaningful measure, the root-mean-square (RMS) measure, is used to take also the area information of the wavefront into account. It is defined as

$$W_{rms} = \sqrt{\langle W^2 \rangle - \langle W \rangle^2} = \sqrt{\frac{1}{A_{ep}} \int \mathrm{dx_p} \int \mathrm{dy_p} \left[W\left(x_p, y_p\right) - W_{mean} \right]^2}. \tag{5.7}$$

A definition including a non uniformly illuminated pupil and apodization effects can be found in [110]. A generalized form of the Rayleigh criterion, the Marechal criterion, can be derived for the RMS value of wave aberrations[1] [110]:

$$\text{Marechal criterion}: \ |W_{rms}| \lesssim \frac{\lambda}{14}. \tag{5.8}$$

5.1.2. Expansion into Zernike Polynomials

For a quantitative analysis and classification of surface deformations, the wavefront is usually expanded into elementary functions of discrete shape and definite size. Depending on the system's

[1] Even though the Marechal criterion is derived for a system that only contains defocus, it can be generalized for other aberration types.

n	m	Functional representation	Interpretation
0	0	1	Piston
1	1	$2\rho sin\left(\phi\right)$	Tilt in x
1	-1	$2\rho sin\left(\phi\right)$	Tilt in y
2	0	$\sqrt{3}\left(2\rho^2-1\right)$	Defocus
2	2	$\sqrt{6}\rho^2 sin\left(2\phi\right)$	Astigmatism 45°
2	-2	$\sqrt{6}\rho^2 cos\left(2\phi\right)$	Astigmatism 0°
3	1	$\sqrt{8}\left(3\rho^3-2\rho\right)sin\left(\phi\right)$	Coma x
3	-1	$\sqrt{8}\left(3\rho^3-2\rho\right)cos\left(\phi\right)$	Coma y
4	0	$\sqrt{5}\left(6\rho^4-6\rho^2+1\right)$	Spherical
3	3	$\sqrt{8}\rho^3 sin\left(3\phi\right)$	Trefoil 30°
3	-3	$\sqrt{8}\rho^3 cos\left(3\phi\right)$	Trefoil 0°

Table 5.1.: Zernike polynomials in the standard formulation used in this work to describe the wave aberrations.

geometry, different sets of basis functions are preferable. In the case of a circular exit pupil these are Zernike polynomials. They form an orthonormal set of functions defined in polar coordinates on the unit circle of the exit pupil ($x_p = \rho \cdot sin\left(\phi\right)$, $y_p = \rho \cdot cos\left(\phi\right)$ with $\rho \in \{0,1\}$ and $\phi \in \{0, 2\pi\}$) and consist of a radial term $R\left(\rho\right)$ and a term depending on the azimuthal angle ϕ [111]

$$Z_n^m\left(\rho,\phi\right) = R_n^m\left(\rho\right) \cdot \begin{cases} \sqrt{2\left(n+1\right)} \cdot sin\left(m\phi\right), & \text{for } m > 0 \\ \sqrt{2\left(n+1\right)} \cdot cos\left(m\phi\right), & for\ m < 0 \\ \sqrt{(n+1)}, & for\ m = 0 \end{cases} \tag{5.9}$$

with

$$R_n^m\left(\rho\right) = \sum_{l=0}^{\frac{n-m}{2}} \frac{\left(-1\right)^l \left(n-l\right)!}{l!\left(\frac{n+m}{2}-l\right)!\left(\frac{n-m}{2}-l\right)!} \rho^{n-2l}. \tag{5.10}$$

The integer values n and m satisfy the two conditions $|m| \leq n$, $n - m = \text{even}$ and denote the radial and azimuthal order of the Zernike polynomial $Z_n^m\left(\rho,\phi\right)$, respectively. The expansion of the wave aberrations can now be written as

$$W\left(\rho,\phi\right) = \sum_{n,m} c_{nm} \cdot Z_n^m\left(\rho,\phi\right), \tag{5.11}$$

where the expansion coefficients are denoted with c_{nm}. Table 5.1 shows a list of all in this thesis considered Zernike polynomials. The first four lowest-order wave aberrations[2] (piston, tilt and defocus) determine the image location and can easily be compensated by accurately positioning the image plane and scale. The next terms are five fourth-order aberrations, which can be identified as the well-known primary third-order Seidel aberrations (astigmatism, coma and spherical aberration) [110]. Finally, the highest-order terms taken into account are two sixth-order aberrations denoted as trefoil, which correspond to secondary fifth-order elliptical coma [110].

[2]The wave aberration order is obtained by the absolute sum of radial and azimuthal order $n + |m|$.

By using the orthonormality of the Zernike polynomials over the unit circle

$$\frac{1}{\pi}\int_0^{2\pi} \mathrm{d}\phi \int_0^1 \mathrm{d}\rho\rho \cdot Z_n^m(\rho,\phi) \cdot Z_{n'}^{m'}(\rho,\phi) = \delta_{n,n'} \cdot \delta_{m,m'}, \tag{5.12}$$

it is straightforward to show that the RMS value of the wave aberrations takes a rather simple form

$$W_{rms} = \sqrt{\sum_{n,m} c_{nm}^2}. \tag{5.13}$$

Combined with the Marechal criterion (Eqn. 5.8), upper limits for the individual expansion coefficients can be given up to that diffraction-limited performance of the optical system is expected: $c_{nm} \leq 0.072\lambda$. However, if several aberrations are simultaneously present, the RMS value must still comply with Eqn. 5.8 and the expansion coefficients can not max out their individual limits.

5.2. Point Spread Function as Characterization Method

Characterizing and measuring wave aberrations of an optical system with high accuracy is a demanding task requiring carefully performed measurements. While there are various different methods, all of them depend on the quality of the light source or the calibration of the measurement device. For example, interferometric methods rely on the quality of the reference wavefront as well as on the device optics. In these methods, the optical system is illuminated with the reference that afterwards is overlapped with the aberrated transmitted wavefront resulting in an interference pattern, which can be analyzed to extract the aberrations [112]. Another option would be to use a Hartmann–Shack wavefront sensor to measure the transmitted wavefront directly. Here, the device's calibration to compensate for residual aberrations introduced by the beam-shaping optics is crucial [108]. A point-like emitter in the focal point of an optical system produces a well-defined wavefront, which gets collimated by the optics and can further be analyzed with a shear plate interferometer [113] or a Hartmann–Shack sensor. The difficulty in this approach is to find an ideal point source, which was investigated, e.g. in [98, 114].
The method used in this thesis is based on imaging a point-like emitter and analyzing the observed intensity distribution - the point spread function (PSF) - in the image plane [115, 116]. The basic idea of this method is linked to the definition of the PSF, given in Fraunhofer diffraction theory as the modulus square of the Fourier transform of the electric field (wavefront) at the pupil. Since the information about the aberrations of the optical system is imprinted onto the emerging wavefront, the observed intensity distribution will be modified by these aberrations. Moreover, the individual contributions (individual Zernike polynomials) have a distinct response in the PSF, thus making this method an ideal tool for identifying different types of aberration.

5.2.1. Image of an Ideal Point Emitter

When considering a single radiant point in the object plane of an optical system emitting a spherical wave, only a blurred image of the ideal point source (the PSF) can be observed. This blurring is caused by the aperture of the imaging optics, which truncates the spherical wave at its boundaries, leading to diffraction effects accompanied by constructive interference of only a subset of the initial partial waves in the image plane (Fig. 5.4). The effects of the imaging system (e.g. the wave aberrations W) will be imprinted on the incident wave and therefore are also present in the PSF, which consequently can

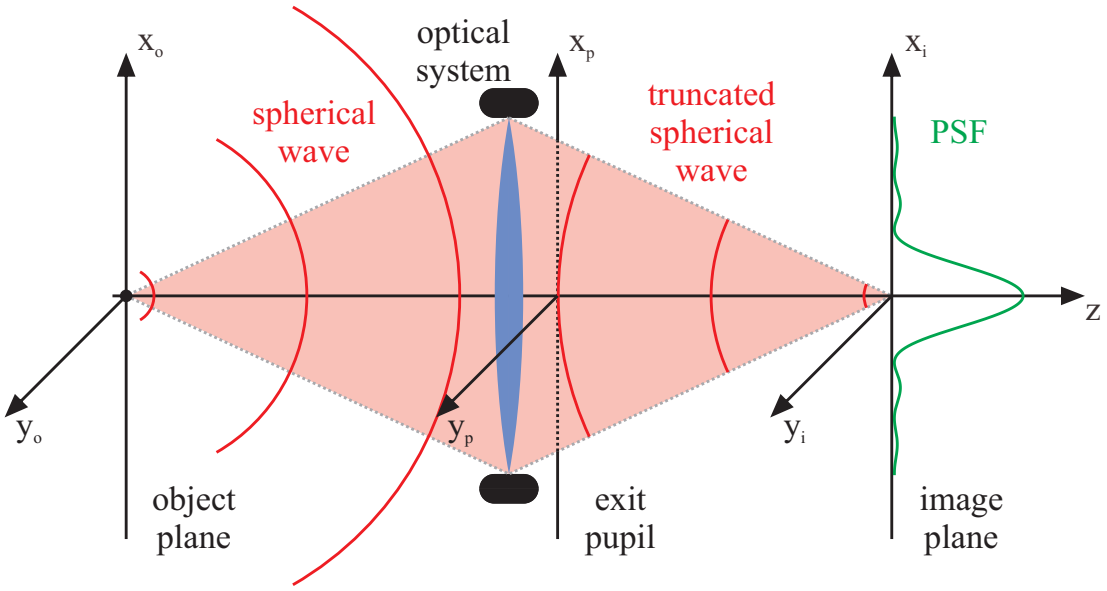

Figure 5.4.: Schematic of the point spread function formation. A point in the object plane emits a spherical wave, which the optical system focuses onto the image plane. However, the finite aperture truncates the spherical wave at its boundaries leading to constructive interference of only a subset of the initial Huygens wavelets and thus also to non-vanishing intensity aside from the central image point. This interference effect causes the intensity distribution to spread over the image plane, forming the point spread function with its minima and secondary maxima.

be used for optical characterization of the system. By applying diffraction integrals in the Fraunhofer approximation, the point spread function in the image plane can be calculated [110]

$$I_{PSF}\left(x_i, y_i\right) = \frac{1}{\left(\lambda\left|z\right|\right)^2}\left|\int \mathrm{dx_p}\int \mathrm{dy_p} E_0\left(x_p, y_p\right) e^{i\frac{2\pi}{\lambda}W\left(x_p, y_p\right)} e^{i\frac{2\pi}{\lambda z}\left(x_i x_p + y_i y_p\right)}\right|^2, \tag{5.14}$$

where the integration is performed over the exit pupil A_{ep}. This equation can be identified with the absolute square of the 2D Fourier transform of the electric field (Eqn. 5.3) by a simple substitution of the Cartesian pupil coordinates with their corresponding spatial frequencies $x_p = \nu_{x_p}\lambda z$ and $y_p = \nu_{y_p}\lambda z$:

$$I_{PSF}\left(x_i, y_i\right) = \left|\mathcal{F}[P\left(\nu_{x_p}, \nu_{y_p}\right) E_0\left(\nu_{x_p}, \nu_{y_p}\right)]\right|^2. \tag{5.15}$$

Here, $P\left(\nu_{x_p}, \nu_{y_p}\right)$ denotes the complex pupil function defined as

$$P\left(\nu_{x_p}, \nu_{y_p}\right) = A\left(\nu_{x_p}, \nu_{y_p}\right) e^{i\frac{2\pi}{\lambda}W\left(\nu_{x_p}, \nu_{y_p}\right)}, \tag{5.16}$$

with the aperture function $A\left(\nu_{x_p}, \nu_{y_p}\right)$ taking the value 1 inside the exit pupil aperture ($\nu_{x_p}, \nu_{y_p} \in A_{ep}$) and 0 outside the aperture ($\nu_{x_p}, \nu_{y_p} \notin A_{ep}$). The formulation of the diffraction integral as a Fourier transform constitutes an important technical detail, reducing the required computation time to analyze the measured data by using optimized Fast Fourier transform algorithms.

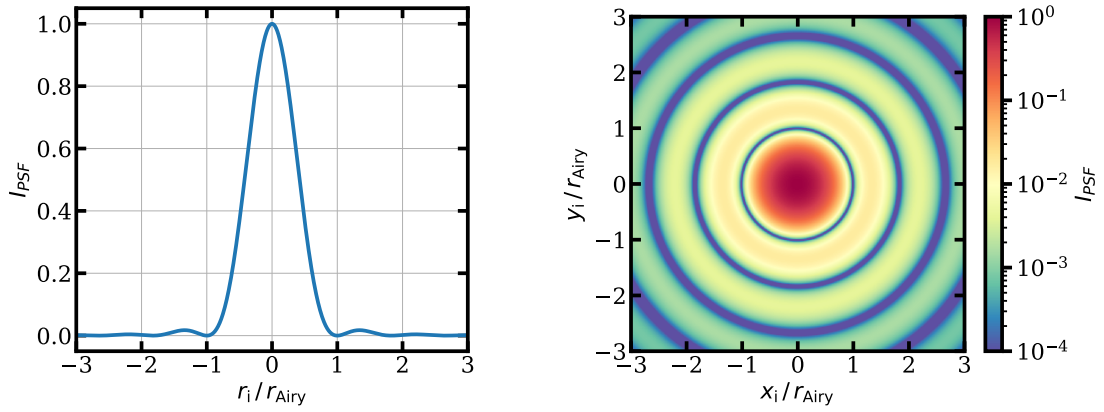

(a) Radial profile of the PSF.

(b) Colormap of the PSF.

Figure 5.5.: Point spread function of an aberration-free idealized system under homogeneous illumination. The radial intensity profile is shown in (a), with r_i denoting the radial distance from the central position on the image plane. The width between the first two zeros defines the Airy diameter D_{Airy}. A 2D colormap of the PSF is shown in (b). A log scale is used to visualize the subtle features of the low-intensity side maxima. In both figures, the maximum intensity is normalized to one.

Idealized System For a start, it is instructive to consider a point spread function of a homogeneous illuminated circular aperture (constant E_0) in the absence of any aberrations as an example of an ideal system. Then, the corresponding diffraction pattern can be calculated by solving Eqn. 5.15 for a circular aperture yielding the well known Airy distribution in the image plane [108]:

$$I_{PSF}\left(x_i, y_i\right) = \left[\frac{2J_1(\frac{2\pi \cdot NA}{\lambda} r_i)}{\frac{2\pi \cdot NA}{\lambda} r_i}\right]^2. \tag{5.17}$$

Here J_1 denotes the Bessel function of order 1, NA is the numerical aperture in image space, and $r_i = \sqrt{x_i^2 + y_i^2}$ is the radial distance in the image plane. The observed pattern reveals a rotationally symmetric, oscillatory behavior with zeros of non-equidistant spacing (Fig. 5.5). The height of the intensity side maxima decreases with increasing diffraction order. The width between the first two zeros defines the Airy diameter D_{Airy} given as

$$D_{Airy} \simeq \frac{1.22\lambda}{NA}. \tag{5.18}$$

For an ideal system, a measurement of the Airy diameter can be used to extract its numerical aperture.

Considering Wave Aberrations In the more general case, when also wave aberrations are considered in the complex pupil function, the expected diffraction pattern in the image plane changes. An overview of PSFs for different types of low order aberrations decomposed in Zernike polynomials (spherical, astigmatism, coma, and trefoil) is shown in Figure 5.6 in a checkerboard-like fashion. With increasing strength of the field aberrations, denoted by the expansion coefficient c, the intensity

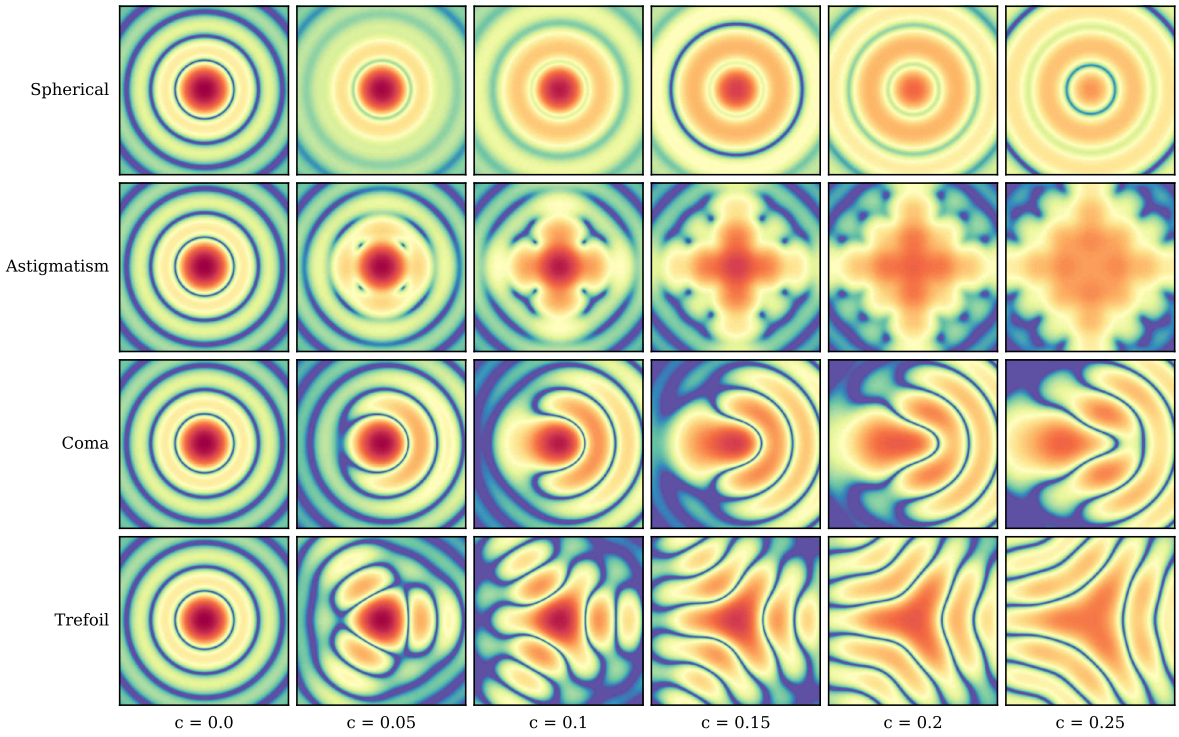

Figure 5.6.: Overview of point spread functions for different wave aberrations. Depending on the strength denoted by the coefficient c (different columns) and type of aberration (different rows), the resulting intensity distribution deviates from the ideal case. The characteristic symmetries of the individual aberrations are clearly visible in the PSFs, and the central intensity maxima decrease with increasing strength c. The same log scale is used for all figures with the intensity maximum in the aberration-free case is normalized to one.

patterns are more and more deformed. A common feature for all aberrations is the reduced height of the central peak intensity caused by progressively worsened conditions for constructive interference at the image point [108]. Moreover, it is quite interesting how different aberrations distinctively manifest their characteristic symmetries in the intensity distributions. For example, spherical aberrations lead to a ring system, astigmatism to an x-y symmetric diamond-shaped structure, coma to a comet-like distribution and trefoil to a three-fold symmetric figure. This clear correspondence lies in the orthogonality of the Zernike polynomials which is utilized to characterize the wave aberrations in the system. Despite these distinctive changes, a quantitative analysis requires a computer-based fit algorithm to precisely deduce the involved aberrations, especially for minor aberrations where the deformation is small. The algorithm determines the individual contributions to the wave aberration using Eqn. 5.15 and a linear least-squares fit to match simulated PSFs to the measured one.

5.2.2. Apodization Effects

The assumption made in Subsection 5.2.1 of a homogeneously illuminated exit pupil is, in general, not fulfilled when considering real systems. As the integration in Eqn. 5.15 is performed over the exit pupil, the non-uniform intensity distribution described by the spatially dependent electric field strength $E_0\left(\nu_{x_p}, \nu_{y_p}\right)$ changes the relative weight of different pupil regions and by this influences

the obtained PSF. The effects caused by this commonly called apodization can become extensive depending on its magnitude. There are various reasons causing an inhomogeneous illumination. For instance, the light source itself, local absorptions, and the system's optical design.

Abbe Sine Condition Even for systems designed to be free from aberrations, it is known that light collected from an ideal point emitter, in general, does not form a collimated beam with a homogeneous intensity profile [117, 118]. Especially for high numerical apertures, this is important and must be included in the calculations. When designing an optical system, it is only possible to make it insensitive against some aberrations by satisfying certain conditions. One example is the so-called Abbe sine condition, which guarantees a constant magnification over all aperture angles and predicts that linear coma vanishes whenever spherical aberrations are compensated [110]. Such systems can be described by ideal lenses with spherical principal planes, from which the apodization function for the Abbe sine condition $A_{Abbe}(\theta)$ is derived under consideration of energy conservation [119]:

$$A_{Abbe}(\theta) = \frac{1}{cos(\theta)}, \tag{5.19}$$

with θ denoting the aperture angle in the object space. The apodization function modifies the electric field strength (Eqn. 5.20), which influences the calculated PSF as discussed in the introductory paragraph of this subsection. For the Abbe sine apodization, pupil regions are weighted more the more they are off the pupil center. The new custom build objectives fulfill the sine condition, and hence the apodization of Eqn. 5.19 must be considered. There also exist other conditions that, when satisfied, guarantee perfect axial imaging in case of the Herschel condition or no distortion (constant magnification over the field of view) for the Helmholtz condition [120].

Realization of a Point Emitter As mentioned before, finding a suitable point emitter that provides a sufficiently smooth emission profile is the main difficulty of the characterization method realized in this work. Therefore, Matthias Seubert built and investigated different sources in his Master thesis [98], including commercially available fibers with an aluminum coated tip of small aperture[3], pinholes manufactured via electron-beam lithography and pinholes produced with a focused ion beam (FIB). In our case, the approach using a tapered fiber tip [116, 123] could not be implemented since all intensity distributions measured for several tips turned out to be severely irregular such that they were unusable for optical characterization. This behavior was not expected following the findings in [124]. Hence, an alternative was needed, which can be provided by a sub-half-wavelength pinhole illuminated by a focused laser beam from the back. By considering plasmonic effects for the transmission of light through a sub-wavelength aperture [125], it has been shown that the expected emission profiles are nearly homogeneous [126]. From the pinholes produced in [98], the one which suits best for our application has a diameter of $362\,\mathrm{nm}$ and was manufactured by focusing an ion beam at a continuous $400\,\mathrm{nm}$ thick gold layer. The emission profile was measured with a camera at a distance of $(7.1 \pm 0.1)\ \mathrm{mm}$ and could be approximated well by a 2D Gaussian distribution with the fitted RMS widths $\sigma_x = 5.613\,\mathrm{mm}$ and $\sigma_y = 5.940\,\mathrm{mm}$. For an optical system with spherical principle planes fulfilling the sine condition, it is demanded to transform the measured emission profile into its radial distribution to incorporate both apodization effects simultaneously. Under the assumption of a point emitter, it is easy to derive the radial emission profile [103], which is further used as apodization function A_{gauss}. A Gaussian-like apodization, with higher illumination in the center than at the pupil's

[3]These fibers are normally used for scanning near field optical microscopy (SNOM) [121, 122]. Batches from two companies were investigated: Lovalite E50-MONO780-AL-200 ($200\,\mathrm{nm}$) and TipsNano MF004 ($185\,\mathrm{nm}$).

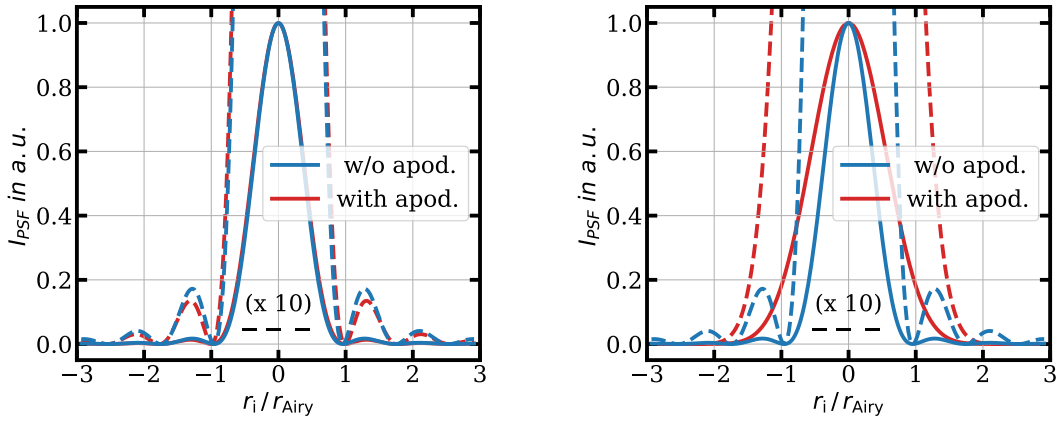

(a) Expected apodization of our system. Only minor deviations from the ideal case are visible, a slightly broader central peak and a marginally reduced height of the secondary intensity maxima.

(b) Apodization with three times smaller Gaussian standard deviations. In this case, the pupil is fully described by a Gaussian distribution, and the side maxima disappear entirely.

Figure 5.7.: Point spread function including apodization effects. Simulated radial intensity distributions of PSFs with (red) and without (blue) apodization are shown. Further, intensity distributions multiplied by a factor of 10 are plotted (dashed lines) to enhance the subtle effects of low apodization. In (a), the expected apodization for our system is applied, and in (b), an apodization with three times smaller Gaussian standard deviations relative to the expected ones of our system are used. The intensity scales for all plots are normalized to one.

edges, leads to two effects in the resulting PSF. Firstly, the central intensity maximum and the Airy diameter get broader and more energy is concentrated in the central peak. Secondly, the side maxima get less prominent and even completely disappear for a pupil fully described by a Gaussian function.

Both apodization effects, the apodization caused by the lens design, and the apodization of the actual emission profile can be included in the calculations by modifying the electric field strength in Eqn. 5.15:

$$E\left(x_p, y_p\right) = E_0 \cdot \sqrt{A_{Abbe}\left(x_p, y_p\right) \cdot A_{gauss}\left(x_p, \sigma_x, y_p \sigma_y\right)}. \tag{5.20}$$

Here the apodizations are expressed in Cartesian coordinates of the exit pupil. A visualization of the apodization effect is depicted in Fig. 5.7, comparing PSFs simulated including apodization with the ideal one of homogeneous illumination.

5.2.3. Strehl Ratio

In Subsection 5.2.1, it has been shown that the intensity distribution of the PSF generally takes a complicated form depending on the individual contributions to the wave aberration (Fig. 5.6). However, the common effect of all aberration types is the reduced height of the central intensity peak. Therefore, a general estimate of the amount of aberrations in a system without considering the detailed structure of the PSF is possible by defining a single number, the so-called Strehl ratio. It is typically defined as the reduced height of the peak intensity in the centroid of the energy of an aberrated system with

respect to the ideal aberration-free system [110]. Mathematically this can be expressed as

$$D_S = \frac{I_{PSF}^{(real)}(0,0)}{I_{PSF}^{(ideal)}(0,0)} = \frac{\left|\int \mathrm{dx_p} \int \mathrm{dy_p} E(x_p, y_p)\, e^{i\frac{2\pi}{\lambda}W(x_p,y_p)}\right|^2}{\left|\int \mathrm{dx_p} \int \mathrm{dy_p} E(x_p, y_p)\right|^2}. \tag{5.21}$$

Note that apodization effects discussed in the previous subsection are included in this formulation. In Eqn. 5.21, it is assumed that the position of the peak intensity and the centroid of the energy coincide, which is, in general, not the case. Especially for coma aberrations, a transverse shift of the peak intensity is expected (Fig. 5.8). Nevertheless, the deviations are negligible for most systems as long as the aberrations are not too strong. Hence, the Strehl ratio is a meaningful quality criterion as long as its value is approximately above 0.6 [110]. While the definition of the Strehl ratio is relatively simple, its calculation, in general, can only be performed numerically. However, in the limit of low aberration, i.e. for systems close to being diffraction-limited, it is possible to find analytic approximations under the assumption of homogeneous illumination. With these considerations, the exponential phase term in Eqn. 5.21 can be expanded as a series. The most common form is the Marechal approximation, which is obtained by stopping the expansion after the first order term [110, 127]:

$$D_S \approx \left|1 - \frac{1}{2}\left(\frac{2\pi}{\lambda} \cdot W_{rms}\right)^2\right|^2 \approx 1 - \left(\frac{2\pi}{\lambda} \cdot W_{rms}\right)^2, \tag{5.22}$$

where for the second approximation of the right side, all terms in W_{rms} with power larger than 2 are omitted. Another variant that also goes under the name of the Marechal approximation is

$$D_S \approx e^{-\left(\frac{2\pi}{\lambda} \cdot W_{rms}\right)^2}. \tag{5.23}$$

This formulation is often be used in calculations for the propagation of aberrated waveforms through atmospheric turbulence and as a general rule of thumb when addressing phase aberrations [127]. Studies investigating the validity of these approximations can be found in [110, 128, 129] with the finding that Eqn. 5.23 approximates the Strehl ratio best with a relative error of less than $10\,\%$ as long as $D_S \gtrsim 0.3$. A simple and practical formula to estimate the Strehl ratio can be obtained by inserting the RMS value of the wave aberrations (Eqn. 5.13) in Eqn. 5.23:

$$D_S \approx e^{-\left(\frac{2\pi}{\lambda}\right)^2 \cdot \sum_{n,m} c_{nm}^2}. \tag{5.24}$$

Furthermore, the wave aberration criteria for diffraction-limited operation (Subsec. 5.1.1) can easily be translated into a criterion for the Strehl ratio by applying the Marechal criterion stated in Eqn. 5.8 ($|W_{rms}| \leq \lambda/14$) to Eqn. 5.23: $D_S \gtrsim 0.8$. For comparison, the exact values of the Strehl ratio for the individual aberration are summarized in Table 5.2.

5.3. Characterization of Optical Components

The previous subsections introduced the theoretical framework to describe and quantitatively characterize optical systems. Applying certain criteria makes it possible to determine the boundaries of diffraction-limited operation for various alignment parameters such as transverse and axial displacement. This subsection will present the experimental realization of characterization measurements for the new high-NA objective and the homemade fiber collimator. First, however, let us quickly recapitulate the idea of how to determine the aberrations introduced by an optical system: Light emitted from

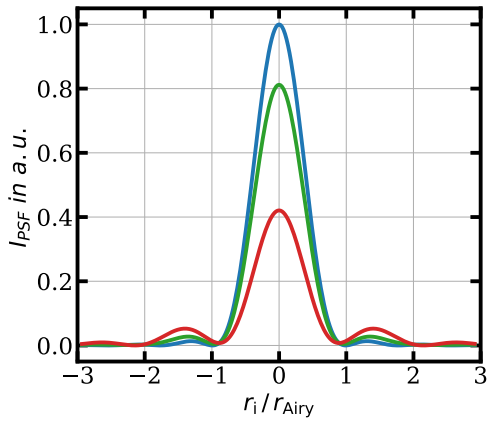

(a) Radial intensity distribution in case of spherical aberration.

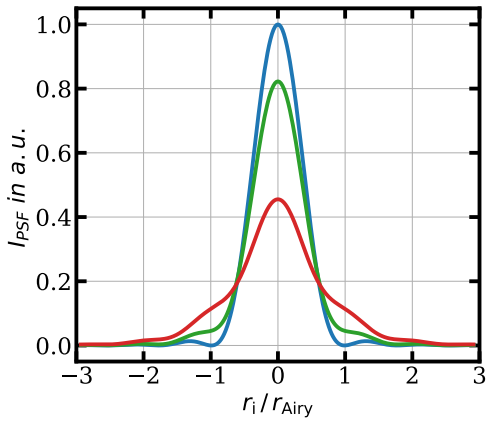

(b) Radial intensity distribution in case of astigmatism.

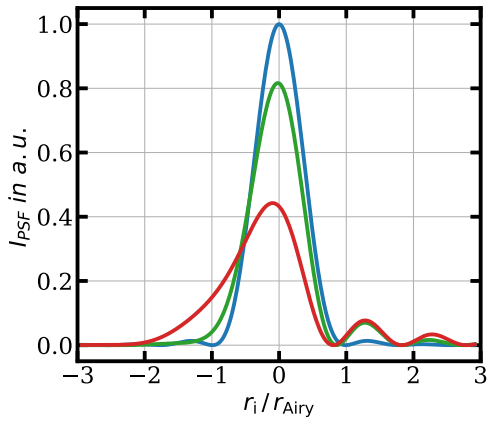

(c) Radial intensity distribution in case of coma. Note, the central peak shifts in the transverse direction with increasing aberration strength.

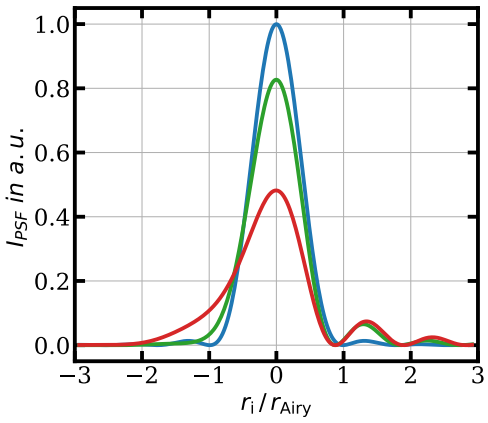

(d) Radial intensity distribution in case of trefoil.

Figure 5.8.: Point spread functions for different types of aberration. The Strehl ratio can be calculated by comparing the central peak height of the aberrated system with $c = 1 \cdot 0.072$ (green) and $c = 2 \cdot 0.072$ (red) to the aberration-free system (blue). In all cases, the expected apodization of our system is included.

Aberration type	n	m	Coefficient	Marechal approximation	Exact Strehl
Defocus	2	0	$c_{20} = 0.072$	0.8141	0.8106
Astigmatism	2	± 2	$c_{2\pm 2} = 0.072$	0.8141	0.8133
Coma	3	± 1	$c_{3\pm 1} = 0.072$	0.8141	0.8127
Spherical	4	0	$c_{40} = 0.072$	0.8141	0.8117
Trefoil	3	± 3	$c_{3\pm 3} = 0.072$	0.8141	0.8155

Table 5.2.: Approximated and exact Strehl ratios for different aberration types. The strengths of the aberrations are chosen such that the Marechal criterion for a diffraction-limited operation is barely satisfied.

a source, approximated well by a point-like emitter, is collected and imaged by the optical system forming a PSF in the image plane. Aberrations of the system are imprinted as a phase term on the electric field leading to a deformation of the observable intensity distribution. The aberrated image is recorded by placing a CMOS (complementary metal-oxide-semiconductor) camera[4] at the image plane. The analysis to determine the individual contributions is performed afterwards by applying a computer-based linear least-squares fit algorithm, which compares simulated PSFs with the recorded picture. Finally, the parameters used for the optimization are the expansion coefficients of the Zernike polynomials (Table 5.1), the NA of the system and the peak intensity. The parameters yielding the best correspondence of simulated and recorded pictures are assigned to the system's aberrations.

5.3.1. Experimental Realization of the Measurement

The point-like emitter utilized in this work is a sub-half-wavelength pinhole (Subsec. 5.2.2) through a gold layer coated on a glass substrate, which is illuminated from the back via a focused laser beam. The laser is locked to the wavelength of the fluorescence light at $780\,\mathrm{nm}$, and hence chromatic aberrations can be excluded. A schematic of the experimental setup is depicted in Figure 5.9. The pinhole is placed in the focal point of the optical system, leading to the collimation of the collected light. An additional lens is introduced in the beam path to image the point source and directly record the PSF with the CMOS camera. The Airy diameter for the new objectives with a NA of 0.5 has a size of $\sim 1.9\,\mu\mathrm{m}$, which is smaller than the single-pixel size of the CMOS camera of $5.5\,\mu\mathrm{m}$. In order to still be able to resolve the PSF, the focal length of the focusing lens needs to be chosen large enough to provide a sufficient magnification in the image plane. Therefore, a lens with $f_{lens} = 2500\,\mathrm{mm}$ is used, yielding a magnification of $f_{lens}/f_{obj.} = 250$, which allows projecting the Airy diameter over 86 pixels and effects caused by the finite pixel size are negligible [115].
The measurement setup is equipped with various alignment stages, allowing for a precise setting of the individual optical components. One example of a motorized three-axis translation stage, which allows for the positioning of the optical system with a precision of $20\,\mathrm{nm}$, is indicated by the green area in Fig. 5.9. The pre-alignment of the optical system with respect to the pinhole is a tedious task since the characterization method requires a point-like emitter, which consequently cannot be resolved optically by the system under test. Therefore, larger marker structures, which uniquely define the pinhole position, are used as guidance for precise transverse positioning. For the axial and angular pre-alignment, the method of auto-collimation is used. To obtain an optimal alignment, the recorded PSFs are visually inspected to minimize the residual aberrations. Further information on the

[4] IDS UI-3370CP Rev. 2

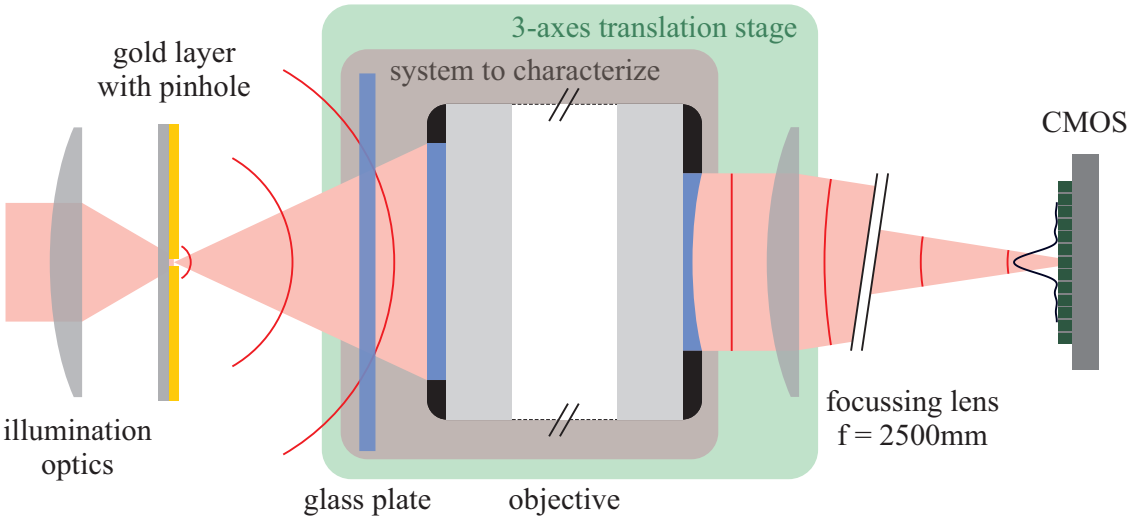

Figure 5.9.: Experimental setup to characterize optical systems. A sub-half-wavelength pinhole is illuminated by a focused laser beam from the back, serving as the point source for the characterization. It is placed in the focal point of the optical system under test (marked by the brown area), which together with an additional focusing lens generates a magnified image at the CMOS camera placed in the image plane of the combined system. The measurement setup enables precise alignment of every individual optical element through various alignment stages, e.g. a three-axis motorized translation stage for the positioning of the optical system (marked by the green area).

alignment procedure can be found in [98].
In order to resolve also subtle deviations of the PSF, especially for small aberrations, the exposure time of the CMOS camera is minimized to keep the noise level low, and the optical power of the illumination light is set such that the 16-bit resolution of the camera is fully used. Performing the measurement in the dark and shielding the entrance of the CMOS camera with tube optics were enough to reduce the remaining stray light to an unnoticeable level. In addition, the cover glass of the camera and the protection glass of the CMOS chip were removed to avoid unwanted interference effects of light reflected at the glass surfaces, which further improves the image quality. Additional post-processing of the recorded data allows for reliable fit results by applying standardized average filters, which reduce the influence of the residual noise. Since fit algorithms tend to underestimate the uncertainty of the fit results, the reliability of the fits was tested separately. Therefore, data sets with known aberrations were simulated with noise comparable to those recorded and subsequently evaluated via the automatized fit algorithm. Comparing the input and output values results for every fit parameter in a distribution of the differences of which the standard deviation is further used as the corresponding fit uncertainty (Table 5.3).

5.3.2. Results for Photon Gear Objective

The microscope objective is the central element of the entire experiment, and its performance influences many steps of the experimental sequence (Subsec. 2.6.3) from which the collection and coupling of the single photon have the highest demands on its optical properties. For this applica-

	Orders (n,m)	Zernike coefficients (λ units)
Defocus	$(2, \quad 0)$	0.0042 ± 0.0043
Astigmatism 45°	$(2, \quad 2)$	-0.0007 ± 0.0025
Astigmatism 0°	$(2, -2)$	-0.0038 ± 0.0033
Coma x	$(3, \quad 1)$	0.0004 ± 0.0017
Coma y	$(3, -1)$	0.0009 ± 0.0015
Spherical	$(4, \quad 0)$	0.0020 ± 0.0058
Trefoil 30°	$(3, \quad 3)$	0.0004 ± 0.0011
Trefoil 0°	$(3, -3)$	0.0001 ± 0.0010
Strehl ratio		0.9985 ± 0.0021

Table 5.3.: Fitted wave aberrations in the case of optimal alignment expressed in terms of Zernike polynomials. All aberrations are well below the threshold given by the Marechal criterion (Eqn. 5.8) for diffraction-limited performance and are compatible with zero. The resulting Strehl ratio yields a value of 0.9985 ± 0.0021, close to the theoretical optimum of 1.

tion, the full NA of 0.5 is needed to maximize the achievable event rate, and the alignment of the microscope objective setup must be well in the specifications given by the manufacturer to guarantee a diffraction-limited operation. The two most important specifications are the angular field of view of $\pm 1.37°$, which translates with the focal length of $10\,\mathrm{mm}$ into a transverse displacement in the image plane of $\pm 239\,\mu\mathrm{m}$, and the relative angle between the objective and the vacuum glass cell of $< 0.1°$. Note, the $3.5\,\mathrm{mm}$ thick wall of the vacuum glass cell is included in the design of the objective and must therefore be considered in all characterization measurements of the objective. This is realized by inserting a suitable glass plate of correct thickness and material into the setup (Fig. 5.9). Separate measurements were performed to target the effects of specific misalignment on the induced aberrations, i.e. axial and transverse displacements as well as tilts of the glass plate. As a reference, the case of optimal alignment is presented first.

Optimal Alignment

An optimal alignment can be achieved by first adjusting the relative angle of the glass plate and the objective, using an interferometric method developed during the Master thesis of Timon Hummel [97], which is described in Subsec. 6.2.2. After that, the combined system consisting of the glass plate and the objective is precisely positioned relative to the pinhole until no noticeable deformations of the PSF are observable anymore. Within the uncertainty of the fit, all aberrations are clearly below $\lambda/14$ and are compatible with zero. The corresponding Zernike coefficients are summarized in Table 5.3. The numerical aperture of the system extracted from the measurement yields a value of 0.5023 ± 0.0026, which is in good agreement with the specified NA of 0.5, and the estimated Strehl ratio takes a value of 0.9985 ± 0.0021, indicating a close to optimal optical performance. Figure 5.10 depicts the measured PSF and its radial intensity distribution in comparison to the intensity distribution of the fitted PSF. The fit represents the measured data well with only minor deviations in the low-intensity regions, mainly caused by the residual statistical noise.

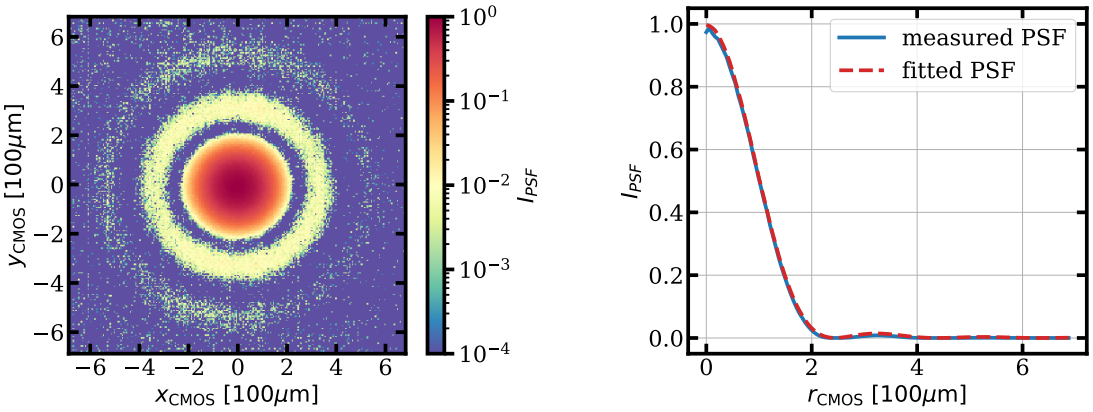

(a) Measured PSF.

(b) Radial intensity distribution of measured PSF (blue) and fitted PSF (red).

Figure 5.10.: Point spread function in the case of optimal alignment. (a) 2D intensity distribution of the PSF measured with the CMOS camera represented in log scale. (b) Radial intensity distributions of the azimuthally integrated PSFs for the measured data and the fitted model based on a wavefront expansion in Zernike polynomials.

Spatial Misalignment

The objective is moved away from the optimal position presented in the previous paragraph to investigate the effect of spatial misalignment on the induced wave aberrations. In actual experiments, this situation can occur due to a non-perfect alignment of the microscope objective setup, which causes a mismatch of the focal positions of the collection optics (zero position) and the optical dipole trap (mean atom position). Even when both foci perfectly overlap, the thermal distribution of the atom inside the ODT generally will lead to a displaced configuration.

Axial Displacement Figure 5.11 depicts wave aberrations expressed in Zernike polynomials, which are induced by the objective depending on the axial misalignment Δz, as well as the corresponding Strehl ratios extracted directly from the recorded data. As expected, defocus is the primary contributor to the wavefront deformation leading to $W < 0$ for smaller separations between the pinhole and the objective ($\Delta z < 0$) and to $W > 0$ for larger separations ($\Delta z > 0$). Furthermore, within axial displacements of $\Delta z = \pm 1.7\,\mu$m, the Strehl ratios yield values $D_S > 0.81$, indicating a diffraction-limited operation of the system according to the Marechal criterion (Subsec. 5.2.3). Example images recorded for different displacements are shown in Figure 5.12. Note, the defocus contribution is already included in the calculations of collection-and-coupling efficiency presented in the previous chapter by the phase term introduced in Eqn. 4.38.

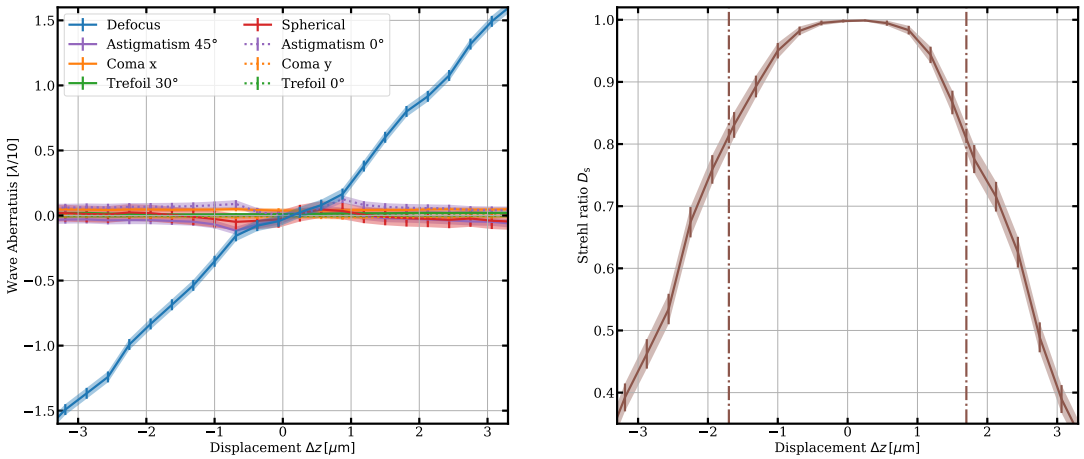

(a) Wave aberrations.

(b) Strehl ratio.

Figure 5.11.: Wave aberrations (a) and Strehl ratio (b) in dependence of axial displacements. The defocus term is the main contribution to the wavefront expansion in Zernike polynomials for axial displacements. The Strehl ratios are extracted directly from the images recorded by the CMOS camera yielding an expected diffraction-limited performance within the boundaries of $\Delta z = \pm 1.7\,\mu\mathrm{m}$ (dashed lines).

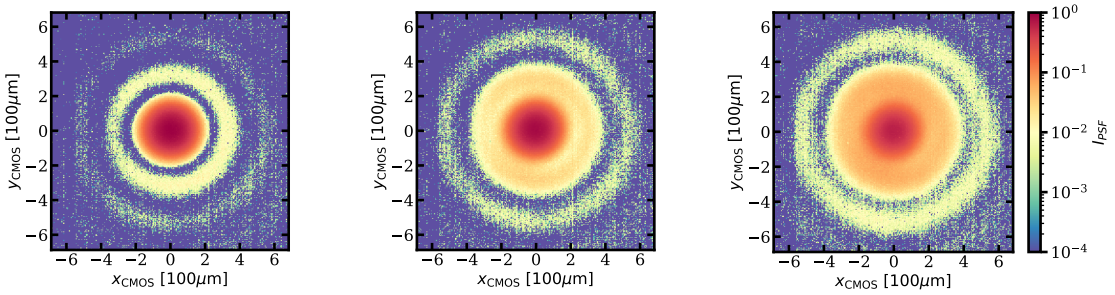

(a) $\Delta z = 0.25\,\mu\mathrm{m}$, $c_{20} = 0.0025$.

(b) $\Delta z = 2.5\,\mu\mathrm{m}$, $c_{20} = 0.0601$.

(c) $\Delta z = 3.4\,\mu\mathrm{m}$, $c_{20} = 0.1076$.

Figure 5.12.: Example images for different axial displacements. The strength of the defocus aberration increases with increasing misalignment Δz, which is indicated by the expansion coefficient c_{20} in units of λ.

Transverse Displacement A transverse displacement of the objective relative to the pinhole introduces a tilt of the collimated collected light with respect to the quantization axis. This tilt changes the beam path after the focusing lens, which causes the observed intensity distribution to be shifted away from the center of the camera. Therefore, for each transverse displacement, the beam path is realigned by two additional mirrors leading to a change in the total optical path length, which effectively results in a shift of the image plane accompanied by an increase of the defocus contribution. Hence, to compensate for this, the image plane is also re-adjusted for every setting minimizing the unwanted defocus term.

Figure 5.13 shows the obtained wave aberrations as a function of the transverse displacement. Up to

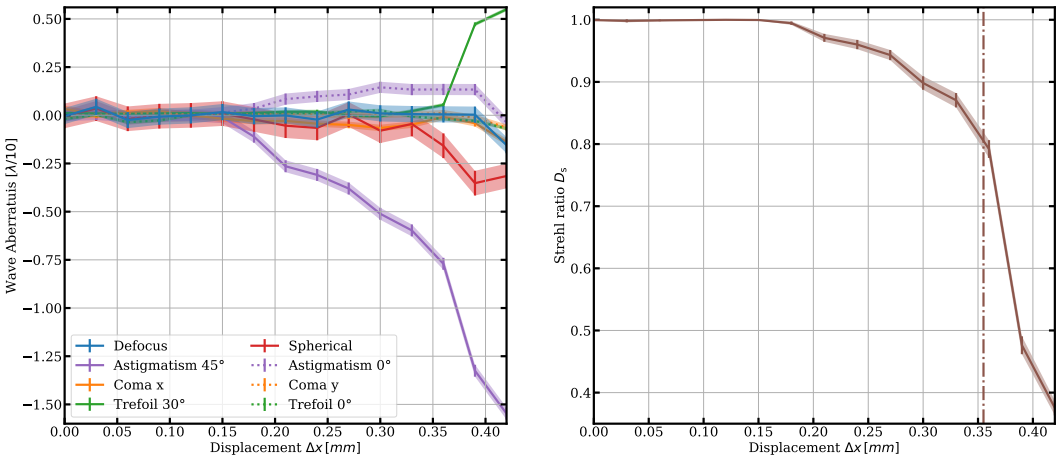

(a) Wave aberrations.

(b) Strehl ratio.

Figure 5.13.: Wave aberrations (a) and Strehl ratio (b) in dependence of transverse displacements. Astigmatism represents the main contribution to the wavefront expansion in Zernike polynomials for transverse displacements. The Strehl ratios are extracted directly from the images recorded by the CMOS camera yielding an expected diffraction-limited performance for misalignments smaller than $\Delta x = 0.355\,\mathrm{mm}$ (dashed line).

a misalignment of $180\,\mu\mathrm{m}$ no noticeable aberrations are introduced, while for larger displacements astigmatism increases. The boundary for diffraction-limited operation stated by the manufacturer is around $\sim 240\,\mu\mathrm{m}$, whereas a significantly larger value of around $\sim 355\,\mu\mathrm{m}$ was measured (see dashed line in Fig. 5.13b). Around this position, other terms also increase, e.g. spherical aberration and trefoil, from which particularly the latter one did not contribute to all other performed measurements. Moreover, for these last two settings (with increased spherical and trefoil terms), larger adjustments of the image plane were necessary to compensate for the defocus. Since the re-alignment of the beam onto the camera is done manually, it cannot be excluded that some errors are introduced by this, causing the aforementioned changes in the fitted wave aberrations. Nevertheless, the measurement clearly shows that a transverse misalignment leads to astigmatic aberrations. Example images of the recorded data are shown in Figure 5.14, which can be identified with the theoretical expectations visualized in Fig. 5.6. For estimating the maximal displacement expected to occur in the actual experiment, the accuracy of the methods to build and implement the microscope objective setups can be used (Chapter 6). For the transverse displacement, the relative angle of the ODT beam with respect to the objective's optical axis is essential. This angle can be set with a precision of $< 0.1°$, which translates into a maximal misalignment of $\lesssim 20\,\mu\mathrm{m}$. Therefore, it can be expected that no aberrations will be induced by the objective caused by a transverse shift. Furthermore, the additional displacement caused by the thermal distribution of the atom is only in the order of a few hundred nm (Subsec. 2.2.3) and can hence be neglected.

Tilt of Glass Plate

As mentioned before, the glass window of the vacuum chamber is included in the design of the objective in which the window's surface normal is assumed to be colinear with the optical axis. The manufacturer guarantees a diffraction-limited operation as long as the objective is well aligned to the

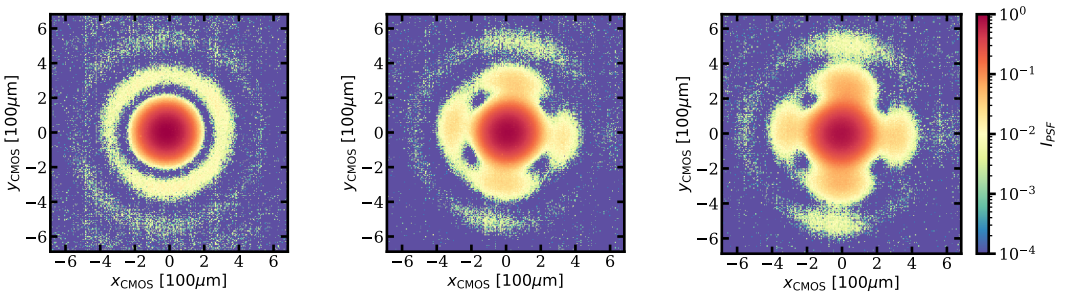

(a) $\Delta x = 0.0\,\mathrm{mm}$, $c_{22} = -0.0004$. (b) $\Delta x = 0.3\,\mathrm{mm}$, $c_{22} = -0.0511$. (c) $\Delta x = 0.36\,\mathrm{mm}$, $c_{22} = -0.0771$.

Figure 5.14.: Example images for different transverse displacements. The strength of the astigmatic aberration increases with increasing misalignment Δx, which is indicated by the expansion coefficient c_{22} (astigmatism 45°) in units of λ.

vacuum window within the range of only $\pm 0.1°$, making this alignment critical for the achievable optical performance. Its influence on the wave aberrations is tested by tilting the glass plate, which represents the vacuum window (Fig. 5.9), and subsequently analyzing the recorded PSFs. The resulting dependencies of the individual aberration types on the tilt angle ϕ are shown in Figure 5.15 with the main contribution given by the coma term. Up to an angle of $\sim 0.45°$, the measured Strehl ratio stays above the threshold for diffraction-limited performance. Surprisingly the design allows for much larger misalignments than stated by the manufacturer. For larger tilts, also other aberrations slightly increase, reaching moderate values always smaller than $\sim \lambda/30$ within the test range. Example images are depicted in Figure 5.16, which again are in good correspondence to the theoretical expectations (Fig. 5.6). The alignment precision of the microscope objective relative to the surface normal of the vacuum glass window is better than $0.02°$ (Subsec. 6.2.2). For such small misalignments, the amount of induced aberrations will not influence the expected optical performance of the microscope objective.

5.3.3. Results for Self Made Fiber Collimator

The apodization effects described in Subsec. 5.2.2 lead to an inhomogeneous illuminated pupil, which influences the results of the characterization measurements. However, the level at which these effects disturb the reconstruction process depends on the numerical aperture of the optical system under test. Therefore, it is necessary to correctly include the pupil apodizations for the characterization of the objective with a NA of 0.5, whereas for the homemade fiber collimator, only minor deviations compared to the results presented in [98] are expected. For completeness, the most important findings are restated in the following.
In the case of optimal alignment, the fitted Strehl ratio reaches a value of $0.9921^{+0.0079}_{-0.0100}$, indicating a nearly perfect system, which introduces only minor aberrations. The numerical aperture was found to be 0.1873 ± 0.0004, which is in excellent agreement with the expected value, considering the hard physical aperture of the mechanical mount on the one side, and the predictions of the optical design software Zemax[5] used to design the lens system (Subsec. 6.1.4) on the other side. One of the leading requirements on the fiber collimator design is large tolerances against misalignments, on the one hand,

[5]Zemax OpticStudio 15.5.

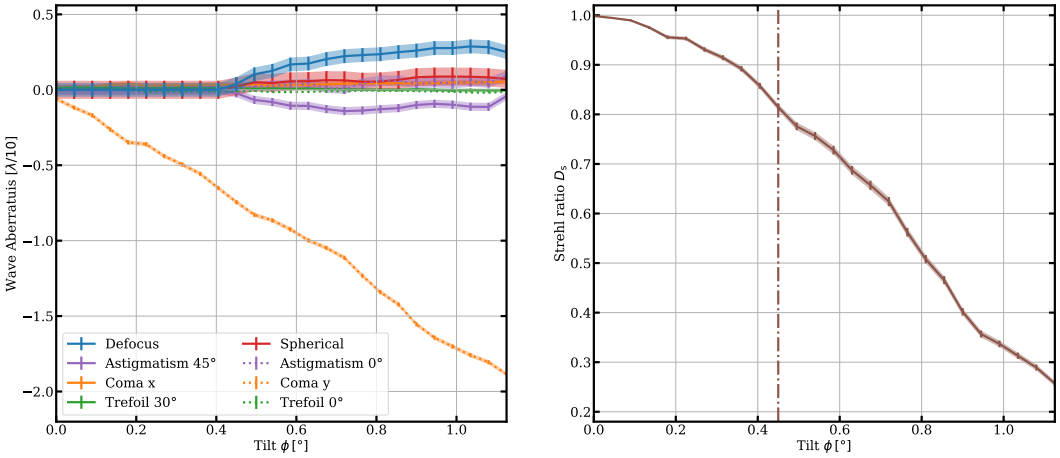

(a) Wave aberrations.

(b) Strehl ratio.

Figure 5.15.: Wave aberrations (a) and Strehl ratio (b) in dependence of different tilt angles. The coma term represents the main contribution to the wavefront expansion in Zernike polynomials for a relative tilt of the glass plate and the objective. The Strehl ratios are extracted directly from the images recorded by the CMOS camera yielding an expected diffraction-limited performance for misalignments smaller than $\phi = 0.45°$ (dashed line).

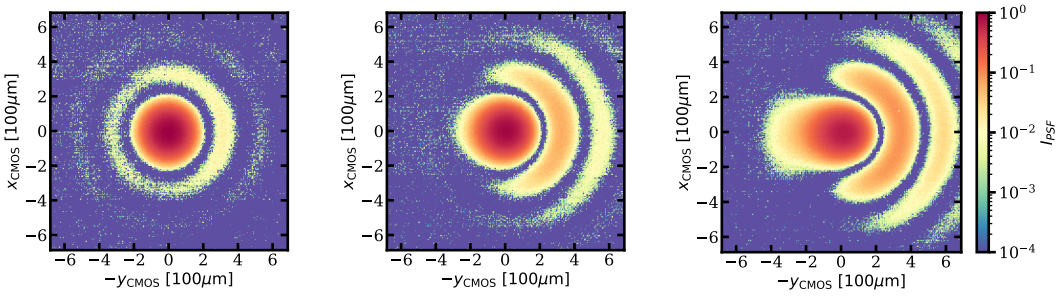

(a) $\phi = 0.0°$, $c_{3-1} = -0.0069$.

(b) $\phi = 0.315°$, $c_{3-1} = -0.0508$.

(c) $\phi = 0.63°$, $c_{3-1} = -0.0991$.

Figure 5.16.: Example images for different tilt angles. The strength of the coma term increases with increasing misalignment ϕ, which is indicated by the expansion coefficient c_{3-1} (coma y) in units of λ. For better comparison to the theoretical expectations of Fig. 5.6, the axes are adjusted accordingly.

of the complete system with respect to the fiber tip and, on the other hand, of the individual elements relative to each other. This robustness reflects itself in the characterization measurements yielding a diffraction-limited operation up to a transverse displacement of the lens system of $\sim 0.71\,\mathrm{mm}$ with the main contribution to wave aberrations given by the astigmatism term, in analogy to the measurements performed at the objective. Moreover, for axial displacements as for tilts of the collimator relative to the optical axis, the system was found to be diffraction-limited over the entire measurement range $\Delta z \in [0\,\mu\mathrm{m}, 8.2\,\mu\mathrm{m}]$, respectively $\phi \in [0^\circ, 1.2^\circ]$. The obtained Strehl ratios, $D_{s,axial} > 0.92$, respectively $D_{s,tilt} > 0.98$, are well above the critical value of $D_s \gtrsim 0.81$. These measurements show that the physical realization of the homemade fiber collimator is well suited to be used in the microscope objective setup without reducing the quality of the collected light mode.

6. High-NA Objective for Efficient Single Photon Coupling

This chapter will discuss details about the new high-NA microscope objectives, which were built, aligned and implemented in both traps during the scope of this work. The importance of the microscope objective for the experiment was mentioned several times before as it is involved in all major parts of the experimental sequence. For instance, the trapping of a single atom is enabled by focusing the optical dipole trap beam and analyzing the collected fluorescence photons (Subsec. 2.2), the achievable entanglement rate highly depends on the efficient single photon coupling into a single-mode fiber (Chapter 4), and the fast atomic state readout relies on the tight focusing of the ionization laser (Subsec. 2.4.2). For all of these tasks, precise alignment of the microscope objective setup, which matches the requirements for a diffraction-limited operation, and the usage of suitable high-quality optical components are needed to guarantee optimal performance. Furthermore, the increased collection-and-coupling efficiency of the new objectives constitutes a substantial improvement of the experiment, which allowed for the realization of long-distance atom-photon entanglement over a distance of $20\,\mathrm{km}$ [79] presented in the next chapter.
In the following, the individual elements used in the microscope objective setups are described, and experimental techniques and tools for an accurate alignment and implementation are introduced. In particular, this includes the design and assembly of the homemade fiber collimator for the collection optics of Lab 2. At the end of this chapter, an overview of the improvements compared to the old objectives [52] is given.

6.1. Optical Setup

Both microscope objective setups are conceptual of identical structure and only differ in some of the individual components used. Therefore, for the following parts of this chapter, it is sufficient to present one of the setups and only, when necessary, mention the differences. The setups are built on separate breadboards such that they can be aligned and optimized completely independent of the experiment. Once implemented, the setups are planned to be used for several years without the need for substantial realignments, which would require their removal. Therefore, to achieve this long-term stability, (opto)mechanical components (including the separate breadboard, optical mounts, spacers, screws, etc.) made out of non-magnetic stainless steel are used whenever possible, providing low thermal expansion hysteresis for moderate temperature fluctuations. At the same time, this reduces the possible disturbing influence of magnetic fields on the atomic state (Subsec. 2.5.1).
Figure 6.1 depicts a schematic overview of the system. The new high-NA objective provides a diffraction-limited photon collection up to a NA of 0.5 at a wavelength of $780\,\mathrm{nm}$. With a focal length of $10\,\mathrm{mm}$ and a working distance of $14\,\mathrm{mm}$, it is designed to be placed outside the vacuum chamber by incorporating the $3.5\,\mathrm{mm}$ thick window of the glass cell into its design. All other optical elements, e.g. fiber collimators, mirrors and dichroic mirrors, are needed to shape, guide, combine, and split the optical beam paths of different wavelengths in order to allow the objective to fulfill its tasks. The components can be divided into three categories. The collection optics to couple light

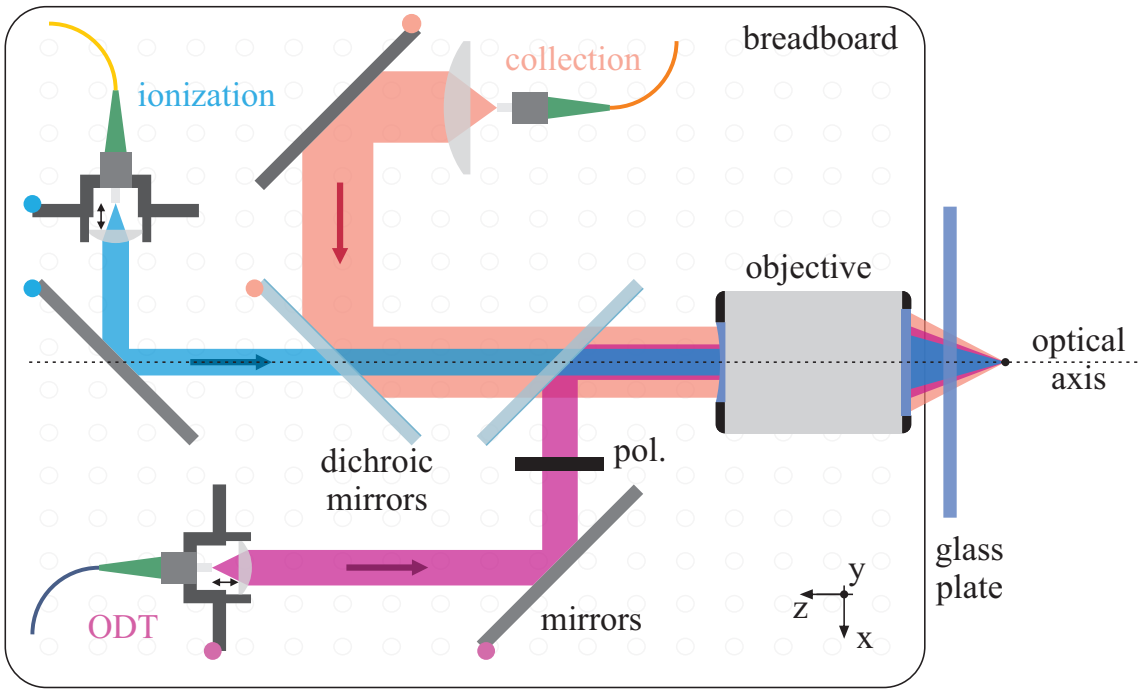

Figure 6.1.: Overview of a microscope objective setup mounted on a separate breadboard. The beam paths of the collection optics (red), the optical dipole trap (magenta) and the ionization (blue) are superimposed by two dichroic mirrors. Once aligned to the optical axis, the beam of the collection optics is used as a reference for the others. The necessary degrees of freedom for the alignment are provided by optomechanical precision mounts and the adjustable collimator lenses of the ODT and ionization. The mounts used for the alignment are marked with a dot in the color of the respective beam. During the alignment of the setup, the window of the vacuum glass cell is accounted for by placing a suitable glass plate of correct thickness and material after the objective.

emitted by the atom at a wavelength of 780 nm into a single-mode fiber, the optics to provide the trapping potential for the ODT at a wavelength of 849.5 nm for Lab 1 (857 nm for Lab 2) and the optics to focus the ionization pulse for the fast atomic state readout at a wavelength of 450 nm for Lab 1 (473 nm for Lab 2). For all of these applications, it is crucial that the foci of the collection optics and the ionization laser coincide with the atom position given by the focus of the ODT beam. This is one of the main alignment requirements to achieve optimal performance, e.g. an efficient photon coupling (Chapter 4).

Two dichroic mirrors superimpose the different beam paths. The first[1], 1″ in diameter, reflects the fluorescence collection and transmits the ionization laser. The second[2], 2″ in diameter, reflects the dipole trap and transmits the ionization laser and the fluorescence collection. The coatings of the dichroic mirrors should preserve the polarization of the transmitted and reflected light to a high degree for two reasons. First, the fidelity of the entangled atom-photon state depends on the indistinguishability of s- and p-polarized light in the sense that the probability of detecting either of them must be equal. This

[1]Laseroptik B-14776: HT450-473nm HR780nm/45° phase optimized
[2]Laseroptik B-14777: HT450-473nm+780nm HR845-865nm/45° phase optimized

indistinguishability cannot be ensured in the case of polarization-dependent dichroic mirrors. Therefore, the coatings are specially designed and optimized to be independent of the polarization under the incident angle of 45°. In [97], this was verified by measuring the reflectivities and transmissivities to be equal better than 99.9%. Second, circular polarization components in the optical dipole trap light lead to decoherence of the atomic state, as discussed in Subsec. 2.5.2. To avoid this, a polarizer in the beam path of the ODT defines the polarization to be perfectly linear before the reflection at the dichroic mirror. Hence, in order to preserve the linear polarization, the relative phase of s- and p-polarized components must be vanishingly small, in addition to the aforementioned equal reflectivity and transmissivity, which was also verified in [97].
In the following, the separate beam paths, their optical components, and the key properties influencing the performance of the objective will be discussed in more detail.

6.1.1. Collection Optics Beam Path

For the alignment of the objective setup, laser light at $780\,\mathrm{nm}$ is sent backwards through the collection optics, and the corresponding focal point indicates the position of optimal photon collection. According to the objective's design, the best performance with a minimum amount of induced aberrations is expected in the case of a collimated incident beam. Consequently, the fiber collimator is set such that the light emitted from the fiber is collimated, and the respective Gaussian waist defines the fiber mode size according to Eqn. 4.40. This mode size is a central parameter in the calculations of Chapter 4, determining the photon coupling efficiency and is therefore of great importance. However, finding a suitable collimator off-the-shelf with a focal length producing a Gaussian beam of the correct size is a non-trivial task.
For the microscope objective setup built for the trap of Lab 1, two commercially available fiber couplers were tested. The first one[3] is based on a monochromatic lens design with a focal length of $50\,\mathrm{mm}$, resulting in a collimated waist of $4.35\,\mathrm{mm}$, close to the theoretical optimum listed in Table 4.2. However, a qualitative characterization of the beam revealed severe aberrations induced by this collimator, which would significantly reduce the expected coupling efficiency [97]. The second one[4] is based on an air-spaced spherical lens design with a focal length of $40\,\mathrm{mm}$, resulting in a mode size of $3.6\,\mathrm{mm}$, which is further away from the theoretical optimum, yielding an estimated reduction in coupling efficiency of about 3% (Subsec. 4.4.1). A qualitative characterization of this collimator did not show any signs of induced aberrations [97]. Note, the quantitative method to characterize optics introduced in Chapter 5 was not developed at that time. The idea of the qualitative characterization used instead is as follows: Aberrations of the system are imprinted as a phase term onto the electric field of the collimated beam. With increasing distance to the optical system, these aberrations will manifest themselves as a deformation of the intensity distribution, which can be measured via optical beam profiling. Furthermore, theoretical predictions of the expected distributions can be calculated by solving diffraction integrals that include the aberrated phase term. Finally, comparing measured and predicted intensity profiles allows for a qualitative estimation of the induced aberrations. A mathematical formulation of this method can be found in [97, 98].
Due to the lack of commercially available alternatives, a fiber collimator that matches the requirements of an optimal mode size without introducing considerable aberrations (Subsec. 5.3.3) has been designed and built for the microscope objective setup of Lab 2 (Subsec. 6.1.4). The homemade fiber collimator is based on an air-spaced spherical lens design with a focal length of $49\,\mathrm{mm}$, which results in a collimated Gaussian waist of $4.2\,\mathrm{mm}$, yielding an expected coupling efficiency practically equal

[3] Schäfter-Kirchhoff 60FC-L-4-M50L-02
[4] Thorlabs C40FC-B

to the theoretical optimum (Table 4.2).
The microscope objective can be connected with the photonic detection setup via a standard single-mode optical patch cable attached to the fiber collimator. For the system in Lab 2, an AR-coated fiber minimizes the reflection losses at the air-glass boundary. The same fiber is used to apply the alignment light in reversed direction. For the optimization itself, the necessary degrees of freedom to align the incident beam to the optical axis are provided by the optomechanical precision mounts of the mirror and the dichroic mirror. Note, the same kind of mounts are also used for the optics of the other beam paths. For the setup of Lab 1, the accurate overlap of the three beams turned out to be a difficult task due to the lack of precision of the alignment screws[5] (100 turns per inch (TPI)). Hence, mounts with much finer threads[6] ($254\,\mathrm{TPI}$) were used for the setup of Lab 2.

6.1.2. Optical Dipole Trap Beam Path

The dipole trap beam is guided to the objective setup via a polarization-maintaining optical patch cable. The Gaussian beam of the ODT is generated by a commercially available fiber collimator, which for the setup of Lab 1 contains a bi-aspheric lens[7] with a focal length of $18.4\,\mathrm{mm}$, resulting in an incoming beam waist of $1.28\,\mathrm{mm}$. For the setup of Lab 2 the fiber collimator contains an achromat[8] with a focal length of $15\,\mathrm{mm}$, yielding a beam waist of $1.15\,\mathrm{mm}$. The polarization of the ODT has a substantial influence on the coherence of the atomic state (Subsec. 2.5), and hence special measures are taken to define and preserve the polarization to be perfectly linear. First, a linear polarizer[9] defines the polarization of the incoming beam, yielding a measured extinction ratio better than $1/1300000$ [97]. Second, the custom-designed coating of the dichroic mirror introduces a vanishing relative phase between s- and p- components and by this does not alter the polarization. Moreover, the order to superimposed the different beam paths on the optical axis is chosen such that the ODT light is only reflected once after passing the polarizer. Since polarization is better preserved in reflection than in transmission, this reduces the possibility of deviations. As the last point, the polarizer is aligned to the polarization eigenaxis of the system using a fine-adjustable rotation mount[10] with a resolution of $< 0.003°$ to minimize the effect of residual birefringence.
Furthermore, the decoherence effect caused by the strongly focused optical dipole trap (Subsec. 2.5.2) depends on the intensity distribution in the focal region. It has been shown that an asymmetry in the beam profile will lead to a non-perfect rephasing of the atomic state, which in turn causes stronger decoherence of the atomic state [53]. Therefore, the fiber collimator and the other optical components must yield a symmetric beam profile. For the setup of Lab 1, the incoming beam is measured to be slightly asymmetric. Fortunately, this asymmetry was not observed in the focal region, and thus one expects no negative influence on the coherence of the atomic state. In order to reduce the strength of the decoherence effect, a fiber collimator leading to a less tight trapping potential for the atom is chosen for the setup of Lab 2.
To optimize the photon coupling efficiency (Chapter 4), the beam paths of the ODT and the collection optics must overlap. Since the fluorescence collection has the highest demands on the optical performance of the objective, the beam path of the collection optics is used as a reference. Hence, the ODT beam is aligned to the reference using the optomechanical precision mounts of the fiber collimator

[5] Radiant Dyes MDI-HSS-2-3025-M6 with 100TPI
[6] Newport SU100TW-F2K with 254TPI screws (AJS254-0.5K-NL)
[7] Schäfter-Kirchhoff 60-FC-4-A18-02
[8] Schäfter-Kirchhoff 60FC-4-M15-37
[9] CODIXX colorPol® IR 1100 BC4 CW02
[10] Radiant Dyes RD-RMP-1´´

and the mirror, and the adjustable collimator lens, which together provide the necessary degrees of freedom. Contrary to the collection optics for which a collimated beam is required by the objective's design, the ODT needs a convergent beam instead. More details about the alignment are presented in Section 6.2.
A constant intensity of the ODT is necessary for the experiment for several reasons. For example, a varying ODT intensity would lead to a change in the induced light shift and thus influences, e.g. the optical cooling of the atom or the atomic state preparation (see Subsec. 2.2). Also, the rephasing of the atomic state due to the strongly focused ODT beam depends on the trap intensity, and hence a high-fidelity state readout is only possible after a multiple of a full transverse trap frequency (Subsec 2.5.3). In order to keep the trap depth constant, the ODT intensity is continuously monitored by focusing the small fraction of light ($T \sim 10^{-4}$) transmitted by the highly reflective dichroic mirror onto an amplified fast photodiode, which is part of a feedback loop that stabilizes the intensity.

6.1.3. Ionization Beam Path

The fiber collimator used in the ionization beam path for the setup of Lab 1 contains a bi-aspheric lens[11] with a focal length of $18.4\,\mathrm{mm}$, resulting in a waist of $1.85\,\mathrm{mm}$. For the setup of Lab 2, a monochromatic collimator[12] with a smaller focal length of $12\,\mathrm{mm}$ is used, yielding a beam waist of $1.14\,\mathrm{mm}$. A smaller focal length of the collimator translates into a larger focus size at the position of the atom, which loosens the demands on the beam alignment. Analog to the ODT, the beam can be aligned to the reference by adjusting the collimator lens and the optomechanical precision mounts. The design of the objective requires a divergent incoming beam to achieve a longitudinal overlap of the foci. As long as the intensity of the ionization beam at the atom position is sufficiently high to ensure a fast atomic state readout, no special actions regarding the beam quality, polarization preservation and transmission losses are necessary.

6.1.4. Homemade Fiber Collimator

As discussed in Chapter 4, the coupling efficiency of light emitted by the atom into a single-mode fiber is determined by the mode overlap of the fiber mode and the emitted photon mode, whereby the latter gets modified by the collection optics. Therefore, using a suitable fiber collimator, for which both modes match best, is crucial for optimal coupling. The essential parameter determining the fiber mode size in the calculations of Chapter 4 is the waist of a corresponding collimated Gaussian beam w_{coll}, which is related to the focal length of the collimator f_{coll} and the fiber's numerical aperture NA_{fiber} according to Eqn. 4.40. This parameterization of the fiber mode size allows for an experimentally easily accessible value specifying the potential of a fiber collimator for the photon coupling process. Furthermore, calculations of this coupling process allow identifying an optimal mode size under certain assumptions, e.g. the geometry of the optical dipole trap and the thermal density distribution of the atom. However, it was not possible to find a commercially available fiber collimator fulfilling the requirements for optimal coupling, leading to the development of a homemade collimator. At the time the homemade collimator was designed, the best estimate for the desired Gaussian waist was $w_{design} = 4.2\,\mathrm{mm}$ (Subsec. 4.4.1). However, this value turned out to be slightly larger than the optimum of Table 4.2 due to a difference in actual and assumed trap geometry and thermal density distribution. In the following, general considerations and the design of the homemade collimator are presented.

[11] Schäfter-Kirchhoff 60-FC-4-A18-01
[12] Schäfter Kirchhoff 60FC-4-M12-33

Design Considerations Some general requirements on the collimator have to be specified, which will afterwards be elaborated in more detail:

- a collimated beam waist of $w_{design} = 4.2\,\mathrm{mm}$ should be generated
- an aberration-free diffraction limited-operation at a wavelength of $780\,\mathrm{nm}$ has to be guaranteed
- the design must be tolerant against misalignment
- only standard high-quality lenses are used
- the system can be assembled in a compact mount.

The optical design software Zemax was used to design and optimize the collimator. The system contains four air-spaced spherical lenses, which allow for a nearly perfect compensation of wave aberrations while ensuring a high tolerance against misalignment of the complete system with respect to the fiber, as well as of the individual elements relative to each other (Subsec. 5.3.3). Especially the latter one enables an easy assembly of the lens system into a compact mount (see below). Another advantage of a spherical lens design is the availability of optical components[13] with excellent surface quality (scratch-dig 10-5) and small wavefront distortion ($< \lambda/10$) for a relatively low price. In general, the performance of an optical system can be improved by using aspheric surfaces since additional degrees of freedom are introduced to the system, which can be used to correct for aberrations. Moreover, allowing for aspheric surfaces in the design can also help to reduce the number of lenses needed without diminishing the achievable performance. However, despite these potential improvements, aspheric lenses of comparable optical quality are more difficult to fabricate and consequently more expensive and, in addition, harder to assemble [110]. Hence, to keep the costs low and the design simple, a conventional solely spherical solution was chosen. Furthermore, all lenses have an anti-reflection coating which reduces the residual reflectivity to $< 0.3\%$ per surface within the wavelength range of $700 - 900\,\mathrm{nm}$.

Optimization For the optimization the design software considers light emitted from a point source, which the lens system should collimate. In the optimal case, the optical path difference for all rays originating from the point emitter vanishes, resulting in a flat wavefront in the image plane. However, this idealized situation cannot be achieved for any actual lens design, and hence the root mean square value of the optical path difference is considered the primary contributor to the merit function. Note, this is the same criterion used to characterize the optical systems in Chapter 5. In order to obtain a system, which generates the desired mode size, its focal length has to match with the numerical aperture of the fiber. Therefore, the NA of several fibers were measured, all yielding similar results with an average value of $\mathrm{NA}_{fiber} \approx 0.085$ and the respective focal length of the collimator is $f_{coll} \approx 49\,\mathrm{mm}$. The system is designed for a numerical aperture of 0.17, conservatively chosen twice as large as the measured fiber NA. By this, in the actual experiment, it can be assumed that also the low-intensity outer regions of the photon mode will be imaged-diffraction limited onto the fiber core with an effectively used NA of the fiber collimator of 0.10[14]. The parameters varied by the optimization algorithm are the radii of curvature of the lenses, their thicknesses and the distance between the individual elements. In addition, two different glass types are used, SCHOTT N-BK7® ($n = 1.51$) and SCHOTT N-SF6 ($n = 1.79$) [130], which enable the optimization software to find a better solution. They are

[13] The lenses are manufactured by Lens-Optics.
[14] The photon mode is truncated by the exit pupil of the objective with a radius of $5\,\mathrm{mm}$.

	Surface No.	Radius of curvature	Distance to next surface	Material
fiber	0	infinity	$10.000\,\mathrm{mm}$	air
lens 1	1	infinity	$2.000\,\mathrm{mm}$	N-BK7
	2	$225.183\,\mathrm{mm}$	$17.630\,\mathrm{mm}$	air
lens 2	3	$-30.760\,\mathrm{mm}$	$10.000\,\mathrm{mm}$	N-SF6
	4	$-25.350\,\mathrm{mm}$	$10.660\,\mathrm{mm}$	air
lens 3	5	$-102.090\,\mathrm{mm}$	$6.280\,\mathrm{mm}$	N-SF6
	6	$-57.540\,\mathrm{mm}$	$0.530\,\mathrm{mm}$	air
lens 4	7	$635.000\,\mathrm{mm}$	$2.900\,\mathrm{mm}$	N-BK7
	8	$-122.460\,\mathrm{mm}$	-	air

Table 6.1.: Surface parameters of the homemade fiber collimator lens design.

chosen such that the difference of their refractive indices is large but still provide an excellent transmittance at the design wavelength.
Without any constraints or boundary conditions, the optimization algorithm will use the full parameter range, which typically leads to unpractical (e.g. extremely large systems) or even unphysical solutions (e.g. overlapping lens surfaces). Therefore, it is necessary to limit the accessible parameter range. For instance, the system is restricted to a total length of $\leq 60\,\mathrm{mm}$ to keep it compact, the edge and center thickness of the lenses must be $\geq 2\,\mathrm{mm}$ to prevent them from becoming too fragile, the radii of curvature are bounded such that the manufacturer can still produce them and the focal length is fixed to $49\,\mathrm{mm}$ to generate the desired mode size. While all of these and more are needed to end up with a suitable system eventually, they also limit the achievable result.
As mentioned above, the design should also incorporate an insensitivity against misalignment and robustness against manufacturing tolerances. Therefore, a set of tolerances is defined, which conservatively considers the uncertainties given by the lens producer and the in-house workshop that fabricates the mechanical lens mount. Tolerances accounting for a transverse displacement or tilt of a lens are specified to $\pm 0.2\,\mathrm{mm}$ and $\pm 1^\circ$, tolerances for the decenter and the tilt of an individual surface are $\pm 0.2\,\mathrm{mm}$ and $\pm 0.2^\circ$, and tolerances of the thickness of a lens or the distance between two lenses are $\pm 0.2\,\mathrm{mm}$. Generally, tolerancing leads to deviations from the unperturbed design and thus degrades the optical performance. Nevertheless, tolerancing is indispensable for a physical realization of the designed system to guarantee the required specifications. In an iterative process, all radii of curvature of the optimized system were exchanged for those offered by the manufacturer as standard to reduce the costs of the lens system. For each step of this process, the radius least sensitive to a variation is replaced by the one fitting best. Finally, the iteration step is completed by a re-optimization of the design with the remaining free parameters. The resulting lens design is depicted in Figure 6.2a, and the corresponding surface parameters are listed in Table 6.1.

Mechanical Mount and Adjustment The four lenses have a diameter of $21.4\,\mathrm{mm}$ and are mounted in an aluminum tube of $21.4\,\mathrm{mm}$ inner and $30.5\,\mathrm{mm}$ outer diameter, which is fully compatible with standard tube optics. A schematic drawing of the mechanical mount is shown in Figure 6.2b. Thin aluminum spacer rings maintain the correct distance between the lenses. They are fabricated such that they have exactly the same radius of curvature as the respective lens surface to minimize the induced stress. Furthermore, the curvature of the spacers supports the lenses to center themselves

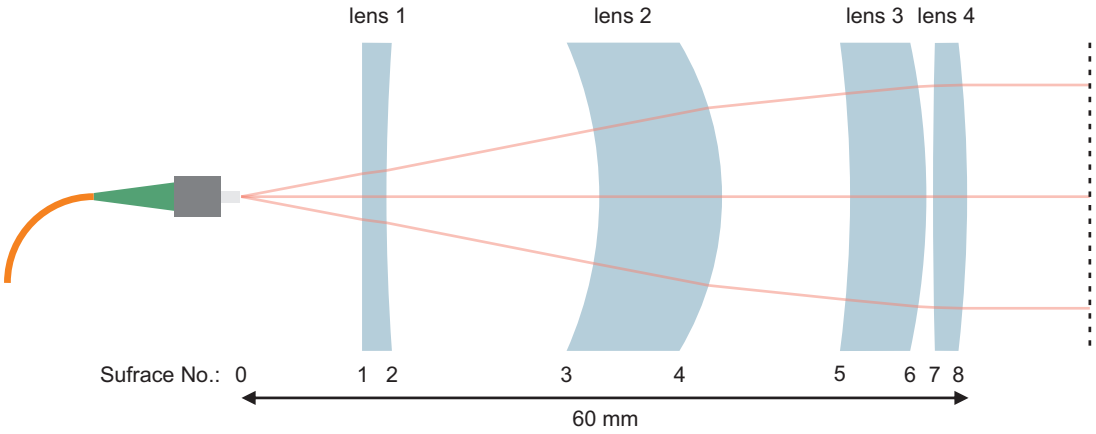

(a) Layout of the lens system. The individual surfaces of the four spherical lenses are labeled from 1 to 8, and the fiber end with 0. The total length of the design is 60 mm.

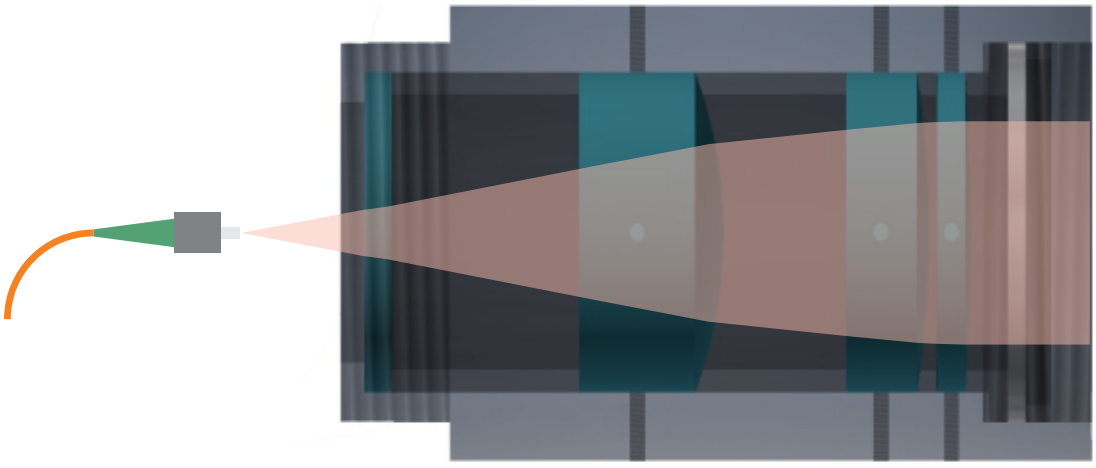

(b) Mechanical mount of the lens system. The four lenses (green) are mounted in a custom made aluminum lens tube, in which spacer rings determine the distances between the lenses. The stacked system is held together by a threaded retainer ring, which presses against a plastic O-ring (white). A fine transverse adjustment of the lenses is possible by sets of alignment screws. The outer dimensions and threads of the aluminum barrel are chosen to be fully compatible with standard tube optics.

Figure 6.2.: Schematic of the homemade fiber collimator with (a) the layout of the lens system and (b) the mechanical lens mount.

once pressure is applied. The stacked system is held in place by a threaded retainer ring, which presses against a plastic O-ring to compensate for some unevenness of the mounts and thus further reduce the induced stress. This is important since mechanical stress induced in the lens material will lead to changes of the refractive index inside the glass that in turn causes wavefront aberrations, which limit the possible performance[15]. The mechanical hard aperture of the system is given by the inner diameter of the last spacer ring (after lens 4) of $18.4\,\mathrm{mm}$ and with that defines the maximal possible numerical aperture of 0.1877, which is in excellent agreement with the value obtained from the characterization measurement (Subsec. 5.3.3). In case the auto-centering of the spherical lenses, favored by the spacer rings, is not good enough, a fine adjustment can be applied by shifting three out of the four lenses with a set of alignment screws. However, due to the successful tolerancing of the lens design, a plug and play assembly of the lens system is possible without the need for any fine adjustment. Once mounted, the complete lens system needs to be aligned relative to the optical fiber. This alignment is realized by a commercially available beam guiding system[16], which provides a complete set of degrees of freedom (x,y,z-translation and θ_x,θ_y tip and tilt) needed for an optimal adjustment. The alignment itself is performed by analyzing beam profiling pictures and iteratively adjusting the lens system to minimize the amount of aberration induced deformations of the intensity profile [98]. Several fixing screws can ultimately lock an optimized position.

6.2. Alignment and Implementation of the Optical Setup

The microscope objective setup is aligned and optimized in a different laboratory independently of the main experiment. This is inevitable for a precise overlap of the three beam paths, especially in the focal region, which would require measurements inside the vacuum. On the other hand, it also has the advantage that the main experiment can still be used while the new objective setup is assembled. Therefore, the new systems are built in a modular form on separate breadboards, which requires planning for the design and dimensions of the components, their positioning and orientation on the breadboard, and the correct beam height to enable an easy implementation into the main experiment. Optimal performance of the objective can only be achieved when all alignment requirements are fulfilled. These involve the alignment of the incident beams and the vacuum glass cell with regard to the optical axis, as well as the precise overlap of the three focused beams both in position and angle. This section describes the methods for the alignment of the optical setup and presents the obtained overlap of the beams.

6.2.1. Incident Beam Alignment

The design of the objective is tolerant against small angular misalignment of the incident beam relative to the optical axis. According to the specification given by the manufacturer, a diffraction-limited photon collection can be expected within an angular field of view of $1.37°$. However, the characterization of the objective presented in Chapter 5 yields a considerably larger value of $2.03°$. This requirement can easily be fulfilled by applying a simple method depicted in Fig. 6.3, which is based on overlapping the incident beam with its back reflection by mounting a mirror perpendicular to the optical axis to the objective's front side. The alignment procedure comprises the following steps:
First, all relevant optics are mounted such that the correct beam height is obtained once the micro-

[15] These stress-induced aberrations were also observed during the characterization measurements of the homemade collimator once the retainer ring was tightened too firmly.
[16] Radiant Dyes RD-BGS-TS

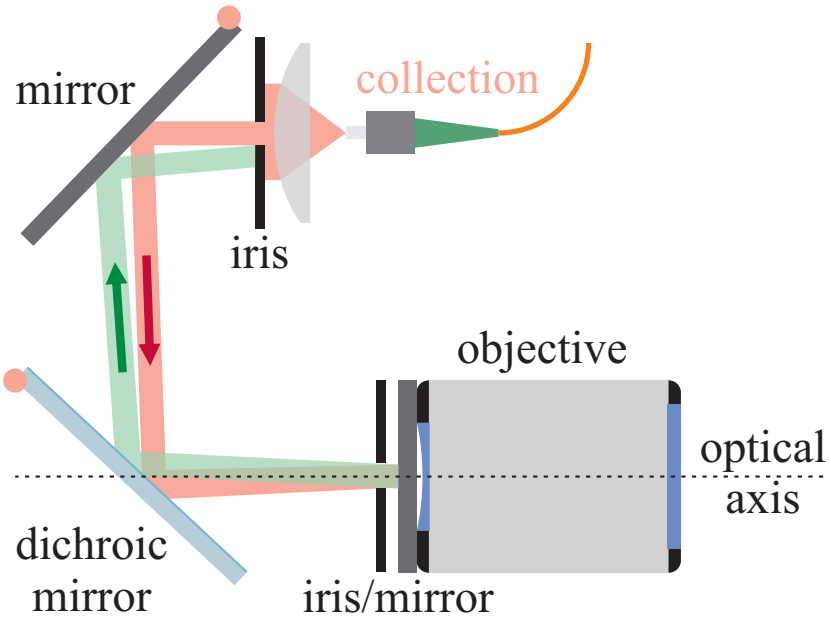

Figure 6.3.: Schematic of the incident beam alignment. The idea of the alignment technique is based on overlapping the incident beam with its back reflection by inserting a mirror perpendicular to the optical axis. Together with an iris, which marks the center of the objective, this construction only leads to overlapping beams in case of an optimal alignment along the optical axis.

scope objective setup is implemented in the main experiment. Next, an iris and a mirror are mounted at the front side of the objective, with the surface normal of the mirror being parallel to the optical axis. The latter is ensured by a suitable reference surface of the objective's mount. The combination of iris and mirror uniquely defines both the center and the optical axis of the objective since any angular misalignment of the incident beam would lead to a non-overlapping reflected beam. Moreover, another iris, marking the center position of the reference beam, is mounted at the front side of the collection optics fiber collimator. With that, an optimal alignment can be achieved by adjusting the optomechanical precision mounts till the back-reflected beam is centered at the iris of the collimator. From the mechanical tolerances and the precision of the measurement, it can be estimated that this alignment method yields an accuracy of $< 0.1°$.

6.2.2. Glass Cell Alignment

Another critical requirement that needs to be fulfilled is the alignment of the objective relative to the window of the vacuum glass cell. The manufacturer guarantees a diffraction-limited performance up to a relative angle of $0.1°$, whereas the characterization measurements of Chapter 5 yielded a significantly higher tolerance against misalignment with a maximum relative angle of $0.45°$. The method used to reach the necessary alignment precision is based on analyzing an interference pattern formed by the back-reflected light of the objective and the glass window. In order to observe the interference pattern, it is necessary to separate the back reflections from the incident light. This is realized with a combination of a beam splitter and a compensation plate, which allows imaging the

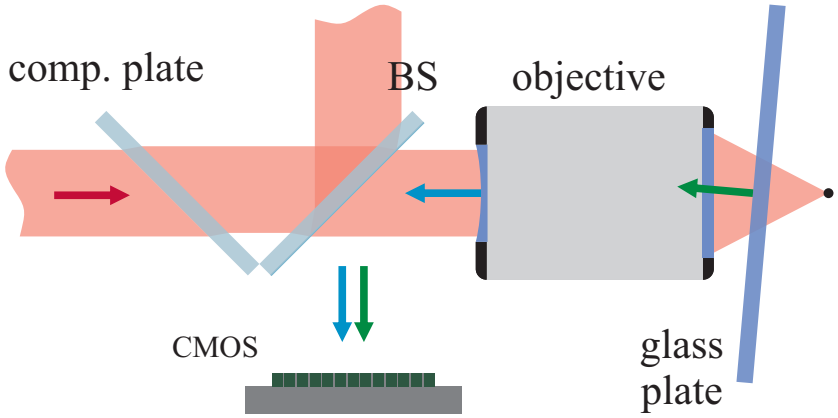

Figure 6.4.: Schematic of the technique used to align the relative angle of objective and glass cell. The back-reflected light of the objective and the glass plate is first separated from the incident light by a BS and afterwards imaged onto a CMOS camera. The resulting interference pattern can be analyzed, which provides a clear and direct feedback signal to adjust the relative angle.

interference pattern onto a CMOS camera without impairing the incident beam alignment (Figure 6.4). Note, the usage of a cube BS would eliminate the necessity of the compensation plate. However, it is not possible to observe the interference pattern with this configuration due to an overexposure of the camera caused by internal reflections of the collimated incident beam inside the cube BS. The internal reflections have several orders of magnitude higher intensities than the generally divergent back reflections of the objective and the glass window. Typical interference patterns for different alignments are depicted in Figure 6.5. The observed patterns consist of several overlayed concentric ring structures, which are unaffected by the alignment. This is because these structures are caused by the interference of reflexes solely originating from either the objective or the glass window. In case of a non-perfect alignment, an additional superimposed stripe pattern can be observed (Figure 6.5), which originates from the interference of reflections from both the objective and the glass window. The orientation, spacing and width of these stripes depend on the actual relative alignment, with the tendency to become broader and further separated the better the alignment is. With that, this method provides a clear and direct feedback signal, which can easily be used to adjust the relative angle. In the situation the objective setup was first built, the glass plate was mounted on an optomechanical mount providing the possibility to adjust the relative angle in a controlled way, which allowed a specification of the accuracy of this method to be better than $0.02°$ [97]. However, for implementing the system into the experiment, a simple adjustment of the relative angle is not possible anymore. Therefore, different tools are used to tilt the complete objective breadboard relative to the vacuum glass cell (Subsec. 6.2.4).

6.2.3. Overlap of the Focused Beams

For all applications of the objective, it is indispensable that the focused beams of the collection optics, the optical dipole trap and the ionization overlap to a high level of accuracy both in position and angle. Therefore, the beam of the collection optics is used as a reference to which the other beams are aligned. Two reasons support this choice. First, the objective's design requires a collimated beam for

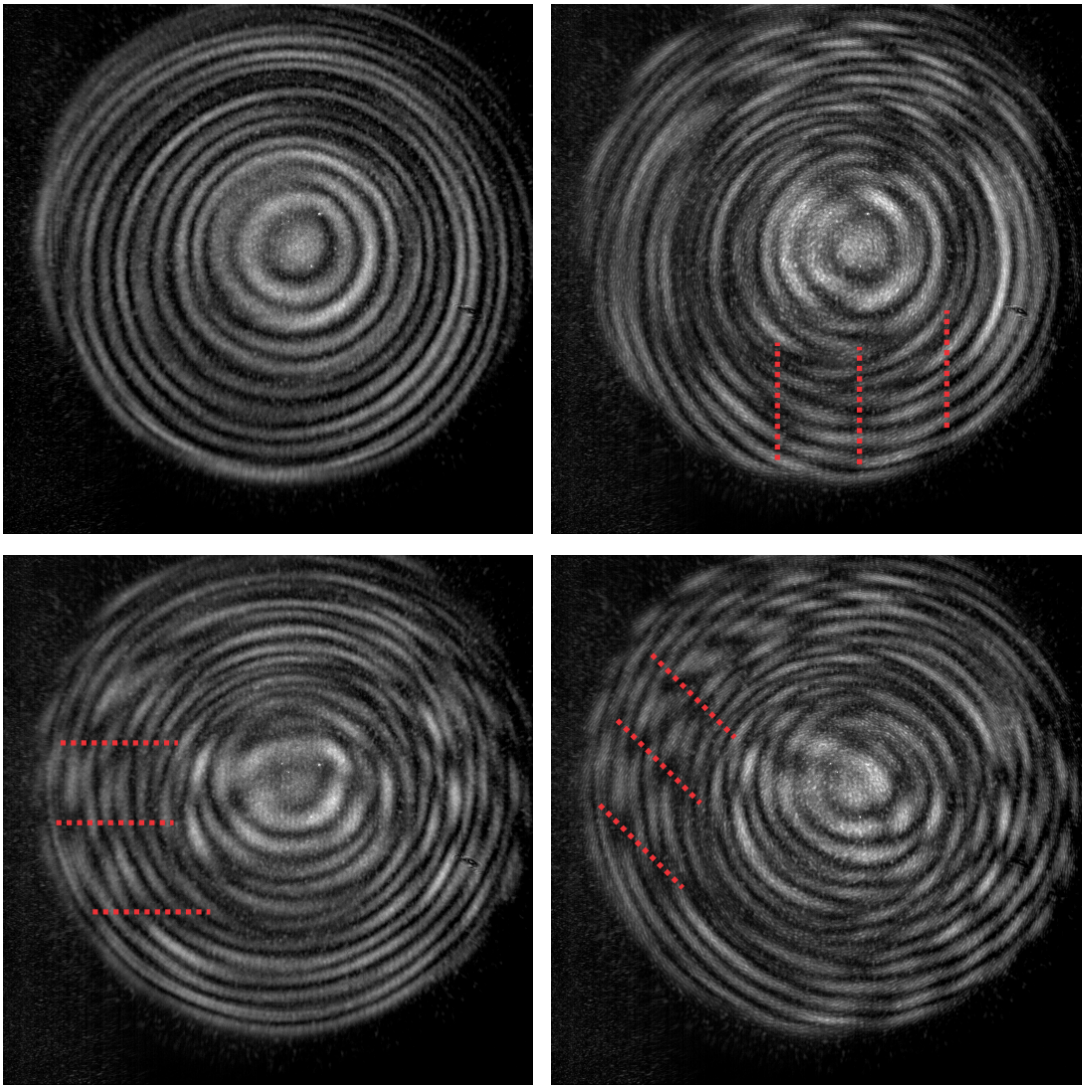

Figure 6.5.: Interference pattern formed by back-reflected light of the objective and the glass window. The upper-left picture shows the situation of a perfectly aligned setup where only concentric ring structures are present. In case of misalignment, an additional strip pattern appears whose orientation, spacing and width depend on the actual relative alignment. The upper-right picture shows a tilt around the vertical axis, the lower-left around the horizontal axis and the lower-right around a diagonal axis.

an optimal photon collection, which constitutes a definite alignment criterion, whereas the ODT and ionization need a convergent, respectively a divergent beam. Second, the collection and coupling of the emitted light have the highest demands on the performance of the objective. Hence, the incident beam of the collection optics should be aligned directly via the method described in Subsec. 6.2.1. A good starting point for the final optimization is obtained by aligning the glass plate with respect to the optical axis using the method described in Subsec. 6.2.2 and overlapping the incident beams of the ODT and the ionization with the reference via optical beam profiling at two locations in a distance of $\sim 0.3\,\mathrm{m}$, respectively $\sim 9\,\mathrm{m}$. This pre-alignment already allows for a good overlap in the transverse direction and angle. However, the necessary accuracy needed for the experiment cannot be achieved. Moreover, no information about the longitudinal alignment is obtained, which requires measuring the beam profiles around the focal region. For the beam parameters and the objective used, typical sizes of the generated foci are on the order of $\sim 1\,\mu\mathrm{m}$. Since these foci are smaller than a single pixel size of available cameras, the simple measurement via beam profiling is not applicable anymore. A standard technique often used to acquire information about the beam's longitudinal and transverse intensity profile is the knife-edge method [131, 132], which also can be applied for small focal sizes.

Knife-edge Method In this technique, a sharp edge of opaque material is gradually moved perpendicular to the propagation direction of the investigated beam, and the total transmitted power is measured with a photodiode as a function of the edge position. The recorded signal can subsequently be analyzed to reconstruct the beam parameters, e.g. the focal position and waist. Following the approach described in [133], the 'knife-edge' is realized by a sharp-edged gold structure coated directly on the surface of the measuring PD. This approach provides the advantage that the transmitted power can immediately be measured without any additional optics to focus the transmitted light onto the PD. Especially for small beam waists with correspondingly large divergent angles this becomes important. Assuming a Gaussian beam, as it is in our situation, the integrated power as a function of the edge coordinates x_e and z is given by:

$$P\left(x_e, z\right) = P_0 + \frac{2}{\pi w^2\left(z\right)} \int_{-\infty}^{+\infty} \mathrm{dy} \int_{-\infty}^{x_e} \mathrm{dx}\, e^{-\frac{2\left(x^2+y^2\right)}{w^2(z)}} = P_0 + P_1 \cdot \mathrm{erf}\left(\frac{\sqrt{2}\left(x_e - x_0\right)}{w\left(z\right)}\right). \quad (6.1)$$

Here P_0 is the background power, P_1 is the laser power, x_0 is the transverse position of the focus, and $w\left(z\right)$ is the beam waist at a certain longitudinal position z. Analogously, the transverse focus positions y_0 along the y-directions can be determined. This function can now be used to determine the four parameters $\left(P_0, P_1, x_0, w\left(z\right)\right)$ by a least-squares fit of the measured data. Further, the focal beam waist w_0 and longitudinal position z_0 can be extracted by repeatedly applying this procedure for several z-positions and fitting the following function:

$$w\left(z\right) = w_0 \sqrt{1 + \left(\frac{M^2\left(z - z_0\right)}{z_R}\right)^2}, \quad (6.2)$$

with the Rayleigh length $z_R = {}^{\pi w_0^2}/_{\lambda}$ and the beam quality parameter M^2 quantifying the deviation of the measured beam profile from a Gaussian form [134].

A three-axis translation stage fully automatizes the knife-edge measurement with a minimum step size of $20\,\mathrm{nm}$. With this, the beam parameters, as well as the position and orientation of the three beams relative to each other, can be determined. By adjusting the optomechanical precision mounts and the collimator lenses of the ODT and ionization optics, their relative alignment to the reference (the collection beam) can iteratively be improved. The final result of the optimization is depicted in

Fig. 6.6 exemplary for the focus measurements along the x-direction. Similar results are obtained for measurements along the y-direction, except for a considerable longitudinal separation of 1.8 µm between the horizontal and vertical focal point of the ODT for setup of Lab 2. It is important to mention that no suitable laser at the correct wavelength of $473\,\mathrm{nm}$ was available for aligning the ionization beam for the setup of Lab 2. Hence, a $450\,\mathrm{nm}$ laser was used instead, which causes a chromatic focal shift of $13\,\mu\mathrm{m}$ according to a Zemax simulation. This shift is accounted for by an intentionally introduced offset between the focal positions of the ionization and the ODT. The limit of the achievable alignment precision was tested while optimizing the setup of Lab 1. Here a longitudinal overlap with an accuracy of $200\,\mathrm{nm}$ and a transverse overlap with an accuracy of $50\,\mathrm{nm}$ were obtained. However, due to mechanical stress during transport of the objective setups to the laboratories of the main experiment, the alignment will drift away from this optimized situation and small re-adjustments after the implementation into the experiment are necessary. Therefore, the setup of Lab 2 is only optimized to the level at which a signal from the atom for re-optimization can be obtained.

6.2.4. Implementation into the Main Experiment

Once the new microscope objective setup is sufficiently well aligned, it can be moved to the laboratory of the main experiment, where it is incorporated into the trap setup by exchanging the new and the old optical system. This delicate procedure must be performed with great care to avoid damages to the systems and minimize possible misalignment. However, due to all the precautions that have been taken during the construction of the objective setup (e.g. dimensioning and positioning of the individual components, accounting for the correct beam height and the construction on a separate breadboard), the implementation turned out to be rather easy. Nevertheless, the new system has to be aligned with respect to the trap setup to match the requirements for optimal performance. To align the relative angle between the objective and the vacuum glass cell with the method described in Subsec. 6.2.2, it is necessary to either tilt the complete vacuum setup, which turns out to be difficult and impractical, or the objective along with all components mounted on the separate breadboard. For the two systems, different approaches needed to be realized to account for the geometry of the respective traps. For the system of Lab 1, the vertical tilt alignment is implemented by using fine-adjustable screws attached to each corner of the breadboard, which press against the optical table to lift the system accordingly. For the system of Lab 2, the breadboard is mounted on height-adjustable feet, which provide the possibility of an accurate alignment. The horizontal tilt alignment and positioning of the objective are realized for both setups by fine-threaded screws attached to the optical table next to the breadboard. After successful integration, atoms can be trapped, and fluorescence light is collected. This signal is used for a re-adjustment of the transverse overlap of the ODT and the collection optics. With that, the system is ready for complete optimization of all experimental parameters to achieve an optimal performance of the entire single atom trap.

6.3. Performance of the New Objectives

In Chapter 4 of this thesis, the collection-and-coupling efficiency of light emitted by the atom is calculated. A perfectly aligned and aberration-free system is assumed for these calculations, which is well justified regarding the alignment measurements of Section 6.2 and the optical characterization presented in Chapter 5. An exception to this is the significant separation of 1.8 µm measured between the horizontal and vertical focal points of the ODT of Lab 2. Moreover, the alignment of the systems

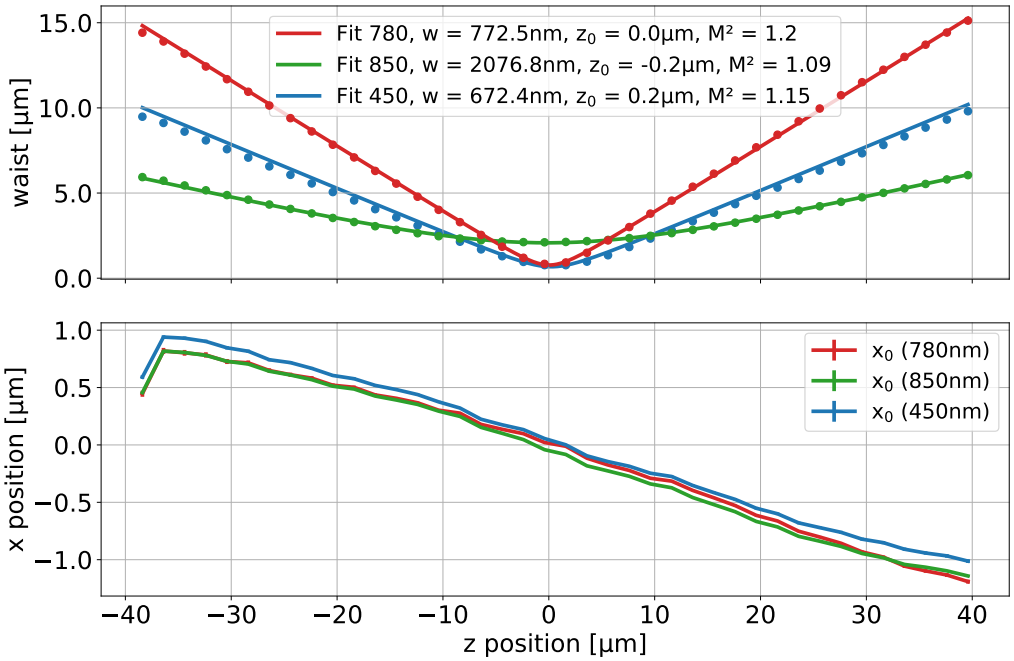

(a) Optimized alignment for the setup of Lab 1.

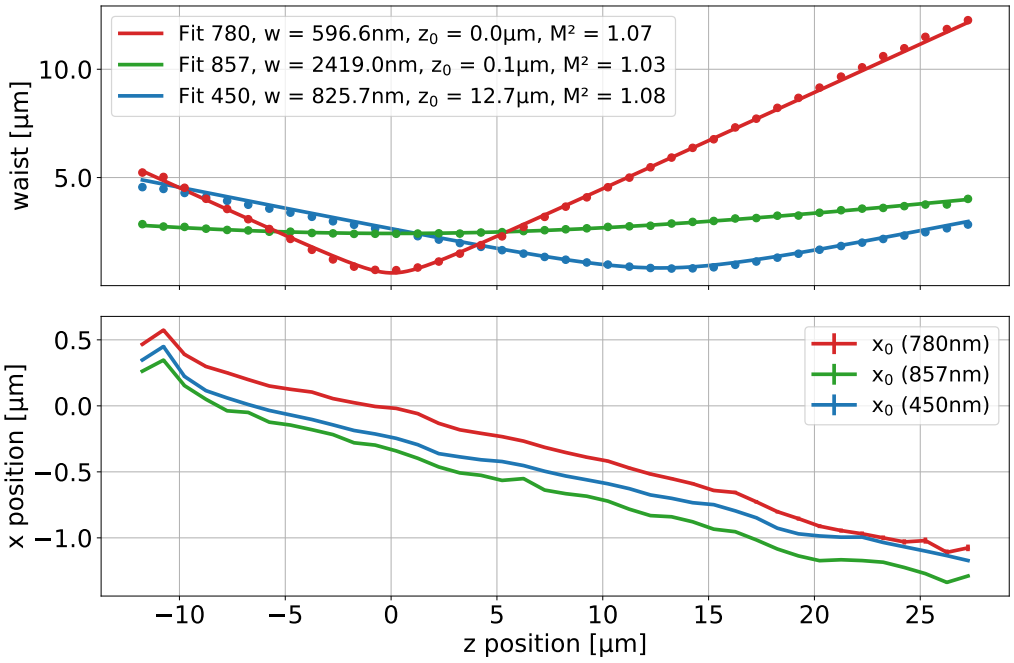

(b) Optimized alignment for the setup of Lab 2.

Figure 6.6.: Final focus measurements of the optimized setup of Lab 1 (a) and the setup of Lab 2 (b). The top view shows the beam waist $w\,(z)$ measured for several longitudinal displacements with the respective least-squares fits for all three beams. The bottom view shows the corresponding x-position of the focus.

can only be guaranteed up to the accuracy of the methods used. Therefore, calculations considering these misalignments and the residual wave aberrations were performed to determine their influence on the expected collection-and-coupling efficiency. As a result, for the setup of Lab 1, a reduction of $\sim$2.5% relative to the value of an ideal system listed in Table 4.4 is expected, whereof the contribution of the residual aberrations is only 0.1%. On the other hand, the estimation for Lab 2 yields a significantly larger reduction of $\sim$7.6% due to the separation of the horizontal and vertical focal points of the ODT.

Once the new objective is integrated and aligned according to the atom trap, it is possible to characterize its performance by measuring the success probability to detect a single photon emitted by the atom after an excitation attempt. The initial atomic state preparation via optical pumping must be optimized for this measurement to yield meaningful results. Figure 6.7 depicts the success probability in dependence of the applied optical power of the excitation laser for both laboratories in comparison to typical values measured with the old objectives. Clearly, the success probabilities obtained with the new objectives are multiple times higher than the old values, yielding a maximum probability of $P_{S_1,max} = 6.70\,‰$ for the setup of Lab 1, and $P_{S_2,max} = 8.61\,‰$ for the setup of Lab 2. The latter is remarkably close to the expected theoretical value of 8.87‰, considering the corrections stated in the first paragraph of this section. However, a comparison with the old measurements only provides limited informational value and needs to be carefully interpreted since the final number of the success probability depends on several parameters (Eqn. 2.33), which might be different and not exactly known for the respective measurement. For instance, a huge uncertainty originates from the single-photon detector efficiencies, which differ from one device to another ($\eta_{det} \simeq 0.45...0.65$) and vary over time due to misalignment or degradation, especially for the detector setup in Lab 1, where the APDs needed to be exchanged frequently due to malfunctioning. The corresponding success probabilities obtained over the years lie within the range of 0.2%...0.38%. Further unknowns for the measurements with the old objectives are the actual alignment of the trap system and the correct settings for an optimal state preparation, whereas these are known to be optimized for the measurements performed with the new objectives shown in Fig. 6.7. With this in mind, the following estimates for improvement factors of the success probability are reasonable: $\gtrsim 2.5$ for the system in Lab 1, and $\gtrsim 3.5$ for Lab 2. As already elaborated in Subsec. 4.4.3, the difference in the improvement factors can partially be attributed to the experimental realization of the systems. However, it cannot account for all.

The atom-atom entanglement rate is another important number indicating the performance of the complete system. After implementing the new objectives, a rate of 8.36 events/min was measured, representing a significant improvement to older values, even compared to the previous best result of 2.13 events/min obtained during the Bell test of 2016 [21]. Analog to the performance estimation via the local success probabilities, a meaningful comparison for the remote entanglement rate is only possible considering the experimental uncertainties mentioned above. An additional factor influencing the obtainable event rate is the duty cycle of the experiment given by the probability of both atoms being simultaneously in the synchronized excitation sequence. Typical event rates observed with the old objectives during the Bell measurements of 2016 and measurements performed in 2018 varied within the range of $\sim$ 1...2 events/min with a mean value of $\sim$ 1.5 events/min. A comparison of this number and the value reached with the new objectives yield an estimated improvement factor of $\sim$ 5.6. Another option to compare the remote entanglement rate independently of the duty cycle is by means of the atom-atom entanglement efficiency given by the ratio of the number of detected coincidences with the number of excitation tries. For the old objectives, values in the range of $0.85...1.10$ ppm were measured, yielding an average of 0.95 ppm. The corresponding value for the new setup is 6.15 ppm, which leads to an estimated improvement factor of $\sim$ 6.5. Furthermore, the remote entan-

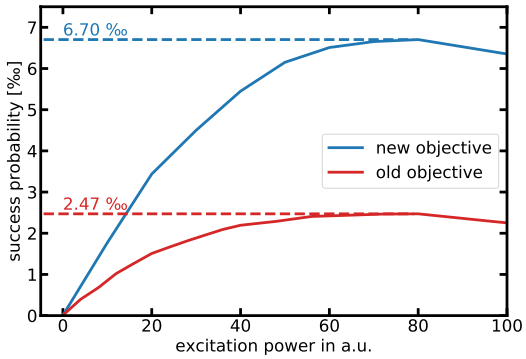

(a) Success probability for the setup of Lab 1.

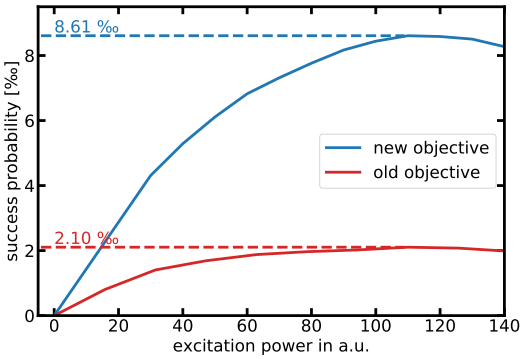

(b) Success probability for the setup of Lab 2.

Figure 6.7.: Local success probability in dependence of the optical power of the excitation laser, (a) for the setup of Lab 1 and (b) for the setup of Lab 2. The measured probabilities for the new systems (blue) clearly indicate a significant improvement relative to the values obtained with the old systems (red).

glement efficiency is also related to the product of the local success probabilities via a simple relation: $P_{AA} = \frac{1}{2} \cdot P_{S_1} \cdot P_{S_2}$, where the factor of $\frac{1}{2}$ accounts for the fact that the BSM can identify only 2 out of 4 Bell states. Inserting typical values measured for the new systems with the single-photon detectors of the BSM ($P_{S_1} \approx 4.8\,‰$ and $P_{S_2} \approx 2.8\,‰$[17]) yield an entanglement efficiency of $6.72\,\mathrm{ppm}$, which is in good agreement with the measured value.

[17]These numbers already include the reduced excitation efficiency of $\eta_{exc} = 0.8$ used to increase the entanglement fidelity (Subsec. 2.7.2), the fiber transmission loss of 0.5 for the photon emitted by the atom in Lab 2, and the difference in the average detector efficiencies $\eta_{det_2} = 1.15\eta_{det_1}$ for the setup of Lab 1 and Lab 2 (Subsec. 4.4.3).

7. Long-Distance Distribution of Atom-Photon Entanglement at Telecom Wavelength

An essential resource for future scalable quantum networks is the ability to share and distribute entanglement between separated quantum memories that are interconnected via photonic channels. There exist a wide variety of suitable systems that allow for the exchange of quantum information via a light-matter interface, e.g. trapped neutral atoms [32, 33], trapped ions [34, 35], atomic ensembles [36–38], color centers in diamond [39, 40], quantum dots [41, 42] or rare-earth ions in solids [43, 44]. However, their optical transitions are typically located outside the low-loss transmission bands of telecom fibers. Therefore, it is indispensable for entanglement distribution over long distances to convert photons from their emission wavelength (visible/NIR range) to the telecom regime, e.g. by employing quantum frequency conversion (QFC). These concepts have been applied to some of the platforms mentioned above, demonstrating entanglement between a telecom photon and the respective quantum node [45, 46, 135–139].
In our case, the quantum memory is formed by a trapped ^{87}Rb atom coherently connected to the telecom regime via QFC, preserving the non-classical property of atom-photon entanglement. Thereby, the realization of this scheme can be divided into the following steps: First, the atomic spin state is entangled with the polarization state of a single photon emitted by the atom in a spontaneous decay process (Subsec. 2.3.2). Second, the following polarization-preserving QFC of the 780 nm photon to the telecom S-band at 1522 nm allows transmitting over fiber links several kilometers in length. Finally, atom-photon state correlations in two bases are measured to analyze and verify the entanglement. This experiment was conducted in collaboration with Matthias Bock, Tobias Bauer and Christoph Becher from Saarland University, who provided the QFC system.

7.1. Setup, Methods and Experimental Procedure

Figure 7.1 depicts an overview of the experimental setup, which is schematically divided into three blocks - a single atom trap (left), a quantum frequency conversion system (middle), and a polarization analysis setup (right). The atom trap in Lab 1 equipped with the custom made high-NA objective is used for the presented experiments. The frequency converter utilizes the $\chi^{(2)}$-nonlinear process of difference frequency generation (DFG) in a periodically poled lithium niobate (PPLN) waveguide[1] to convert the collected single photons from their emission wavelength at 780 nm to the telecom S-band at 1522 nm via DFG with a high-power cw pump laser at 1600 nm. The polarization analyzer contains all optical elements to set an arbitrary measurement basis and two superconducting nanowire single-photon detectors (SNSPDs) to detect the converted telecom photons. In addition, several spectral filtering stages are implemented to isolate the single photon from the intense pump laser and efficiently suppress noise mainly caused by anti-Stokes Raman scattering of pump light in the waveguide. In the

[1] NTT Electronics

following, more details about the individual components of the setup and their functioning will be explained.

7.1.1. Single Atom Trap

The basics of the atom trap and its operation are presented in Chapter 2, yet a few adjustments are made for realizing the QFC experiment.

Experimental Control

The experimental control of a single atom trap experiment is, in principle, similar to the two atom-trap case described in Subsec. 2.6.3, without the need for additional synchronization with a second laboratory. Correspondingly, a PC is used to set most of the experimental parameters like laser powers and frequencies, monitor and control the loading sequence, and store the measurement data registered in a TDC device. The control unit is used to switch between different parts of the experimental sequence (e.g. entanglement generation and atomic state readout), set the correct timings for the different lasers, define acceptance time windows and send marker signals to the TDC for the data analysis. The QFC system is equipped with its own control electronics and therefore operates independently of the atom trap.

Experimental Sequence

In previous measurements performed, the same detectors monitoring the fluorescence counts for the loading sequence are also used for the polarization analysis of the single photon. For the conversion setup, this is not possible anymore since the narrow-band spectral filtering of the converted photons to 27 MHz (see below) is optimized to suppress all frequencies except the one of the single photon. Hence, it also filters out the fluorescence photons due to a 6.8 GHz frequency difference between the cooling transition and the transition used for the entanglement generation. Therefore, a micro-electromechanical systems (MEMS) fiber optic switch[2] guides the fluorescence photons during the loading procedure to a Si-based APD or, once an atom is successfully trapped, the single photons to the frequency converter (Fig. 7.1). After a single atom is loaded, atom-photon entanglement is generated by repeatably applying pulses for the atomic state preparation and excitation (Subsec. 2.3.2) until the SNSPDs detect a telecom photon within a certain acceptance time window. After 40 preparation-excitation cycles, the sequence is paused for a $350\,\mu$s cooling period to counteract the heating from photon scattering. This additional cooling period increases the lifetime of the atom while at the same time decreases decoherence effects influenced by its thermal motion (Subsec. 2.5). Eventually, the atomic state is read out via the state selective ionization scheme introduced in Subsection 2.4.2, in which the atomic measurement basis is defined by the polarization of the readout laser, which can be set with a motorized half-wave plate (HWP). Since the atomic state readout is also based on the collection of fluorescence photons, the MEMS switch now guides the scattered photons to the single APD. A schematic of the experimental sequence is shown in Fig. 7.2. The time between consecutive excitation pulses is mainly determined by the photon transmission time through the optical fiber, which in the case of a 20 km long fiber is around $102\,\mu$s. By including $3\,\mu$s for each state preparation and $350\,\mu$s for the cooling period, an effective excitation rate of 8.9 kHz is obtained.

[2] Sercalo Microtechnology SN-2x2-4

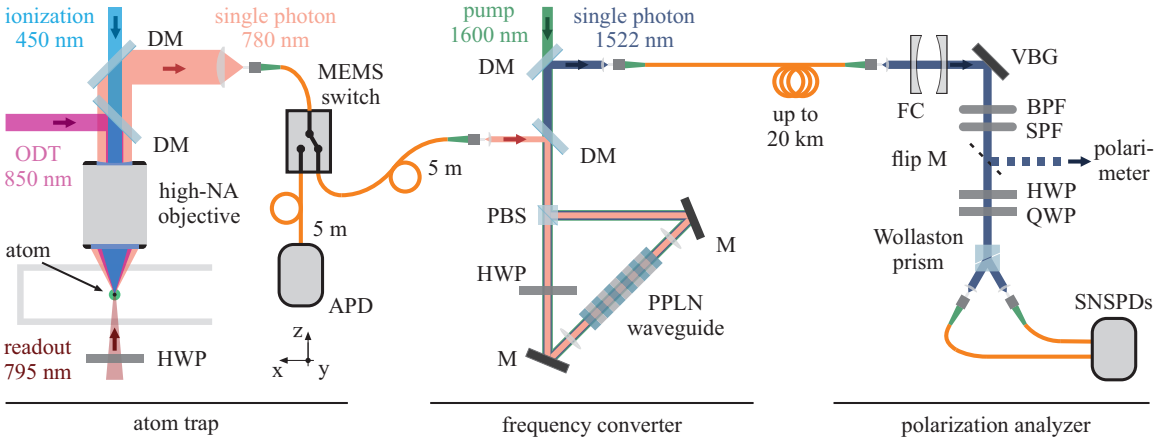

Figure 7.1.: Overview of the quantum frequency conversion setup [79]. A single trapped neutral ^{87}Rb atom, used as quantum memory, is confined and laser-cooled in a tightly focused optical dipole trap. The same high-NA objective that focuses the trapping beam also efficiently collects and couples photons emitted by the atom into a single-mode fiber. Atom-photon entanglement is generated in the spontaneous decay from the excited state $5^2P_{3/2}\,|F'=0, m_{F'}=0\rangle$. The MEMS switch is used to either guide fluorescence photons to an APD during loading of the trap and the atomic state readout or to the quantum frequency converter when testing the entanglement generation. The polarization-preserving QFC is realized in a Sagnac-type configuration, using a PPLN waveguide, which enables conversion of the 780 nm single photon to the telecom S-band at 1522 nm via difference frequency generation with a 1600 nm pump laser. The frequency converter is connected to the polarization analysis setup via an up to 20 km long optical fiber. The single photon is spectrally filtered by a dichroic mirror (DM), a Fabry-Perot filter cavity (FC), a volume Bragg grating (VBG), a bandpass filter (BPF), and two short pass filters (SPF) to suppress noise induced by the conversion process. The telecom photon is analyzed by setting the analysis basis with a combination of a half-wave plate (HWP) and a quarter-wave plate (QWP) before splitting its polarization components by a Wollaston prism into two paths, each of them fiber coupled to an SNSPD detector. Compensating unitary rotations of the polarization state caused by fibers and optical components placed between the atom and the detection setup is realized by analyzing classical reference light reflected with a flip mirror onto a polarimeter.

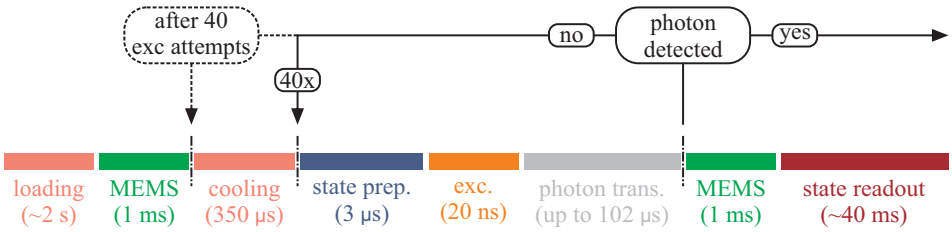

Figure 7.2.: Experimental sequence of the conversion experiment: After an atom is successfully loaded into the trap (light red), the CU is triggered to run the entanglement generation sequence, and the MEMS switch guides the photons to the SNSPDs. Here, up to 40 cycles of state preparation (blue), excitation (orange) and a fiber-length-depending waiting time (grey) are followed by a 350 μs long cooling period. Once a single photon is detected, the atomic state readout (red) is initiated, and the MEMS switch guides the scattered fluorescence photons to the single APD.

Atomic State Coherence

As discussed in Subsection 2.5, the atomic spin state is susceptible to external decoherence effects in the time between the emission of the single photon and the atomic state readout. With increasing fiber lengths, this becomes more and more critical due to longer photon transmission times. As can be seen from the time-resolved measurements of the atomic spin states in Fig. 2.12, residual magnetic field noise (~ milligauss) unable to be compensated by the active magnetic field stabilization reduces the achievable contrast by approximately 10 % after a delay of 100 μs. Therefore, to prolong the coherence time up to several hundreds of microseconds, a 42 mG magnetic guiding field is applied along the y-axis, which suppresses the field noise and fluctuations for the transverse directions. However, by these means, it is not possible to compensate for the position-dependent effective magnetic fields caused by the strongly focused optical dipole trap (Subsec. 2.5.2). Hence, this dephasing and rephasing mechanism remains the limiting contribution to the atomic state decoherence. Furthermore, it is crucial to match the period of the Larmor precession of the guiding field as well as the timing of the atomic state readout with the aforementioned periodic rephasing of the atomic state to maximize the readout fidelity.

7.1.2. Quantum Frequency Conversion System

The QFC system is built in a modular form on three standalone platforms, each of them coming with its own set of control electronics enabling an operation independent of the atom trap. In addition, this design allows for a relative easy relocation and integration of the QFC system into an existing quantum optics experiment. The different platforms are the pump system and the QFC device located in the same laboratory as the atom trap and a narrow-band spectral filtering stage that, together with the telecom polarization analyzer, is placed in a neighboring laboratory due to logistical reasons. The QFC system was provided to us within a collaboration with Saarland University. Hence, only the most important features of the system are targeted here, and for more details, the reader is referred to the supplementary material of [79].

Pump System

In the DFG process of the frequency conversion, a high-power pump laser is required that has a fixed and long-term stable frequency relative to the emission transition of the single photon ($5^2P_{3/2}, F' = 0 \rightarrow 5^2S_{1/2}, F = 1$). The latter is required because of the narrow-band spectral filtering applied to the converted photons to reduce the noise to the single photon level. The pump laser - a tunable, single-frequency diode laser[3] at 1600 nm - is indirectly locked relative to the emission transition via a transfer cavity lock. For this, the length of the transfer cavity is stabilized to another tunable single-frequency diode laser at 780 nm, which itself is locked by Doppler-free saturation spectroscopy to the desired emission transition. The necessary high optical pump power is generated by an Erbium-doped fiber amplifier (EDFA) with an output of around 1.2 W. Besides pumping the QFC, the pump laser light is also used to lock the filter cavity for the narrow spectral filtering (see below).

QFC Device

The frequency conversion utilizes different frequency generation in a temperature-stabilized optically nonlinear PPLN waveguide, which is part of a Sagnac interferometer constructed with a PBS, an HWP and two silver mirrors (Fig. 7.1). The intrinsic phase stability of this configuration lifts the technical necessity of an active path length stabilization needed in Mach-Zehnder-type configurations, e.g. [137]. Two dichroic mirrors are used, on the one hand, to overlap the photons collected by the objective with the strong pump field and, on the other hand, to separate the converted photons from the pump field.
It is essential that the QFC device preserves the polarization state of the incoming photon; however, the DFG process itself is intrinsically polarization dependent. Therefore, the Sagnac-type approach from [46] is adapted such that the combination of PBS and HWP ensures s-polarized light fields in the waveguide for all three wavelengths. Ideally, this should lead to identical conversion efficiencies for the s- and p-polarization components. Yet, due to small asymmetries and differences in the experimental realization, the observed efficiencies vary by a few per cent. Nevertheless, the optical power of the pump field can be adjusted separately for both of the interferometer paths, which allows fine-tuning of the individual conversion efficiencies. In addition, all optical elements were specially selected to increase the mode overlap in the waveguide, maximize transmissions, and optimize fiber couplings. Starting from the high internal conversion efficiency of 96.2%, an overall external device efficiency of 57% is obtained by accounting for all individual loss mechanisms, i.e. transmission through optical elements (82.6%), fiber coupling (87.8%), waveguide coupling (90.0%), and spectral filtering (90.7%).

Narrow-band Spectral Filtering

The experiment must be able to efficiently isolate the single photon from the strong pump field (~1.2 W optical power) as well as from pump-induced noise. While the dichroic mirror at the conversion device already separates most of the pump from the converted photon, several additional spectral filtering stages are required to remove the remains of the pump light and reduce the noise to the single-photon level. The main contribution to the noise of the QFC system originates from anti-Stokes Raman scattering of the pump light in the waveguide. A Fabry-Perot filter cavity with a finesse of 700 and a bandwidth of 27 MHz FWHM is used to minimize this broadband ASR noise in the vicinity of the target wavelength (Fig 7.1). The filter cavity features a double-resonance for the converted light

[3] Toptica Photonics DL pro

and the pump laser, whereby the latter one is used to stabilize the cavity length. This guarantees a high transmission of the emitted photons since the pump laser frequency is referenced to the single photon emission transition via the transfer cavity lock mentioned above. A volume Bragg grating (25 GHz FWHM) separates the transmitted light of the pump laser from the converted light. An additional stack of three broadband interference filters - a band-pass filter (center wavelength: 1535 nm; 30 nm FWHM) and two short-pass filters (1560 nm cut-off) - further reduces the residual noise level.

7.1.3. Polarization Analysis

The converted photon's polarization state is analyzed by using a half-wave plate, a quarter-wave plate, and a Wollaston prism, which splits the polarization components into two paths, each of them fiber-coupled to an SNSPD (Fig. 7.1). Both wave plates are motorized, which allows for conveniently setting an arbitrary photonic measurement basis. The quantum efficiencies and dark count rates for the utilized single-photon detectors yield values of 32% and 36%, and 70 cps and 53 cps, respectively. By tuning the bias current of the detectors, an optimized ratio of detector efficiency to dark count rate could be achieved. That resulted in the final configuration used in the experiment with detector efficiencies of 16% and 18% and dark count rates of 10 cps and 8 cps, respectively.
Right before the first element of the polarization analyzer, a flip mirror provides the possibility to reflect reference light to a home-built polarimeter. With that, possible rotations of the polarization state, which are caused by fibers and optical components between the atom and the detection setup, can be compensated by a manual polarization controller. A regularly automatized compensation of polarization rotations as it is realized for the two atom-trap experiments (Subsec. 2.6.3) is not required since the long fiber is kept on a spool in an air-conditioned environment.

7.1.4. Atom-Photon Correlations

The entanglement shared by the atom and the photon is verified and characterized by atom-photon state correlation measurements. For this, the polarization of the photon is measured in two mutually unbiased bases, i.e. $^{H}/_{V}$ and $^{+}/_{-}$, using the polarization analysis setup described in the preceding subsection. For each photon basis, the atomic analysis angle α (Eqn. 2.9) is rotated from 0° to 180° in steps of 22.5°, which projects the atomic state on the dark state of the respective readout polarization (Eqn. 2.11). The obtained measurement data represent the dark state population conditioned on the polarization of the photon. For an entangled atom-photon state, an oscillatory behavior is expected for all photonic basis settings (see Fig. 7.3 for the measured data), and its experimental observation indicates the presence of entanglement in the system. In order to quantify the quality of the entanglement, sinusoidal functions $A^{(\sin(2\cdot\alpha+\phi)+1)}/_{2}$ are fitted to the data, which allows extracting the peak-to-peak amplitude A of the individual atom-photon fringes. These amplitudes, or visibilities, typically get reduced by infidelities of the state readout as well as atomic state decoherence effects like magnetic field fluctuations and effective magnetic fields from the strongly focused ODT. Note that the measurements are affected differently by these decoherence effects depending on the photon polarization and the atomic analysis angle. For instance, due to the guiding field applied along the y-direction, magnetic field fluctuations along the x- and z-direction are suppressed, leaving the atomic state $|\uparrow\rangle_x$, prepared by the projection onto a V photon, almost unaffected (Subsec. 2.5). However, for all other photon projections, the respective atomic states can, at least partially, be influenced by magnetic y-fields and will hence suffer from decoherence. As described in Subsec. 2.5, the effective magnetic fields caused by the ODT are also oriented along the y-axis, and correspondingly, the accompanied dephasing of the atomic state will affect all photon fringe measurements except the one associated with a projected

V photon.
The fidelity of the experimentally measured atom-photon state with respect to the maximally entangled one $|\psi_{AP}\rangle$ of Eqn. B.1 can be estimated by modeling the state in the 2x3 space spanned by $|L\rangle$, $|R\rangle$ and $|\downarrow\rangle_z, |1,0\rangle, |\uparrow\rangle_z$. Under the assumption of an isotropic dephasing towards white noise in the 2x3 state space, the density matrix of the experimental state can be expressed as [140]

$$\hat{\rho} = \bar{V} |\psi_{AP}\rangle \langle\psi_{AP}| + \frac{1}{6}\left(1 - \bar{V}\right)\hat{1}, \tag{7.1}$$

with the average visibility $\bar{V}$ being the mean of the individual atom-photon fringe visibilities obtained from the sinusoidal fits. This modeling of the state is similar to the one in [140]. However, it is necessary to include the third spin state of the atomic spin-1 system $|1,0\rangle$, which can be populated, e.g. by magnetic fields not coinciding with the quantization axis. Furthermore, it is assumed that the results for the unmeasured $^{R}/_{L}$ basis are equal to the $+/-$ basis ones. While this assumption is not necessarily valid, it is well justified since all previously described decoherence effects affect the measurements of both bases in the same manner. By taking the above into account, a lower bound on the fidelity of the measured atom-photon state is given by

$$\mathcal{F} \geq \langle\psi_{AP}| \hat{\rho} |\psi_{AP}\rangle = \frac{1}{6} + \frac{5}{6}\bar{V}. \tag{7.2}$$

7.2. Measurement Results

In the course of the conversion experiment, atom-photon state correlation measurements were performed in four different experimental configurations, which will further be denoted with (R) and (I) - (III). The first measurement (R) serves as a reference for the expected performance of the atom trap without the conversion system. Here, the 5 m long single-mode fiber of the microscope objective is directly connected to the 780 nm BSM (Subsec. 2.6.2). In the other three measurements, the single photons were converted to telecom wavelength and transmitted to the polarization analyzer via optical fibers of different lengths: 50 m (I), 10 km (II), and 20 km (III). For a better comparison between the measurements, an additional delay of the atomic state readout of $51\,\mu$s, which corresponds to the photon transmission time of (II), is introduced for the measurements (R) and (I) to account for the reduction in fidelity caused by the decoherence of the atomic state. The observed atom-photon state correlations are shown in Fig. 7.3, and the corresponding results are summarized in Table 7.1.
Despite quite different success probabilities of detecting a photon after an excitation attempt, an entanglement rate of about 35 events/min is obtained for all measurements. The reason for this behavior stems from the applied atomic readout scheme, in which the atom gets ionized in approximately half of the cases, and reloading of the atom trap is required, which takes about 2 s. With the repetition rate of the entanglement generation of a few kHz (8.9 kHz for (III)) and success probabilities in the order of a few ‰ (0.26 ‰ for (III)), the atom gets ionized, and hence lost, in less than a second after loading. Therefore, the entanglement rate is limited by the reloading time of the atom trap, which is the same for all measured configurations. For the telecom measurements (I) - (III), more than 15000 photons were detected within measurement times of a few hours (13 h for (III)), and the resulting photon arrival time histograms are depicted in Fig. 7.3.
The signal-to-noise ratio (SNR) of the photon detection is another factor that limits the achievable state fidelity, especially for the conversion measurements (I) - (III). Here, the pump-induced noise of the QFC and detector dark counts significantly decrease the SNR compared to the reference case of (R). The SNR can be determined from the photon detection time histogram by comparing the number

of counts within a certain acceptance time window (indicated by dashed lines in Fig. 7.3) around the photon wavepacket to the average noise level after the wavepacket. By adjusting the time window, an optimized SNR can be obtained by post-selecting the events with respect to the photon arrival time. It was found that a time window of 50 ns yields the best trade-off between the number of remaining events (~66%) and the observed SNR (Table 7.1). Note, these results could only be obtained due to the exceptionally high external device conversion efficiency of $\eta_{dev} = 57\%$ and the increased photon collection efficiency of the new microscope objective with an improvement factor of ~2.5. For all measurements, the observed values correspond well to our expectations, which are based on the success probabilities to detect a photon after an excitation attempt of $P_S^{(I)} = 1.28\,‰$, $P_S^{(II)} = 0.22\,‰$, and $P_S^{(III)} = 0.17\,‰$ (obtained from the post-selected data), and independently measured noise and detector dark count rates (DCR) of $R_n \approx 677\,\mathrm{cps}$, and $R_{dcr}^{(I)} \approx 123\,\mathrm{cps}$, $R_{dcr}^{(II/III)} \approx 18\,\mathrm{cps}$, respectively. The limiting effect of the dark counts on the SNR becomes more and more important for increasing fiber lengths. Aiming to increase the SNR, the bias currents to operate the SNSPDs were changed after measurement (I) to reduce the detector dark counts for the measurements (II) and (III), which comes at the cost of reduced detector efficiencies by roughly a factor of 2. However, due to smaller success probabilities in (II) and (III), the SNR turned out to be lower. At this point, it is important to clarify that neither length-dependent absorption in optical fibers nor different detector efficiencies should lead to a significant change in the SNR since pump-induced noise photons are influenced in the same way as the converted single photons. The theoretically expected SNRs can now be calculated by determining the probability to detect a background photon in a time window of 50 ns:

$$\mathrm{SNR}_{\mathrm{theo}}^{(\mathrm{I})} = \frac{P_S^{(I)}}{50\,\mathrm{ns} \cdot \left(R_n + R_{dcr}^{(I)}\right)} \approx 32, \tag{7.3}$$

$$\mathrm{SNR}_{\mathrm{theo}}^{(\mathrm{II})} = \frac{P_S^{(II)}}{50\,\mathrm{ns} \cdot \left(\frac{1}{2} \cdot R_n \cdot T_{10\,\mathrm{km}} \cdot T_{\mathrm{ff}} + R_{dcr}^{(II/III)}\right)} \approx 21, \tag{7.4}$$

$$\mathrm{SNR}_{\mathrm{theo}}^{(\mathrm{III})} = \frac{P_S^{(III)}}{50\,\mathrm{ns} \cdot \left(\frac{1}{2} \cdot R_n \cdot T_{20\,\mathrm{km}} \cdot T_{\mathrm{ff}} + R_{dcr}^{(II/III)}\right)} \approx 23, \tag{7.5}$$

considering the transmission of the 10 km fiber ($T_{10\,\mathrm{km}} = 0.63$), the 20 km fiber ($T_{20\,\mathrm{km}} = 0.42$), and additional fiber-to-fiber connectors ($T_{\mathrm{ff}} = 0.9$). The noise counts of measurements (II) and (III) are reduced by a factor of $1/2$ due to the lower detector efficiencies. Variations in the observed, as well as in the expected SNR between the measurements (I), (II), and (III) can be attributed to atom loss during the atomic state preparation and excitation sequence, which stayed unnoticed due to spectral filtering of fluorescence photons originating from the cooling transition (Subsec. 7.1.1). After a predefined time (100 ms for (I) and 500 ms for (II), (III)), the excitation sequence is interrupted to check if the atom is still there. Hence, for longer fiber lengths, the lifetime of the atoms becomes more important since the average time to obtain a single photon increases due to a reduced repetition rate and a larger fiber attenuation. This results in an enhanced probability to lose an atom during the excitation sequence in measurements (II) and (III), which effectively reduces the observed success probabilities. An interesting number that puts the performance of the objective in perspective to the values discussed in Sec. 6.3 is the expected maximum success probability $\widetilde{P}_{S,max}^{(I)}$, deduced from the optimized value

of (I) and corrected for all additional losses induced by the conversion measurement:

$$\widetilde{P}_{S,max}^{(I)} = \frac{P_S^{(I)}}{T_{\mathrm{mems}} \cdot \eta_{dev} \cdot \eta_{snspd}/\eta_{apd} \cdot T_{\mathrm{w}} \cdot \eta_{exc}} = 8.34\,‰. \tag{7.6}$$

Here, the individual contributions that reduce the success probability are the transmission of the MEMS switch ($T_{mems} = 0.75$), the external device efficiency ($\eta_{dev} = 0.57$), the detector efficiencies for the SNSPDs ($\eta_{snspd} = 0.34$ for measurement (I)) and the APDs ($\eta_{apd} = 0.5$), the ratio of accepted photons within the time window ($T_w = 0.66$), and the excitation efficiency ($\eta_{exc} = 0.8$). This number is even higher than the explicitly measured maximum success probability of 6.7 ‰ from Sec. 6.3. However, its absolute value must be considered with caution since it is measured with much lower statistics and only indirectly determined via other parameters. Nevertheless, it still shows that the system was operated under optimal conditions, and the SNR of measurement (I) can be seen as an upper limit of what can be achieved with the current system and employed experimental sequence. Note, by solving the issue of atom loss during the excitation sequence, an even higher SNR should be possible.

The conducted atom-photon state correlation measurements (Fig. 7.3) are analyzed to obtain estimated values of the entanglement fidelity. In the first step, the peak-to-peak amplitudes of the atom-photon fringes are determined by fitting sinusoidal curves (solid lines) to the data. The obtained visibilities are reduced by several factors, some of which are equal for all measurements like imperfections in the entanglement generation or the atomic state readout, while others can vary from one measurement to another, e.g. the SNR, polarization rotations in fibers, and atomic state decoherence. Especially the latter one becomes more and more critical for longer readout delays and, as already described in Subsec. 7.1.4, affects the measurement differently depending on the actual setting, i.e. the measured photon polarization and the atomic analysis angle. With a magnetic guiding field along the y-direction, transverse field fluctuations are suppressed, which leaves the strong effective y-fields from the ODT as the dominant decoherence contribution. By projecting the photon onto the $|V\rangle$ polarization state, the atom gets prepared in the state $|\uparrow\rangle_x$, which is an eigenstate of a magnetic y-field and therefore insensitive to the atomic state decoherence. This behavior can be seen in the measurement, as the visibilities of the atom-photon fringes associated with a projected $|V\rangle$ photon (red lines) are quite similar for all measurements. On the contrary, the largest influence of the decoherence is expected and observed at an analysis angle of $\alpha = 90°$ for a projected $|H\rangle$ photon (blue lines), which prepares the atom in the state $|\downarrow\rangle_x$. However, with a V polarized readout beam ($\alpha = 0°$), magnetic y-fields and thus the atomic decoherence cannot be measured (Subsec. 2.5.3). The other two fringes related to the projection of a $|+\rangle$ or $|-\rangle$ photon (green, respectively orange lines) are affected in both their maximum and minimum points. The detection of background counts from the detectors or the frequency converter will accidentally initiate the atomic state readout, leading to completely uncorrelated results independent of the measurement setting. Here, the reduction in visibility is determined by the SNR. Likewise, polarization drifts in optical fibers lead, in general, to reduced visibilities and only in special cases to an uncritical pure phase shift of the atom-photon fringes.

For each measurement, averaged visibilities can be calculated from the fitted peak-to-peak amplitudes of the individual correlation curves. This results in visibilities of $(87.6 \pm 0.8)\,\%$, $(85.6 \pm 0.6)\,\%$, $(81.2 \pm 1.1)\,\%$, and $(74.2 \pm 1.0)\,\%$ for the measurements (R), (I), (II), and (III), respectively. Inserting these numbers in Eqn. 7.2 yield the corresponding estimated fidelities of $(89.7 \pm 0.7)\,\%$ (R), $(88.0 \pm 0.8)\,\%$ (I), $(84.3 \pm 0.9)\,\%$ (II), and $(78.5 \pm 0.9)\,\%$ (III) relative to the maximally entangled state of Eqn. B.1. For the reference measurement (R) without the QFC system, the loss in fidelity can be attributed to imperfections in the entanglement generation (~2%), the atomic state readout (~3%),

Measurement	(R)	(I)	(II)	(III)
Wavelength	780 nm	1522 nm	1522 nm	1522 nm
Fiber length	5 m	50 m	10 km	20 km
Readout delay	51 μs	51 μs	51 μs	102 μs
SNR	934.2	32.3	23.2	25.1
Fidelity (%)	89.7 ± 0.7	88.0 ± 0.8	84.3 ± 0.9	78.5 ± 0.9
S (CHSH)	2.49 ± 0.03	2.41 ± 0.03	2.37 ± 0.04	2.12 ± 0.05

Table 7.1.: Results of the four atom-photon state correlation measurements. The experimental configurations (R), (I), (II), and (III) differ in detection wavelength, fiber length, and atomic state readout delay. The measurement data is visualized in Fig. 7.3.

and atomic state decoherence (~5%). The comparison between measurements (R) and (I), with fidelities $(89.7 \pm 0.7)\,\%$ and $(88.0 \pm 0.8)\,\%$, respectively, is best suited to examine the influence of the QFC on the entangled state since their experimental configurations are most similar, e.g. concerning fiber lengths and readout delays. Here, alone the lower SNR of (I), with an expected reduction in fidelity of about 2.5%, can already account for the total observed difference in fidelity. The situation changes when comparing fidelities of measurement (I) $(88.0 \pm 0.8)\,\%$ and (II) $(84.3 \pm 0.9)\,\%$, where the SNR can only account for about 1% of the difference. The remaining 3% of the fidelity reduction is associated with experimental instabilities like polarization rotations in the 10 km long fiber, magnetic field fluctuations, or laser power drifts. In principle, the latter two instabilities should be equal to the ones of measurement (I) since the same lasers and readout delay were applied. However, they turned out to be more severe in measurement (II). The further loss in fidelity from measurement (II) $(84.3 \pm 0.9)\,\%$ to (III) $(78.5 \pm 0.9)\,\%$ is mainly caused by larger atomic state decoherence (~5%) due to the longer readout delay. From all of this, one can conclude that the atom-photon entanglement is well preserved while converting the single photon with the QFC system.
Furthermore, all correlation measurements also include the necessary basis settings to determine the S-parameter of the CHSH Bell inequality (Subsec. 3.1); ($^{H}/_{V}$ and $^{+}/_{-}$) for the photons, and ($\alpha = 22.5°$ and $\alpha' = 67.5°$), or ($\alpha = 112.5°$ and $\alpha' = 157.5°$) for the atomic state readout. The analysis of the measured data yields S values of 2.49 ± 0.03 (R), 2.41 ± 0.03 (I), 2.37 ± 0.04 (II), and 2.12 ± 0.05 (III), all clearly violating Bell's inequality.

7.3. Outlook for Future Experiments

The results presented in this chapter show that the current system can generate, distribute, and verify entanglement between an atom and a telecom photon propagating through up to 20 km of optical fiber with a fidelity of $(78.5 \pm 0.9)\,\%$. While this is an interesting result on its own, the experiment also revealed the main limitations of the system concerning its entanglement rate and fidelity. These limitations, together with some possible improvements for future experiments, are briefly summarized in the following.
The atom-photon entanglement rate is limited by the loading rate of the trap since the applied atomic readout scheme in which the atom gets ionized and lost in approximately half of the cases makes reloading of an atom necessary. This reduction can only be lifted with a more deterministic loading scheme or a non-destructive state readout, both of which were not investigated so far for our ex-

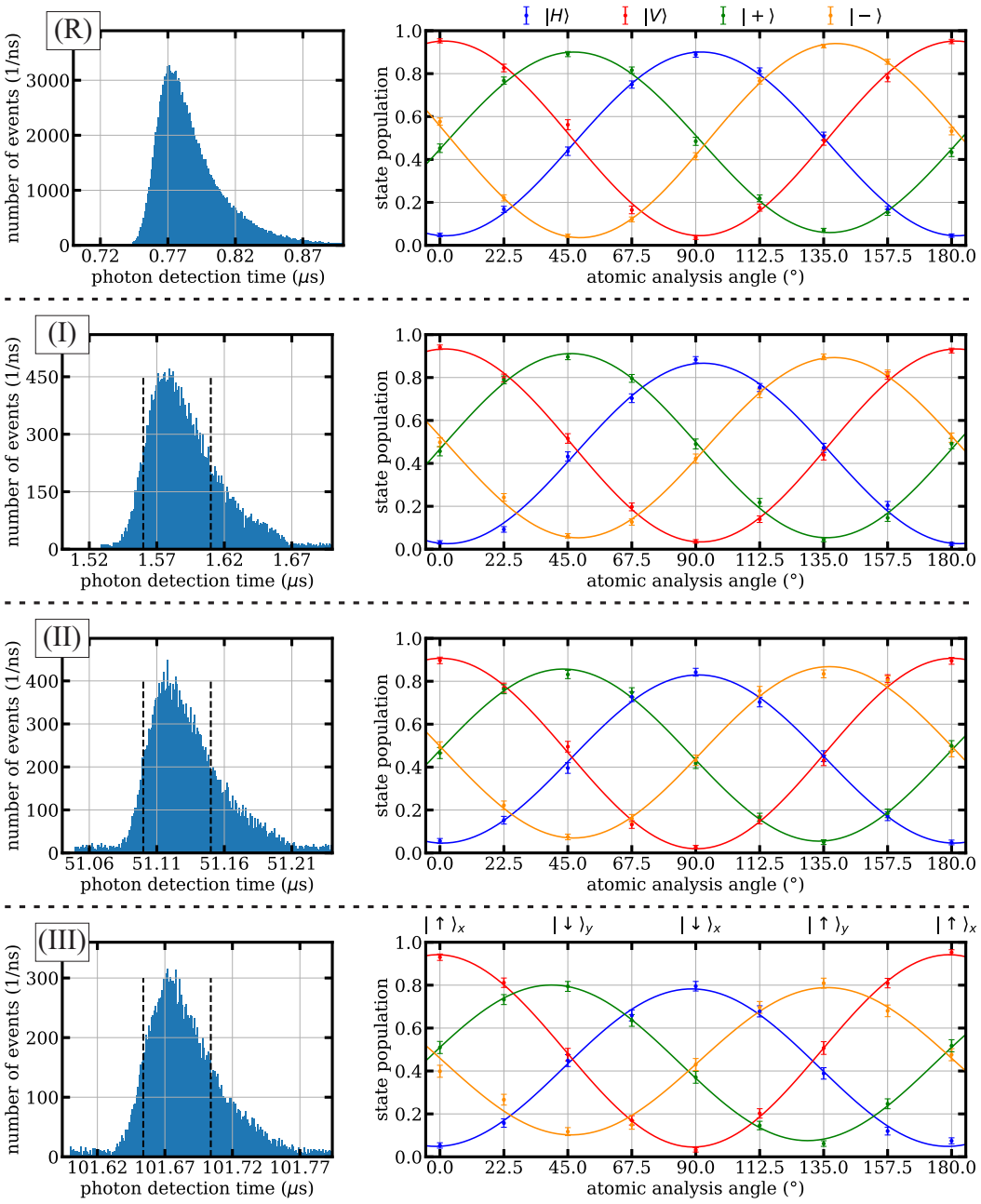

Figure 7.3.: Experimental data of the atom-photon state correlation measurements. Measurement (R) is a reference measurement at 780 nm without the conversion system, while in the other measurements, the converted photons at 1522 nm are detected after 50 m (I), 10 km (II), and 20 km (III) of optical fiber. The figures on the left show the photon detection time histograms, where the dashed lines in (I) - (III) indicate the 50 ns photon acceptance time window to increase the SNR. The figures on the right side show the atom-photon state correlations in two mutually unbiased photon bases (H/V and +/-) for different atomic analysis angles. The respective dark states of the readout polarization for specific analysis angles are displayed on top of figure (III). The solid lines are sinusoidal fits to the individual atom-photon fringes, used to estimate the entanglement fidelity.

periment. However, the situation completely changes when considering an atom-atom entanglement experiment with its rather low remote entanglement efficiency. Now, the rate is mainly limited by the local success probabilities and only a little influenced by the loading time of the atom (Sec. 2.7). An increased atom-atom entanglement rate can be achieved by replacing lossy elements like the MEMS switch ($T_{mems} = 0.75$) or fiber-to-fiber couplings ($T_{ff} = 0.9$) and using better detector systems ($\eta_{det} > 0.85$) optimized for the target wavelength at 1522 nm to increase the local success probabilities. A visualization of the expected entanglement rate can be found in Fig. 2.16.
One of the parameters that reduce the entanglement fidelity is the SNR. For the current system (and experimental sequence), the new microscope objective setup and the quantum frequency converter are already set up in a way yielding a nearly optimal SNR due to the enhanced collection efficiency, and reduced background noise due to the narrow spectral filtering. Within this configuration, only marginal improvements of the QFC are still possible, e.g. by reducing the pump power or even narrower filtering. However, this comes at the cost of a substantially reduced external device conversion efficiency (see Supplementary material of [79]). Another configuration, requiring an entirely new QFC system, would allow for a considerable increase of the SNR by converting the single photon from 780 nm to the telecom O band at 1310 nm. Here, the advantage is the enlarged wavelength separation between the pump laser (~ 1930 nm) and the converted single photon (~ 1310 nm), for which the ASR noise at the target wavelength is expected to be several orders of magnitude smaller; analog to the system presented in [137]. On the downside, photons at 1310 nm suffer from a larger attenuation in optical fibers (~0.4 dB/km) compared to photons at 1522 nm (~0.2 dB/km), leading to higher losses for longer fibers. However, the current system has a significant technical advantage when considering an atom-atom entanglement experiment, for which two sets of QFC systems are necessary. Achieving a good interference contrast requires the telecom photons to be indistinguishable in all degrees of freedom and thus also in their frequency. One way to guarantee this is to use the same master laser that generates the pump light for the DFG process for both QFC systems (see Supplementary material of [79]). For the current configuration, this is possible since the wavelength of the pump light at 1600 nm can be distributed over several kilometers with low absorption losses, whereas for the conversion system to the telecom O-band the 1930 nm pump laser would suffer from substantial attenuation losses of ~20 dB/km. Hence, two independent sets of pump laser systems with the corresponding locking electronics and high finesse cavities would be necessary to achieve an absolute frequency reference.
Another factor that reduces the entanglement fidelity is the decoherence of the atomic state caused by magnetic field fluctuations and the position-dependent effective magnetic fields originating from the longitudinal field components of the strongly focused ODT. In Section 2.7, this issue was already discussed, and possible improvements were suggested. For instance, a magnetic guiding field together with a Raman state transfer of the qubit states to a specific combination of the hyperfine ground states [77] should allow for a reduction in sensitivity to magnetic field fluctuations in all directions by several orders of magnitude. Furthermore, a standing wave optical dipole trap has the potential of canceling the longitudinal field components of the ODT completely and thus eliminating the primary decoherence source of the current system [69]. However, the realization of the latter would require considerable changes or even a complete redesign of the atom trap setup.

The next crucial step for the development of the experiment is the realization of entanglement distribution between two distant atomic quantum nodes using the entanglement swapping protocol mediated by telecom converted single photons, which enables transmission over several kilometers of optical fiber. Analog to the fidelity of the atom-photon state of Eqn. 7.2, the fidelity of the entangled atom-atom state can be estimated by $\mathcal{F}_{aa} \geq \frac{1}{9} + \frac{8}{9}\bar{V}_{aa}$, with the averaged visibility $\bar{V}_{aa}$ of an atom-atom correlation. The atom-atom visibility, in turn, can be estimated by the square of the corresponding

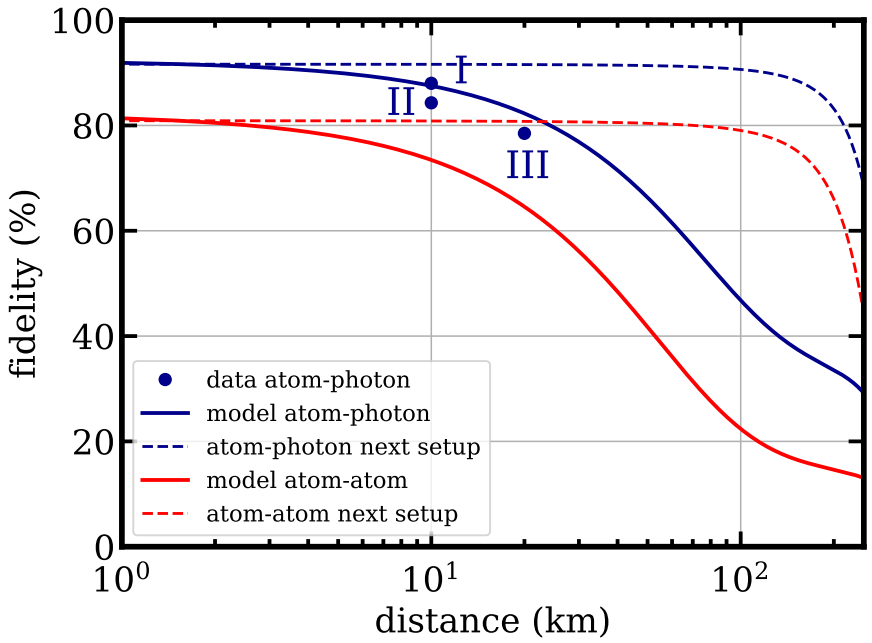

Figure 7.4.: Atom-photon (blue) and atom-atom (red) fidelity estimations [79]. The blue dots labeled with I, II, and III represent the data points of the three telecom measurements discussed in this chapter. Note, the fidelities obtained in measurements II and III are below the expected curve (solid blue line) due to reduced SNRs caused by non-optimal experimental settings for the collection efficiencies. Below 1 km, all fidelities are determined by imperfections of the entanglement generation and the atomic state readout. For larger distances, the current system is limited by atomic state decoherence, whereas the expected fidelities are almost unaffected up to 100 km for the future setup. However, for distances longer than 100 km, detector dark counts ultimately become the limiting factor.

atom-photon visibility multiplied by the non-perfect two-photon interference contrast of 94 % [51]. In order to visualize the expected behavior in dependence of the separation of the atomic qubits, the atom-photon visibility is modeled in consideration of expected values for the detector efficiency and dark count rate, the SNR, and the atomic decoherence caused by magnetic field fluctuations and dephasing due to longitudinal field components of the ODT. Note, a symmetrical configuration with the BSM located in the middle between both atoms is assumed, and thus the coherence time required to distribute entanglement over a certain distance is the same for the atom-photon and the atom-atom case. Figure 7.4 depicts the expected atom-photon and atom-atom fidelities for the current as well as a potential future system that includes the improvements to enhance the atomic state coherence mentioned above (e.g. a standing wave dipole trap). For relatively short distances of below 1 km, the expected fidelities are limited by the non-perfect state preparation and readout, while for larger separations, the atomic state decoherence becomes the dominant effect, which reduces the fidelities in the current configuration. In contrary to that, assuming decoherence times of several milliseconds, the fidelities of the future setup are nearly unaffected by the atomic decoherence. However, they are eventually limited by the detector dark counts for distances above 100 km. These estimations show that the entanglement distribution between two stationary quantum memories over several tens of kilometers with high fidelity comes into reach.

8. Conclusion and Outlook

This work presented experiments based on long-distance entanglement with neutral Rubidium-87 atoms serving as single atom quantum nodes. Here, the implementation of new high NA microscope objectives significantly improved the system performance, which enabled the realization of a first quantum communication application, i.e. long-distance distribution of atom-photon entanglement at telecom wavelength.

The microscope objectives are the central optical elements of the experiment that affect all fundamental experimental operations, especially the entanglement generation. The entanglement between the atomic spin and the polarization of the photon was generated in a spontaneous emission process subsequent to an optical excitation of the atom. Based on that, two widely separated atoms were entangled by employing an entanglement swapping scheme. With the new high-NA objective setups, local success probabilities for atom-photon entanglement of $P_{S_1} = 6.70\,‰$ and $P_{S_2} = 8.61\,‰$ were obtained, which compared to previous measurements constitute improvement factors of ~ 2.5 and ~ 3.5 for the system in Lab 1 and Lab 2, respectively. For the combined experiment, an atom-atom entanglement efficiency of 6.15 ppm was achieved, which corresponds to an improvement by a factor of 6.5. Crucial for the successful implementation of the new lens systems was a detailed analysis of the collection-and-coupling process of single photons, an optical characterization that determined the quality of the optics in terms of wavefront aberration, and a detailed description of the objective setups, their construction, alignment, and implementation.

For the analysis of the collection-and-coupling process, a model was developed to calculate the probabilities of collecting an emitted single photon and coupling an already collected photon into a single-mode fiber. The model considers the polarization-dependent dipole emission characteristics and accounts for the thermal distribution of the atom inside the optical dipole trap. For the current trap parameters (e.g. depth, focal size, wavelength, and atomic temperature), combined collection-and-coupling efficiencies were calculated, yielding values of $\eta_{cc,1} = 4.05\,\%$ for the setup of Lab 1 and $\eta_{cc,2} = 3.53\,\%$ for the setup of Lab 2. Further, it was found that unwanted photon couplings, i.e. a photon is coupled with the orthogonal polarization as emitted or a π-polarized photon is coupled, are highly suppressed, and hence the fidelity of the entangled atom-photon state is only negligibly reduced. Moreover, the optimal fiber mode size required for a maximal coupling efficiency was determined to select the fiber collimators for the objective setups. Since all commercially available fiber collimators did not fulfill the necessary requirements, the collimator closest to the optimum was chosen for Lab 1, whereas a suitable lens system was designed and implemented in Lab 2. The homemade fiber collimator is expected to yield a 2.5% higher coupling efficiency compared to the setup of Lab 1.

One of the high-NA objectives and the homemade fiber collimator were optically characterized by quantifying the amount of wave aberrations, which might reduce their optical performances. Therefore, an experimental test setup was assembled in which the optical system under examination was inserted to image a point-like emitter. Analyzing the resulting point spread functions with a computer-based linear least-squares fit algorithm allowed identifying the wave aberrations. Moreover, alignment criteria were specified up to those a diffraction-limited operation is guaranteed. For the microscope objective, this resulted in a numerical aperture of 0.5023 ± 0.0026 and a Strehl ratio of 0.9985 ± 0.0021,

resembling a nearly perfect system. The objective turned out less sensitive against misalignment as expected from the specifications provided by the manufacturer yielding a larger range for a diffraction-limited operation. For the homemade fiber collimator, a numerical aperture of 0.1873 ± 0.0004 and a Strehl ratio of $0.9921^{+0.0079}_{-0.0100}$ were obtained, both in good agreement with the lens design. The measurements also verified the high tolerances of the collimator against misalignment.

The first experiment presented in this thesis was a test of Bell's inequality performed on pairs of entangled atoms separated by a distance of 398 m. The locality and the detection loophole were closed simultaneously by ensuring space-like separated measurements and using an event-ready entanglement scheme. A CHSH S-parameter of $S = 2.221 \pm 0.033$ was achieved, which violates the LHV predictions by more than six standard deviations, and allowed for a strong rejection of local realism with a P-value of $1.739 \cdot 10^{-10}$. A violation of Bell's inequality also forms the basis of several DI applications, e.g. generation of random numbers, certification of entanglement, and device-independent quantum key distribution. While the quality of the obtained measurement results was sufficient to demonstrate the first two, as presented in [55], the application of DIQKD was still out of reach. However, the system was not yet upgraded with better collection optics and hence did not benefit from the improved system performance.

After both high-NA objectives were implemented, a successful proof-of-concept demonstration of a DIQKD protocol was realized on the quantum network link formed by the distant atoms. As will be described in more detail elsewhere, the atom-atom state fidelity was significantly improved to $\mathcal{F}_{aa} = 0.892 \pm 0.019$ by applying optimized acceptance conditions for the Bell state measurement of the entanglement swapping process, as suggested in [55]. The optimization reduced the total number of events by a factor of four. In combination with the additional losses caused by the specific implementation of the protocol, a realization with a reasonable rate (0.7 events/min) was only possible due to the enhanced photon coupling efficiencies obtained by the new objectives. The measurement yielded a QUBER of 0.078 ± 0.009 and a CHSH S-parameter of $S = 2.578 \pm 0.075$, allowing for an asymptotic key rate of 0.157 with a confidence level of 99.4%.

An essential resource for quantum communication applications is the ability to distribute entanglement over large distances. Limiting for the achievable distance is hereby the attenuation in optical fibers for the emission wavelengths (visible/NIR range) of suitable quantum memories that provide a light-matter interface to exchange quantum information. To overcome this limitation, quantum frequency conversion to the low-loss transmission bands of telecom fibers is necessary. In this work, a polarization-preserving QFC system was incorporated into the experiment, which allowed to convert single photons emitted during the entanglement generation from their emission wavelength of 780 nm to the telecom S-band at 1522 nm while preserving the non-classical property of atom-photon entanglement. Narrow spectral filtering to the single photon level was required for efficiently suppressing the high noise of the conversion system. The enhanced photon coupling efficiency of the new objective, together with the high external device conversion efficiency of $\eta_{dev} = 57\,\%$, resulted in a signal-to-noise ratio of 25.1, which only slightly reduced the state fidelity. Applying a magnetic guiding field to suppress small magnetic field fluctuations extended the atomic coherence time to hundreds of microseconds. With that, it was possible to distribute and verify entanglement between a ^{87}Rb atom and a telecom photon over 20 km of optical fiber with a fidelity of $78.5 \pm 0.9\,\%$, and a CHSH S-parameter of $S = 2.12 \pm 0.05$ was obtained.

The next step towards large-scale quantum networks is to extend the distance between the atomic quantum memories using entanglement swapping of telecom converted single photons, which can be transmitted over several tens of kilometers. Here, the enhanced photon coupling efficiencies of the new objectives will help overcome additional losses of the conversion systems and counteract the reduced repetition rate caused by longer photon and signal transmission times. Furthermore, in the

employed event-ready scheme, the coherence of the atomic state needs to be improved significantly for longer distances. For instance, a magnetic guiding field together with a Raman state transfer of the qubit states to the hyperfine ground states should reduce the sensitivity to magnetic field fluctuations by several orders of magnitude [77]. Another possibility is to lower the temperature of the atoms, which reduces the influence of longitudinal field components of the strongly focused optical dipole trap. Moreover, using a standing wave optical dipole trap has even the potential of canceling the longitudinal field components completely and thus eliminating the primary decoherence source of the current system [69].

A. Physical Constants and Properties of ^{87}Rubidium

constant	description	value
$\hbar = \frac{h}{2\pi}$	reduced Planck constant	$1.054571726 \cdot 10^{-34}\,\mathrm{J \cdot s}$
c	speed of light in vacuum	$2.99792458 \cdot 10^{8}\,{}^{m}/_{\mathrm{s}}$
μ_0	permeability of free space	$1.25663770614 \cdot 10^{-6}\,{}^{N}/_{\mathrm{A}^2}$
$\epsilon_0 = \frac{1}{c^2\mu_0}$	permittivity of free space	$8.8541878176 \cdot 10^{-12}\,{}^{F}/_{\mathrm{m}}$
e	elementary charge	$1.602176565 \cdot 10^{-19}\,\mathrm{C}$
u	atomic mass unit	$1.660538921 \cdot 10^{-27}\,\mathrm{kg}$
k_B	Boltzmann constant	$1.38064852{\cdot}10^{-23}\,\frac{\mathrm{m^2 \cdot kg}}{\mathrm{s^2 \cdot K}}$

Table A.1.: Physical constants [56]

constant	description	value
m	mass	$86.90918020 \cdot u$
E_0	ground state energy	$4.177127\,\mathrm{eV}$
	ionization limit	$296.817\,\mathrm{nm}$
Γ_{D1}	decay rate of the $D1$ transition	$2\pi \cdot 5.7500\,\mathrm{MHz}$
τ_{D1}	life time of $5^2\mathrm{P}_{1/2}$ excited state	$27.70\,\mathrm{ns}$
d_{D1}	dipole matrix element of the $D1$ transition	$2.537 \cdot 10^{-29}\,\mathrm{C \cdot m}$
λ_{D1}	$D1$ transition wavelength	$794.979\,\mathrm{nm}$
Γ_{D2}	decay rate of the $D2$ transition	$2\pi \cdot 6.0666\,\mathrm{MHz}$
τ_{D2}	life time of the $5^2\mathrm{P}_{3/2}$ excited state	$26.24\,\mathrm{ns}$
d_{D2}	dipole matrix element of the $D2$ transition	$3.584 \cdot 10^{-29}\,\mathrm{C \cdot m}$
λ_{D2}	$D2$ transition wavelength	$780.241\,\mathrm{nm}$

Table A.2.: Atomic properties of ^{87}Rb [56]

B. Definition of the Polarization and Atomic States

This appendix introduces definitions of the coordinate system, the light polarization, and the corresponding atomic states, necessary for a consistent description of the performed experiments. The following definitions are a reduced and adapted version of the ones given in [55].
In the experiment, a right-handed coordinate system is used with its origin at the focal spot of the dipole trap, i.e. the position of the atom. The z-axis is defined by the optical axis of the microscope objective oriented along the direction of the photon collection. As such, the z-axis represents the natural choice for the quantization axis of the atomic system. The x-axis is defined parallel to the optical table (horizontal plane) and orthogonal to the z-axis. The y-axis is defined perpendicular to the table, pointing upwards in the vertical direction.

Definition of Polarization and Photon States

In the reference frame of the laboratory, the polarization of light is defined according to [55]:

1. H is a linear polarization parallel to the surface of the optical table (x-z plane).

2. V is a linear polarization vertical to the surface of the optical table (y-axis).

3. $+$ is a linear polarization rotated 45° right-hand side in traveling direction with respect to V.

4. $-$ is a linear polarization rotated 45° left-hand side in traveling direction with respect to V.

5. L is a circular polarization with right-hand rotation in the direction of propagation (historic left-hand rotation for the counter propagating direction)

6. R is a circular polarization with left-hand rotation in the direction of propagation (historic right-hand rotation for the counter propagating direction)

The connection to the reference frame of the atom with a quantization axis $\mathcal{Z}$ is obtained by considering the conservation of angular momentum in the combined system of a photon emitted by the atom. The polarization of the photon is defined as σ^+ (right-hand rotation in the traveling direction) for a change of $\Delta m_{f,\mathcal{Z}} = -1$, or σ^- (left-hand rotation of the polarization in traveling direction) with a change of $\Delta m_{f,\mathcal{Z}} = +1$, or π (linear polarization parallel to $\mathcal{Z}$) with a change of $\Delta m_{f,\mathcal{Z}} = 0$. For photons propagating with a wave vector $\vec{k}$ along the quantization axis $\mathcal{Z} = z$, this leads to the following correspondence: $L \mathrel{\hat{=}} \sigma^+$ and $R \mathrel{\hat{=}} \sigma^-$. This allows defining the photon states for the collected photons and the readout beam as shown in Table B.1 [55].

polarization state	composition in $\|\sigma^+\rangle$ and $\|\sigma^-\rangle$	E-field for light in z-direction
$\|L\rangle$	$\|\sigma^+\rangle$	$\frac{1}{\sqrt{2}}\|E\|\begin{pmatrix} e^{-i\frac{\pi}{2}} \\ 1 \\ 0 \end{pmatrix} e^{i(kz-\omega t)}$
$\|R\rangle$	$\|\sigma^-\rangle$	$\frac{1}{\sqrt{2}}\|E\|\begin{pmatrix} e^{i\frac{\pi}{2}} \\ 1 \\ 0 \end{pmatrix} e^{i(kz-\omega t)}$
$\|H\rangle$	$\frac{i}{\sqrt{2}}\left(\|\sigma^+\rangle - \|\sigma^-\rangle\right)$	$\|E\|\begin{pmatrix} 1 \\ 0 \\ 0 \end{pmatrix} e^{i(kz-\omega t)}$
$\|V\rangle$	$\frac{1}{\sqrt{2}}\left(\|\sigma^+\rangle + \|\sigma^-\rangle\right)$	$\|E\|\begin{pmatrix} 0 \\ 1 \\ 0 \end{pmatrix} e^{i(kz-\omega t)}$
$\|+\rangle$	$\frac{1}{\sqrt{2}}e^{-i\frac{\pi}{4}}\left(\|\sigma^+\rangle + i\|\sigma^-\rangle\right)$	$\frac{1}{\sqrt{2}}\|E\|\begin{pmatrix} -1 \\ 1 \\ 0 \end{pmatrix} e^{i(kz-\omega t)}$
$\|-\rangle$	$\frac{1}{\sqrt{2}}e^{i\frac{\pi}{4}}\left(\|\sigma^+\rangle - i\|\sigma^-\rangle\right)$	$\frac{1}{\sqrt{2}}\|E\|\begin{pmatrix} 1 \\ 1 \\ 0 \end{pmatrix} e^{i(kz-\omega t)}$

Table B.1.: Definition of the polarization states of the photon

Atomic States

The atomic qubit is encoded in the Zeeman states $F = 1, m_F = \pm 1$ of the $5^2S_{1/2}$ ground state (Fig. 2.2) and $|1,-1\rangle = |\downarrow\rangle_z$, and $|1,+1\rangle = |\uparrow\rangle_z$ are defined as the eigenvectors to the Pauli operator $\hat{\sigma}_z$. Representations of the qubit states in the eigenbasis of the $\hat{\sigma}_x$ and $\hat{\sigma}_y$ are listed in Table B.2. Note, these definitions are chosen to fit the definition of the photon states in Table B.1.

qubit state	in qubit z states	composition in m_F
$\|\downarrow\rangle_z$	$\|\downarrow\rangle_z$	$\|1,-1\rangle$
$\|\uparrow\rangle_z$	$\|\uparrow\rangle_z$	$\|1,+1\rangle$
$\|\downarrow\rangle_x$	$\frac{-i}{\sqrt{2}}(\|\downarrow\rangle_z - \|\uparrow\rangle_z)$	$\frac{-i}{\sqrt{2}}(\|1,-1\rangle - \|1,+1\rangle)$
$\|\uparrow\rangle_x$	$\frac{1}{\sqrt{2}}(\|\downarrow\rangle_z + \|\uparrow\rangle_z)$	$\frac{1}{\sqrt{2}}(\|1,-1\rangle + \|1,+1\rangle)$
$\|\downarrow\rangle_y$	$\frac{1}{\sqrt{2}}e^{i\frac{\pi}{4}}(\|\downarrow\rangle_z - i\|\uparrow\rangle_z)$	$\frac{1}{\sqrt{2}}e^{i\frac{\pi}{4}}(\|1,-1\rangle - i\|1,+1\rangle)$
$\|\uparrow\rangle_y$	$\frac{1}{\sqrt{2}}e^{-i\frac{\pi}{4}}(\|\downarrow\rangle_z + i\|\uparrow\rangle_z)$	$\frac{1}{\sqrt{2}}e^{-i\frac{\pi}{4}}(\|1,-1\rangle + i\|1,+1\rangle)$

Table B.2.: Atomic-qubit state definition

Entangled Atom-Photon State

The relations given in Tables B.1 and B.2 allow to transform the entangled atom-photon state (Eqn. 2.8) in three conjugate bases:

$$\begin{aligned} |\Psi\rangle_{AP} &= \frac{1}{\sqrt{2}}(|\mathrm{L}\rangle|\downarrow\rangle_z + |\mathrm{R}\rangle|\uparrow\rangle_z) \\ &= \frac{1}{\sqrt{2}}(|\mathrm{H}\rangle|\downarrow\rangle_x + |\mathrm{V}\rangle|\uparrow\rangle_x) \\ &= \frac{1}{\sqrt{2}}(|+\rangle|\downarrow\rangle_y + |-\rangle|\uparrow\rangle_y)\,. \end{aligned} \tag{B.1}$$

Read-out Polarization and Corresponding $|B\rangle$ and $|D\rangle$ States

The measurement basis of the atomic state analysis is determined by the read-out polarization χ_{ro} (2.9), which allows to calculate the bright state $|B\rangle$ (2.10) and dark state $|D\rangle$ (2.11) in the state selective ionization scheme (Subsec. 2.4.2). A list of $|B\rangle$ and $|D\rangle$ for the six polarizations χ_{ro} defined in Table B.1 can be found in Table B.3.

χ_{ro}	$\|B\rangle$	$\|D\rangle$
L	$\|\downarrow\rangle_z$	$\|\uparrow\rangle_z$
R	$\|\uparrow\rangle_z$	$\|\downarrow\rangle_z$
H	$\frac{1}{\sqrt{2}}(\|\downarrow\rangle_z + \|\uparrow\rangle_z)$	$\frac{-i}{\sqrt{2}}(\|\downarrow\rangle_z - \|\uparrow\rangle_z)$
V	$\frac{-i}{\sqrt{2}}(\|\downarrow\rangle_z - \|\uparrow\rangle_z)$	$\frac{1}{\sqrt{2}}(\|\downarrow\rangle_z + \|\uparrow\rangle_z)$
+	$\frac{1}{\sqrt{2}}e^{-i\frac{\pi}{4}}(\|\downarrow\rangle_z + i\|\uparrow\rangle_z)$	$\frac{1}{\sqrt{2}}e^{i\frac{\pi}{4}}(\|\downarrow\rangle_z - i\|\uparrow\rangle_z)$
-	$\frac{1}{\sqrt{2}}e^{i\frac{\pi}{4}}(\|\downarrow\rangle_z - i\|\uparrow\rangle_z)$	$\frac{1}{\sqrt{2}}e^{-i\frac{\pi}{4}}(\|\downarrow\rangle_z + i\|\uparrow\rangle_z)$

Table B.3.: Polarization of the read-out pulse and resulting bright $|B\rangle$ and dark states $|D\rangle$

C. Complete Data of the Statistical Analysis of Generated Random Input Bits

The data of the statistical analysis of all generated random input bits for the two Bell tests started on 15th April 2016 and on 14th June 2016 are shown here for completeness. For the Bias, the time evolution of the observed values for both runs and both QRNGs are depicted in C.1. The mean values for the correlation data up to lag 56 and the time evolution of the observed SCC_1 values are given in C.2. The artifacts in the P-value distribution of the test row "smultin_MultinomialBitsOver" of the standardized test suit "TestU01 Alphabit battery" can be reproduced by the model introduced in Subsection 3.4.3. In order to show that it fits the observed data also for different lengths of bit sequences, additional plots are given in C.3.

C.1. Additional Bias Data

Figure C.1 shows the time evolution of the observed bias values of generated random input bits of the Bell measurements. Each data point contains $360\,\mathrm{Gb}$ of data and corresponds to a time interval of $2\,\mathrm{h}$. The chosen data size is a trade-off between reducing the statistical noise to be smaller than the observed value and the observability of potential long term drifts. One standard deviation for this data size is given by $\sigma = 8.33 \cdot 10^{-7}$. The shaded areas colored in red indicate the $\pm\sigma$ interval.

C.2. Additional Correlation Data

In Tables C.1-C.4, the mean values of the correlations SCC_l defined in Eqn. 3.4 are listed up to lag 56 for the generated random input bits of the Bell measurements. Figure C.1 shows the time evolution of the observed SCC_1 correlation values. Each data point contains $360\,\mathrm{Gb}$ of data and corresponds to a time interval of $2\,\mathrm{h}$. One standard deviation for the chosen data size is given by $\sigma = 1.67 \cdot 10^{-7}$. The shaded areas colored in red indicate the $\pm\sigma$ interval.

C.3. Additional Histograms of P-Value Distribution

All tests of the standardized test suit "TestU01 Alphabit battery" were applied to the generated random bit sequences, which are organized in 115420 files. For each file and each test, a P-value is calculated, forming a distribution of P-values. Testing this distribution for uniformity finally tests the hypothesis of randomness. In the test row "smultin_MultinomialBitsOver", a skew in the P-value distribution was observed, which leads to failing this uniformity test. The model introduced in the main text 3.4.3 reflects this behavior. In order to show that the expected distribution fits well with the observed data also for different lengths of bit sequences, additional plots are given in C.3.

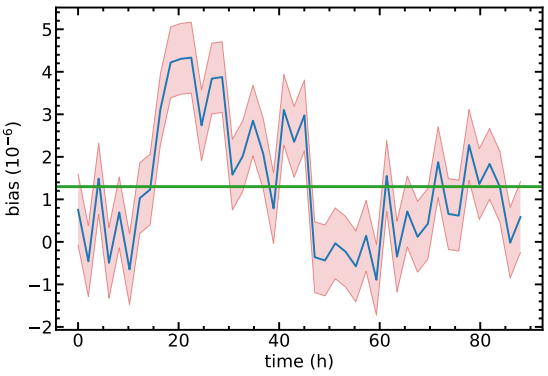

(a) Measurement run from 15th April 2016 in Lab 1

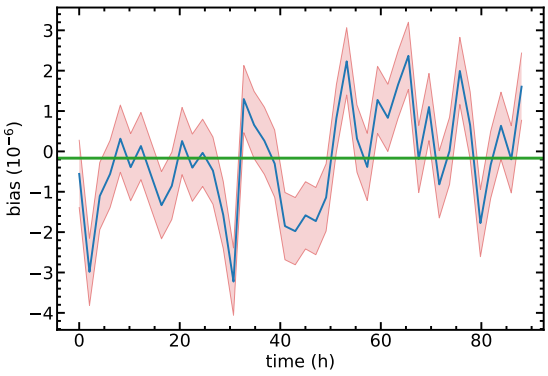

(b) Measurement run from 15th April 2016 in Lab 2

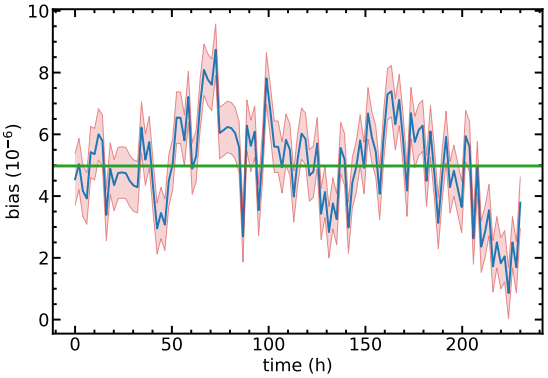

(c) Measurement run from 14th June 2016 in Lab 1

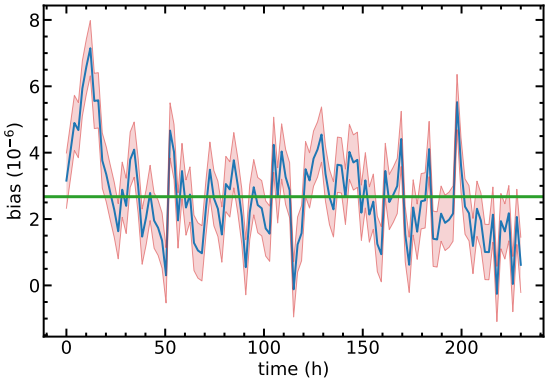

(d) Measurement run from 14th June 2016 in Lab 2

Figure C.1.: The time evolution of the bias observed for the measurement runs from 15th April 2016 and 14th June 2016 in both labs (blue lines). Each data point contains 360 Gb of data and represents a measurement time of 2 h. The areas shaded in red indicates the $\pm\sigma$ interval, and the green lines show the average bias values.

l	SCC_l	l	SCC_l	l	SCC_l	l	SCC_l
1	$1.34 \cdot 10^{-5}$	17	$-3.78 \cdot 10^{-8}$	33	$-3.70 \cdot 10^{-7}$	49	$-1.46 \cdot 10^{-7}$
2	$5.39 \cdot 10^{-7}$	18	$-1.44 \cdot 10^{-8}$	34	$-7.08 \cdot 10^{-7}$	50	$-5.49 \cdot 10^{-8}$
3	$4.74 \cdot 10^{-7}$	19	$-8.59 \cdot 10^{-8}$	35	$-2.50 \cdot 10^{-8}$	51	$3.09 \cdot 10^{-7}$
4	$1.43 \cdot 10^{-7}$	20	$2.37 \cdot 10^{-7}$	36	$-1.49 \cdot 10^{-7}$	52	$-2.00 \cdot 10^{-7}$
5	$-3.13 \cdot 10^{-7}$	21	$-2.94 \cdot 10^{-8}$	37	$-5.51 \cdot 10^{-8}$	53	$-2.37 \cdot 10^{-7}$
6	$4.53 \cdot 10^{-8}$	22	$-2.72 \cdot 10^{-7}$	38	$-5.82 \cdot 10^{-8}$	54	$3.56 \cdot 10^{-8}$
7	$4.19 \cdot 10^{-7}$	23	$-6.20 \cdot 10^{-7}$	39	$-1.01 \cdot 10^{-7}$	55	$-1.00 \cdot 10^{-9}$
8	$-1.31 \cdot 10^{-7}$	24	$-2.49 \cdot 10^{-7}$	40	$-1.73 \cdot 10^{-7}$	56	$3.30 \cdot 10^{-8}$
9	$2.55 \cdot 10^{-7}$	25	$-2.36 \cdot 10^{-8}$	41	$-3.61 \cdot 10^{-7}$		
10	$-6.18 \cdot 10^{-7}$	26	$-1.65 \cdot 10^{-7}$	42	$-1.41 \cdot 10^{-7}$		
11	$1.21 \cdot 10^{-7}$	27	$-3.13 \cdot 10^{-7}$	43	$3.47 \cdot 10^{-8}$		
12	$-8.60 \cdot 10^{-8}$	28	$-3.73 \cdot 10^{-8}$	44	$-3.26 \cdot 10^{-8}$		
13	$1.53 \cdot 10^{-7}$	29	$-2.19 \cdot 10^{-7}$	45	$-4.74 \cdot 10^{-7}$		
14	$-1.54 \cdot 10^{-7}$	30	$1.17 \cdot 10^{-7}$	46	$-4.45 \cdot 10^{-7}$		
15	$-4.33 \cdot 10^{-7}$	31	$-4.30 \cdot 10^{-8}$	47	$-2.33 \cdot 10^{-7}$		
16	$-2.58 \cdot 10^{-7}$	32	$-1.08 \cdot 10^{-7}$	48	$-1.52 \cdot 10^{-7}$		

Table C.1.: The average correlation values SCC_l in Lab 1 for the measurement run from 15th April 2016. The statistical error for all values is given by $\sigma = 2.49 \cdot 10^{-7}$.

l	SCC_l	l	SCC_l	l	SCC_l	l	SCC_l
1	$1.15 \cdot 10^{-5}$	17	$-4.75 \cdot 10^{-9}$	33	$1.06 \cdot 10^{-7}$	49	$1.28 \cdot 10^{-7}$
2	$7.93 \cdot 10^{-7}$	18	$-2.51 \cdot 10^{-7}$	34	$1.85 \cdot 10^{-8}$	50	$-2.50 \cdot 10^{-7}$
3	$-6.56 \cdot 10^{-8}$	19	$2.72 \cdot 10^{-7}$	35	$2.87 \cdot 10^{-7}$	51	$9.78 \cdot 10^{-8}$
4	$4.89 \cdot 10^{-7}$	20	$-3.14 \cdot 10^{-7}$	36	$-1.06 \cdot 10^{-7}$	52	$-1.32 \cdot 10^{-7}$
5	$1.33 \cdot 10^{-7}$	21	$-2.46 \cdot 10^{-7}$	37	$-1.48 \cdot 10^{-7}$	53	$-3.98 \cdot 10^{-7}$
6	$2.55 \cdot 10^{-7}$	22	$1.39 \cdot 10^{-7}$	38	$2.95 \cdot 10^{-7}$	54	$-6.67 \cdot 10^{-7}$
7	$-7.97 \cdot 10^{-8}$	23	$-2.30 \cdot 10^{-7}$	39	$5.28 \cdot 10^{-8}$	55	$1.44 \cdot 10^{-7}$
8	$-1.88 \cdot 10^{-8}$	24	$2.53 \cdot 10^{-7}$	40	$-2.69 \cdot 10^{-7}$	56	$3.83 \cdot 10^{-7}$
9	$1.42 \cdot 10^{-8}$	25	$-8.43 \cdot 10^{-8}$	41	$2.26 \cdot 10^{-7}$		
10	$4.11 \cdot 10^{-7}$	26	$-1.45 \cdot 10^{-7}$	42	$-2.75 \cdot 10^{-7}$		
11	$-8.71 \cdot 10^{-8}$	27	$2.06 \cdot 10^{-8}$	43	$-1.17 \cdot 10^{-7}$		
12	$2.28 \cdot 10^{-7}$	28	$-1.17 \cdot 10^{-8}$	44	$-2.21 \cdot 10^{-7}$		
13	$1.53 \cdot 10^{-7}$	29	$-1.68 \cdot 10^{-7}$	45	$1.99 \cdot 10^{-7}$		
14	$2.23 \cdot 10^{-7}$	30	$-1.13 \cdot 10^{-7}$	46	$-1.83 \cdot 10^{-7}$		
15	$1.62 \cdot 10^{-7}$	31	$-2.55 \cdot 10^{-7}$	47	$7.93 \cdot 10^{-8}$		
16	$6.36 \cdot 10^{-8}$	32	$1.26 \cdot 10^{-7}$	48	$-2.89 \cdot 10^{-8}$		

Table C.2.: The average correlation values SCC_l in Lab 2 for the measurement run from 15th April 2016. The statistical error for all values is given by $\sigma = 2.49 \cdot 10^{-7}$.

l	SCC_l	l	SCC_l	l	SCC_l	l	SCC_l
1	$1.32 \cdot 10^{-5}$	17	$5.42 \cdot 10^{-8}$	33	$8.53 \cdot 10^{-8}$	49	$-2.90 \cdot 10^{-7}$
2	$1.47 \cdot 10^{-7}$	18	$6.01 \cdot 10^{-8}$	34	$2.52 \cdot 10^{-8}$	50	$1.65 \cdot 10^{-8}$
3	$-9.79 \cdot 10^{-8}$	19	$1.49 \cdot 10^{-7}$	35	$-1.22 \cdot 10^{-7}$	51	$1.57 \cdot 10^{-7}$
4	$3.41 \cdot 10^{-8}$	20	$-7.91 \cdot 10^{-8}$	36	$6.94 \cdot 10^{-8}$	52	$-3.43 \cdot 10^{-7}$
5	$5.87 \cdot 10^{-9}$	21	$-2.46 \cdot 10^{-7}$	37	$1.19 \cdot 10^{-7}$	53	$-5.15 \cdot 10^{-8}$
6	$-8.19 \cdot 10^{-8}$	22	$-1.60 \cdot 10^{-7}$	38	$-1.99 \cdot 10^{-8}$	54	$1.49 \cdot 10^{-7}$
7	$-4.74 \cdot 10^{-8}$	23	$1.94 \cdot 10^{-7}$	39	$9.53 \cdot 10^{-8}$	55	$2.20 \cdot 10^{-7}$
8	$1.38 \cdot 10^{-7}$	24	$4.48 \cdot 10^{-8}$	40	$-2.39 \cdot 10^{-7}$	56	$9.64 \cdot 10^{-9}$
9	$1.62 \cdot 10^{-7}$	25	$1.42 \cdot 10^{-7}$	41	$-3.33 \cdot 10^{-7}$		
10	$2.19 \cdot 10^{-7}$	26	$-1.22 \cdot 10^{-7}$	42	$2.74 \cdot 10^{-7}$		
11	$-2.13 \cdot 10^{-7}$	27	$-1.79 \cdot 10^{-7}$	43	$5.56 \cdot 10^{-10}$		
12	$-2.40 \cdot 10^{-7}$	28	$-3.26 \cdot 10^{-7}$	44	$1.04 \cdot 10^{-7}$		
13	$-1.52 \cdot 10^{-7}$	29	$-4.92 \cdot 10^{-8}$	45	$2.13 \cdot 10^{-8}$		
14	$-1.75 \cdot 10^{-8}$	30	$1.56 \cdot 10^{-8}$	46	$-2.45 \cdot 10^{-7}$		
15	$-3.31 \cdot 10^{-8}$	31	$-2.97 \cdot 10^{-7}$	47	$-2.83 \cdot 10^{-8}$		
16	$-1.60 \cdot 10^{-8}$	32	$8.58 \cdot 10^{-8}$	48	$-2.43 \cdot 10^{-7}$		

Table C.3.: The average correlation values SCC_l in Lab 1 for the measurement run from 14th June 2016. The statistical error for all values is given by $\sigma = 1.55 \cdot 10^{-7}$.

l	SCC_l	l	SCC_l	l	SCC_l	l	SCC_l
1	$1.15 \cdot 10^{-5}$	17	$-3.09 \cdot 10^{-7}$	33	$-1.12 \cdot 10^{-7}$	49	$-2.04 \cdot 10^{-7}$
2	$4.41 \cdot 10^{-7}$	18	$1.26 \cdot 10^{-7}$	34	$-1.56 \cdot 10^{-7}$	50	$-2.42 \cdot 10^{-7}$
3	$1.06 \cdot 10^{-8}$	19	$-1.17 \cdot 10^{-7}$	35	$3.33 \cdot 10^{-8}$	51	$-1.70 \cdot 10^{-7}$
4	$-6.43 \cdot 10^{-8}$	20	$1.75 \cdot 10^{-7}$	36	$-2.38 \cdot 10^{-7}$	52	$-1.04 \cdot 10^{-7}$
5	$-1.17 \cdot 10^{-8}$	21	$1.06 \cdot 10^{-8}$	37	$6.56 \cdot 10^{-8}$	53	$-2.23 \cdot 10^{-7}$
6	$-1.32 \cdot 10^{-7}$	22	$-3.82 \cdot 10^{-9}$	38	$-8.75 \cdot 10^{-10}$	54	$2.95 \cdot 10^{-7}$
7	$-1.90 \cdot 10^{-7}$	23	$-2.10 \cdot 10^{-7}$	39	$-2.38 \cdot 10^{-8}$	55	$-1.85 \cdot 10^{-8}$
8	$2.76 \cdot 10^{-7}$	24	$-6.97 \cdot 10^{-8}$	40	$-1.40 \cdot 10^{-7}$	56	$-1.14 \cdot 10^{-7}$
9	$2.19 \cdot 10^{-8}$	25	$-1.11 \cdot 10^{-7}$	41	$-1.02 \cdot 10^{-7}$		
10	$-6.00 \cdot 10^{-8}$	26	$4.13 \cdot 10^{-8}$	42	$-6.61 \cdot 10^{-7}$		
11	$9.20 \cdot 10^{-8}$	27	$-3.18 \cdot 10^{-7}$	43	$3.89 \cdot 10^{-7}$		
12	$-1.19 \cdot 10^{-7}$	28	$-2.13 \cdot 10^{-7}$	44	$-1.29 \cdot 10^{-7}$		
13	$1.49 \cdot 10^{-7}$	29	$-1.63 \cdot 10^{-7}$	45	$-2.82 \cdot 10^{-7}$		
14	$-1.67 \cdot 10^{-7}$	30	$2.55 \cdot 10^{-7}$	46	$2.13 \cdot 10^{-7}$		
15	$5.17 \cdot 10^{-8}$	31	$-1.63 \cdot 10^{-7}$	47	$-4.35 \cdot 10^{-8}$		
16	$5.19 \cdot 10^{-8}$	32	$-1.38 \cdot 10^{-8}$	48	$-7.97 \cdot 10^{-8}$		

Table C.4.: The average correlation values SCC_l in Lab 2 for the measurement run from 14th June 2016. The statistical error for all values is given by $\sigma = 1.55 \cdot 10^{-7}$.

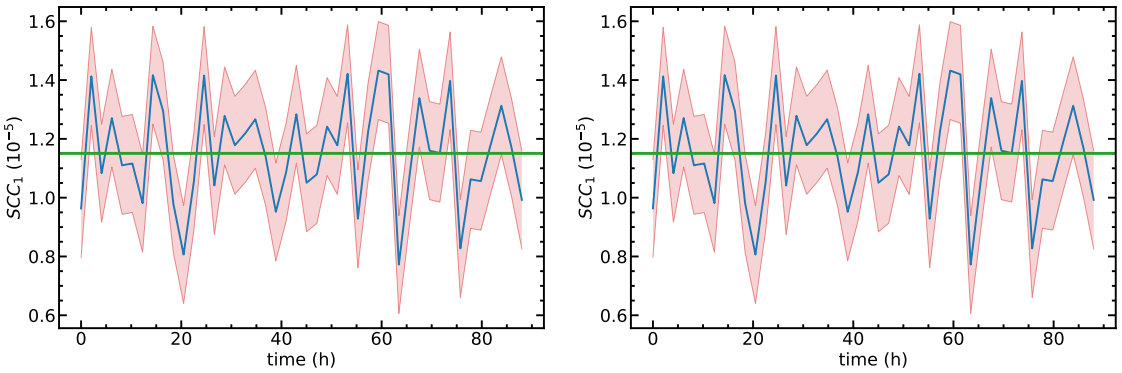

(a) Measurement run from 15th April 2016 in Lab 1

(b) Measurement run from 15th April 2016 in Lab 2

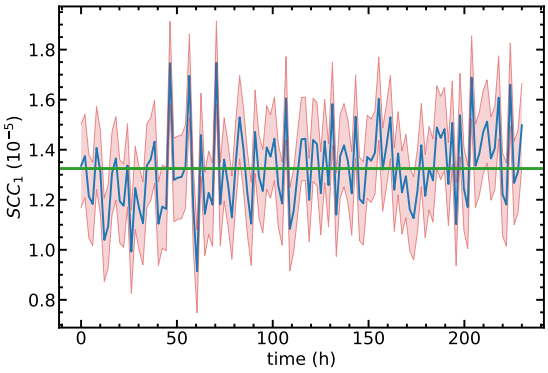

(c) Measurement run from 14th June 2016 in Lab 1

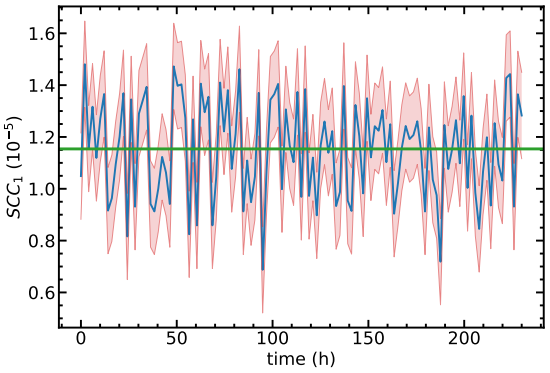

(d) Measurement run from 14th June 2016 in Lab 2

Figure C.2.: The time evolution of SCC1 observed for the measurement runs from 15th April 2016 and 14th June 2016 in both labs (blue lines). Each data point contains 360Gb of data and represents a measurement time of 2 h. The areas shaded in red indicates the $\pm\sigma$ interval, and the green lines show the average correlation values.

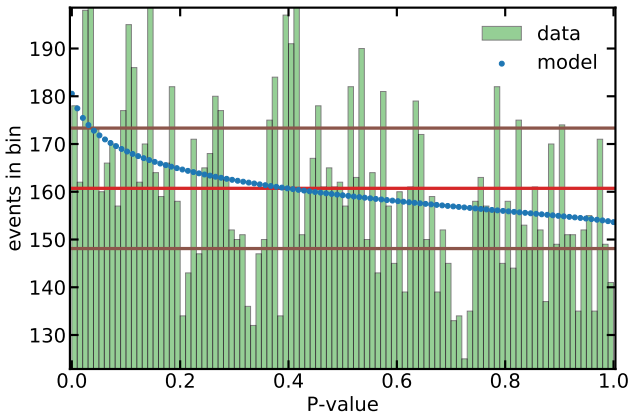

(a) Sequences of 2 bits (L=4)

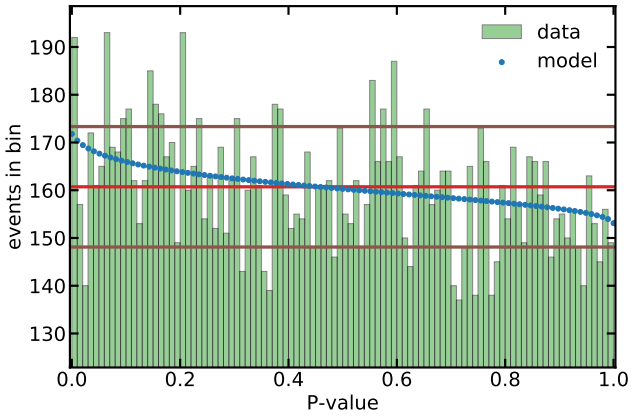

(b) Sequences of 4 bits (L=16)

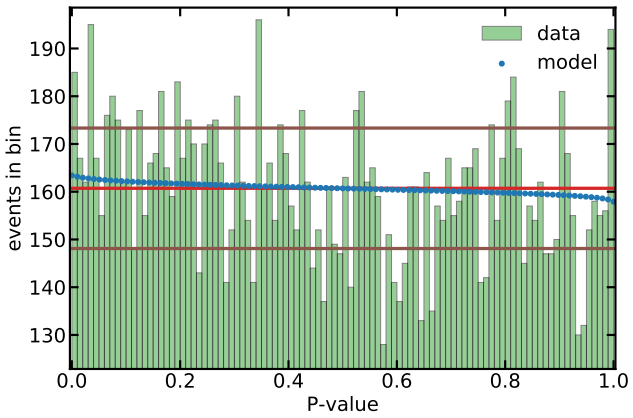

(c) Sequences of 8 bits (L=256)

Figure C.3.: Histograms of the P-value distributions for the test ”smultin_MultinomialBits“ (sequences of 2 bits (L=4), 4 bits (L=16) and 8 bits (L=256)) are applied to the data of Lab 1 in the measurement run of 15th April 2016. The blue dots represent the expected behavior of the model based on the observed bias and next neighbor correlation of this data set. The mean value and the $\pm\sigma$ interval for the histogram bins are shown as red and brown lines, respectively.

D. General Expressions of the Dipole Emission Characteristic

The electric field $\mathbf{E}^{(p)}(\mathbf{r})$ radiated by a dipole (Eqn. (4.2)) of arbitrary oscillation direction $\mathbf{e}_p = (p_x, p_y, p_z)$ located in the origin of the coordinate system is given by

$$\begin{aligned}\mathbf{E}^{(p)}(\mathbf{r}) &= E_0 \frac{e^{ikr}}{r}\left[(\mathbf{e}_\mathrm{r} \times \mathbf{e}_\mathrm{p}) \times \mathbf{e}_\mathrm{r}\right] = E_0 \frac{e^{ikr}}{r}\left[\mathbf{e}_\mathrm{p} - \mathbf{e}_\mathrm{r}(\mathbf{e}_\mathrm{r} \cdot \mathbf{e}_\mathrm{p})\right] \\ &= E_0 \frac{e^{ikr}}{r}\begin{pmatrix} p_x\left(1 - sin^2(\theta)\, cos^2(\phi)\right) + \frac{p_y}{2}\left(-sin^2(\theta)\, sin(2\phi)\right) + \frac{p_z}{2}\left(-sin(2\theta)\, cos(\phi)\right) \\ \frac{p_x}{2}\left(-sin^2(\theta)\, sin(2\phi)\right) + p_y\left(1 - sin^2(\theta)\, sin^2(\phi)\right) + \frac{p_z}{2}\left(-sin(2\theta)\, sin(\phi)\right) \\ \frac{p_x}{2}\left(-sin(2\theta)\, cos(\phi)\right) + \frac{p_y}{2}\left(-sin(2\theta)\, sin(\phi)\right) + p_z\left(1 - cos^2(\theta)\right) \end{pmatrix}\end{aligned} \tag{D.1}$$

with $E_0 = {}^{k^2}/_{4\pi\epsilon_0\epsilon_r}$ and $\|p_x\|^2 + \|p_y\|^2 + \|p_z\|^2 = 1$. Inserting Eqn. (D.1) in Eqn. (4.6) results in the dipole emission characteristic $\frac{\mathrm{dP^{(p)}}}{\mathrm{d}\Omega}(\mathbf{r})$ for an arbitrary oscillation direction:

$$\begin{aligned}\frac{\mathrm{dP^{(p)}}}{\mathrm{d}\Omega}(\mathbf{r}) =& \frac{1}{N_{norm}} r^2 \left\|\mathbf{E}^{(p)}(\mathbf{r})\right\|^2 \\ =& \frac{3}{8\pi}\Big(\|p_x\|^2\left(1 - sin^2(\theta)\, cos^2(\phi)\right) \\ &+ \|p_y\|^2\left(1 - sin^2(\theta)\, sin^2(\phi)\right) \\ &+ \|p_z\|^2\left(1 - cos^2(\theta)\right) \\ &+ \frac{\left(p_x p_y^* + p_x^* p_y\right)}{2}\left(-sin^2(\theta)\, sin(2\phi)\right) \\ &+ \frac{\left(p_x p_z^* + p_x^* p_z\right)}{2}\left(-sin(2\theta)\, cos(\phi)\right) \\ &+ \frac{\left(p_y p_z^* + p_y^* p_z\right)}{2}\left(-sin(2\theta)\, sin(\phi)\right)\Big).\end{aligned} \tag{D.2}$$

Here $N_{norm} = \frac{8\pi}{3}E_0^2$ and $(\cdot)^*$ denotes the complex conjugate. For the special cases of $\mathbf{e}_p = \mathbf{e}_{\sigma^\pm} = {}^1/\sqrt{2}\,(\mp i, 1, 0)$ and $\mathbf{e}_p = \mathbf{e}_\pi = (0, 0, 1)$, Equation (D.2) leads to the dipole emission characteristic for $\sigma^\pm$- and π-light (Eqn. (4.8) and Eqn. (4.9)).

Expressions for Arbitrary Atom Locations The general expressions of the electric field $\mathbf{E}^{(p)}(\mathbf{r} - \mathbf{r}')$ radiated by a dipole oscillating along $\mathbf{e}_p = (p_x, p_y, p_z)$ at location $\mathbf{r}'$ is given in Cartesian coordinates by

$$\mathbf{E}^{(p)}\left(\mathbf{r}-\mathbf{r}^{\prime}\right)=E_0\frac{e^{ik\sqrt{(x-x')^2+(y-y')^2+(z-z')^2}}\sqrt{z-z'}}{\left((x-x')^2+(y-y')^2+(z-z')^2\right)^{7/4}} \tag{D.3}$$
$$\cdot\begin{pmatrix} p_x\left((y-y')^2+(z-z')^2\right)+p_y\left(-(x-x')(y-y')\right)+p_z\left(-(x-x')(z-z')\right)\\ p_x\left(-(x-x')(y-y')\right)+p_y\left((x-x')^2+(z-z')^2\right)+p_z\left(-(y-y')(z-z')\right)\\ p_x\left(-(x-x')(z-z')\right)+p_y\left(-(y-y')(z-z')\right)+p_z\left((x-x')^2+(y-y')^2\right)\end{pmatrix}$$

and the dipole emission characteristic $\frac{\mathrm{dP^{(p)}}}{\mathrm{dA}}\left(\mathbf{r}-\mathbf{r}^{\prime}\right)$

$$\begin{aligned}\frac{\mathrm{dP^{(p)}}}{\mathrm{dA}}\left(\mathbf{r}-\mathbf{r}^{\prime}\right)=&\frac{3}{8\pi}\frac{(z-z')}{\left((x-x')^2+(y-y')^2+(z-z')^2\right)^{5/2}}\\ &\cdot\left(\|p_x\|^2\left((y-y')^2+(z-z')^2\right)\right. &\text{(D.4)}\\ &+\|p_y\|^2\left((x-x')^2+(z-z')^2\right) &\text{(D.5)}\\ &+\|p_z\|^2\left((x-x')^2+(y-y')^2\right) &\text{(D.6)}\\ &+\left(p_xp_y^*+p_x^*p_y\right)\left(-(x-x')(y-y')\right) &\text{(D.7)}\\ &+\left(p_xp_z^*+p_x^*p_z\right)\left(-(x-x')(z-z')\right) &\text{(D.8)}\\ &\left.+\left(p_yp_z^*+p_y^*p_z\right)\left(-(y-y')(z-z')\right)\right). &\text{(D.9)}\end{aligned}$$

Bibliography

[1] M. K. E. L. Planck. Zur Theorie des Gesetzes der Energieverteilung im Normalspektrum. In *Verhandlungen der Deutschen Physikalischen Gesellschaft*, volume 2, pages 237–245. 1900.

[2] N. Bohr. I. On the constitution of atoms and molecules. *The London, Edinburgh, and Dublin Philosophical Magazine and Journal of Science*, 26(151):1–25, jul 1913. doi: 10.1080/14786441308634955. URL https://doi.org/10.1080/14786441308634955.

[3] W. Heisenberg. Über quantentheoretische Umdeutung kinematischer und mechanischer Beziehungen. *Zeitschrift für Physik*, 33(1):879–893, 1925. doi: 10.1007/BF01328377. URL https://doi.org/10.1007/BF01328377.

[4] W. Heisenberg. Über den anschaulichen Inhalt der quantentheoretischen Kinematik und Mechanik. *Zeitschrift für Physik*, 43(3):172–198, 1927. doi: 10.1007/BF01397280. URL https://doi.org/10.1007/BF01397280.

[5] E. Schrödinger. Quantisierung als Eigenwertproblem. *Annalen der Physik*, 384(4):361–376, 1926. doi: 10.1002/andp.19263840404. URL https://doi.org/10.1002/andp.19263840404.

[6] S. A. Camejo. *Die Bohr-Einstein-Debatte*, In *Skurrile Quantenwelt*, pages 87–101. Springer Berlin Heidelberg, 2006. ISBN 978-3-540-29721-5. doi: 10.1007/3-540-29721-9_10. URL https://doi.org/10.1007/3-540-29721-9_10.

[7] A. Einstein et al. Can Quantum-Mechanical Description of Physical Reality Be Considered Complete? *PR*, 47:777–780, 1935. doi: 10.1103/PhysRev.47.777. URL https://doi.org/10.1103/PhysRev.47.777.

[8] N. Bohr. Can Quantum-Mechanical Description of Physical Reality be Considered Complete? *PR*, 48:696–702, 1935. doi: 10.1103/PhysRev.48.696. URL https://doi.org/10.1103/PhysRev.48.696.

[9] E. Schrödinger. Discussion of Probability Relations between Separated Systems. *Mathematical Proceedings of the Cambridge Philosophical Society*, 31(4):555–563, 1935. doi: 10.1017/S0305004100013554. URL https://doi.org/10.1017/S0305004100013554.

[10] E. Schrödinger. Probability relations between separated systems. *Mathematical Proceedings of the Cambridge Philosophical Society*, 32(3):446–452, 1936. doi: 10.1017/S0305004100019137. URL https://doi.org/10.1017/S0305004100019137.

[11] J. S. Bell. On the Einstein Podolsky Rosen paradox. *Physics Physique Fizika*, 1:195–200, Nov 1964. doi: 10.1103/PhysicsPhysiqueFizika.1.195. URL https://doi.org/10.1103/PhysicsPhysiqueFizika.1.195.

[12] J. F. Clauser et al. Proposed Experiment to Test Local Hidden-Variable Theories. *PRL*, 23: 880–884, 1969. doi: 10.1103/PhysRevLett.23.880. URL https://doi.org/10.1103/PhysRevLett.23.880.

[13] S. J. Freedman and J. F. Clauser. Experimental Test of Local Hidden-Variable Theories. *PRL*, 28:938–941, 1972. doi: 10.1103/PhysRevLett.28.938. URL https://doi.org/10.1103/PhysRevLett.28.938.

[14] J. F. Clauser and A. Shimony. Bell's theorem. Experimental tests and implications. *Reports on Progress in Physics*, 41:1881–1927, 1978. doi: 10.1088/0034-4885/41/12/002. URL https://doi.org/10.1088/0034-4885/41/12/002.

[15] A. Aspect et al. Experimental Realization of Einstein-Podolsky-Rosen-Bohm Gedankenexperiment: A New Violation of Bell's Inequalities. *PRL*, 49:91–94, 1982. doi: 10.1103/PhysRevLett.49.91. URL https://doi.org/10.1103/PhysRevLett.49.91.

[16] A. Aspect et al. Experimental Test of Bell's Inequalities Using Time-Varying Analyzers. *PRL*, 49:1804–1807, 1982. doi: 10.1103/PhysRevLett.49.1804. URL https://doi.org/10.1103/PhysRevLett.49.1804.

[17] J.-Å. Larsson. Loopholes in Bell inequality tests of local realism. *Journal of Physics A: Mathematical and Theoretical*, 47:424003, 2014. doi: 10.1088/1751-8113/47/42/424003. URL https://doi.org/10.1088/1751-8113/47/42/424003.

[18] B. Hensen et al. Loophole-free Bell inequality violation using electron spins separated by 1.3 kilometres. *Nature*, 526:682–686, 2015. doi: 10.1038/nature15759. URL https://doi.org/10.1038/nature15759.

[19] L. K. Shalm et al. Strong Loophole-Free Test of Local Realism. *PRL*, 115:250402, 2015. doi: 10.1103/PhysRevLett.115.250402. URL https://doi.org/10.1103/PhysRevLett.115.250402.

[20] M. Giustina et al. Significant-Loophole-Free Test of Bell's Theorem with Entangled Photons. *PRL*, 115:250401, 2015. doi: 10.1103/PhysRevLett.115.250401. URL https://doi.org/10.1103/PhysRevLett.115.250401.

[21] W. Rosenfeld et al. Event-Ready Bell Test Using Entangled Atoms Simultaneously Closing Detection and Locality Loopholes. *PRL*, 119:010402, 2017. doi: 10.1103/PhysRevLett.119.010402. URL https://doi.org/10.1103/PhysRevLett.119.010402.

[22] C. H. Bennett and S. J. Wiesner. Communication via one- and two-particle operators on Einstein-Podolsky-Rosen states. *PRL*, 69:2881–2884, Nov 1992. doi: 10.1103/PhysRevLett.69.2881. URL https://doi.org/10.1103/PhysRevLett.69.2881.

[23] V. Giovannetti et al. Quantum-Enhanced Measurements: Beating the Standard Quantum Limit. *Science*, 306(5700):1330–1336, 2004. doi: 10.1126/science.1104149. URL https://doi.org/10.1126/science.1104149.

[24] R. P. Feynman. Simulating physics with computers. *International Journal of Theoretical Physics*, 21:467–488, 1982. doi: 10.1007/BF02650179. URL https://doi.org/10.1007/BF02650179.

[25] F. Arute et al. Quantum supremacy using a programmable superconducting processor. *Nature*, pages 505–510, 2019. doi: 10.1038/s41586-019-1666-5. URL https://doi.org/10.1038/s41586-019-1666-5.

[26] C. H. Bennett et al. Teleporting an unknown quantum state via dual classical and Einstein-Podolsky-Rosen channels. *PRL*, 70:1895–1899, Mar 1993. doi: 10.1103/PhysRevLett.70.1895. URL https://doi.org/10.1103/PhysRevLett.70.1895.

[27] M. Zukowski et al. "Event-ready-detectors" Bell experiment via entanglement swapping. *PRL*, 71:4287–4290, 1993. doi: 10.1103/PhysRevLett.71.4287. URL https://doi.org/10.1103/PhysRevLett.71.4287.

[28] A. K. Ekert. Quantum cryptography based on Bell's theorem. *PRL*, 67:661–663, 1991. doi: 10.1103/PhysRevLett.67.661. URL https://doi.org/10.1103/PhysRevLett.67.661.

[29] D. Mayers and A. Yao. Quantum cryptography with imperfect apparatus. In *FOCS '98*, pages 503–509. IEEE Computer Society, IEEE Computer Society Washington, DC, USA, 1998. ISBN 0-8186-9172-7. doi: 10.1109/SFCS.1998.743501. URL https://doi.org/10.1109/SFCS.1998.743501.

[30] S. Pironio et al. Random numbers certified by Bell's theorem. *Nature*, 464:1021–1024, 2010. doi: 10.1038/nature09008. URL https://doi.org/10.1038/nature09008.

[31] H. J. Kimble. The quantum internet. *Nature*, 453:1023–1030, 2008. doi: 10.1038/nature07127. URL https://doi.org/10.1038/nature07127.

[32] J. Volz et al. Observation of Entanglement of a Single Photon with a Trapped Atom. *PRL*, 96: 030404, 2006. doi: 10.1103/PhysRevLett.96.030404. URL https://doi.org/10.1103/PhysRevLett.96.030404.

[33] S. Ritter et al. An elementary quantum network of single atoms in optical cavities. *Nature*, 484:195–200, 2012. doi: 10.1038/nature11023. URL https://doi.org/10.1038/nature11023.

[34] B. B. Blinov et al. Observation of entanglement between a single trapped atom and a single photon. *Nature*, 428(6979):153–157, 2004. doi: 10.1038/nature02377. URL https://doi.org/10.1038/nature02377.

[35] L.-M. Duan and C. Monroe. Colloquium: Quantum networks with trapped ions. *Rev. Mod. Phys.*, 82:1209–1224, Apr 2010. doi: 10.1103/RevModPhys.82.1209. URL https://doi.org/10.1103/RevModPhys.82.1209.

[36] M. D. Lukin et al. Entanglement of Atomic Ensembles by Trapping Correlated Photon States. *PRL*, 84:4232–4235, May 2000. doi: 10.1103/PhysRevLett.84.4232. URL https://doi.org/10.1103/PhysRevLett.84.4232.

[37] A. Kuzmich et al. Generation of nonclassical photon pairs for scalable quantum communication with atomic ensembles. *Nature*, 423(6941):731–734, 2003. doi: 10.1038/nature01714. URL https://doi.org/10.1038/nature01714.

[38] N. Sangouard et al. Quantum repeaters based on atomic ensembles and linear optics. *Rev. Mod. Phys.*, 83:33–80, Mar 2011. doi: 10.1103/RevModPhys.83.33. URL https://doi.org/10.1103/RevModPhys.83.33.

[39] C. Kurtsiefer et al. Stable Solid-State Source of Single Photons. *PRL*, 85:290–293, Jul 2000. doi: 10.1103/PhysRevLett.85.290. URL https://doi.org/10.1103/PhysRevLett.85.290.

[40] N. Kalb et al. Entanglement distillation between solid-state quantum network nodes. *Science*, 356:928–932, 2017. doi: 10.1126/science.aan0070. URL http://doi.org/10.1126/science.aan0070.

[41] C. Santori et al. Indistinguishable photons from a single-photon device. *Nature*, 419(6907): 594–597, 2002. doi: 10.1038/nature01086. URL https://doi.org/10.1038/nature01086.

[42] L. Childress et al. Fault-tolerant quantum repeaters with minimal physical resources and implementations based on single-photon emitters. *PRA*, 72:052330, Nov 2005. doi: 10.1103/PhysRevA.72.052330. URL https://doi.org/10.1103/PhysRevA.72.052330.

[43] C. Laplane et al. Multimode and Long-Lived Quantum Correlations Between Photons and Spins in a Crystal. *PRL*, 118:210501, May 2017. doi: 10.1103/PhysRevLett.118.210501. URL https://doi.org/10.1103/PhysRevLett.118.210501.

[44] K. Kutluer et al. Solid-State Source of Nonclassical Photon Pairs with Embedded Multimode Quantum Memory. *PRL*, 118:210502, May 2017. doi: 10.1103/PhysRevLett.118.210502. URL https://doi.org/10.1103/PhysRevLett.118.210502.

[45] Y. O. Dudin et al. Entanglement of Light-Shift Compensated Atomic Spin Waves with Telecom Light. *PRL*, 105:260502, Dec 2010. doi: 10.1103/PhysRevLett.105.260502. URL https://doi.org/10.1103/PhysRevLett.105.260502.

[46] R. Ikuta et al. Polarization insensitive frequency conversion for an atom-photon entanglement distribution via a telecom network. *Nature Communications*, 9(1):1997, 2018. doi: 10.1038/s41467-018-04338-x. URL https://doi.org/10.1038/s41467-018-04338-x.

[47] H.-J. Briegel et al. Quantum Repeaters: The Role of Imperfect Local Operations in Quantum Communication. *PRL*, 81:5932–5935, 1998. doi: 10.1103/PhysRevLett.81.5932. URL https://doi.org/10.1103/PhysRevLett.81.5932.

[48] M. Weber. *Quantum optical experiments towards atom-photon entanglement*. PhD thesis, Ludwig-Maximilians-Universität München, 2005. URL https://xqp.physik.uni-muenchen.de/publications/theses_phd/phd_weber.html.

[49] J. Volz. *Atom-Photon Entanglement*. PhD thesis, Ludwig-Maximilians-Universität München, 2006. URL https://xqp.physik.uni-muenchen.de/publications/theses_phd/phd_volz.html.

[50] J. Hofmann et al. Heralded Entanglement Between Widely Separated Atoms. *Science*, 337: 72–75, 2012. doi: 10.1126/science.1221856. URL https://doi.org/10.1126/science.1221856.

[51] J. Hofmann. *Heralded Atom-Atom Entanglement*. PhD thesis, Ludwig-Maximilians-Universität München, 2014. URL https://xqp.physik.uni-muenchen.de/publications/theses_phd/phd_hofmann.html.

[52] N. Ortegel. *State readout of single Rubidium-87 atoms for a loophole-free test of Bell's inequality*. PhD thesis, Ludwig-Maximilians-Universität München, 2016. URL https://xqp.physik.uni-muenchen.de/publications/theses_phd/phd_ortegel.html.

[53] D. Burchardt. *A Rigorous Test of Bell's Inequality and Quantum Teleportation Employing Single Atoms*. PhD thesis, Ludwig-Maximilians-Universität München, 2018. URL https://xqp.physik.uni-muenchen.de/publications/theses_phd/phd_burchardt.html.

[54] M. Fürst et al. High speed optical quantum random number generation. *Opt. Express*, 18: 13029–13037, 2010. doi: 10.1364/OE.18.013029. URL https://doi.org/10.1364/OE.18.013029.

[55] K. Redeker. *Entanglement of Single Rubidium Atoms: From a Bell Test Towards Applications*. PhD thesis, Ludwig-Maximilians-Universität München, 2020. URL https://xqp.physik.uni-muenchen.de/publications/theses_phd/phd_redeker.html.

[56] D. A. Steck. Rubidium 87 D Line Data. Version 2.2.1 from 21 November 2019. URL http://steck.us/alkalidata/rubidium87numbers.pdf.

[57] E. L. Raab et al. Trapping of Neutral Sodium Atoms with Radiation Pressure. *PRL*, 59: 2631–2634, 1987. doi: 10.1103/PhysRevLett.59.2631. URL https://doi.org/10.1103/PhysRevLett.59.2631.

[58] S. Chu et al. Experimental Observation of Optically Trapped Atoms. *PRL*, 57:314–317, 1986. doi: 10.1103/PhysRevLett.57.314. URL https://doi.org/10.1103/PhysRevLett.57.314.

[59] J. Dalibard and C. Cohen-Tannoudji. Laser cooling below the Doppler limit by polarization gradients: simple theoretical models. *Journal of the Optical Society of America B*, 6(11): 2023–2045, 1989. doi: 10.1364/JOSAB.6.002023. URL https://doi.org/10.1364/JOSAB.6.002023.

[60] R. Grimm et al. Optical Dipole Traps for Neutral Atoms. 42:95–170, 2000. doi: 10.1016/S1049-250X(08)60186-X. URL https://doi.org/10.1016/S1049-250X(08)60186-X.

[61] N. Schlosser et al. Collisional Blockade in Microscopic Optical Dipole Traps. *PRL*, 89: 023005, Jun 2002. doi: 10.1103/PhysRevLett.89.023005. URL https://doi.org/10.1103/PhysRevLett.89.023005.

[62] J. D. Jackson. *Classical electrodynamics*. Wiley, New York, NY, 3rd ed. edition, 1999. ISBN 9780471309321. URL http://cdsweb.cern.ch/record/490457.

[63] R. Gehr et al. Cavity-Based Single Atom Preparation and High-Fidelity Hyperfine State Readout. *PRL*, 104(20):203602, May 2010. doi: 10.1103/physrevlett.104.203602. URL https://doi.org/10.1103/PhysRevLett.104.203602.

[64] J. Bochmann et al. Lossless State Detection of Single Neutral Atoms. *PRL*, 104:203601, May 2010. doi: 10.1103/PhysRevLett.104.203601. URL https://doi.org/10.1103/PhysRevLett.104.203601.

[65] F. Henkel. *Photoionisation detection of single Rb-87 atoms using channel electron multipliers*. PhD thesis, Ludwig-Maximilians-Universität München, 2011. URL https://xqp.physik.uni-muenchen.de/publications/theses_phd/phd_henkel.html.

[66] M. Krug. *Ionization Based State Read Out of a single Rb-87 Atom*. PhD thesis, Ludwig-Maximilians-Universität München, 2018. URL http://xqp.physik.uni-muenchen.de/publications/theses_phd/phd_krug.html.

[67] W. Rosenfeld. *Experiments with an Entangled System of a Single Atom and a Single Photon*. PhD thesis, Ludwig-Maximilians-Universität München, 2008. URL https://xqp.physik.uni-muenchen.de/publications/theses_phd/phd_rosenfeld.html.

[68] C. Cohen-Tannoudji, B. Diu, and F. Laloë. *Quantum Mechanics*, chapter VI, page 659. Wiley, New York, 1977. ISBN 978-3-527-82271-3.

[69] D. Taray. Towards Increasing Atomic Coherence Times with a Standing Wave Dipole Trap. Master's thesis, Ludwig-Maximilians-Universität München, 2020.

[70] E. Wolf. Electromagnetic diffraction in optical systems - I. An integral representation of the image field. *Proceedings of the Royal Society of London A: Mathematical, Physical and Engineering Sciences*, 253:349–357, 1959. doi: 10.1098/rspa.1959.0199. URL https://doi.org/10.1098/rspa.1959.0199.

[71] B. Richards and E. Wolf. Electromagnetic diffraction in optical systems, II. Structure of the image field in an aplanatic system. *Proceedings of the Royal Society of London A: Mathematical, Physical and Engineering Sciences*, 253:358–379, 1959. doi: 10.1098/rspa.1959.0200. URL https://doi.org/10.1098/rspa.1959.0200.

[72] J.-W. Pan et al. Experimental Entanglement Swapping: Entangling Photons That Never Interacted. *PRL*, 80:3891–3894, 1998. doi: 10.1103/PhysRevLett.80.3891. URL https://doi.org/10.1103/PhysRevLett.80.3891.

[73] C. K. Hong et al. Measurement of subpicosecond time intervals between two photons by interference. *PRL*, 59:2044–2046, 1987. doi: 10.1103/PhysRevLett.59.2044. URL https://doi.org/10.1103/PhysRevLett.59.2044.

[74] W. Rosenfeld et al. Towards high-fidelity interference of photons emitted by two remotely trapped Rb-87 atoms. *Optics and Spectroscopy*, 111:535, 2011. doi: 10.1134/S0030400X11110233. URL https://doi.org/10.1134/S0030400X11110233.

[75] W. Rosenfeld et al. Towards Long-Distance Atom-Photon Entanglement. *PRL*, 101(26): 260403, 2008. doi: 10.1103/PhysRevLett.101.260403. URL https://doi.org/10.1103/PhysRevLett.101.260403.

[76] L.-M. Duan et al. Long-distance quantum communication with atomic ensembles and linear optics. *Nature*, 414:413–418, 2001. doi: 10.1038/35106500. URL https://doi.org/10.1038/35106500.

[77] M. Körber et al. Decoherence-protected memory for a single-photon qubit. *Nature Photonics*, 12:18–21, 2018. doi: 10.1038/s41566-017-0050-y. URL https://doi.org/10.1038/s41566-017-0050-y.

[78] J. Huang and P. Kumar. Observation of quantum frequency conversion. *PRL*, 68:2153–2156, Apr 1992. doi: 10.1103/PhysRevLett.68.2153. URL https://doi.org/10.1103/PhysRevLett.68.2153.

[79] T. van Leent et al. Long-Distance Distribution of Atom-Photon Entanglement at Telecom Wavelength. *PRL*, 124:010510, 2020. doi: 10.1103/PhysRevLett.124.010510. URL https://doi.org/10.1103/PhysRevLett.124.010510.

[80] B. S. Cirel'son. Quantum generalizations of Bell's inequality. *Letters in Mathematical Physics*, 4:93–100, 1980. doi: 10.1007/BF00417500. URL https://doi.org/10.1007/BF00417500.

[81] A. Garg and N. D. Mermin. Detector inefficiencies in the Einstein-Podolsky-Rosen experiment. *PRD*, 35:3831–3835, 1987. doi: 10.1103/PhysRevD.35.3831. URL https://doi.org/10.1103/PhysRevD.35.3831.

[82] J.-Å. Larsson. Bell's inequality and detector inefficiency. *PRA*, 57:3304–3308, 1998. doi: 10.1103/PhysRevA.57.3304. URL https://doi.org/10.1103/PhysRevA.57.3304.

[83] M. A. Rowe et al. Experimental violation of a Bell's inequality with efficient detection. *Nature*, 409:791–794, 2001. doi: 10.1038/35057215. URL https://doi.org/10.1038/35057215.

[84] G. Weihs et al. Violation of Bell's Inequality under Strict Einstein Locality Conditions. *PRL*, 81(23):5039–5043, 1998. doi: 10.1103/PhysRevLett.81.5039. URL https://doi.org/10.1103/PhysRevLett.81.5039.

[85] J. Barrett et al. Quantum nonlocality, Bell inequalities, and the memory loophole. *PRA*, 66: 042111, 2002. doi: 10.1103/PhysRevA.66.042111. URL https://doi.org/10.1103/PhysRevA.66.042111.

[86] J. S. Bell. An Exchange on Local Beables. *Dialectica*, 39(2):85–96, 1985. doi: 10.1111/j.1746-8361.1985.tb01249.x. URL https://doi.org/10.1111/j.1746-8361.1985.tb01249.x.

[87] R. D. Gill. Time, Finite Statistics, and Bell's Fifth Position. In *Proceedings of "Foundations of Probability and Physics - 2",*, Ser. Math. Modelling in Phys., Engin., and Cogn. Sc., pages 179–206. Växjö University, 2003. URL https://arxiv.org/abs/quant-ph/0301059v2.

[88] N. Brunner et al. Bell nonlocality. *RMP*, 86:419–478, 2014. doi: 10.1103/RevModPhys.86.419. URL https://doi.org/10.1103/RevModPhys.86.419.

[89] D. Elkouss and S. Wehner. (Nearly) optimal P values for all Bell inequalities. *Npj Quantum Information*, 2:16026, 2016. doi: 10.1038/npjqi.2016.26. URL https://doi.org/10.1038/npjqi.2016.26.

[90] R. Loudon. *The Quantum Theory of Light*. Oxford University Press, third edition edition, 2000. ISBN 0-19-850176-5.

[91] R. J. Glauber. *The Initiation of Superfluorescence*, In *Quantum Theory of Optical Coherence*, chapter 13, pages 531–536. John Wiley & Sons, Ltd, 2006. ISBN 9783527610075. doi: 10.1002/9783527610075.ch13. URL https://doi.org/10.1002/9783527610075.ch13.

[92] P. L'Ecuyer and R. Simard. TestU01: A C Library for Empirical Testing of Random Number Generators. *ACM Trans. Math. Softw.*, 33(4), August 2007. doi: 10.1145/1268776.1268777. URL https://doi.org/10.1145/1268776.1268777.

[93] M. Jeng. A selected history of expectation bias in physics. *American Journal of Physics*, 74: 578–583, 2006. doi: 10.1119/1.2186333. URL https://doi.org/10.1119/1.2186333.

[94] C. McDiarmid. On the method of bounded differences. In J. Siemons, editor, *Surveys in Combinatorics*, London Mathematical Society Lecture Note Series, pages 148–188. Cambridge University Press, Cambridge, 1989. doi: 10.1017/cbo9781107359949.008. URL https://doi.org/10.1017/cbo9781107359949.008.

[95] D. Mayers and A. Yao. Self testing quantum apparatus. *Quantum Info. Comput.*, 4:273–286, 2004. doi: 10.26421/QIC4.4. URL https://doi.org/10.26421/QIC4.4.

[96] J.-D. Bancal et al. Self-testing with finite statistics enabling the certification of a quantum network link. *Quantum*, 5:401, March 2021. doi: 10.22331/q-2021-03-02-401. URL https://doi.org/10.22331/q-2021-03-02-401.

[97] T. Hummel. Increasing Photon Collection Efficiency for Generating Long-distance Entanglement of Atoms. Master's thesis, Ludwig-Maximilians-Universität München, 2018. URL https://xqp.physik.uni-muenchen.de/publications/theses_master/master_hummel.html.

[98] M. Seubert. Analyzing and Optimizing the Process of Single Photon Collection. Master's thesis, Ludwig-Maximilians-Universität München, 2020.

[99] M. O. Scully and M. S. Zubairy. *Quantum Optics*. Cambridge University Press, 1997. doi: 10.1017/CBO9780511813993. URL https://doi.org/10.1017/CBO9780511813993.

[100] I. V. Hertel and C.-P. Schulz. *Atome, Moleküle und optische Physik 1*, volume 1. Springer, 2008. ISBN 978-3-662-46807-4. doi: 10.1007/978-3-662-46808-1. URL https://doi.org/10.1007/978-3-662-46808-1.

[101] W. Nolting. *Electrodynamics*, In *Theoretical Physics 3*, pages 207–419. Springer, 2016. ISBN 978-3-319-40168-3. doi: 10.1007/978-3-319-40168-3_4. URL https://doi.org/10.1007/978-3-319-40168-3_4.

[102] K. Zimmerman. Developing the Rendering Equations, 2010. URL https://www.cs.princeton.edu/courses/archive/fall10/cos526/papers/zimmerman98.pdf.

[103] M. Sondermann et al. Maximizing the electric field strength in the foci of high numerical aperture optics. *arXiv:0811.2098*, 2008. URL https://arxiv.org/abs/0811.2098.

[104] M. Wilson. Collecting Light: The Importance of Numerical Aperture in Microscopy. https://www.leica-microsystems.com/science-lab/collecting-light-the-importance-of-numerical-aperture-in-microscopy/, 2017.

[105] M. Sondermann and G. Leuchs. *Photon-Atom Coupling with Parabolic Mirrors*, In *Engineering the Atom-Photon Interaction: Controlling Fundamental Processes with Photons, Atoms and Solids*, pages 75–98. Springer International Publishing, Cham, 2015. ISBN 978-3-319-19231-4. doi: 10.1007/978-3-319-19231-4_3. URL https://doi.org/10.1007/978-3-319-19231-4_3.

[106] D. Gloge. Weakly Guiding Fibers. *Appl. Opt.*, 10(10):2252–2258, Oct 1971. doi: 10.1364/AO.10.002252. URL https://doi.org/10.1364/AO.10.002252.

[107] L. J. Stephenson et al. High-Rate, High-Fidelity Entanglement of Qubits Across an Elementary Quantum Network. *PRL*, 124:110501, Mar 2020. doi: 10.1103/PhysRevLett.124.110501. URL https://doi.org/10.1103/PhysRevLett.124.110501.

[108] H. Gross, F. Blechinger, and B. Achtner. *Fundamentals of Technical Optics*, volume 1. Wiley Online Library, January 2005. ISBN 9783527699223. doi: 10.1002/9783527699223. URL https://doi.org/10.1002/9783527699223.

[109] R. Barakat. Rayleigh Wavefront Criterion. *J. Opt. Soc. Am.*, 55(5):572–573, May 1965. doi: 10.1364/JOSA.55.000572. URL https://doi.org/10.1364/JOSA.55.000572.

[110] H. Gross, H. Zügge, M. Peschka, and F. Blechinger. *Aberration Theory and Correction of Optical Systems*, volume 3. Wiley Online Library, December 2007. ISBN 9783527699254. doi: 10.1002/9783527699254. URL https://doi.org/10.1002/9783527699254.

[111] R. J. Noll. Zernike polynomials and atmospheric turbulence*. *J. Opt. Soc. Am.*, 66(3): 207–211, Mar 1976. doi: 10.1364/JOSA.66.000207. URL https://doi.org/10.1364/JOSA.66.000207.

[112] E. P. Goodwin and J. C. Wyant. *Field Guide to Interferometric Optical Testing*, volume FG10. September 2006. ISBN 9780819465108.

[113] W. Alt. An objective lens for efficient fluorescence detection of single atoms. *Optik*, 113(3): 142–144, 2002. doi: 10.1078/0030-4026-00133. URL https://doi.org/10.1078/0030-4026-00133.

[114] F. Kleißler. Assembly and Characterization of a High Numerical Aperture Microscope for Single Atoms. Master's thesis, 2014. URL http://quantum-technologies.iap.uni-bonn.de/de/group-members/188-felix-kleissler.html.

[115] A. Alberti et al. Super-resolution microscopy of single atoms in optical lattices. *New Journal of Physics*, 18(5):053010, may 2016. doi: 10.1088/1367-2630/18/5/053010. URL https://doi.org/10.1088/1367-2630/18/5/053010.

[116] C. Robens et al. High numerical aperture (NA = 0,92) objective lens for imaging and addressing of cold atoms. *Opt. Lett.*, 42(6):1043–1046, Mar 2017. doi: 10.1364/OL.42.001043. URL https://doi.org/10.1364/OL.42.001043.

[117] S.-U. Hwang and Y.-G. Lee. Simulation of an oil immersion objective lens: A simplified ray-optics model considering Abbe's sine condition. *Opt. Express*, 16(26):21170–21183, Dec 2008. doi: 10.1364/OE.16.021170. URL https://doi.org/10.1364/OE.16.021170.

[118] J. H. Burge et al. Use of the Abbe Sine Condition to Quantify Alignment Aberrations in Optical Imaging Systems. In *International Optical Design Conference and Optical Fabrication and Testing*, page ITuD5. Optical Society of America, 2010. doi: 10.1364/IODC.2010.ITuD5. URL https://doi.org/10.1364/IODC.2010.ITuD5.

[119] H. H. Hopkins. The airy disc formula for systems of high relative aperture. *Proceedings of the Physical Society*, 55(2):116–128, mar 1943. doi: 10.1088/0959-5309/55/2/305. URL https://doi.org/10.1088/0959-5309/55/2/305.

[120] C. Sheppard and M. Gu. Imaging by a High Aperture Optical System. *Journal of Modern Optics*, 40(8):1631–1651, 1993. doi: 10.1080/09500349314551641. URL https://doi.org/10.1080/09500349314551641.

[121] E. Betzig and R. J. Chichester. Single Molecules Observed by Near-Field Scanning Optical Microscopy. *Science*, 262(5138):1422–1425, 1993. doi: 10.1126/science.262.5138.1422. URL https://doi.org/10.1126/science.262.5138.1422.

[122] J. A. Veerman et al. Single molecule mapping of the optical field distribution of probes for near-field microscopy. *Journal of Microscopy*, 194(2-3):477–482, 1999. doi: 10.1046/j.1365-2818.1999.00520.x. URL https://doi.org/10.1046/j.1365-2818.1999.00520.x.

[123] C. Robens. *Testing the Quantumness of Atom Trajectories*. PhD thesis, 2017. URL http://quantum-technologies.iap.uni-bonn.de/de/group-members/167-carsten-robens.html.

[124] C. Obermüller et al. Transmitted radiation through a subwavelength-sized tapered optical fiber tip. *Ultramicroscopy*, 61(1):171–177, 1995. doi: 10.1016/0304-3991(95)00128-X. URL https://doi.org/10.1016/0304-3991(95)00128-X.

[125] J. Weiner. The physics of light transmission through subwavelength apertures and aperture arrays. *Reports on Progress in Physics*, 72(6):064401, may 2009. doi: 10.1088/0034-4885/72/6/064401. URL https://doi.org/10.1088/0034-4885/72/6/064401.

[126] L. Martín-Moreno et al. Theory of Highly Directional Emission from a Single Subwavelength Aperture Surrounded by Surface Corrugations. *PRL*, 90:167401, Apr 2003. doi: 10.1103/PhysRevLett.90.167401. URL https://doi.org/10.1103/PhysRevLett.90.167401.

[127] T. S. Ross. Limitations and applicability of the Maréchal approximation. *Appl. Opt.*, 48(10): 1812–1818, Apr 2009. doi: 10.1364/AO.48.001812. URL https://doi.org/10.1364/AO.48.001812.

[128] G. Martial. Strehl ratio and aberration balancing. *J. Opt. Soc. Am. A*, 8(1):164–170, Jan 1991. doi: 10.1364/JOSAA.8.000164. URL https://doi.org/10.1364/JOSAA.8.000164.

[129] V. N. Mahajan. Strehl ratio for primary aberrations: some analytical results for circular and annular pupils. *J. Opt. Soc. Am.*, 72(9):1258–1266, Sep 1982. doi: 10.1364/JOSA.72.001258. URL https://doi.org/10.1364/JOSA.72.001258.

[130] Schott AG. Optical glass, data sheets. https://www.schott.com/d/advanced_optics/ac85c64c-60a0-4113-a9df-23ee1be20428/1.1/schott-optical-glass-collection-datasheets-english-17012017.pdf, 2017.

[131] J. A. Arnaud et al. Technique for Fast Measurement of Gaussian Laser Beam Parameters. *Appl. Opt.*, 10(12):2775–2776, Dec 1971. doi: 10.1364/AO.10.002775. URL https://doi.org/10.1364/AO.10.002775.

[132] A. H. Firester et al. Knife-edge scanning measurements of subwavelength focused light beams. *Appl. Opt.*, 16(7):1971–1974, Jul 1977. doi: 10.1364/AO.16.001971. URL https://doi.org/10.1364/AO.16.001971.

[133] P. Marchenko et al. Interaction of highly focused vector beams with a metal knife-edge. *Opt. Express*, 19(8):7244–7261, Apr 2011. doi: 10.1364/OE.19.007244. URL https://doi.org/10.1364/OE.19.007244.

[134] B. E. A. Saleh and M. C. Teich. *Beam Optics - Fundamentals of Photonics*, In *Fundamentals of Photonics*, chapter 3, pages 80–107. John Wiley and Sons, Ltd, 2001. ISBN 9780471213741. doi: 10.1002/0471213748.ch3. URL https://doi.org/10.1002/0471213748.ch3.

[135] B. Albrecht et al. A waveguide frequency converter connecting rubidium-based quantum memories to the telecom c-band. *Nature Communications*, 5(1):3376, 2014. doi: 10.1038/ncomms4376. URL https://doi.org/10.1038/ncomms4376.

[136] Y. Yu et al. Entanglement of two quantum memories via fibres over dozens of kilometres. *Nature*, 578:240–245, 2020. doi: 10.1038/s41586-020-1976-7. URL https://doi.org/10.1038/s41586-020-1976-7.

[137] M. Bock et al. High-fidelity entanglement between a trapped ion and a telecom photon via quantum frequency conversion. *Nature Communications*, 9(1):1998, 2018. doi: 10.1038/s41467-018-04341-2. URL https://doi.org/10.1038/s41467-018-04341-2.

[138] V. Krutyanskiy et al. Light-matter entanglement over 50 km of optical fibre. *npj Quantum Information*, 5(1):72, 2019. doi: 10.1038/s41534-019-0186-3. URL https://doi.org/10.1038/s41534-019-0186-3.

[139] A. Tchebotareva et al. Entanglement between a Diamond Spin Qubit and a Photonic Time-Bin Qubit at Telecom Wavelength. *PRL*, 123:063601, Aug 2019. doi: 10.1103/PhysRevLett.123.063601. URL https://doi.org/10.1103/PhysRevLett.123.063601.

[140] W. Rosenfeld et al. Towards a Loophole-Free Test of Bell's Inequality with Entangled Pairs of Neutral Atoms. *Advanced Science Letters*, 2(4):469–474, 2009. doi: 10.1166/asl.2009.1059. URL https://doi.org/10.1166/asl.2009.1059.

Danksagung

An dieser Stelle möchte ich all jenen Personen meinen großen Dank aussprechen, die mich während der letzten Jahre stets unterstützt, motiviert und aufgemuntert haben und mir somit diese Arbeit erst ermöglichten. Mein besonderer Dank gilt:

- Prof. Dr. Harald Weinfurter für die Aufnahme in seiner Arbeitsgruppe und die damit verbundende Möglichkeit mit vielen Freiheiten an einem spannenden Forschungsprojekt mitgewirkt haben zu dürfen.
- Wenjamin Rosenfeld für seine unermütliche Hilfsbereitschaft und sein großes Engagement, welche sich in etlichen lehrreichen und fruchtbaren Diskussionen wiederspiegelten, die für mich persönlich, sowie für das Gelingen dieser Arbeit von unschätzbaren Wert waren. Während dieser Zeit habe ich ihn als Kollege, Mentor und Freund sehr zu schätzen gelernt.
- Meinen langjährigen Kollegen Norbert Ortegel, Kai Redeker, Daniel Burchardt, Tim van Leent und Wei Zhang für eine angenehme, produktive aber auch lustige Atmosphäre, sei es im Labor, auf Konferenzen oder abseits der Arbeit.
- Meinen beiden Masterstudenten Timon Hummel und Matthias Seubert die mir beim Entwerfen, Charakterisieren und Implementieren der Objektiv-Aufbauten sehr geholfen haben.
- Matthias Bock, Tobias Bauer und Prof. Dr. Christoph Becher für die gelungene Zusammenarbeit beim Telekom-Konversionsexperiment, hierbei insbesondere Matthias für die schönen Monate im Labor.
- Allen weiteren Kollegen aus dem Atomprojekt wie meinen nachfolgenden Doktoranden Florian Fertig, Yiru Zhou und Pooja Malik, sowie den weiteren Masterstudenten Paul Koschmieder, Derya Taray, Sebastian Eppelt und Anastasia Reinl.
- Allen Mitgliedern der Arbeitsgruppe Weinfurter für die spannenden Gespräche, das angenehme Arbeitsumfeld und die schöne Zeit. Hervorzuheben ist Martin Zeitlmair für seine Unterstützung, Beständigkeit und Geduld beim Beschichten der Knife-Edge-Messdioden, sowie der Herstellung der Punktquelle für die Charakterisierungsmessungen.
- Dem gesamten Werkstatt-Team geführt von Jürgen Aust und Thomas Großhauser für ihre hervorragende Arbeit und der präzisen Anfertigung von zahlreichen Haltern und Werkzeugen für die Objektiv-Aufbauten.
- Meinen Eltern, Bruder, Schwiegereltern und Schwager für die anhaltende und bedingungslose Unterstützung der letzten Jahre und insbesondere für die Fürsoge und Liebe die sie seit Geburt gegenüber unserer kleine Tochter aufbringen.
- Meiner Frau Buket für ihre Geduld wenn es später wurde, für das Schaffen von Freiräumen für meine Hobbies, für ihre Unterstützung und Rückhalt wenn mal wieder etwas schief lief und für unsere Tochter Sophia, die unser beider Leben von Grund auf bereichert.